Université de Montréal

The hydrodynamics associated with instream large roughness elements in gravel-bed rivers

(L'hydrodynamique associée aux éléments de rugosité dans les rivières à lit de graviers)

par

R.W. Jay Lacey

Département de géographie

Faculté des arts et des sciences

Thèse présentée à la Faculté des études supérieures

en vue de l'obtention du grade de

Philosophiae Doctor (Ph.D.) en géographie

Décembre, 2007

Univesité de Montréal

Faculté des études supérieures

Cette thèse intitulée:

The hydrodynamics associated with instream large roughness elements in gravel-bed rivers

(L'hydrodynamique associée aux éléments de rugosité dans les rivières à lit de graviers)

présentée par:

R.W. Jay Lacey

a été évaluée par un jury composé des personnes suivantes:

Lael Parrott - présisent-rapporteur

André Roy - directeur de recherche

Michel Lapointe – codirecteur de recherche

Pascale Biron - membre du jury

Ian Reid - examinateur externe

Robert Owens - représentant du doyen de la FES

RÉSUMÉ

Cette thèse constitue une étude de la distribution spatiale hydrodynamique autour des éléments larges de rugosité (ÉLRs) tel que les amas de galets et les blocs erratiques dans les rivières à lit de graviers. Les ÉLRs sont les éléments microtopographiques les plus fréquents dans les rivières à lit de graviers peu triées. Ils semblent être distribués aléatoirement dans le chenal et augmentent la stabilité du lit. Le transport de sédiments est diminué par l'imbrication des ÉLRs avec le substrat environnant, limitant la disponibilité de particules transportables et retardant leur mouvement initial. Il a été montré que les ÉLRs fournissent un habitat qui est préféré par les poissons; cependant, les raisons qui expliqueraient cette relation positive n'ont pas été clairement identifiées. À ce jour, aucune étude à notre connaissance n'a examiné l'hydrodynamique *in situ* à une échelle fine autour des ÉLRs submergés; une telle investigation permettra d'améliorer notre compréhension du rôle que jouent les ÉLRs dans l'hydrodynamique à échelle locale et à échelle de la rivière ainsi que dans l'habitat aquatique. Les objectifs spécifiques de cette thèse sont : 1) d'identifier et de quantifier l'effet de l'échelle spatiale sur les variables de turbulence de l'écoulement obtenues à partir d'un plan vertical au-dessus d'un ÉLR en utilisant des techniques statistiques multivariées; 2) de caractériser le champ d'écoulement tridimensionnel (3D) *in situ* avec et sans un ÉLR submergé isolé et d'analyser l'effet hydrodynamique des ÉLRs sur les structures turbulentes d'écoulement à grande échelle (GÉ); 3) de décrire et de quantifier en détail les couches de cisaillement des ÉLRs et les processus d'échappement associés ainsi que le comportement des structures d'échappement à échelle moyenne sous l'influence des structures d'écoulement à GÉ; 4) de déterminer l'effet de conditions d'écoulement variées (niveau d'eau et composante de vitesse longitudinale moyenne) et de la géométrie des ÉLRs (forme, grosseur, orientation) sur le champ d'écoulement turbulent 3D *in situ* et sur l'échange de momentum turbulent.

Cette thèse intègre l'utilisation de plusieurs techniques complémentaires d'échantillonnage sur le terrain et d'analyses statistiques pour atteindre les objectifs présentés et obtenir une caractérisation détaillée du champ d'écoulement autour des ÉLRs dans les rivières à lit de graviers. Jusqu'à quatre vélocimètres acoustiques Doppler

(ADVs) ont été utilisés pour les mesures de vitesse 3D à haute fréquence. Des mesures 2D précédemment obtenues à partir de courantomètres électromagnétiques (ECMs) ont également été analysées pour répondre à l'objectif 1. Une technique nouvelle de mesures simultanées provenant d'ADVs synchronisées avec la visualisation de l'écoulement a été utilisée pour résoudre l'objectif 3, permettant l'étude détaillée de la couche de cisaillement des ÉLRs et des structures d'échappement associées. Des analyses statistiques multivariées ont été utilisées pour étudier les relations d'échelle dans les données spatialement distribuées et également pour trouver des relations fonctionnelles entre l'écoulement moyen et les variables morphométriques des ÉLRs et les variables turbulentes estimées à partir de la zone de sillage.

La quantification de patrons spatiaux à différentes échelles a été obtenue par l'utilisation d'une analyse canonique de redondance (RDA) et d'une analyse de coordonnées principales des matrices de voisinage (PCNM). La RDA, très exploité dans le domaine de l'écologie, est rarement utilisée dans le domaine des ressources d'eau. L'analyse PCNM est une méthode nouvellement développée de partitionnement statistique basée sur les échelles; son utilisation dans cette thèse est une première application pour les sciences de ressources de l'eau. Cette analyse a été faite à partir d'un plan vertical de mesure au-dessus d'un ÉLR. Les analyses présentées dans les chapitres subséquents de cette thèse utilisent des plans de mesures horizontaux permettant d'évaluer adéquatement l'importance de l'influence hydrodynamique latérale des ÉLRs. Les changements dans le champ d'écoulement induits par un ÉLR isolé ont été évalués par l'échantillonnage des vitesses dans deux plans horizontaux avec et sans un ÉLR. Des analyses spectrales et de corrélations croisées (espace-temps) ont permis la quantification de la périodicité des structures d'échappement dans la couche de cisaillement et le comportement des structures cohérentes d'écoulement à GÉ lors de leur passage au-dessus d'un ÉLR. La technique de mesures simultanées provenant des ADVs et de la visualisation de l'écoulement a été utilisée pour identifier le comportement de l'échappement et de la couche de cisaillement au passage d'évènements d'écoulement à GÉ. Alors que la partie précédente de cette thèse étudiait des ÉLRs isolés pour évaluer l'influence hydrodynamique spécifique associée à un ÉLR, la dernière partie de la thèse porte sur plusieurs ÉLRs de différentes géométries sous des

conditions d'écoulement variées. Finalement, les implications de cette thèse sont discutées dans un contexte plus large, abordant des enjeux en géomorphologie fluviale et des enjeux qui concernent l'habitat des poissons.

Les principaux résultats de cette thèse montrent que les ÉLRs génèrent une turbulence 3D intense dans la zone de sillage avec des valeurs extrêmes des indicateurs principaux de turbulence (par exemple l'énergie cinétique turbulente, k_e, et le cisaillement de Reynolds) 5 – 10 fois plus grandes que les valeurs non obstruées. Ces valeurs élevées se présentent dans une zone relativement localisée en dessous du sommet des ÉLRs et directement en aval des ÉLRs. La zone turbulente de sillage a été montrée comme étant bien structurée par la taille de l'ÉLR et par la vitesse longitudinale non obstruée moyenne, qui explique plus de 70 – 80% de la variance de k_e et du cisaillement longitudinal-vertical de Reynolds, $-\rho\overline{uw}$. Un processus bimodal d'échappement a été observé en aval des ÉLRs, où des vortex d'instabilité initiale à échelle fine s'amalgamaient à intermittence en des structures d'échappement plus grandes à échelle moyenne avec des fréquences d'échappement d'approximativement de 5 Hz et 1 Hz, respectivement. La fréquence d'échappement des structures d'écoulement à échelle moyenne correspondait approximativement aux valeurs prédites à partir du nombre de Strouhal. Les valeurs de cisaillement de Reynolds élevées sont apparues selon des patrons particuliers dans la zone de sillage des ÉLRs. Des valeurs de cisaillement longitudinal-latéral (uv) de Reynolds élevées, $-\rho\overline{uv}$, ont formé des zones allongées +ve et –ve en aval, attribuées à des vortex tournant en sens contraire le long de l'axe vertical s'échappant des côtés latéraux du ÉLR. Des valeurs élevées de $-\rho\overline{uw}$ ont été observées occupant la plus grande partie de la zone de sillage apparaissant concurremment avec des valeurs élevées de $-\rho\overline{uv}$ et souvent dominant l'échange de momentum turbulent. Utilisant la visualisation simultanée de l'écoulement, les valeurs élevées de $-\rho\overline{uw}$ ont été directement associées à des vortex latéraux s'échappant du sommet des ÉLRs. L'interaction entre les structures de la couche de cisaillement et les structures cohérentes d'écoulement à GÉ a été observée comme étant intermittente. Les structures d'écoulement à GÉ ont été montrées comme étant relativement peu affectées par les structures d'échappement, alors qu'à l'opposé les structures de la couche de cisaillement ont été observées s'échappant à intermittence vers le haut et se contractent

vers le lit avec le passage respectif des éjections et des incursions à GÉ. L'étude de l'hydrodynamique *in situ* à échelle fine autour des ÉLRs présentée dans cette thèse contribue à élucider le rôle des ÉLRs dans les rivières à lit de graviers et sera profitable aux domaines de la géomorphologie fluviale, de l'ingénierie en rivière et de la biologie aquatique.

Mots Clés : turbulence; éléments de rugosité; amas de galets; ADV; visualisation; structures turbulentes d'écoulement; statistiques multivariées; spectrales; spatiales; corrélations croisées; vortex; habitat aquatique; lit de graviers.

SUMMARY

This thesis investigates the spatially distributed hydrodynamics associated with submerged large roughness elements (LREs) such as boulders, cobbles and pebble clusters in gravel-bed rivers. Instream LREs have been argued to constitute the most frequent microtopographic feature in poorly sorted gravel-bed rivers. These features appear to be randomly distributed over the channel bed and have been found to enhance bed stability. Reduced bedload fluxes are associated with LREs, as they interlock and imbricate with the surrounding substrate limiting the availability of readily transportable particles and delaying their incipient motion. LREs have been shown to provide preferred habitat for fish, yet the reasons for this positive relationship are not clear. To date, no studies to our knowledge have examined the fine-scale *in situ* hydrodynamics around submerged LREs, the detailed investigation of which will advance the understanding of the role LREs play in local and river hydrodynamics and aquatic habitat. The specific objectives of this thesis are: 1) to identify and quantify the spatial scale-dependence of turbulent flow variables obtained from a vertical plane crossing over a LRE through the use of multivariate statistical techniques; 2) to characterise the *in situ* 3D turbulent flow field with and without an isolated submerged LRE and investigate the hydrodynamic effect of LREs on large-scale (LS) turbulent flow structures advecting from upstream; 3) to describe and quantify in detail LRE shear layers and associated shedding processes and the behaviour of meso-scale shedding structures under the influence of LS flow structures; 4) to determine the effect of varied flow conditions (stage and mean longitudinal component velocity) and of LRE geometries (shape, size, orientation) on the *in situ* 3D turbulent flow field and turbulent momentum exchange.

This thesis integrates the use of multiple complementary field sampling instrumentation techniques and statistical analyses to fulfil the outlined objectives and obtain a comprehensive characterization of the flow field around LREs in gravel-bed rivers. Multiple acoustic Doppler velocimeters (ADVs) were the primary instruments used for 3D high-frequency velocity measurements. Previously obtained 2D measurements from electromagnetic current metres (ECMs) were also analysed to

address objective 1. A novel technique of concurrent ADV measurements with flow visualization was used to accomplish objective 3 permitting a detailed investigation of the LRE shear layer and associated flow structures. Multivariate statistical analyses were used to investigate scale relationships in the spatially distributed data as well as to find functional relationships between mean flow and LRE morphometric variables and turbulence variables estimated from the wake.

The quantification of scale-dependent spatial patterns was obtained through the use of canonical redundancy analysis (RDA) and principal coordinates of neighbour matrices (PCNM) analysis. RDA, while commonly used in ecology sciences, is rarely used in the field of water resources. PCNM analysis is a newly developed method of statistical scale partitioning and its use in this thesis represents a first time application to water resource sciences. This analysis was carried out on a vertical measurement plane crossing over a LRE. Subsequent chapters of this thesis focussed on horizontal measurement planes to properly assess the importance of the lateral hydrodynamic influence of LREs. Changes in the flow field induced by an isolated LRE were assessed by sampling velocities over two horizontal planes with the LRE present and resampling identical locations after the LRE was removed. Spectral and space-time correlation analyses provided a quantification of shear layer periodicity and a characterization of the behaviour of downstream advecting LS turbulent coherent flow structures as they passed overtop of the LRE. The concurrent ADV measurements and flow visualization technique was used to identify shedding and shear layer behaviour to the passage of LS flow events. While the preceding portion of the thesis focused on isolated LREs in order to assess the hydrodynamic influence specifically associated with a LRE, the latter portion of the thesis focused on multiple LREs with different geometries under varying flow conditions. This allowed for a more generalized description of the hydrodynamic influence of LREs. Finally, the implications of the thesis for broader fluvial geomorphological issues and fish habitat were discussed.

The main results of the thesis show that LREs generate intense 3D turbulence in the wake with peak values in the main turbulent indicators (e.g., turbulent kinetic energy, k_e, and Reynolds shear stresses) 5 – 10 times greater than free-stream values. These high values occur in a relatively localized narrow zone below the tops and directly

downstream of the LREs. Wake turbulence was shown to be well structured by LRE size and mean free-stream longitudinal velocity which explained upwards of 70 – 80% of the variance in k_e, and longitudinal-vertical Reynolds shear stress, $-\rho\overline{uw}$. A bimodal shedding process was observed in the lee of LREs where small-scale initial instability vortices intermittently amalgamated into larger meso-scale flow structures with shedding frequencies of approximately 5 Hz and 1 Hz, respectively. The shedding frequency of the meso-scale flow structures corresponded adequately to predicted values using a Strouhal number of 0.18. Elevated Reynolds shear stresses occurred in particular patterns in the wake of LREs. High longitudinal-lateral Reynolds shear stress $-\rho\overline{uv}$ occurred in downstream elongated +ve and –ve zones attributed to counter rotating vertical axis vortices shedding from the lateral sides of the LRE. High $-\rho\overline{uw}$ was observed to occupy much of the wake occurring over large scales $\Delta x = 5h_s - 10h_s$ concurrently with high $-\rho\overline{uv}$ and often dominating the turbulent momentum exchange. Using the concurrent flow visualization the high $-\rho\overline{uw}$ and turbulent events were directly associated with lateral axis vortices shedding from the top of the LREs. The interaction between the shear layer structures and LS coherent flow structures was observed to be intermittent. LS flow structures were shown to be relatively unaffected by LRE shedding flow structures, while conversely the shear layer structures were seen to intermittently shed upwards and contract downwards towards the bed with the passage of LS ejections and sweeps, respectively. The fine-scale *in situ* hydrodynamics around LREs characterised in this thesis provide valuable insight on the role of LREs in gravel-bed rivers which will be helpful for the fields of fluvial geomorphology, river engineering and aquatic biology.

Key words: turbulence; large roughness elements; pebble clusters; ADV; visualization; coherent flow structures; variation partitioning; spatial; spectral; space-time correlation; multivariate analysis; shear layer; vortices; aquatic habitat; gravel-bed rivers.

TABLE OF CONTENTS

LIST OF TABLES

LIST OF FIGURES

LIST OF SYMBOLS

A_s	lateral projection area, m^2.
A_{wk}	planar wake area, m^2.
$cor\text{-}L_{u,x}$	coherent flow structure correlation length-scale, u component, longitudinal direction, x, m.
D_{50}	median grain size, m.
f	frequency, s^{-1}.
f_f'	Darcy-Weisbach friction factor.
f_{50}	half-power frequency, s^{-1}.
g	gravitational acceleration, m s^{-2}.
h_s	maximum pebble cluster height, m.
h_s	large roughness element protrusion height, m.
I	velocity turbulent intensity.
I_*	shear velocity turbulent intensity.
I_n	image intensity time series.
ITS_u, ITS_v, ITS_w	integral time scale, u, v, and w components, s.
k	wavenumber, cm^{-1}.
k_e	turbulent kinetic energy, cm^2 s^{-2}.
k_s	equivalent sand roughness, m.
K_i	Kurtosis coefficient.
L_u	turbulent macro-scale, u component, m
L_{wk}	wake length, m.
p	probability.
r	correlation coefficient.
r^2	coefficient of determination.
R^2	unadjusted coefficient of multiple determination
$Can\ R^2$	unadjusted bimultivariate redundancy statistic
R_a^2	adjusted bimultivariate redundancy statistic.
Re_*	Reynolds shear number.
R_h	hydraulic radius, m.
R_{ii}	autocorrelation coefficient.
R_{ij}	time-shifted cross-correlation coefficient.
Sk_i	Skewness coefficient.
S_o	water surface slope.
S_{ii}	spectral density function, cm^2 s^{-1}.
U, W, V	longitudinal, lateral and vertical velocity, cm s^{-1}.

$\overline{U}$, $\overline{V}$, $\overline{W}$	time-averaged longitudinal, lateral and vertical velocity, cm s^{-1}.
u, v, w	instantaneous longitudinal, lateral and vertical velocity, cm s^{-1}.
u', v', w'	root mean square of the longitudinal, lateral and vertical velocity fluctuations, cm s^{-1}.
u_*	shear velocity, cm s^{-1}.
$\overline{U}_c$	mean advection velocity of coherent structures, cm s^{-1}.
x, y, z	longitudinal, lateral and vertical distance, m.
x^* , y^* , z^*	dimensionless longitudinal, lateral and vertical distance
Z	mean water depth, m.
z_o	characteristic roughness length, m.
α	statistical significance level.
δ	boundary layer thickness, m.
Δt	time step, s.
Δx, Δy, Δz	longitudinal, lateral and vertical separation distance, m.
Δx_{ke}	longitudinal separation distance to maximum k_e , m.
λ_i	canonical eigenvalues.
ξ	intermittency factor.
v	arbitrary velocity component, cm^2 s^{-2}.
$-\rho\overline{uv}$, $-\rho\overline{uw}$ $-\rho\overline{vw}$	uv, uw and vw component mean Reynolds shear stress, N m^{-2}.
τ_o	bed shear stress, N m^{-2}.
ν	kinematic viscosity, m^2 s^{-1}.
ρ	water density, kg m^3.
$\emptyset_s$, $\emptyset_{wk}$	roughness element and wake lateral width, m.
overbar	temporal mean values.
angled parentheses <·>	spatial mean values.
double angled parentheses <<·>>	double spatial mean values

DEDICATION

This thesis is dedicated with much love to my father Alan Michael Lacey (1941-2007) who encouraged me wholeheartedly throughout my studies and who would have liked to have seen me finish.

Rage, rage against the dying of the light,
Do not go gentle into that good night

Dylan Thomas

ACKNOWLEDGEMENTS

J'aimerais tout d'abord remercier André Roy pour m'avoir accueilli, malgré un laboratoire déjà bien rempli, et guidé à travers l'incroyable aventure que fut mon doctorat. Conduire mes recherches en rivière naturelle fut une expérience riche et unique. Pour tous ses conseils judicieux et pour l'énergie, le souci du détail et la rigeur avec lesquels il a corrigé mes articles et résumés, peu importe le délai (parfois très court). Merci également pour les nombreuses opportunités de présenter mes travaux dans des congrès internationaux et le support financier durant les dernières années.

J'aimerais aussi remercier mon codirecteur de recherche Michel Lapointe et les membres de mon comité doctoral, Pascale Biron et Lael Parrott, pour leur direction et pour les nombreuses discussions et réunions. J'aimerais remercier Pierre Legendre pour rendre le monde des statistiques multivariées si passionant et aussi accessible, et pour sa disponibilité durant mon doctorat. Aussi merci à Daniel Borcard pour les discussions sur les PCNM. Merci à Tom Buffin-Bélanger pour la permission d'utiliser ses anciennes données et pour ses commentaires sur une version préliminare du Chapitre 3. Thanks to Richard Allix the senior machine shop technician at Concordia University who fabricated my very solid ADV support frame which was fundamental to my *in situ* sampling.

Merci au groupe fluvial, le laboratoire était pour moi un endroit joyeux, favorable au travail et aux discussions, surtout les vendredis "fluviaux" à 16:00 (qui tout de même auraient pu être les jeudis). Thanks to my pal Bruce MacVicar for our fruitful discussions, Matlab collaborations and oh…I don't recall. Hélène Lamarre and Eva Enders for questions asked and answered. Special thanks to Geneviève Marquis for field, visualization and general all round help and conference partner. I would like to thank my numerous field helpers without whom this research would not have taken place, Éric Beaulieu, Valérie Champagne, Lara Hoshizaki, Julie Thérien, Mathieu Roy, Christine Rozon.

Et finalement, j'aimerais aussi remercier Rosalie Léonard, qui m'a enduré pendant toute ma thèse. Qui m'a supporté mentalement, physiquement, pour quelques scans ici et là, et pour plusieurs plusieurs traductions. Qui avec son regard positif et son immense patience m'a aidé à passer à travers les moments difficiles (quand rien n'aboutit) et les multiples difficultés qui font d'un doctorat un doctorat.

I would like to thank the National Sciences and Engineering Research Council of Canada for the doctoral scholarship I was awarded, without which I would most likely not be in research. J'aimerais également remercier la Faculté des Études Supérieures de l'Université de Montréal pour la bourse fin de doctorat. Funding for this research was provided by the National Sciences and Engineering Research Council of Canada as well the Canadian Foundation for Innovation. This research was conducted as part of the program of the Canada Research Chair in fluvial dynamics.

1. INTRODUCTION

Turbulence is a ubiquitous characteristic of flows occurring in natural environments: from atmospheric flows to the flow of water in oceans and rivers. Turbulent flows are three dimensional and are characterised by high levels of fluctuating vorticity. In gravel-bed rivers the turbulent velocity fluctuations in the flow are driven by shear with the bed or through flow separation in the lee of bluff bodies. The turbulence is strongly influenced by the heterogeneous substrate made up of discrete particles which protrude randomly from the bed. Significant feedbacks exist between the turbulent boundary layer structure, the bed microtopographic features and sediment transport [*Leeder*, 1983]. Grains and bedforms exert a significant influence on the flow and may greatly modify the turbulent boundary layer structure [*Best*, 1993]. The role of particle roughness and protrusion on the structure of the turbulent flow becomes increasingly important when the particles are large enough to create their own flow field capable of influencing erosion, transportation and deposition of other grains [*Best*, 1996]. These large roughness elements (LREs) consisting of boulders, cobbles or pebble clusters form an integral part of the substrate and are considered to be the most prevalent microtopographic feature of poorly sorted gravel-bed rivers occupying as much as 10% of the channel floor [*Brayshaw*, 1984]. LREs play an important role in the local and global hydrodynamics of the river. They have been found to enhance bed stability and reduce bedload fluxes as they interlock and imbricate with the surrounding substrate limiting the availability of readily transportable particles and delaying their incipient motion [*Dal Cin*, 1968; *Brayshaw*, 1984; *Reid et al.*, 1992; *Biggs et al.*, 1997; *Wittenberg and Newson*, 2005]. While their spatial distribution is for the most part non-periodic or quasi-random [*Brayshaw*, 1984; *Lamarre and Roy*, 2001], it has been argued that their spatial arrangement maximizes flow resistance [*Hassan and Reid*, 1990]. LREs in gravel-bed rivers have as well been associated with higher salmonid fish densities believed to be an effect of the heterogeneous flow conditions they impart [*Van Zyll de Jong et al.*, 1997; *Mitchell et al.*, 1998].

While the general effects of submerged LREs on flow resistance and benefits to fish habitat in flumes or in gravel-bed rivers have been investigated, several fundamental

questions remain on the hydrodynamic influence of LREs in gravel-bed rivers and the role they play for aquatic biota. LREs generate complex three-dimensional (3D) turbulent flow patterns that very few studies have investigated *in situ*. Many questions need to be elucidated on: the spatial scales of turbulence generated; the two-dimensional (2D) and 3D spatial patterns and extent of the hydrodynamic effect; the details of the shedding processes; the effect of flow stage and changing LRE geometry on the hydrodynamics; and the interaction of LREs with large-scale (LS) coherent structures. LS flow structures are a predominant feature of gravel-bed rivers and through their associated sweeps and ejections play an important role in sediment transport and entrainment [*Williams et al.*, 1989]. Furthermore conflicting results in the biological literature have arisen on the effects of turbulence such as generated by LREs and fish [*Enders et al.*, 2003; *Smith et al.*, 2005; 2006; *Liao* 2007]. These differences in results are difficult to reconcile without a full understanding of the fine-scale 3D hydrodynamics associated with LREs in gravel-bed rivers. Through innovative *in situ* sampling techniques and turbulent data analyses this thesis is an attempt to advance current knowledge on the fine-scale *in situ* 3D hydrodynamics of submerged LREs in gravel-bed rivers.

This thesis is composed of eight chapters. A general review of the basics of turbulent flow over smooth and rough boundaries, turbulent coherent flow structures, LRE hydrodynamics and aquatic biota interactions with LREs is given in Chapter 2. This review presents and discusses past and current knowledge of turbulent flow processes associated with LREs in gravel-bed rivers and helps situate the objectives and results of this thesis within the broader gravel-bed river context. The detailed thesis objectives and methodology are presented in Chapter 3. The main results of the thesis are presented in Chapters 4 through 7. These chapters are written in journal article publication format for submission to internationally recognized research journals. Liaison paragraphs are included between the article chapters. Chapter 8 examines the broader implications of the thesis results for gravel-bed rivers and aquatic biota.

The chapters presenting new results are organized as follows: In Chapter 4 we quantify the spatial scale dependence of turbulent flow parameters in a longitudinal-vertical, x-z plane, crossing over a naturally occurring pebble cluster in a gravel-bed

river. The scale dependent spatial patterns are obtained through the use of multivariate statistical techniques: canonical redundancy analysis (RDA) and principal coordinates of neighbour matrices (PCNM) analysis. RDA, while commonly used in ecological sciences, is not often used in the field of water resources. Chapter 4 shows the utility of RDA and PCNM analysis to investigate relationships between spatially distributed turbulence variables over a LRE which have a broad range of applications in water resources and earth sciences. The application of this technique will reveal the dominant scales at which turbulence manifestations occur. This article is now published in *Water Resources Research*. In Chapter 5, the horizontal distribution of turbulent flow parameters over and around an isolated LRE in a gravel-bed river is characterised over two longitudinal-lateral (x-y) planes. Spectral and space-time correlation analyses are used to quantify shear layer periodicity and the response of advecting LS turbulent coherent flow structures to the mesoscale flow structures shedding from the LRE shear layer. The main results of this article are now published as a technical note in *Water Resources Research*. In Chapter 6, concurrent flow visualization and 3D velocity measurements are used to investigate the fine-scale characteristics of the shear layer and shedding coherent flow structures of an isolated *in situ* LRE. Through the concurrent measurement technique, identified turbulent flow events can be visually characterised leading to a better understanding of the turbulent flow processes occurring in the lee of LREs. Due to the fine-scale characterization and the extensive turbulent flow statistical analysis this article was submitted and has now been accepted for publication by the *Journal of Hydraulic Engineering*. In Chapter 7, several isolated and multiple LREs are investigated in a gravel-bed river under varying flow conditions. RDA is used to identify the dominant flow parameters for structuring the turbulence generated in the wake. The investigation of several LREs at varying flow stages allows for a more generalized description of the hydrodynamic influence of LREs. This article will be submitted to *Geomorphology*. Chapter 8 explores the implications of the findings reported in the thesis for four particular areas: sediment transport, the channel-scale spatial distribution of LREs, LS coherent turbulent flow structures and fish habitat. A general conclusion establishes the contribution of the thesis and proposes directions for future work.

2. BACKGROUND

2.1. Context

In gravel-bed rivers, the hydrodynamics are strongly influenced by the heterogeneous topography of the bed resulting from the arrangement of discrete particles of various shape, size and orientation. Seemingly distributed at random locations, the large roughness elements (LREs) are either isolated boulders or cobbles or are the agglomeration and imbrications of several large or small particles such as in pebble clusters or in ribs or steps. As these LREs protrude from the bed, they have a potentially stronger influence on the local and global hydrodynamics of the river. The hydrodynamics in turn govern the dispersion and distribution within the water column of sediments, nutrients, and influence the availability of preferred habitats of macrophytes, periphyton, and fish. LREs are a fundamental component of gravel-bed rivers, yet their *in situ* hydrodynamics have for the most part been ignored and their consideration would lead to a greater understanding of gravel-bed river processes.

In the following chapter, a comprehensive review of the basics of turbulent flow, coherent flow structures and their association with LREs is given so that the research questions, objectives and general methodology presented at the end of the chapter can be better understood. The review is composed of four parts: 1) turbulent flow over smooth and rough beds; 2) turbulent coherent flow structures; 3) LREs in gravel-bed rivers; and 4) LREs and aquatic biota. Initially, the basic flow properties and turbulence statistics for flow over smooth- and rough-beds are compared to show the effects of roughness on commonly estimated turbulence statistics. The rough-boundary layer results have particular importance for gravel-bed rivers (which are very rough bedded) and the statistical descriptors and estimation techniques presented were used throughout this thesis to characterise the hydrodynamics around LREs. A review of several types of coherent turbulent flow structures is presented from small to large-scale (LS) over smooth- and rough-beds. These flow structures are particularity important for understanding the results of this thesis and its focus on turbulence as they are intricately related to the characterization of the hydrodynamics around LREs. Following on the turbulence and coherent flow structure background presented in Sections 2.1 and 2.2,

current knowledge on LRE spatial distribution, LRE hydrodynamic effect and the known interaction between LRE shedding structures and LS coherent flow structures is reviewed. This subsection is important for contextualizing this thesis with what is currently known of LRE hydrodynamics. Finally in Section 2.4, a brief review of the effect of LREs on periphyton, macroinvertebrates and fish is given as it is hoped that the main results of this thesis may answer some of the conflicting results found in the literature regarding aquatic biota preference for LREs and the biological stresses imparted by turbulent motions. Sections 2.5, 2.6 and 2.7 discuss where research is needed in understanding the role of LREs in gravel-bed rivers, the objectives of this thesis and the general methodology which will be used throughout.

2.1.1. Boundary layer theory over smooth and rough beds

As water flows over a smooth or rough surface it undergoes a resisting force causing it to shear due to the no-slip condition occurring on the bed (wall). The amount of shearing or resistance to shearing within the fluid is determined by its viscosity. The velocity close to the bed is most retarded and a velocity gradient develops throughout the fluid up until a height where the influence of the bed is no longer detectable. The layer of fluid where the frictional effects of the bed are strongly felt is termed the boundary layer (Figure 2.1).

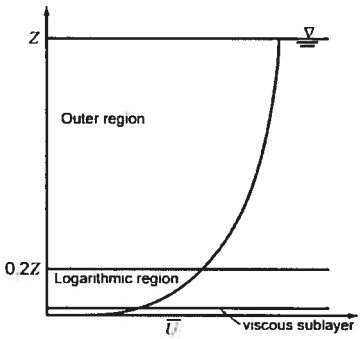

Figure 2.1. Boundary layer structure for shallow open channels.

Boundary layers and flow in general are characterised by one of three states: laminar, transitional or turbulent. In laminar conditions, the fluid flows in layers which do not cross or mix: the streamlines are linear and parallel. Whereas in turbulent flows there is a strong "chaotic" mixing of fluid parcels or turbulent momentum exchange

throughout the water column. Flows in rivers are almost always turbulent, yet laminar boundary layers can form overtop of individual large roughness elements (LREs) such as boulders, cobbles and pebble clusters. The thickness of the turbulent boundary layer, δ, in shallow wide channels and rivers is generally considered to be the water depth, Z, and will be defined as such for the following discussion (i.e., $\delta = Z$). The boundary layer over a relatively smooth wall is separated into three regions (Figure 2.1). The first layer very-close to the bed is termed the viscous or laminar sublayer. In this region viscosity dominates the frictional stresses. In most gravel-bed rivers with relatively coarse substrates the roughness elements protrude past and fully disrupt the viscous sublayer [*Carling*, 1992; *Nezu and Nakagawa*, 1993]. This rough-turbulent condition occurs at dimensionless roughness heights $k_s^+ = k_s u_* / \nu > 70$, where k_s is the equivalent sand roughness, u_* is the shear velocity and ν is the kinematic viscosity of water (1.31×10^{-6} $m^2\ s^{-1}$). For fully developed boundary layers, the inner or wall region is limited to $z/Z < 0.2$, where z is the vertical height above the bed. In this region, turbulence is scaled by inner variables such as u_* and ν. This scaling is not appropriate for developing or disrupted boundary layers such as those induced by flow separation [*McLean et al.*, 1994].

For uniform two-dimensional flow (2D) the inner layer velocity profile is well described by the Prandtl-von Karman law – a logarithmic function referred to as the log-law:

$$\frac{\overline{U}_z}{u_*} = \frac{1}{\kappa} \ln\left[\frac{z}{z_o}\right] \tag{2.1}$$

where $\overline{U}_z$ is the mean longitudinal velocity at height z (the overbar represents time-averaged quantities); κ is the universal Kàrmàn constant, $\kappa = 0.4$; and z_o is the characteristic roughness length. In the outer region $z/Z > 0.2$ there is a slight but systematic deviation in the velocity profile from the log-law which can be described by the addition of a wake function, $W_k(z/Z)$, to Equation 2.1: *Coles* [1956] trigonometric wake function is commonly used:

$$W_k(z/Z) = \frac{2\Pi}{\kappa} \sin^2\left[\frac{\pi z}{2Z}\right] \tag{2.2}$$

where Π is the Coles wake strength parameter.

The log-law has been shown to give a good fit of laboratory velocity data over smooth and rough channels [*Grass*, 1971; *Nezu and Nakagawa*, 1993; *Kironoto and Graf*, 1994] and promising results have as well been obtained in gravel-bed river applications. *Nikora and Smart* [1997] found an adequate fit of the log-law with the lower-half of the velocity profiles obtained by their *in situ* gravel-bed river measurements. They suggest that the wake function (Equation 2.2) is close to zero and can be ignored as its adjustment to the velocity profile is smaller than the accuracy of *in situ* velocity measurements. Deviations in the velocity profile were observed by *Nikora and Smart* [1997] at some sites close to the bed $z < 3D_{50}$ where D_{50} is the bed median grain size (B orthogonal axis). This deviation in the velocity profiles close to the gravel bed is highly dependent on the physical roughness properties (i.e., size distribution, packing and imbrication) and has also been observed in gravel-bed flume studies [*Lawless and Robert*, 2001]. Supporting results on the applicability of the logarithmic profile to gravel-bed rivers was further provided in a detailed study by *Smart* [1999]. R*obert et al.* [1992] and *Lamarre and Roy* [2005] observed relatively well developed log-linear relationships in their *in situ* velocity profiles obtained over complex gravel-bed configurations.

The inner variable u_* is a key scaling parameter of fully developed boundary layers and can be estimated in a number of ways including Equation 2.1. Methods of estimating u_* include the use of:

i) the energy gradient method obtained from the water surface slope, S_o, assuming uniform 2D flow:

$$u_* = \sqrt{gZS_o} \tag{2.3}$$

where g is the acceleration due to gravity (g = 9.81 m s^{-2}). This method gives a reach averaged u_* value which provides good results over rough beds when the slope is not very small [*Kironoto and Graf*, 1994]. It assumes, however, a uniform flow, a condition that may not be present in natural rivers when in flood or in the cases of flow acceleration and deceleration.

ii) the mean longitudinal velocity profile using $\overline{U}_z$. This method assumes the logarithmic velocity profile described in Equation 2.1 and its use on smooth beds is well established [*Hinze*, 1959; *Raupach et al.*, 1980]. Inconsistent results on the accuracy of this method have been obtained over rough beds and in gravel-bed rivers. *Raupach et al.* [1980] found limited or non-existent log-linear regions for velocity profiles measured over small roughness elements and could therefore not be used directly to estimate u_*. *Bridge and Jarvis* [1977] found the log-law method inaccurately predicted u_* over non-uniform beds (with bedforms such as dunes and LREs). For a gravel-bed river, *Wilcock* [1996] observed estimates of u_* from the slope of the near-bed velocity profile to be the least precise and required the most restrictive flow conditions for accuracy. Conversely, *Kironoto and Graf* [1994], *Babaeyan-Koopaei1 et al.*, [2002] and *Robert et al.* [1992] found the log-law method to offer good estimations of u_* over uniform rough-beds, in sand-bed rivers, and gravel-bed rivers, respectively. The discrepancies between studies on the successful use of the log-law occur generally in the presence of rough beds with LREs. It has been recognized that the log-linear velocity-profile is segmented in the presence of LREs in two distinct slopes representing skin friction, τ', and form (or pressure) drag, τ'' associated with the LREs [*Wooding et al.*, 1973, *Nowell and Church*, 1977; *Robert*, 1990]. It is thought τ' is predominantly responsible for sediment transport and should be partitioned from the form drag in order to give an accurate prediction of bed shear stress, τ_0. Using the velocity segmentation approach, *Lawless and Robert* [2001] obtained consistent estimates of τ' from profiles taken between or on the top of pebble clusters in a flume study.

iii) the direct measurement of the Reynolds shear stresses, $-\rho\overline{\upsilon_i\upsilon_j}$ (where υ represents fluctuations from the mean of the velocity component either longitudinal, u, lateral, v, or vertical, w, and i and j represent indices of individual velocity components) is a measure of the mean momentum flux due to the turbulent fluctuations. $-\rho\overline{\upsilon_i\upsilon_j}$ represents the stress generated by the turbulent part of the flow. In 2D open-channel flows the total shear stress τ is well approximated by the uw Reynolds stress:

$$\tau = -\rho\overline{uw} = \rho u_*^2(1 - z/Z) \quad (2.4)$$

This relationship holds over most of the depth, $0.05 < z/Z < 1$ for a fully developed turbulent boundary layer, particularly for high Reynolds numbers, *Re* [*Tennekes and Lumley*, 1972; *Nezu and Nakagawa*, 1993; *Kironoto and Graf*, 1994]. u_* is obtained by extrapolating the linear stress profile to $z/Z = 0$. If a vertical stress profile is not available, u_* can be estimated directly from $-\rho\overline{uw}$ values obtained close to the bed. The Reynolds stress extrapolation method of estimating u_* has been widely used in flume studies, and *in situ* environments such as gravel-bed rivers and has been found to give unbiased estimation of u_* [*Voulgaris and Trowbridge*, 1998; *Nikora and Goring*, 2000; *Song and Chiew*, 2001; *Biron et al.*, 2004]. In a comparative study of u_* estimation methods, *Biron et al.* [2004] recommended the $-\rho\overline{uw}$ extrapolation method for uniform flows. In the wake of LREs and complex flow environments the vertical $-\rho\overline{uw}$ profile may not be linear and therefore u_* may be estimated from single point near-bed $-\rho\overline{uw}$ observations. Single point estimations do not dependent on z and represent the unbiased estimation of u_* [*Kim et al.*, 2000]. The Reynolds stress estimation of u_* is susceptible to errors due to improper sensor alignment [*Kim et al.*, 2000; *Biron et al.*, 2004] (i.e., if the velocity sensor is not aligned with the longitudinal u velocity direction, $-\rho\overline{uw}$ estimated values will be contaminated by v component velocity fluctuations). With 3D velocity measurements, such as obtained with an acoustic Doppler velocimeter (ADV), a rotation of the data is recommended to correct for obvious misalignment [*Roy et al.*, 1996]. In complex 3D flow environments, 2D uniform flow can no longer be assumed and the $-\rho\overline{uw}$ stress profile deviates from the linear relation of Equation 2.4 [*Nezu and Nakagawa*, 1993] and may underpredict true u_* values [*Papanicolaou and Hilldale*, 2002]. In complex flow environments, both vertical momentum flux components $-\rho\overline{uw}$ and $-\rho\overline{vw}$ should therefore be included in u_* estimations following *Nikora et al.* [2002a].

iv) measurements at a single-point near the bed ($z = 0.1Z$) of the 3D turbulent kinetic energy, k_e:

$$k_e = 0.5(u'^2 + v'^2 + w'^2) \tag{2.5}$$

$$u_* = \sqrt{\frac{C_1 k_e}{\rho}} \tag{2.6}$$

where the prime denotes the root mean square (RMS) values of the instantaneous velocity measurements and C_1 is an empirical proportionality constant (*c.* 0.20) which is assumed to be constant under widely varying conditions [*Soulsby*, 1983]. While this method incorporates the influence of all three velocity components, it is dependent on an empirical constant obtained from atmospheric and marine boundary layers which may not hold for gravel-bed rivers or complex flows. The TKE method of estimating u_* has been shown to give comparable results to other estimation methods in an annular smooth-bed flume experiment and in a tidal boundary layer [*Thompson et al.*, 2003; *Kim et al.*, 2000]. In a mobile sand-bed flume experiment by *Biron et al.* [2004], the spatial distribution of u_* estimates using the TKE method produced the best match with topographic scour hole patterns formed adjacent to flow deflectors. In this complex flow study, the TKE method was found to give more reliable results than the Reynolds stress method.

The foregoing discussion has identified the theoretical differences between smooth and rough boundary layers and discussed some of the discrepancies in applying 2D fully developed boundary layer theory to gravel-bed rivers. The logarithmic velocity profile is likely disrupted by LREs and should not be used to estimate u_*. While the TKE method of estimating u_* shows promises, it has not been fully tested in gravel-bed rivers with LRE and due to its reliance on an empirical constant should be used with caution. Prudence should as well be observed when using the Reynolds stress method for estimating u_* in the presence of LREs, yet this method has been well tested in gravel-bed rivers and is based on sound boundary layer theory. The following subsection discusses the effect of increasing bed roughness on standard turbulence statistics.

2.1.2. Turbulence intensities, correlations, macroscales and spectra

The dependence of the mean u component velocity, $\overline{U}$, and shear velocity, u_*, on the roughness characteristics of the channel boundary are well known, forming an integral part of the law of the wall (Equation 2.1) and giving rise to the resistance equation for 2D fully developed turbulent flow over rough surfaces:

$$\frac{\overline{U}}{u_*} = \sqrt{\frac{8}{f_f'}} = \frac{1}{\kappa}\ln\left(\frac{R_h}{k_s}\right) + C \tag{2.7}$$

where f_f' is the Darcy-Weisbach friction factor, R_h is the hydraulic radius (assumed as Z for wide channels), and C is a constant of integration which varies depending on relative submergence, Z/k_s [*Kironoto and Graf*, 1994]. Equation 2.7 demonstrates that an increase in bed roughness represented by f_f' or k_s results in a decrease in $\overline{U}$ and/or an increase in u_*. Atmospheric flume studies investigating the specific effects of roughness on turbulence statistics have supported the relationships defined in Equation 2.7 [*Mulhearn*, 1978; *Raupach et al.*, 1980]. In both these studies, decreases in $\overline{U}$ and increases in $-\rho\overline{uw}$ (and u_*) were observed with increased bed roughness from smooth to rough. The bed roughness effect on $\overline{U}$ and $-\rho\overline{uw}$ was most evident in the inner or logarithmic boundary layer region. In *Mulhearn*'s [1978] experiments, u'^2 and w'^2 (i.e., mean square values) increase near the bed, but little effect of roughness was observed on v'^2; there was a similar near-bed increase in $-\rho\overline{uw}$ by a factor of 1.5. In order to compare results between studies with differing flow conditions and to develop universal expressions, turbulence statistics are commonly scaled by the inner variables u_* and ν. While this facilitates comparison, it can obscure the behaviour of individual turbulence statistics. For instance, u component turbulence intensity, $I_{*u} = u'/u_*$, shows a near-bed decrease with an increase in bed roughness even though u' has a positive relationship with bed roughness. Figure 2.2 presents rough open channel laboratory experimental values of I_{*u} over varying bed roughnesses as a function of relative depth z/Z [*Grass*, 1971; *Nezu and Nakagawa*, 1993]. The dimensionless roughness height, k_s^+, is used to represent the varying roughness scales and is shown to effect the three turbulent intensity components (I_{*u}, I_{*v}, and I_{*w}) differently. Near the wall, the roughness effect

on the turbulent intensity magnitudes is clearly visible. In the logarithmic region ($0.05 < z/Z < 0.2$), I_{*u} is observed to decrease with an increase in roughness scale from $k_s^+ = 0$ to 136, while I_{*w} shows a slight increase (note: v defines the vertical velocity component in Figure 2.2) suggesting that w' is much more affected by bed roughness than u'. *Krogstad and Antonia* [1999] observed similar changes in I_{*u} and I_{*w} with bed roughness, yet observed a sensitivity of I_{*w} and $-\rho\overline{uw}^+$ to the geometric characteristics of the bed roughness (e.g., wire mesh versus lateral rods). This indicates that not only is roughness height an important variable, but so are the morphometric characteristics and the spacing between individual bed roughness elements.

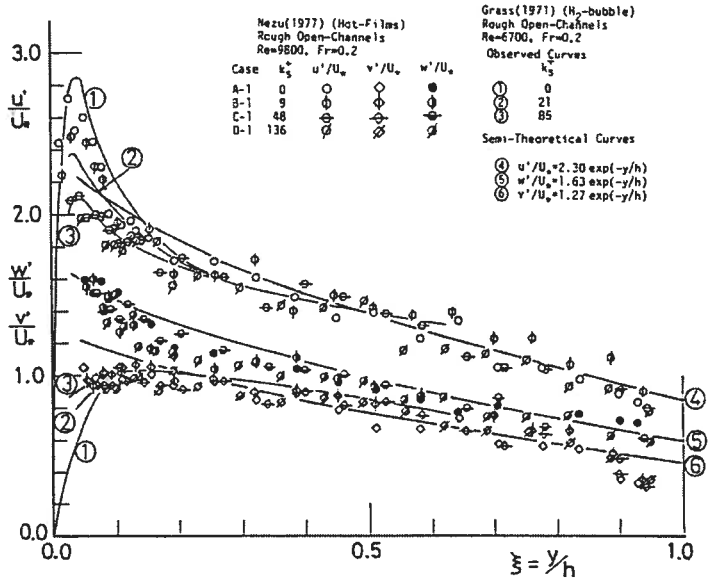

Figure 2.2. Variation of turbulent intensities, I_*, over smooth and rough beds as a function of relative height z/Z for a range of dimensionless roughness values, k_s^+ [*Nezu and Nakagawa*, 1993].

The effect of $\overline{U}$ on I_{*u} over a surface of constant grain roughness was shown by *Ligrani and Moffat* [1986] where close to the bed $z/Z < 0.1$, an inverse relationship was found between $\overline{U}$ and I_{*u} and a positive relationship was observed with I_{*w}. Quadrant analysis conducted over smooth and rough beds has indicated a marked change in dominant quadrants with increased roughness (and roughness geometries) [*Raupach*, 1981; *Krogstad and Antonia*, 1999]. When bed roughness is present, sweep events

(defined as $u > 0$ and $w < 0$) dominate the near-bed Reynolds stress contribution while higher up from the bed ejection events dominate (defined as $u < 0$ and $w > 0$).

Earlier research on the effects of bed roughness was carried out under conditions of relatively small k_s and large Z/k_s and suggested the influence of roughness on turbulence statistics is limited to the inner or log-layer [*Grass*, 1971; *Mulhearn*, 1978; *Raupach et al.*, 1980]. *Grass* [1971] suggested that in the outer boundary layer $z/Z > 0.2$, turbulence intensity becomes solely dependent on Z and u_* and can therefore be described by universal relationships. The more recent wind tunnel experiments by *Krogstad and Antonia* [1999] identified an influence of bed roughness up to $z/Z < 0.6$ even for relatively small k_s. Due to the conflicting results, these experiments were repeated by one of the preceding authors under a more rigorous experimental protocol [*Bakken et al.*, 2005] and the authors were unable to observe an effect of bed roughness beyond $5h_s$ or $z/Z > 0.2$. This reaffirms the hypothesis that flow outside of the inner layer is not dependent on the specific characteristics of the turbulence generated at the bed and can therefore be universally scaled by u_* and Z. These studies illustrate the relatively local hydrodynamic characteristics induced by roughness elements. While this hypothesis may hold for relatively small h_s, as bed roughness increases in size relative to flow depth $z/h_s < 5$ it is likely to influence the characteristics in the outer boundary layer.

While $-\rho\overline{uw}$ increases with bed roughness, laboratory studies have found the vertical distribution of the correlation coefficient, r_{uw}, between u and w to be universal over a variety of bed roughnesses from pipe flows and open channels. The vertical distribution r_{uw} for different k_s^+ are presented in Figure 2.3 (note: v defines the vertical velocity component in Figure 2.3) [*Nezu and Nakagawa*, 1993]. The strong negative correlation between u and w is fundamental to a wall bounded 2D shear flow with a fully developed turbulent boundary layer such as presented in Figure 2.1 and gives rise to the uw Reynolds shear stress. Under a fully developed turbulent boundary layer (Figure 2.1), there is a well defined velocity gradient with depth. Put simply, a parcel of fluid which moves up in the water column (+ve w fluctuation) retains a slower than average longitudinal velocity (-ve u) with the surrounding fluid at the new height z. Similarly a -ve w fluctuating parcel of fluid retains a higher than average u compared with the surrounding fluid at the lower z. In this way momentum is exchanged over the z velocity

gradient. The exchange is not always -ve as described above and results in r_{uw} correlation values of r_{uw} = -0.4 to -0.5 as can be observed in Figure 2.3 (note: negative r_{uw} values are presented). In the presented laboratory studies, the correlation between u and w is strongest at a relative distance of $z/Z = 0.2$, but is generally constant throughout the vertical profile approaching zero near the water surface. A similar r_{uw} distribution to that shown in Figure 2.3 was obtained by *Nikora and Goring* [2000] from a gravel-bed channel supporting its independence from mean flow and wall roughness characteristics [*Nezu and Nakagawa*, 1993]. The generalized r_{uw} distribution is likely to hold in gravel-bed rivers where 2D turbulent flow conditions dominate, but is unlikely to hold under 3D flow conditions or disrupted boundary layers such as those induced by flow separation.

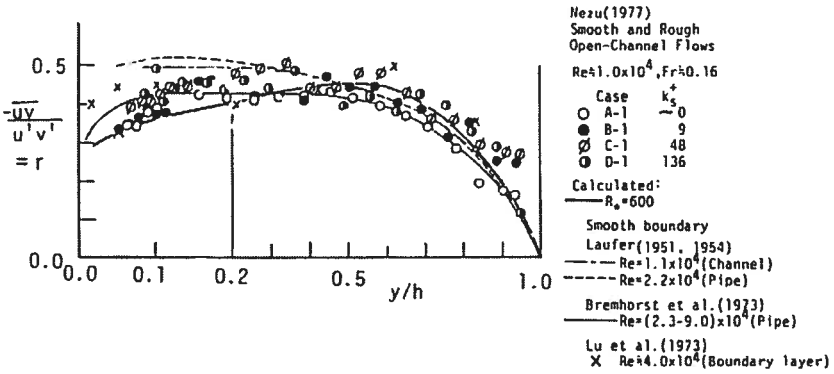

Figure 2.3. Correlation coefficients r_{uw} for a range of dimensionless roughness values, k_s^+ [*Nezu and Nakagawa*, 1993].

The turbulent macroscale, L_u, corresponding to a mean size of the turbulent coherent structures (or eddies) at a specific measurement height, z, [*Townsend*, 1976] is the scale which interacts most effectively with the mean flow to extract energy [*Nowell and Church*, 1979]. It is often determined through the integral of the autocorrelation function of the longitudinal velocity time series multiplied by a characteristic local mean velocity of the fluid (either $\overline{U}$ [*Cenedese et al.*, 1991; *Nezu and Nakagawa*, 1993] or the coherent advection velocity, $\overline{U}_c$ [*Perry et al.*, 1987; *Rhoads and Sukhodolov*, 2004]). $\overline{U}_c$ is the mean advective velocity of coherent flow structures within a shear layer. Estimating L_u and the spatial properties of turbulence from point measurements of velocity time series assumes that Taylor's frozen turbulence hypothesis (FTH) holds

which is generally the case when $I = u'/\overline{U} << 1.0$ [*Townsend*, 1976]. The assumption requires that flow characteristics do not change appreciably with downstream distance and velocity fluctuations in time at a point are the same as the instantaneous distribution of spatial fluctuations in the mean flow direction. While $I << 1.0$ is generally the case for fully developed 2D boundary layers, in complex flow environments such as shear layers or developing boundary layers, I can be relatively large. Complex patterns of vortex growth, interaction and amalgamation in shear layers may produce hydrodynamic conditions that do not conform to the FTH. The use of the FTH was tested by *Rhoads and Sukhodolov* [2004] in a confluence shear layer with favourable results.

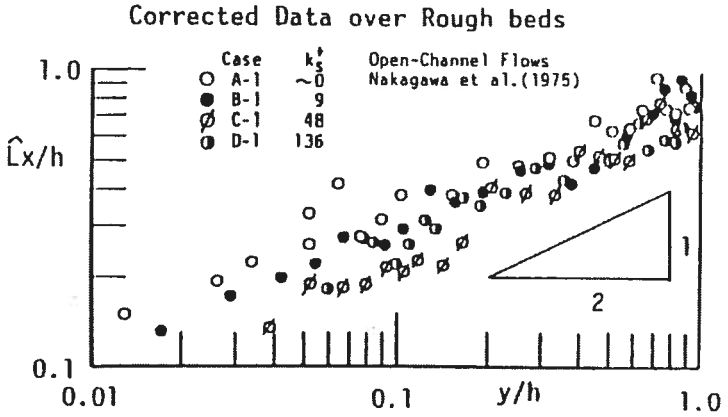

Figure 2.4. Distributions of macroscale L_u as a function of z/Z for a range of dimensionless roughness values, k_s^+ [*Nezu and Nakagawa*, 1993].

L_u can also be estimated using the peak of the logarithmic power spectrum of the velocity time series. Figure 2.4 shows an increase in L_u with distance from the bed [*Nezu and Nakagawa*, 1993]. This is expected from theory, as the mean flow instability and velocity shear generate a hierarchy of eddies attached to the wall so that their characteristic scales are proportional to the distance from the wall [*Nikora*, 1999]. The increase in L_u with z has also been observed in gravel-bed rivers [*Roy et al.*, 1996]. Figure 2.4 also shows the effect of bed roughness on L_u and indicates an inverse relationship between roughness and L_u throughout the vertical profile, which is most apparent in the inner boundary layer as with the previously discussed effects of roughness on $-\rho\overline{uw}$ and I_u. With larger roughness elements, *Webel and Schatzmann* [1984] found this inverse relationship extended over the whole flow depth strongly

suggesting that large eddies are broken down by roughness elements [*Nezu and Nakagawa*, 1993]. *Krogstad et al.* [1992] have similarly observed length scales to decrease by approximately half with bed roughness (for $z/Z < 0.5$)

Spectral analysis is a commonly used method for investigating periodicity and the scales of turbulent motion within velocity time series. Typical u component velocity spectra for velocity measurements obtained over a rough surface in a flume and in a gravel-bed river are presented in Figure 2.15. Theory predicts that for sufficiently high *Re*, velocity spectra will display two inverse power-law regions exhibiting scalings of f^{-1} and $f^{-5/3}$ [*Perry et al.*, 1986; *Cenedese et al.*, 1991; *Nikora*, 1999]. The f^{-1} represents the region where energy production and the cascade of energy coexist while $f^{-5/3}$ indicates evidence for the existence of an inertial subrange where turbulence becomes isotropic. In the inertial subrange there is no production or dissipation of energy and Kolmogorov theory predicts that energy cascades from large to small eddies. Measurements in open-channel turbulence confirm the validity of the -5/3 power law, irrespective of the *Fr* and wall roughness for sufficiently large *Re*, $R_L >> 100$ (based on u' and L_x) [*Nezu and Nakagawa*, 1993]. f^{-1} and $f^{-5/3}$ are outlined in the u component velocity spectra obtained over rough-bed laboratory measurements of *Nowell and Church* [1979] (Figure 2.5a). These spectra have been normalized so the effect of reduced energy with distance from the bed is removed. They observed that the $f^{-5/3}$ region was undetectable close to the tops of the roughness elements ($z/Z = 0.13$) and attributed this to the complex flow dynamics close to the elements. In comparison, *Perry et al.* [1987] observed both f^{-1} and $f^{-5/3}$ for u component velocity spectra over rough-beds for heights very close to the wall ($z/Z = 0.04$) (yet still above the top of the bed roughness used). Figure 2.5b presents typical u component velocity spectra obtained from a gravel-bed river under bedload transport conditions *Dinehart* [1999]. The spectra are not normalized by L_x and spectral energies can therefore be seen to increase closer to the bed. Again $f^{-5/3}$ over more than a decade are observed in all spectra. The extension of $f^{-5/3}$ into lower frequencies for *Dinehart*'s [1999] observations is a reflection of the very high *Re* number flow conditions ($Re > 10^6$) as the range of $f^{-5/3}$ is predicted to increase with *Re* [*Stapleton and Huntley*, 1995].

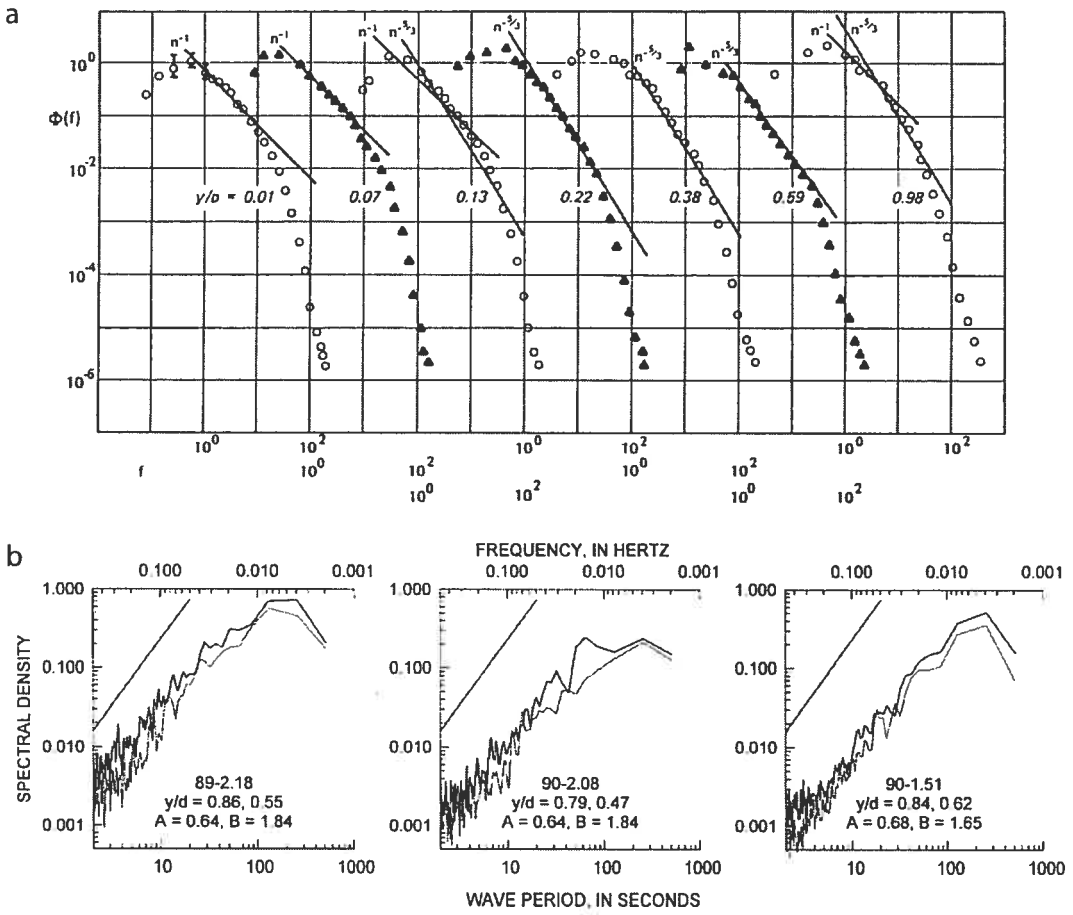

Figure 2.5. *u* component velocity spectra (a) for seven depths over a rough-bed [*Nowell and Church*, 1979]. (b) for a gravel-bed river under bedload movement flow conditions. The heavy line represents the spectrum for the lowest sensor in the array (lowest *z/Z*) [*Dinehart*, 1999]

The foregoing examples from the literature have shown the typical characteristics of fully developed 2D boundary layer flow over smooth and rough surfaces. In general, the effect of boundary roughness is to increase the generation of turbulence along the bed resulting in increased Reynolds shear stress, turbulent mixing and a reduction in mean flow velocities. u', w' and $-\rho\overline{uw}$ increase in the inner boundary layer and possibly throughout the depth with increased roughness. There is even a suggestion (although contested) that relatively small bed roughness with $Z/h_s = 50$ can have a marked influence on the main turbulence statistics in the intermediate boundary layer region $z/Z = 0.5$ [*Krogstad and Antonia*, 1999]. The interactions and the transfer of

turbulence (momentum exchange) between the bed and boundary layer regions are due to self-forming coherent flow structures which are responsible for the behaviour of the turbulence statistics that we have presented. The following section will examine the main processes and coherent flow structures observed under various flow conditions in open channel flow (including gravel-bed rivers).

2.2. Turbulent coherent flow structures

Coherent flow structures are an integral component of fully developed turbulent flows. Depending on the flow conditions, turbulent coherent flow structures range in sizes from small to large scale. The smallest scale in a turbulent flow is limited by the fluid viscosity and is estimated by the Kolmogorov microscale, $\eta = (\nu^3/\varepsilon)^{1/4}$ where ε is the turbulent energy dissipation rate. The largest scale corresponds to flow depth or some multiple thereof. The higher the Reynolds number the broader the range of scales. It is usually the energy containing scales that exhibit the most evident structure [*Holmes et al.*, 1996]. The general definition commonly used for turbulent coherent structures is of a three-dimensional (3D) region of flow over which one fundamental flow variable exhibits significant correlation with itself or another variable over a range of space and/or time [*Robinson*, 1991]. Characteristics of coherent structures are that the structures are on the whole unsteady and do not repeat in detail, even though they may remain in more or less the same place and maintain roughly the same size [*Holmes et al.*, 1996]. This definition is not fully shared by all researchers, some believe that dynamical properties such as vorticity are a defining characteristic of coherent structures [*Hussain*, 1986]. The inclusion of vorticity in the definition of coherent structures is somewhat restrictive (and extremely difficult to measure in natural settings with available instrumentation), therefore the former more general definition of coherent structures is used throughout this thesis.

Since early statistical descriptions and visual observations of turbulent coherent structures in boundary layers [*Theodorsen*, 1952; *Grant*, 1958; *Kline et al.*, 1967; *Townsend*, 1976], determining their characteristics and the effect they have on flow dynamics has been the focus of many turbulence research papers. While most of the initial studies on turbulent coherent flow structures occurred in laboratory settings,

coherent structures have become the focus of many instream studies [*Jackson*, 1976; *Williams et al.*, 1989; *Kostaschuk and Church*, 1993; *Clifford*, 1993; *Dinehart*, 1999; *Lane et al.*, 2000; *Jirka*, 2001; *Roy et al.*, 2004]. These studies have shown the underlying importance of turbulent coherent flow structures in fluvial physical processes such as sediment transport, turbulent mixing and the formation of bedforms and morphological units. Further studies have characterised the behaviour of coherent structures around LREs [*Roy et al.*, 1999; *Buffin-Bélanger et al.*, 2001a; *Tritico and Hotchkiss*, 2005] and aquatic vegetation [*Raupach et al.*, 1996; *Ghisalberti and Nepf*, 2002]. Given the general definition of turbulent coherent structures many forms exist and have been documented both in the laboratory and in natural rivers. The following subsections focus on three specific types: small-scale inner layer smooth and rough boundary structures, large depth-scaled coherent structures, and shear layer vortices.

2.2.1. Turbulent coherent flow structures in smooth and rough boundary layers

Through the combined results of many detailed boundary layer flow studies, several of which are based on flow visualization, it is now generally admitted that horseshoe or hairpin vortices generated along the boundary are the main structure in the inner layer. These vortices are associated with a whole range of turbulent manifestations known as streaks, sweeps and ejections or bursts. Low-speed streaks occur close to the wall, $z^+ = zu_*/\nu < 10$ (Figure 2.6) and were first visually identified by *Kline et al.* [1967]. Streaks are elongated wavy structures aligned in the longitudinal direction and are separated by zones of higher speed fluid. For smooth walled flows over a wide range of *Re* the average lateral spacing of streaks has been found to be $\Delta y^+ = \Delta y u_*/\nu = 100$ [*Kline et al.*, 1967]. They are produced predominantly in the viscous sublayer next to the wall and slowly lift up off the wall. They are created as fluid is pumped away from the wall in a strong eruption due to the passage of counter rotating vortices constituting the tails of hairpin vortices [*Blackwelder and Eckelman*, 1979; *Smith*, 1996]. A study by *Grass et al.* [1991] was able to show the existence of streaks in a rough walled flume experiment over uniform grain roughness. While *Grass et al.* [1991] suggested their experiments point to the universal existence of streaks over smooth and rough beds, it is likely that the results obtained over a tightly packed homogenous rough-bed can not be generalized

to heterogeneous beds where elements protrude at random heights as pointed out by *Best* [1993].

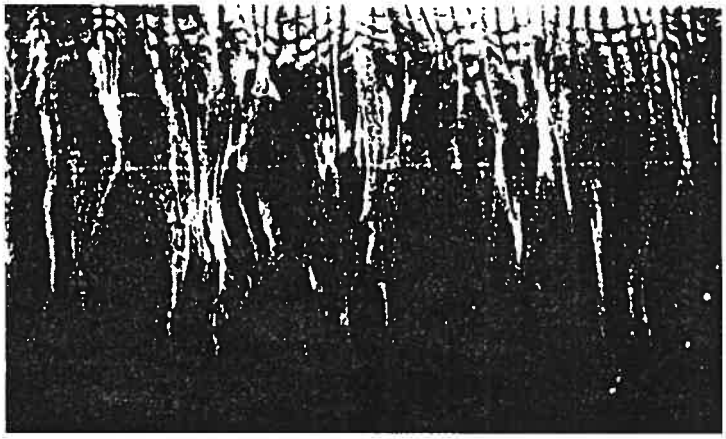

Figure 2.6. Plan view of streak structure of a flat plate turbulent boundary layer close to the wall at $z^+ = 2.7$ [*Kline et al.*, 1967].

Hairpin vortices develop due to high curvature in the vorticity field above the wall in the presence of a shear flow. The degree of lateral growth and deformation is critically dependent on the level of local shear [*Smith et al.*, 1991]. Due to the shearing, the hairpin vortex shape is stretched and the head undergoes strong lateral expansion as it rises away from the wall into regions of reduced shear where it erupts [*Smith et al.*, 1991]. This eruption of fluid away from the wall and into the outer layer is termed the bursting or ejection process and is small-scale given the size of individual hairpin vortices. Fluid eruptions occur from either the hairpin vortex head or the streak region between its legs and may combine and amalgamate with other hairpin heads to give rise to somewhat larger structures. The upward ejections are balanced by high-speed motion towards the bed as fluid away from the wall encounters the slower speed ejection and is redirected towards the wall to conform with fluid continuity. This redirected fluid is as well influenced by the negative pressure gradient as the ejecting fluid accelerates away from the wall. Both these mechanisms give rise to sweeps which penetrate the water column towards the wall [*Smith*, 1996]. *Smith*'s [1996] conceptual model of streaks, ejections and sweeps is presented in Figure 2.7. Researchers have suggested other models to explain streaks, sweeps and ejections. For instance, *Kaftori et al.* [1994] have

suggested longitudinally elongated funnel-shaped vortical structures as an alternative to the hairpin vortex model. Their model adequately describes sweeps and ejections through the upward and downward rolling motion of the funnel vortex. The vortex funnels are suggested to advect downstream in shifting parallel lines thus creating a mechanism for low-speed streaks.

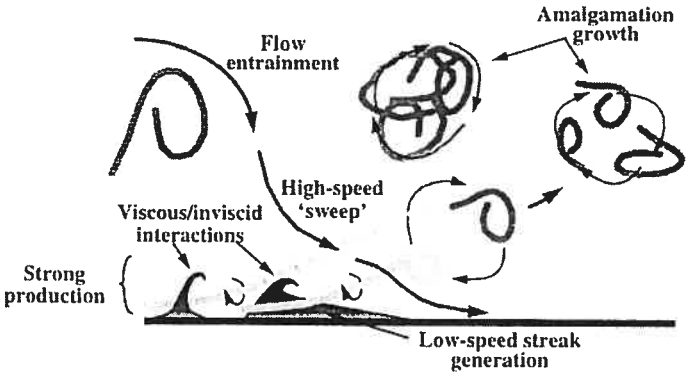

Figure 2.7. Conceptual smooth-bed model of streaks, ejections and sweeps [*Smith*, 1996].

With the exception of *Grass et al.* [1991] all of the visualization studies investigating near-wall coherent flow structures have been conducted on smooth bed boundary layers at low Reynolds numbers. The hairpin model is dependent on the roll-up and formation of vortices very close to the wall at or below the interface with the viscous sublayer where the low-speed streaks form and then uplift ($0 < z^+ < 10$). The viscous sublayer is implicit within the hairpin model and may be disrupted or absent due to the presence of appreciable grain roughness thereby putting into question the validity of the model for rough boundary layers [*Best*, 1993]. *Grass et al.* [1991] observed low-speed streak zones occurring over uniform glass beads of various diameters. Subsequent results by *Grass and Monsour-Tehrani* [1996] suggest a universal lateral spacing when scaled by k_s^+ and a near-wall "effective" viscosity. These studies were performed for relatively low k_s^+ values, as k_s^+ increases into the fully rough regime $k_s^+ > 70$ and bed sediment height is non-uniform the disruption of the viscous sublayer requires a different model for the generation of the hairpin vortices. Several studies have suggested that vortices shed by individual clasts provide this mechanism [*Kirkbride*, 1993; *Smith*,

1996]. Smith suggested for the rough-bed case that initial hairpin-like vortices shed from individual clasts increase proportionally with roughness scale. The subsequent evolution of large-scale structures via vortex amalgamation and interaction is suggested to proceed in basically the same manner as for a smooth-walled case (Figure 2.8). Vortices shedding from individual roughness elements visually appear quite similar to the smooth-wall hairpin vortices [*Acarlar and Smith*, 1987; *Grass*, 1991] and will be discussed further on in this thesis. *Smith* [1996] suggested a similar generation mechanisms for sediment ridges and ripples where again initial hairpin vortices are generated from individual ripples amalgamating into ejections and interacting with high-speed sweeps.

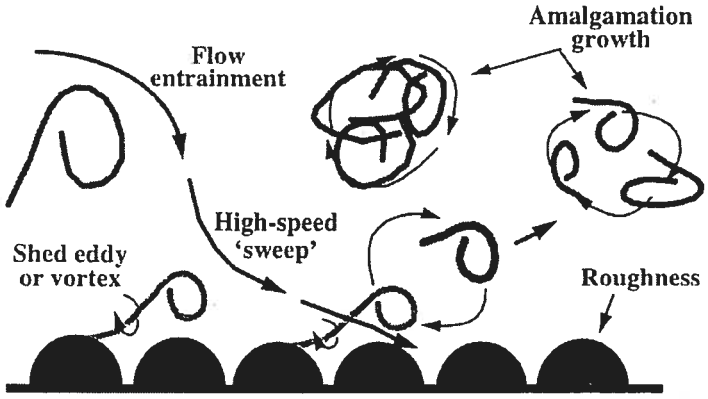

Figure 2.8. Conceptual fully-rough bed model of the generation of hairpin vortices [*Smith*, 1996].

Ejections play a dominant role in the interaction and transfer of momentum between the inner and outer regions of the flow and are believed to determine the structure of the entire turbulent boundary layer [*Kline et al.*, 1967]. The streak, ejection, sweep structures described here are relatively small in size and have all been observed in the inner boundary layer close to the wall on the order of $z^+ = 1$ to 500 [*Kline et al.*, 1967]. It is uncertain if these structures penetrate into the outer boundary layer, yet a relatively recent PIV study by *Adrian et al.* [2000] suggest the existence of larger flow structures consisting of longitudinally aligned hairpin vortices in the outer layer. Models of these larger depth-scaled flow structures will be discussed in the following section.

2.2.2. Large-scale turbulent coherent flow structures

Large-scale (LS) turbulent coherent flow structures are a predominant feature of open channel flow whether in laboratory flumes or in gravel-bed rivers [*Falco,*1977; *Nakagawa and Nezu*, 1981; *Roy and Buffin-Bélanger*, 2001; *Shvidchenko and Pender*, 2001; *Roy et al.*, 2004]. These structures consist of depth scaled intermittent fronts (or wedges) of high- and low-speed fluid. While LS structures are composed of several types of fluid motion, high-speed structures consist mainly of rapid downward motion (sweeps), and low-speed structures are mainly associated with slow upward motions (ejections) with angles of inclination between the two motions at 20°-36° in the downstream direction [*Nezu and Nakagawa*, 1993; *Buffin-Bélanger et al.*, 2000]. As with the near-bed coherent structures previously discussed, flow visualization techniques have been instrumental in identifying and characterizing LS coherent flow structures. Figure 2.9 presents a sequence of images recorded in a gravel-bed river where the sequential passage of high- and low-speed wedges can be clearly observed. The low angle of inclination between the two motions is apparent in the image sequence.

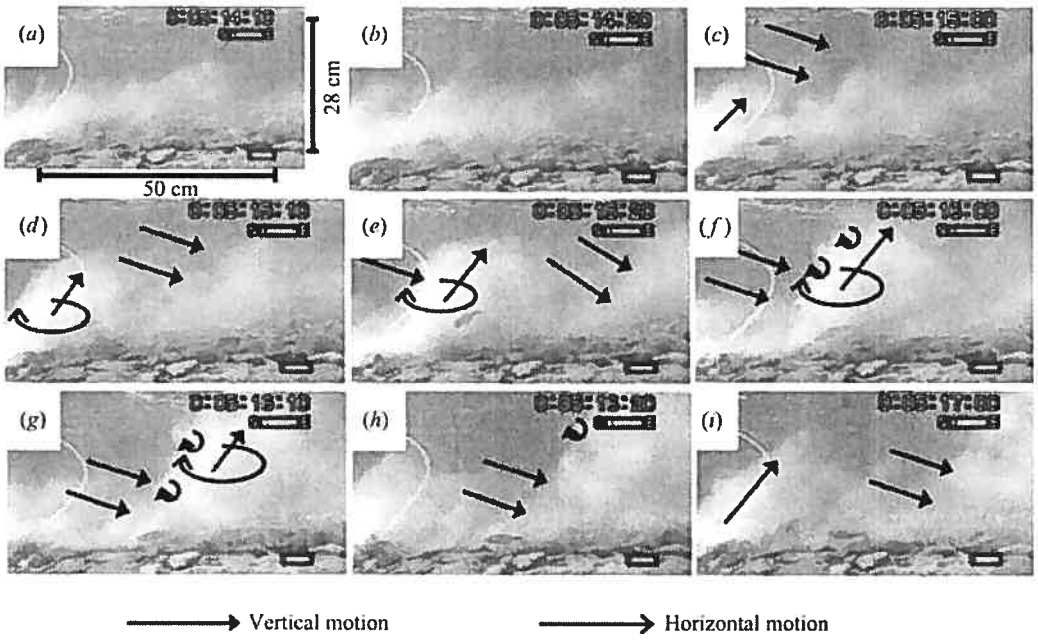

Figure 2.9. Images extracted from a flow visualization sequence in a gravel-bed river. The 2.5 s visual sequence illustrates the passage of a high-speed wedge followed by a low-speed wedge which takes the form of a violent ejection [*Roy et al.*, 2004].

Further laboratory visualization studies by *Shvidchenko and Pender* [2001] have related high- and low-speed wedges to depth-scale eddies (4-5Z) advecting downstream at the bulk flow velocity (Figures 2.10 and 2.11). These depth-scale vertical movements (downward and upward vorticity) were responsible for generating alternating high- and low-speed zones and played a critical role in mobilizing sediments on the bed through their fluctuating lift and drag hydrodynamic forces on the bed particles. This supports the suggestion by Nezu and Nakagawa [1993] that LS coherent flow structures are 3D vortical movements. *Shvidchenko and Pender* [2001] found the LS flow structures could as well be scaled by the mean velocity ($0.4\overline{U}$). Recent work by *Marquis and Roy* [2006a] supports mean velocity as a scaling parameter for LS ejection events. The positive relationship of $\overline{U}$ and LS structure size is likely related to the addition stretching of the LS structures in the longitudinal direction as flow is increased.

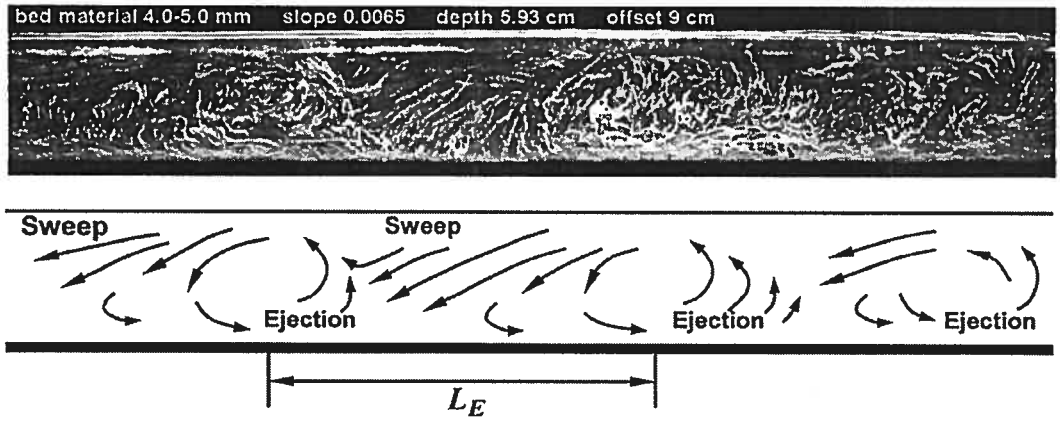

Figure 2.10. Visualization of large-scale turbulent structures of open-channel flow over mobile gravel beds (camera is moving with mean flow velocity). Flow is right to left. [*Shvidchenko and Pender*, 2001].

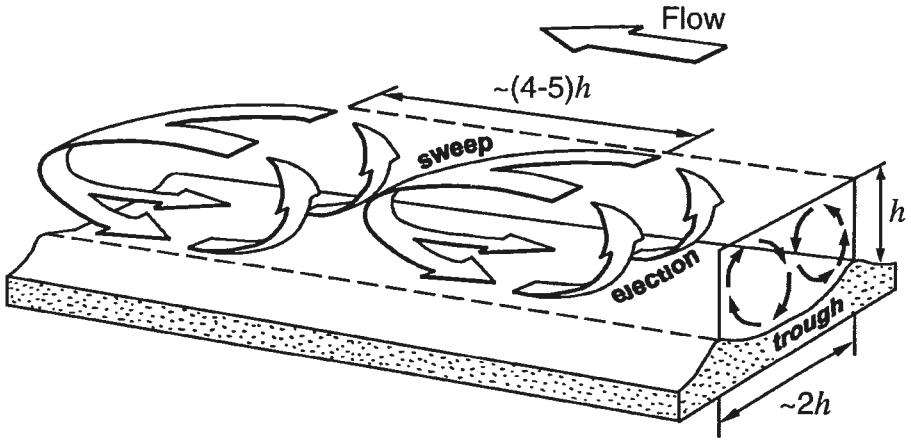

Figure 2.11. Conceptual model of LS turbulent coherent flow structures [*Shvidchenko and Pender*, 2001].

The origin of LS coherent structures is still unclear. LS sweep and ejection motions are similar to the smaller scale sweep and ejection motions originating from the hairpin vortices, only LS motions are of a much bigger scale. There is a general school of thought proposing that they originate in the inner layer of the bed as hairpin vortices and expand upward coalescing into larger and larger structures [*Kline et al.*, 1967; *Perry et al.*, 1986; *Yalin*, 1992; *Nezu and Nakagawa*, 1993; *Smith*, 1996; *Kim and Adrian*, 1999; *Adrian et al.*, 2000]. Figure 2.12 presents a conceptual model for the generation of LS coherent structures proposed by *Kim and Adrian* [1999] showing longitudinal alignment of many hairpin vortex packets initiating from the bed. The smaller packets are nested within larger packets, creating the appearance of multiple zones of uniform longitudinal momentum. This model is supported by the smooth-bed PIV studies by *Adrian et al.* [2000] with Re = 7705 (Figure 2.13). Apparent in Figure 2.13 is the alignment of vortices of similar velocity which convect upwards into the outer boundary layer $z/Z = 0.7$. The PIV results of *Adrian et al.* [2000] have much in common with the observation and model by *Falco* [1977; 1991] obtained through fog-oil visualization studies. At Re = 21 300, small-scale "typical eddies" were observed to ride on top of LS motions.

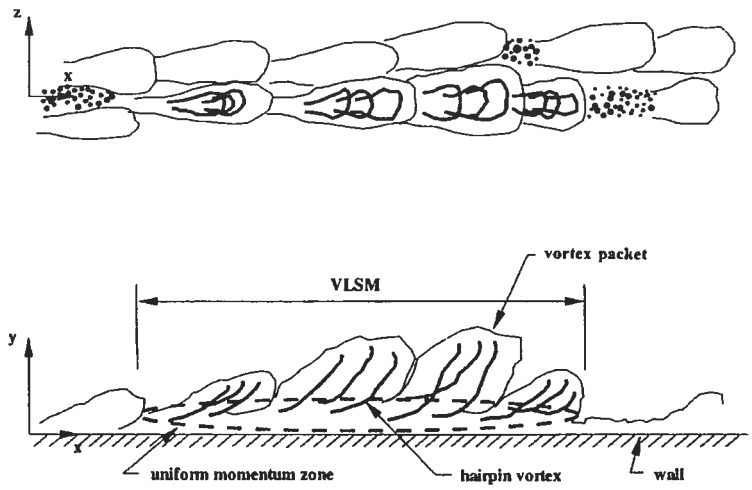

Figure 2.12. Conceptual model of LS turbulent coherent flow structures formation process [*Kim and Adrian*, 1999].

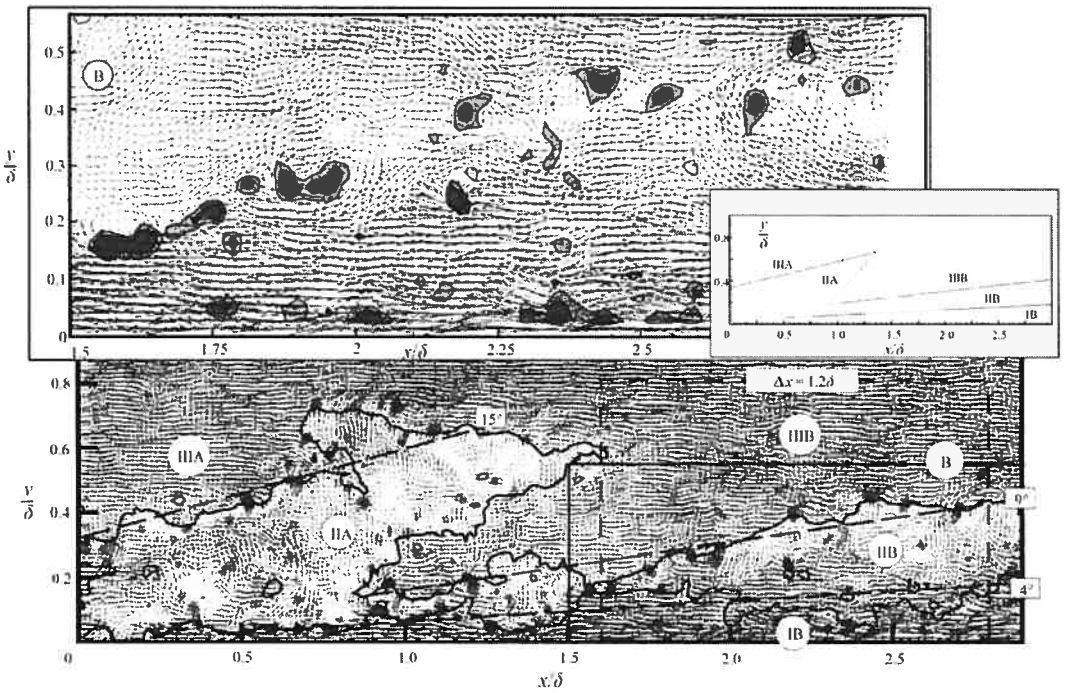

Figure 2.13. PIV of large-scale structure of hairpin vortex packets at *Re* = 7705. The solid lines are contours of constant longitudinal velocity at 61% and 79% of the free-stream velocity. Grey levels indicate swirling strength and flow is from left to right [*Adrian et al.*, 2000].

LS coherent structures exist under highly variable bed roughness conditions from smooth-wall laboratory studies [*Falco*, 1991] to very rough wall gravel-bed river studies

[*Kirkbride*, 1993; *Kirkbride and Ferguson*, 1995; *Buffin-Bélanger et al.*, 2000; *Roy et al.*, 2004]. The *Kim and Adrian* [1999] smooth-wall model is based on the rollup and generation of hairpin vortices in the viscous sublayer (very close to the wall). As previously mentioned, under rough-bed conditions the viscous sublayer cannot develop due to the roughness length exceeding the sublayer thickness [*Carling*, 1992; *Kirkbride*, 1993]. For rough-wall boundary conditions, an alternative vortex generation process has been proposed whereby shear layer vortices are shed from individual roughness elements. These vortices in turn interact to generate the LS turbulent coherent flow structures [*Smith*, 1996]. A similar model has been proposed by *Kirkbride* [1993] where the assemblage of roughness elements of different shapes and sizes results in the shedding of many multi-sized vortices which interact and coalesce to produce more resilient structures of larger spatial scale. *Dinehart* [1999] has suggested LS flow structures are produced by topographic features such as changes in channel geometry and separation of flow over bedforms.

Even though the origins of LS coherent flow structures in gravel-bed rivers are still unclear, it is unlikely that LS flow structures should be scaled by inner boundary layer variables which result in dimensionless heights of the order of $z^+ = 3000$ to 4000 [*Roy et al.*, 2004]. If inner flow variables are not relevant in the dynamics of these structures a much more appropriate scaling parameter is flow depth. Table 2.1 modified from *Roy et al.* [2004] provides a summary of the estimated characteristic dimensions of LS flow structures from different experiments conducted in different flow media, and boundary conditions at a wide range of Reynolds numbers. Despite the diverse experimental conditions and methods used to estimate the scales of the structures, the similarity among various estimates of the size of the structures is remarkable [*Roy et al.*, 2004]. In general, the lengths of LS structures are two to three times the flow depth, Z, with widths and heights nearly equal to the flow depth. The dependence of LS structures on flow depth supports the notion that Z functions in some meaningful way to limit the scale for turbulent eddies in rivers [*Church*, 2007]. The relationships between relevant scaling parameters and small- to large-scale motions in gravel-bed rivers were suggested by *Nikora* [2007] (Figure 2.14). Velocity fluctuations induced by coherent flow structures cover a wide range of spatial scales from sub-millimetre to tens of kilometres.

Turbulent fluctuations can be scaled by a number of geomorphic characteristics depending on the size of the fluctuations ranging in order of smallest to largest as: inner flow variables, roughness height, flow depth and channel width.

Table 2.1. Dimensions of large-scale flow structures (modified from *Roy et al.* [2004])

	Flow type	*Re*	Length	Width	Height
Blackwelder and Kovasznay [1972]	air	27500[a]	1.1δ[d]		
Falco [1977]	air	1000–4000[b]	1.6δ		
Brown and Thomas [1977]	air	10160[b]	2δ		
Nakagawa and Nezu [1981]	water	4200–12000[c]	$1.5Z$		$(0.5–1)Z$
Imamoto and Ishigaki [1987]	water	6100–7800[c]	$2Z$	Z	Z
Komori et al. [1989]	water	11000[c]	$2Z$	Z	$0.5Z$
Yalin [1992]	water	Not given	$6Z$	$2Z$	Z
Schvidchenko and Pender [2001]	water	12000–98000[c]	$(4–5)Z$	$2Z$	Z
Liu et al. [2001]	water	10756–59870[c]	$(1–2)Z$		$0.25Z$
Roy et al. [2004]	water	150 000–200 000[c]	$(1–10)Z$	$(0.5–1)Z$	Z

[a]Based on the boundary layer thickness, δ.
[b]Based on the momentum thickness, θ.
[c]Based on flow depth, Z.
[d]Estimated from figure.

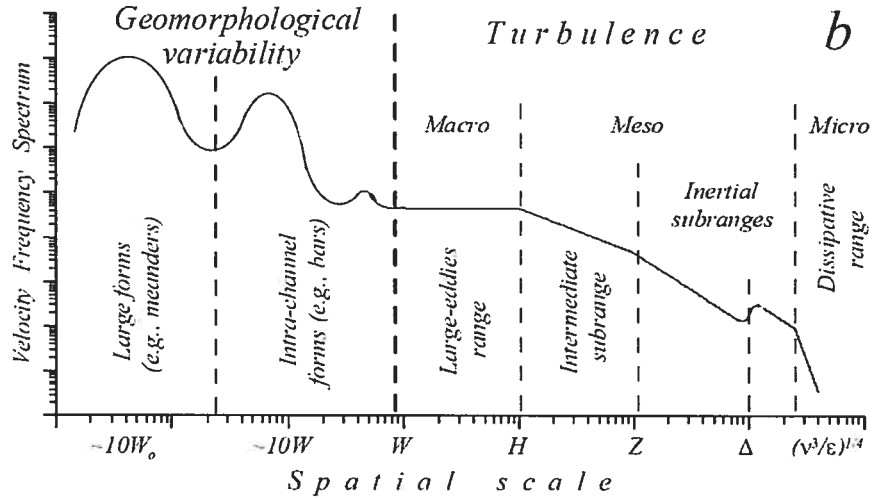

Figure 2.14. Schematised velocity spectra in gravel-bed rivers related to scaling parameters. (note: W_o, W, H, Z, and Δ are defined here as river valley and river channel widths, flow depth, height above the bed, and grain size, respectively) [*Nikora*, 2007].

2.2.3. Coherent turbulent flow structures in shear layers

2.2.3.1. Mixing layers

In all shear flows there exist identifiable, characteristic turbulent structures [*Fuchs et al.*, 1980]. While some characteristics and behaviours are specific to the type of shear flow and boundary conditions under investigation, there are many characteristics which are more or less universal such as the generation of coherent vortices. The region between two parallel streams moving at different speeds is the simplest shear flow (mixing layer) to consider (Figure 2.15). Mixing layers can also develop due to gradients in pressure, density and heat. The planar interface (shear or mixing layer) between the two flows contains a wavy linear instability caused by the amplification of small disturbances in pressure: referred to as a Kelvin-Helmholtz instability. With amplification, the wavy pattern progresses into fully developed coherent vortices. The vortices are connected together in the longitudinal direction by filaments of low-rotational fluid known as braids. The energy required to drive the vorticity is obtained by the velocity difference (gradient) between the two streams. The vortices grow downstream from the point of initial mixing by entraining fluid from both streams advecting downstream with a mean velocity of the two parallel flows.

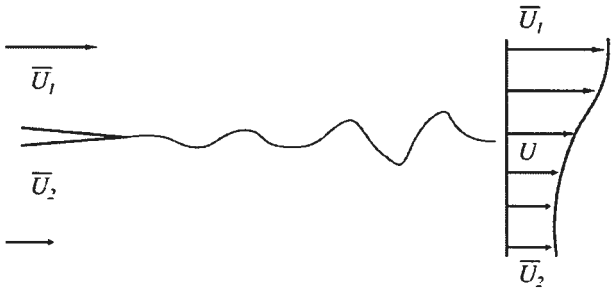

Figure 2.15. Schematic of shear mixing layer between two parallel flows with different mean velocities $\overline{U}_1$ and $\overline{U}_2$.

In shear layers, individual vortices have as well been found to interact and coalesce into larger vortices where their individual identities are smoothed out through viscous diffusion (Figure 2.16) [*Winant and Browand*, 1974]. The pairing and entrainment processes continue until the mixing layer thickness has grown to the order of the channel depth, Z, at which point the bottom boundary and the free-surface inhibit further growth [*Winant and Browand*, 1974].

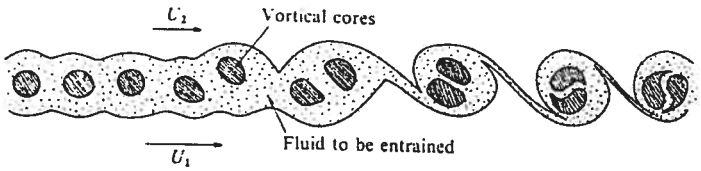

Figure 2.16. Pairing mechanism of shearing vortices [*Winant and Browand*, 1974].

In a fully turbulent shear layer other modes of interaction between vortices occur at higher Reynolds numbers such as fractional pairings and tearings [*Hussain and Zaman*, 1985]. As the Reynolds number increases, individual structures may vary in shape, size, orientation, strength, convection velocity [*Hussain and Zaman*, 1985] therefore the frequency of shedding becomes more difficult to determine. Coalescence is a universal feature of turbulent mixing [*Browand and Weidman*, 1976], yet within a fully developed mixing layer turbulent fluctuations of considerable smaller scale do occur. In 2D mixing layers marked increases in *uv* component Reynolds shear stresses are observed compared with free-stream values [*Browand and Weidman*, 1976]. In rivers, mixing layers occur at stream confluences and have been extensively investigated [*Biron et al.*, 1993; *Leclair and Roy,* 1997; *DeSerres et al.*, 1999; *Rhoads and Sukhodolov*, 2004; *Boyer et al.* 2006]. The bed heights at river conferences are often discordant resulting in complex 3D deformation of the mixing layers [*Best and Roy*, 1991]. These types of free-shear layers can be associated with relatively much higher *uw* component Reynolds shear stress [*Biron et al.*, 1993].

2.2.3.2. Isolated bluff bodies – away from the wall

A bluff body is an obstacle placed in a flowing fluid (or traveling through a stationary fluid) about which flow separation occurs. The term "bluff body" is used because the precise cross-section and shape has only a secondary influence on the form of the wake as all such wakes are generally similar in structure [*Holms et al.*, 1996]. As flow moves around the body, the boundary layer separates producing a shear layer which is subject to a Kelvin-Helmholtz instability. The shear layer rolls up due to the strong velocity and pressure gradients and forms coherent vortices which are similar in form and behaviour

to the mixing layer vortices [*Nezu and Nakagawa*, 1989]. Through flow visualization, *Achenbach* [1974] observed this roll-up and periodic shedding of distinct hairpin vortices in the wake of an isolated suspended sphere at $Re_{\emptyset} = 10^3$. The coherent flow structures in the sphere wake were complex and three-dimensional. The boundary layer which forms on the leading edge or upstream face of the body is initially laminar (regardless of the state of the free-stream fluid) but may become turbulent with sufficient distance downstream depending on particle Reynolds number, $Re_{\emptyset}$, and the roughness of the boundary (where $Re_{\emptyset}$ is based on free stream $\overline{U}$ and characteristic dimension of the bluff body, $\emptyset$, i.e., cylinder diameter).

For a bluff-body placed in a turbulent flow, the effect of further increasing the free-stream *Re* causes the laminar to turbulent transition point of the bluff body boundary layer to migrate further upstream until the boundary layer on the object itself becomes turbulent (i.e., in the order of 1. wake transition, 2. shear layer transition, 3. boundary layer transition) [*Williamson*, 1996]. When the boundary layer of the bluff body becomes turbulent the wake narrows resulting in a significant reduction in drag and base suction coefficients [*Singh and Mittal*, 2005]. This state is referred to as the drag crisis and occurs around $Re_{\emptyset} \approx 3 \times 10^5$ [*Achenbach*, 1974].

The classical example of the effect of $Re_{\emptyset}$ on bluff body wakes is the formation of a Kármán vortex street at $Re_{\emptyset} > 49$ for an isolated vertical cylinder which is caused by the fundamental wake instability [*Williamson*, 1996]. With increasing $Re_{\emptyset} > \sim 200$ the vortex street breaks down and is lost downstream into the fully developed turbulent flow. In general, when flow is laminar, instabilities are suppressed due to viscosity while in transitional or turbulent flow instabilities are amplified downstream. In the transition zone flow is very unpredictable and often changes back and forth between laminar and turbulent.

For $Re_{\emptyset} > \sim 1200$, the shear layer close to the separation point in the near wake undergoes an initial instability mode where the shear layer rolls up to form initial small-scale shear layer instability vortices scaled by the shear layer thickness. These can be observed shedding from a sphere in the smoke visualization study of *Teneda* [1978] where $Re_{\emptyset} = 10^4$ (Figure 2.17a). Through fluid entrainment, merging and pairing, the vortices amalgamate into the second mode of larger-scale primary Kármán vortices

scaled by h_s before shedding downstream [*Fuchs et al.*, 1980; *Hasan*, 1992; *Williamson*, 1996]. The amalgamation process of the initial shear layer vortices was observed in a PIV study by *Lin et al.* [1995] for flow around a cylinder for $Re_{\emptyset} = 10^4$ (Figure 2.17b). Initial shear layer vortices are outlined on either side of the cylinder by the vorticity contours. In the wake of the cylinder the small-scale vortices are shown to amalgamate into larger coherent flow structures.

At moderate $Re_{\emptyset}$ ($Re_{\emptyset} = 10^4 - 10^5$), the initial shear layer instability vortices shed downstream away from the surface of the bluff body. With increasing $Re_{\emptyset}$ the small-scale vortices migrate upstream towards the surface of the bluff-body. When $Re_{\emptyset}$ reaches a critical value ($Re_{\emptyset} \approx 3 \times 10^5$) the point of instability migrates very close to the original boundary layer separation point on the surface of the cylinder. The instability vortices cause increased mixing between outer flow and the boundary layer inducing reattachment of the boundary layer and a delay of the general onset of separation. This delay of boundary layer separation results in a much narrower wake and reduced drag forces and is termed the drag crisis. The generation of initial shear layer vortices and the physical processes involved with the drag crisis for flow around a cylinder was investigated by *Singh and Mittal* [2005] using a 2D large eddy simulation (LES) (Figure 2.18). At the onset of the drag crisis ($Re_{\emptyset} = 10^6$) a general narrowing of the wake is clearly observed, compared to the presented cases at lower $Re_{\emptyset}$. *Singh and Mittal* [2005] found that at $Re_{\emptyset} = 10^7$, the instability of the shear layer propagates further upstream causing mixing of a significant portion of the boundary layer prior to its eventual separation resulting in an increase in Reynolds stresses and skin drag in this region. While the drag crisis is an interesting physical process, it should be rare in gravel-bed rivers as for a 0.3 m boulder $\overline{U}$ would have to be greater than 3.3 m s^{-1} in order to obtain $Re_{\emptyset} = 10^6$.

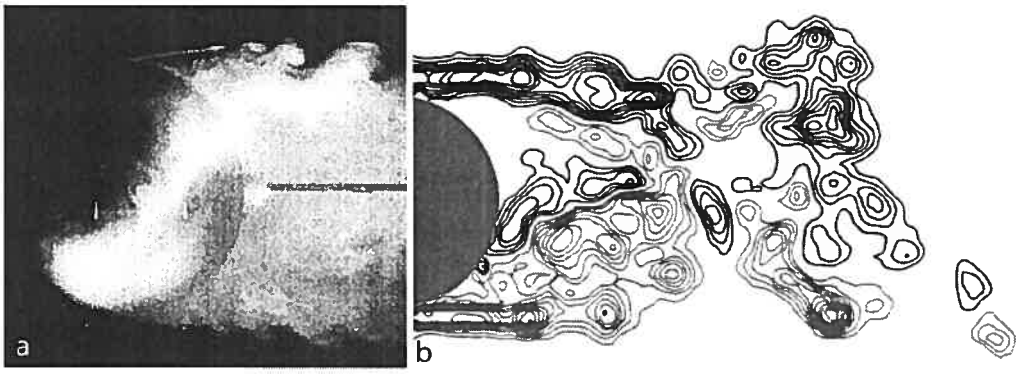

Figure 2.17. Initial shear layer instability vortices: (a) smoke visualization in the wake of a sphere, $Re_{\emptyset} = 10^4$ [*Taneda,* 1978]; (b) PIV contours of positive and negative vorticity in the wake of a cylinder, $Re_{\emptyset} = 10^4$ [*Lin et al.*, 1995]. Flow is from left to right.

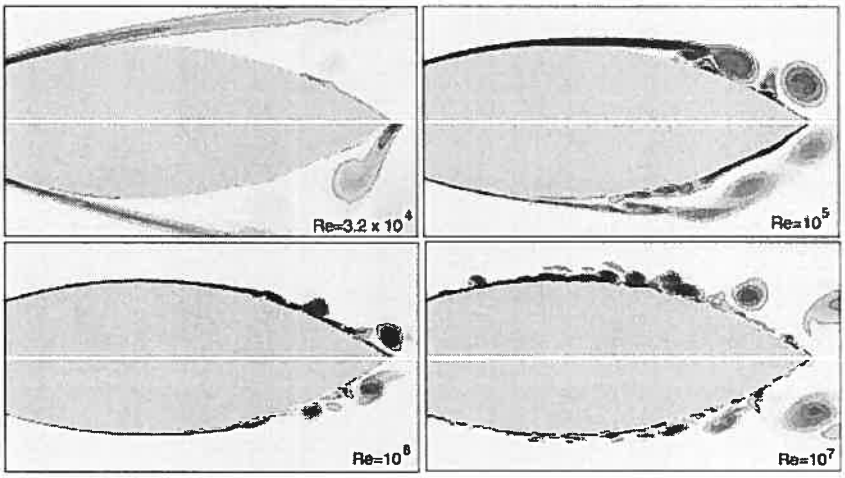

Figure 2.18. Numerical 2D LES of shear layer instability vortices and drag crisis for a cylinder placed in flow. Close-up view of either side of the cylinder. Flow is from left to right. Drag crisis is observed for $Re = 10^6$ subplot where the wake is significantly narrowed and separation of the initial instability vortices is delayed further downstream along the cylinder. [*Singh and Mittal*, 2005].

2.2.3.3. Backward facing steps, dunes and wall positioned bluff bodies

Backward facing steps, dunes and bluff bodies positioned on the wall surface pose additional complexity due to the curvature of the shear layer towards the wall and subsequent reattachment [*Hasan*, 1992; *Bennett and Best*, 1995]. A schematic description of a backward facing step by *Nezu and Nakagawa* [1989] is presented in Figure 2.19.

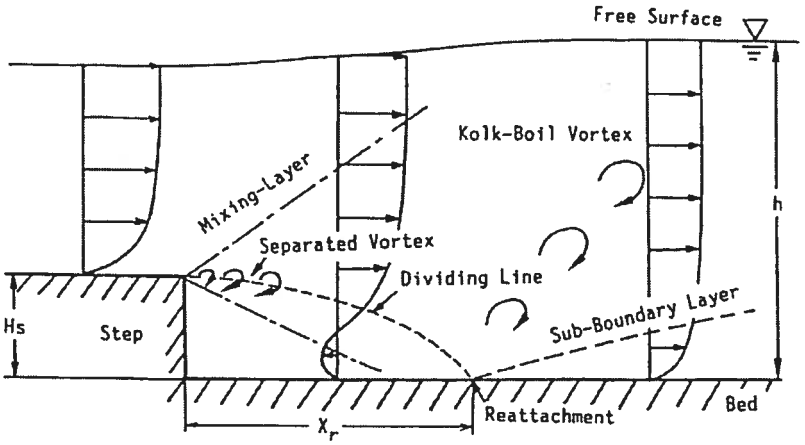

Figure 2.19. Backward facing step features [*Nezu and Nakagawa*, 1989]

The downstream flow structure is strongly dependent on the upstream velocity distribution and local geometry of the surface around detachment [*Simpson*, 1989]. Initially the shear layer is much like a plane mixing layer as the flow lines are only slightly curved and the shear layer is thin enough not to be affected by the wall [*Simpson*, 1989]. Shear layer vortices are formed and grow downstream through pairing and fluid entrainment. Flow separation (or detachment) occurs near the sharp edges of the body (downstream edge of the step) with accompanying large variations in velocity and pressure around the detachment location [*Simpson*, 1989]. Downstream, the separated shear layer curves sharply downward and impinges on the wall. A portion of shear-layer fluid is deflected upstream into the recirculation zone due to the strong adverse pressure gradient and wall interaction. The peak in magnitude of the Reynolds shear stress lies in the path followed by the separated vortices created in the shear layer [*Kadota and Nezu*, 1999]. This observation is also reported by *Simpson* [1989] who found maximum Reynolds shearing stress to occur near the maximum velocity gradient, $\partial \overline{U} / \partial z$, and move towards the wall as reattachment is approached. Similar peak $-\rho\overline{uw}$ values directed towards the wall have been observed for 2D laboratory dune studies where separation occurs at the bed form crest [*Nelson et al.*, 1993; *McLean et al.*, 1994]. A rapid decay of Reynolds normal and shear stress occurs within the reattachment zone [*Simpson*, 1989]. Similarly, *-uw* correlations are quite high within the shear layer while in the recirculation zone they are close to zero [*Simpson*, 1989].

Further downstream topographic acceleration along the stoss side slope of the dunes was found to play a significant roll in damping turbulence for the 2D bedforms considered [*Nelson et al.*, 1993]. Results from the laboratory 2D dune study by *Bennett and Best* [1995] offer a good example of the general characteristic patterns of $-\rho\overline{uw}$ observed in the wake of dunes and backward facing steps (Figure 2.20). Maximum values for $-\rho\overline{uw}$ of 9 N m^{-2} occur along the shear layer and just downstream of reattachment. The shear layer is observed to curve downward towards the bed and reattachment occurs at $x = 4.25h_s$ downstream of the separation point. Figure 2.20 illustrates that fluid turbulence and turbulent momentum exchange is greatest along the separated shear layer.

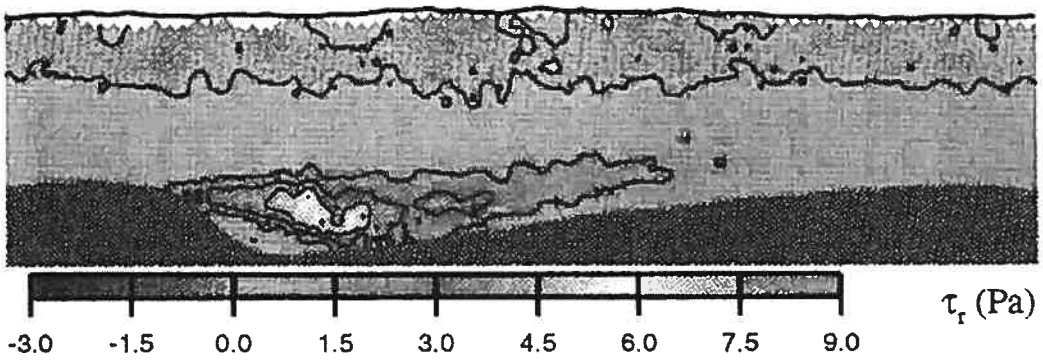

Figure 2.20. Contour map of $-\rho\overline{uw}$ over a dune, Re = 5.7 x 10^4. Flow is from left to right. [*Bennett and Best*, 1995].

Flows with separation and reattachment are complex, highly unsteady, and are associated with high turbulent intensities, localized mean or instantaneous reverse flows and the presence of low-frequency unsteadiness associated with a flapping of the shear layer [*Hasan*, 1992]. This flapping is a low frequency up/down vertical movement of the shear layer which is correlated with strong flow reversals in the vicinity of reattachment. The flapping of the shear layer results in an increase in turbulence intensity in detached flows of 5 – 10% compared with plane mixing layers [*Simpson*, 1989]. *Simpson* [1989] has suggested that the reason for the low-frequency fluctuation is due to LS turbulent structures which pass through the reattachment region as shown in Figure 2.21. Figure 2.21 presents *Simpson et al.*'s [1981] flow separation model and interaction with δ-scaled coherent flow structures. The separation point "D" occurs where $-\rho\overline{uw} = 0$ on the bed. LS flow structures which intermittently pass through the separation zone from

the free-stream region supply most of the near-wall backflow. This separation model is applicable for wall mounted bluff bodies and is supported by the observations of *Buffin-Bélanger et al.* [2001a], who noticed "flapping" (expansion and contraction of the wake) with the passage of LS turbulent coherent flow structures around a pebble cluster in a gravel-bed river (this is discussed in further detail in Section 2.3.2). An alternative mechanism is that at reattachment shear layer coherent turbulent flow structures are alternatively directed up or downstream thereby inducing the unsteadiness in the recirculation zone [*Bradshaw and Wong*, 1972]. The time averaged reattachment length shows a strong inverse relationship with *Re* for $Re < 6000$, but as *Re* increases above 6000 there is an increased insensitivity for subcritical flow conditions (i.e., $Fr < 1$) with $x/h_s \approx 5$, where x is measured from the lee edge of the step [*Nezu and Nakagawa*, 1989]. This value is in agreement with the isolated hemisphere investigated by *Best and Brayshaw* [1985], yet is larger than for the isolated hemisphere study of *Shamloo et al.* [1999] (where $x/h_s \approx 2$) and the dune study of *Kadota and Nezu* [1999]. For dunes *Kadota and Nezu* [1999] proposed that the comparatively shorter distance, $x/h_s = 4$, is due to the effects of the next downstream dune and associated flow acceleration (as seen by *Nelson et al.* [1993]). The reattachment location is not temporally steady and has been found to fluctuate by as much as $\pm 2\ h_s$ [Simpson, 1989] and the fluctuation has been related to the u component signal [*Nezu and Nakagawa*, 1989; *Kadota and Nezu*, 1999].

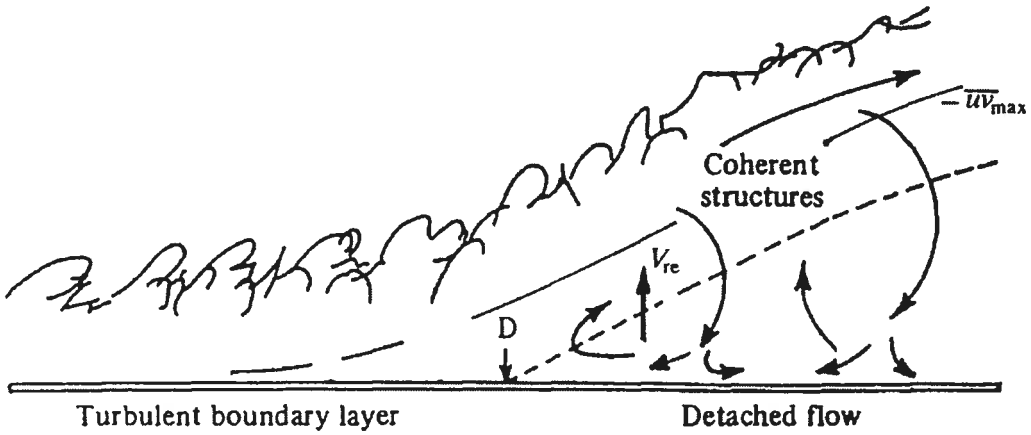

Figure 2.21. Flow separation model and interaction with LS coherent turbulent structures. D denotes detachment location. V_{re} denotes the mean re-entrainment velocity. Dotted line denotes $\overline{U} = 0$. Solid line denotes maximum $-\overline{uw}$ [*Simpson et al.*, 1981].

Acarlar and Smith [1987] conducted a fine-scale laboratory visualization study of flow over a wall positioned hemisphere at relatively low Reynolds numbers, $30 \leq Re_{\emptyset} \leq 3400$. Figure 2.22 presents their coherent turbulent flow structure conceptual model based on their observations showing the generation of 3D hairpin vortices which roll up and shed from the hemisphere shear layer. These hairpin structures and those shedding from suspended spheres previously discussed [*Achenbach*, 1974] appear quite similar to the near-wall hairpin vortices previously described over a smooth boundary layer [*Smith*, 1996] suggesting the presence of a universal turbulent structure. As with the plane mixing layer and shear layer generated by the backwards facing step, as *Re* increases the hairpin vortices lose their individual character soon after roll up and coalesce into large structures [*Achenbach* 1974; *Acarlar and Smith*, 1987].

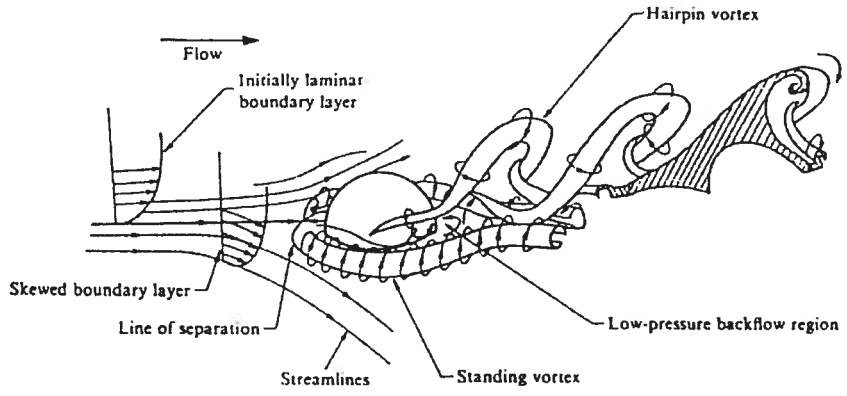

Figure 2.22. Conceptual model of flow over a grounded hemisphere in a laminar flow at $Re_{\emptyset} \leq 3400$ [*Acarlar and Smith*, 1987]

The *Acarlar and Smith* [1987] model is similar to that proposed by *Achenbach* [1974], yet it includes an additional turbulent coherent flow structure not present in the shear layers previously discussed. With wall mounted bluff bodies, a standing (stationary) horseshoe vortex forms close to the wall with the vortex head oriented upstream (Figure 2.22). This vortex is generated at the upstream stagnation point and results from the rolling up of impinging vortex sheets and the downwash of fluid on the upstream face of the bluff body. The stationary vortex legs follow the contours of the hemisphere and trail far downstream. *Paola et al.* [1986] have described the stationary vortex as being stretched around the obstacle by diverging and accelerating mean flows

which reattaches downstream forming a pair counter-rotating vortices. As the stationary vortex legs wrap around the obstacle a low pressure zone is created at the bed due to flow acceleration (Figure 2.23) [*Brayshaw et al.*, 1983; *Best and Brayshaw*, 1985]. Figure 2.23 illustrates the high pressure estimated at the upstream face due to flow retardation and at the reattachment zone due to the impinging shear layer. The low pressure zone located on the leeside of the obstacle is due to flow separation and is dependent on obstacle size, Z and Re [*Brayshaw et al.*, 1983; *Nezu and Nakagawa*, 1989].

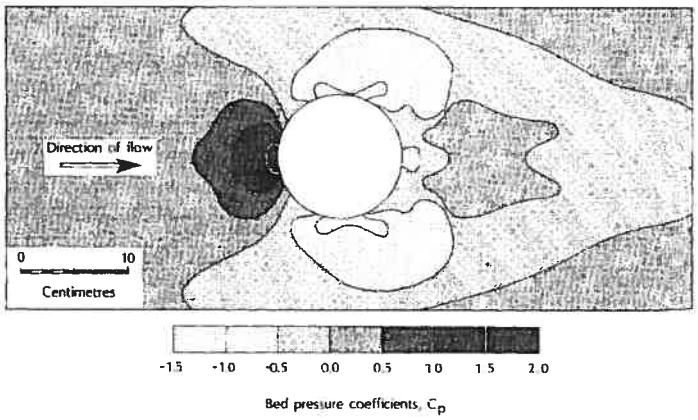

Figure 2.23. Bed pressure coefficients surrounding an isolated hemisphere at $Re_{\varnothing} = 5.2 \times 10^4$ [*Brayshaw et al.*, 1983].

The laboratory experiment of *Brayshaw et al.* [1983] included a detailed investigation of drag and lift forces by two longitudinally aligned hemispheres with sequentially increasing separation distances. Both drag (Figure 2.24) and lift estimated from the second downstream hemisphere decreased markedly when it was positioned immediately downstream of the stationary obstacle. Figure 2.24 also shows that when the mobile downstream hemisphere is smaller than the stationary obstacle the reduction in drag is again increased. The extent of the downstream influence was dependent on the stationary to mobile size ratio and ranged from 4.6 to $5.2h_s$ (where h_s is the height of the upstream hemisphere [estimated as diameter/2]).

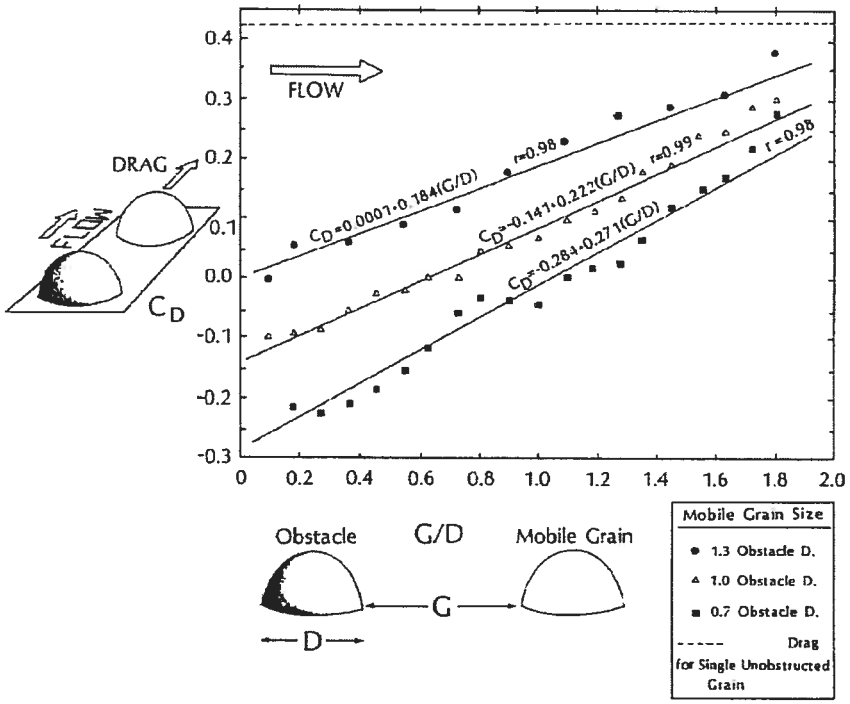

Figure 2.24. Drag coefficient for varying longitudinally aligned hemisphere separation distances [*Brayshaw et al.*, 1983].

A number of laboratory experiments have investigated the effect of surface mounted roughness element proximity (or density) on drag or flow resistance. When roughness elements are closely packed together a decrease in flow resistance occurs because the main flow is primarily conveyed along the top of the roughness elements – termed 'skimming flow' [*Morris*, 1955]. This effect has been found in many laboratory studies where the distance between LREs was varied [*Mirajgaoker and Charlu*, 1963; *Herbich and Shulits*, 1964; *Nowell and Church*, 1979; *Hassan and Reid*, 1990]. 'Wake interaction' flow has been described to occur when the spatial arrangement (or density) of LREs is such that the length of the turbulent wake is approximately equal to the distance downstream to the next aligned LRE [*Morris*, 1955]. *Nowell and Church* [1979] associated 'wake interaction' flow with the maximum flow resistance which in their laboratory study occurred for intermediate packing densities. According to *Hassan and Reid* [1990], the arrangement of protruding particles in gravel-bed rivers tend towards this 'wake interaction' condition.

Most if not all of the previous studies were either performed on 2D bedforms or only 2D velocity measurements were obtained (i.e., u and w components). The gravel-bed flume study of *Lawless and Robert* [2001] shows the effect of small surface mounted bedforms (pebble clusters) on the 3D hydrodynamics. This study did not investigate the isolated flow patterns associated with a single cluster, but rather the combined effect of clusters staggered in a diamond pattern on the flume bed. Their results showed a mean flow lateral divergence at the stoss side of the clusters and a lateral convergence on the lee side of the clusters. While *Lawless and Robert* [2001] did not estimate $-\rho\overline{u'v'}$ or $-\rho\overline{v'w'}$ they did show that peak values in v' were equal to u' and were observed in the cluster wake zone and to the lateral sides of the clusters. Given the cluster configuration in their study, it is difficult to distinguish whether the peaks in v' to the sides of a cluster are related to the cluster in question or result from the flow disturbance of an upstream laterally spaced cluster. A flume study by *Buffin-Bélanger and Roy* [2003] investigated 3D instantaneous velocities in a x-z plane crossing over the centre of a constructed pebble cluster in a flume. Their results suggested the wake turbulence (maximum k_e) was poorly scaled by Reynolds number, even though Z and $\overline{U}$ were shown to have a marked effect on k_e magnitudes.

2.2.4. Shedding frequency

Many studies investigating the hydrodynamics of bluff bodies and steps have focused on the vortex shedding frequency and the empirical Strouhal number [*Roshko*, 1961; Gerrard, 1966; *Achenbach*, 1974; *Hasan*, 1992; *Nakamura*, 1996]. The frequency of shedding coherent vortices can be quantified and reasonably well predicted from $\overline{U}$ and h_s using the empirically derived Strouhal number, S_t:

$$f = S_t \overline{U} / h_s \tag{2.8}$$

where f is the frequency of vortex shedding and h_s is the body or step height (cross-stream dimension). The Strouhal number is a function of particle Reynolds number. S_t for $Re_\varnothing < 3000$ is quite variable and ranges from 0.15 to 1.0 [*Achenbach*, 1974; *Acarlar and Smith*, 1987]. While at higher $Re_\varnothing$ ($6000 < Re_\varnothing < 3 \times 10^5$) the range is much narrower as S_t is typically between 0.13 and 0.21 [*Achenbach*, 1974]. *Nakamura* [1996] showed a negative relationship between the morphometric ratio of longitudinal body

length over cross-stream body length and argued that S_t depends strongly on the cross-sectional geometry, while *Tritton* [1998] contested the fact suggesting that the wake structure from different bluff bodies gives quite similar S_t values: typically $S_t = 0.2$. At high enough $Re_{\emptyset}$, the drag crisis region is attained from $3 \times 10^5 < Re_{\emptyset} < 3 \times 10^6$ and the shedding frequency is no longer well represented by the Strouhal number. In this range, the periodicity of the wake is lost except for very close to the bluff body as the boundary layer undergoes a transition from laminar to turbulent accompanied by a drop in pressure drag [*Achenbach*, 1974; *Tritton*, 1988; *Singh and Mittal*, 2005]. Similarly to the Strouhal number, *Jackson* [1976] has suggested a universal relationship for the return periods of large scale ejection/bursting events "kolks" observed in geophysical flows which have been shown to play a major role in sediment suspension [*Kostaschuk and Church*, 1993]. Most commonly associated with sand-bed rivers and dunes, this relationship $\overline{U}\ T_r/Z = 7.6$, where T_r is the return period, is very similar to the S_t, except that the length scale is now the boundary layer thickness instead of the characteristic bluff-body dimension. *Lapointe*'s [1992] study of the Fraser River, BC, suggests that the relationship between the recurrence period of bursting events and extreme flux events is threshold dependent and is therefore not as simple as suggested by *Jackson* [1976].

Spectral analysis of velocity time series can give accurate estimations of shedding frequency provided the instantaneous velocities are measured within the shear layer and the signal is not disrupted by surrounding flow patterns. Figure 2.25 presents two examples from the literature where velocity spectra were used to potentially characterise the shedding frequency from different types of shear layers. The first example (Figure 2.25a) from *Rhoads and Sukhodolov* [2004] illustrates the difficulty of obtaining a clear shedding frequency in an *in situ* river environment at high *Re*. Spectra were estimated from ADV measurement at three locations within a confluence shear layer ($Re \approx 10^5$). Tracer visualization identified shedding structures with vertical vorticity, yet no distinct hump or peak is observed in the power spectra over the expected range of periodicity $f =$ 0.1 Hz to 1.0 Hz. Typical of river environments, for $f > 0.7$ Hz, the spectra do show a power law relationship of constant slope of approximately -5/3 which from Kolmogorov theory indicates the existence of the inertial subrange. The power spectra presented in Figure 2.25b were estimated from laser Doppler anemometer (LDA) measurements in a

laboratory dune study. Under controlled flume conditions at moderate Reynolds numbers (Re = 2500), *Kadota and Nezu* [1999] were able to observe peaks shedding frequencies from the LDA measurements. With downstream distance (from x/h_s = 3.5 to 5.4) the peak in the power spectra decreases in frequency from f = 0.3 Hz to 0.1 Hz (Figure 2.25b). These estimated shedding frequencies were supported through concurrent visualization using dye injection. A frequency shift in peak spectral energy is an indication of the coalescence or growth of shedding vortices [*Uijttewaal and Tukker*, 1998]. *Kadota and Nezu* [1999] suggested the downstream peak frequency was related to kolk-boil vortices directed towards the surface through the interaction of coalesced shedding vortices with ejections from the reattachment zone. This model is supported by *Lapointe* [1992] who suggests both boundary layer bursting and shedding disturbances may contribute to kolks. Contrarily, *Bennett and Best* [1995] proposed that the kolk-boil vortex structures over dunes do not originate from classical boundary layer bursting as suggested by *Jackson* [1976], but can be solely attributed to the amalgamation and pairing of shear layer vortices into larger structures which advect towards the surface – a model supported by *Muller and Gyr* [1986].

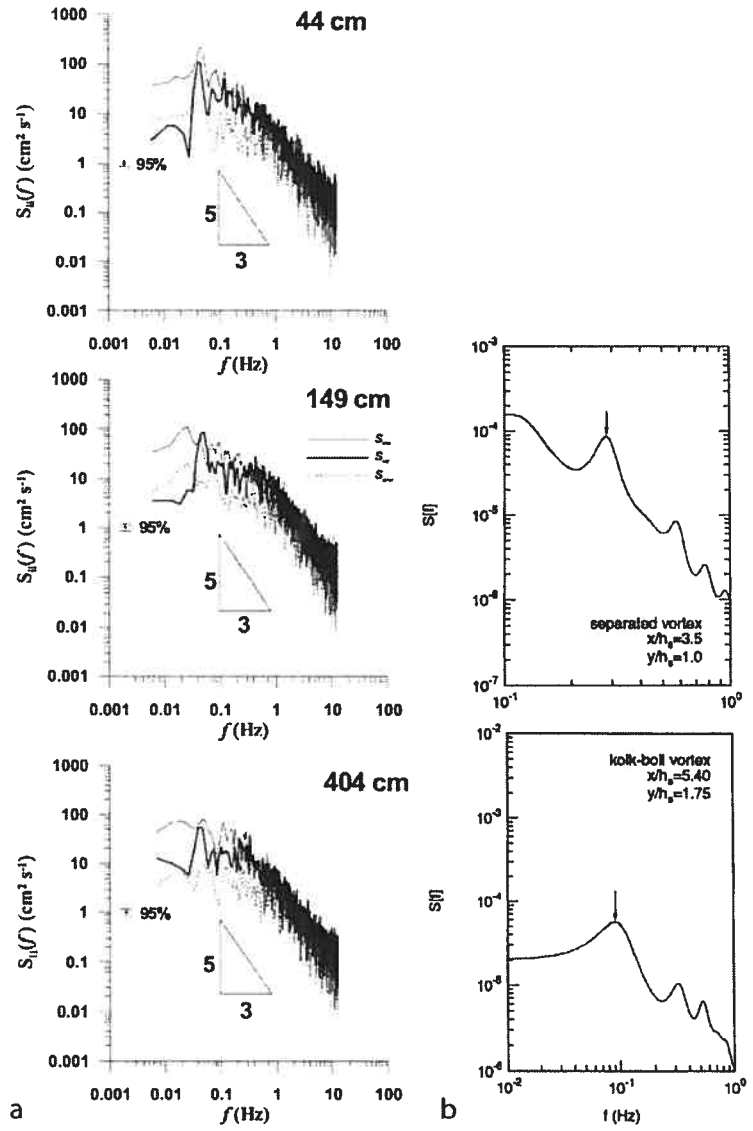

Figure 2.25. Velocity power spectra obtained from two types of shear layers: a) river confluence, $Re = 10^5$ [*Rhoads and Sukhodolov*, 2004]; b) dune – flume experiment, Re = 2500 [*Kadota and Nezu*, 1999].

Figure 2.25 shows that while velocity spectra can under controlled environments be used to investigate shedding frequencies, the highly turbulent environment and large *Re* numbers associated with rivers can interfere and blur the shedding signal in spectra making it indistinguishable. Furthermore, *Rubin and McDonald* [1995] have suggested that reattaching shear layers are nonperiodic and in their flume study peak shedding frequencies could only be identified in power spectra estimated from measurements

close to the initial separation point. Both *Rhoads and Sukhodolov* [2004] and *Kadota and Nezu* [1999] used flow visualization as a second means of identifying shedding coherent flow structures. Flow visualization offers invaluable information on the characteristics of flow structures especially if images are recorded concurrently with instantaneous velocity measurements. Yet, the *in situ* application of simultaneous visualization and velocity measurements can be quite difficult due to sampling logistics and the quick dissipation of flow tracer in high *Re* environments.

The foregoing discussion shows that turbulent coherent flow structures are fundamental units of turbulent flow and are responsible for generation and transfer of Reynolds stresses throughout the boundary layer. The identification of coherent flow structures in the majority of these studies was in part dependent on flow visualization techniques, demonstrating its utility in hydrodynamic studies – "seeing is believing". The discussion of coherent flow structures is of high relevance for this thesis especially the shedding shear layer structures and the depth-scaled high- and low-speed wedges discussed. The following section discusses current knowledge of LREs and associated coherent flow structures in the context of gravel-bed rivers with an initial review on the instream physical description and spatial distribution of LREs.

2.3. Large roughness elements in gravel-bed rivers

In rivers, the role of particle roughness and protrusion on the structure of the turbulent flow becomes very important when the particles eventually create their own flow field capable of influencing erosion, transportation and deposition of other grains [*Best*, 1996]. Large roughness elements (LREs) such as pebble clusters and boulders are considered to be the most prevalent microtopographic feature of poorly sorted gravel-bed rivers and have been found to occupy as much as 10% of the channel floor [*Brayshaw*, 1984]. Researchers have suggested that these features enhance bed stability as they interlock and imbricate with the surrounding substrate limiting the availability of readily transportable particles and delaying their incipient motion [*Dal Cin*, 1968; *Brayshaw*, 1984; *Reid et al.*, 1992; *Biggs et al.*, 1997; *Wittenberg and Newson*, 2005]. Through their interlocking with the surrounding substrate and constituent clasts they delay bedload flux rates [*Reid et al.*, 1992]. Figure 2.26 outlines the characteristics of an

average pebble cluster and depicts the obstacle clast or key stone – shaded in gray – around which develop an upstream imbricated coarse grained stoss deposit and a downstream fine grained wake or lee deposit [*Brayshaw*, 1985]. *Wittenberg and Newson* [2005] observed all pebble clusters to be comprised of stoss-side deposits while only 50% had lee-side fines and attributed this to a lack of available fine sediments or a low h_s of the obstacle clasts. Pebble clusters are generally aligned with the mean flow direction and individual clasts are angled slightly downstream. Keystones generally have grain sizes of D_{90} or greater (D_{90} refers to the 90 percentile sized clast) [*Brayshaw*, 1984; *Wittenberg and Newson*, 2005].

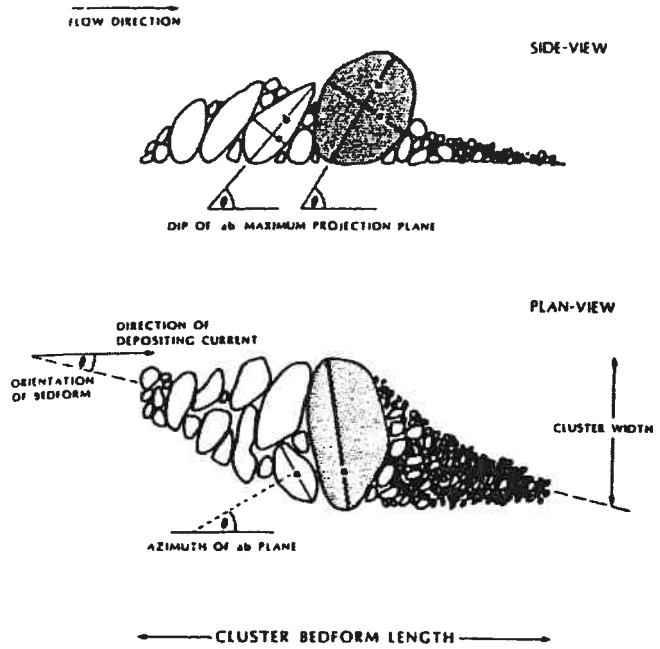

Figure 2.26. Pebble cluster bedform [*Brayshaw*, 1984].

2.3.1. The spatial distribution of large roughness elements

The formation of clusters has been linked with bed armouring and channel gradient [*Biggs et al.*, 1997]. *Hassan and Reid* [1990] investigated the spatial distribution of pebble clusters in two reaches and rarely found that clusters were positioned immediately downstream from each other. They suggested that the spatial arrangement tends towards maximum flow resistance. This is supported by the work of *de Jong and Ergenzinger* [1995] who observed clusters to form in a diamond shape pattern. They propose a subcritical ($Fr < 1$) "shear wave" model where upstream clasts cause shear

waves to propagate downstream and promote the deposition of other clusters at shear wave intersections. The irregular spacing between clusters is controlled by individual LRE size and shape and their effect on the local flow patterns. *Wittenberg and Newson* [2005] observed cluster spacing to be relatively regular with the density of obstacle clasts negatively related to their h_s, while *Brayshaw* [1984] has suggested the spatial distribution to be non-periodic. *Clifford et al.* [1992] suggested that near-bed turbulence, such as k_e and eddy shedding size, plays an important role in the structural arrangement of coarse particles. Fluid turbulence would effect the short-term short-distance movements of these particles influencing the occurrence of clusters and their degree of structuring. *Clifford et al.* [1992] have also argued that the spacing of LREs should reflect the eddy characteristics associated with one or more dimensions of the LRE. *Lamarre and Roy* [2001] conducted a comprehensive study of the spatial distribution of LREs in three gravel-bed rivers with bankfull widths of 7 to 24 m. They compared the observed spatial distributions of LREs to a random distribution of the same number of LREs (by randomizing the x and y coordinates of each LRE within the sample space). While most of the observed and random distance distributions were quite similar, they found that the randomly distributed LREs had minimum distances significantly closer than for the observed LREs, suggesting that some interaction process occurs between LREs limiting their proximity. An inverse relationship was as well observed between the frequency of LREs and flow depth [*Lamarre and Roy*, 2001].

2.3.2. Large roughness element hydrodynamics

Laboratory studies and numerical simulations are primarily used to isolate and characterize the hydrodynamic processes and the behaviour of turbulent coherent flow structures around bluff bodies and backward facing steps. This approach allows for the control of the flow conditions and for the isolation and exploration of the effects of individual independent variables. The results of these studies provide an important background and supporting evidence for the *in situ* observations of turbulent flow around boulders and pebble clusters. They can clarify instream processes which can often be clouded due to uncontrollable natural conditions (e.g., unsteady flow stages, and measurement positioning uncertainty due to access and water transparency). Gravel-

bed rivers are in generally highly turbulent ($Re > 10^5$) complex flow environments with many superimposed scales of turbulent flow structures originating from different sources (i.e., grains, bedforms and channel morphological units) [*Dinehart*, 1999; *Nikora*, 2005]. The variance observed in instantaneous velocity time series is a reflection of these compounding scales of turbulence, is dependent on measurement height, and is as well influenced by independent variables such as rainfall induced variations in flow depth. A large number of turbulence statistics (i.e., RMS, Reynolds stresses, integral time scales, quadrants) are commonly used to describe flow fields around bedforms such as dunes or LREs [*Bennet and Best*, 1995; *Buffin-Bélanger and Roy*, 1998]. The turbulence statistics are often analysed and presented in turn making it difficult to clearly observe the dominant trends in the data. With so many interrelated factors, the study of *in situ* turbulent flow fields lends itself to the use of multivariate statistical techniques. Multivariate statistical analyses are able to efficiently summarise dependent variables and relationships in data sets which included large numbers (hundreds or thousands) of interrelated variables. Such an approach, commonly used in ecological sciences, may be able to quantitatively investigate the spatial dependence of turbulence statistics and identify the dominant independent variables structuring the turbulent flow field.

Robert et al. [1996] conducted one of the initial studies investigating the spatial patterns of turbulence statistics around LREs in gravel-bed rivers. Spatial patterns were inferred from 10 vertical profiles over a 10 m transect crossing over several LREs. They observed marked increases in $-\rho\overline{uw}$ associated with the tops and lee side separation zone of the LREs on the bed. Their 2D study although a first of its kind, was limited due to the lack of fine-scale spatial resolution of turbulence. Relatively few studies have investigated the fine-scale hydrodynamics associated with large roughness elements in gravel-bed rivers. *Buffin-Bélanger and Roy* [1998] conducted a very detailed 2D study of the turbulent flow field in a *x-z* plane crossing over the centre of an instream pebble cluster. Their conceptual model (Figure 2.27) presents six distinct flow regions which include zones of acceleration, shedding, recirculation, reattachment and downstream upwelling.

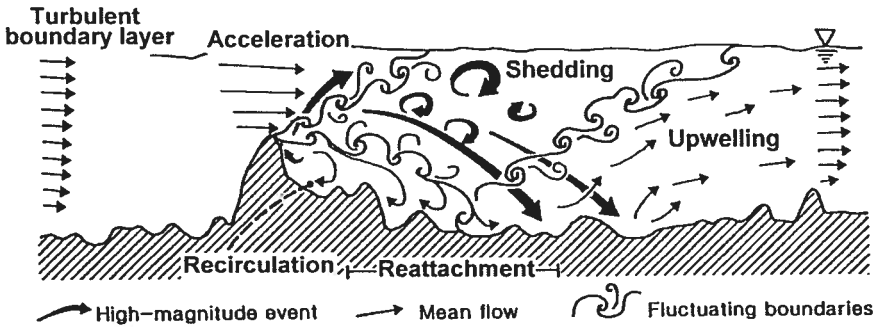

Figure 2.27. Conceptual model of flow over a pebble cluster based on detailed velocity measurements over a dense sampling grid [*Buffin-Bélanger and Roy*, 1998].

The similarities between Figure 2.27 and the previously presented conceptual model for a backward facing step (Figure 2.19) is remarkable and suggest that under certain LRE geometries, instream LREs may influence the flow field in a manner similar to backward facing steps and dunes along the LRE centreline plane. These similarities may be due to the somewhat rounded streamline geometry of many large roughness elements (such as pebble clusters) where flow separation initiates only at the lee edge instead of at the front face as with rectangular blocks or fences [*Simpson*, 1989]. The study by *Buffin-Bélanger and Roy* [1998] was innovative in its fine-scale high density *in situ* measurements, but the presented model does suffer from a lack of generalization as it is based on a single LRE using only 2D velocity measurements. Many questions remain on the shedding processes and how these are affected by LRE shape, relative submergence and general flow conditions. Furthermore while *Buffin-Bélanger and Roy* [1998] presented many turbulent spatial patterns, a greater understanding of the turbulent processes would be gained by determining the scale-dependence of the turbulence statistics and their interrelationships.

While backward facing steps and dunes have much in common with the LRE study by *Buffin-Bélanger and Roy* [1998] some differences exist. *Buffin-Bélanger and Roy* [1998] observed relatively higher values of $-\rho\overline{uw}$ along the shear layer, primarily directed towards the water surface reflecting the primary direction of shedding structures. The upward inclination of intense $-\rho\overline{uw}$ somewhat contradicts previous laboratory experiments on 2D steps and dunes [*Nezu and Nakagawa*, 1989; *Nelson et al.*, 1993; *Bennett and Best*, 1995] and previously discussed theory suggesting the shear

layer is directed towards and impinges on the bed. The upwards direction is perhaps due to the specific geometry of the cluster investigated, 3D effects such as the influence of lateral shearing and/or the splitting off of shear layer vortices ejecting towards the surface. *In situ* lateral shearing around water surface protruding LREs was investigated by *Tritico and Hotchkiss* [2005]. While $-\rho\overline{u'w'}$ was dominant along the LRE centerline, their study showed an important Reynolds shear stress contribution from the longitudinal-lateral velocity components as $-\rho\overline{u'v'}$ dominated the turbulent momentum exchange to the side of the boulders. The high values of $-\rho\overline{u'v'}$ were visually attributed to vertical axis vortices shedding from the sides of the boulders. Yet, *Tritico and Hotchkiss* [2005] investigated solely surface protruding boulders which would not generate a shear layer at the top of the boulder. Such a shear layer seems to dominate the flow field around submerged elements. With the exception of *Tritico and Hotchkiss* [2005] who investigated surfacing protruding elements; there are no other studies investigating the fine-scale 3D hydrodynamics around LREs in gravel-bed rivers to our knowledge.

The *in situ* response of LREs shear layer to the passage of LS coherent flow structures has been investigated through visualization studies [*Kirkbride*, 1993; *Roy et al.*, 1999; *Buffin-Bélanger et al.*, 2001a; *Roy and Buffin-Bélanger*, 2001]. The results remain speculative as very few studies have provided evidence for the shedding processes and the flow field in these experiments was not fully characterised around the LRE. In these studies, the shear layer was observed to expand upwards with the passage of low-speed events. Low-speed wedges were suggested to cause the oblique upwards shedding of a train of vortices which grew in size and were responsible for the transport of slow fluid from the separation zone into the rapid flow above the LRE [*Roy and Buffin-Bélanger*, 2001]. *Kirkbride* [1993] suggested the ejecting fluid from the shear layer interferes with the outer layer fluid causing an inrush of high momentum fluid towards the wall and thereby suppressing the LRE shear layer. Similarly, *Roy and Buffin-Bélanger* [2001] have suggested that the passage of a high-speed event causes an extension of the shedding vortices towards the bed coinciding with a displacement of the reattachment point downstream. They as well hypothesized that the shedding structures rotate becoming 3D and producing elevated turbulence intensities. *Buffin-Bélanger et al.*

[2001a] and *Roy and Buffin-Bélanger* [2001] have also argued for that a positive feedback mechanism exists between LS flow structures and shedding processes. The passage of high-speed wedges was associated with the triggering of the shedding motion from the LRE several time-steps later; the shedding motions thereby coinciding with the passage of low-speed wedges and reinforcing them through the ejection of low-speed fluid towards the surface. Figure 2.28 presents a conceptual model by *Roy and Buffin-Bélanger* [2001] on the fundamental role high- and low-speed wedges play in the hydrodynamics of gravel-bed rivers. The feedback mechanisms between classical boundary layer sweep and ejection events, wedges, strong and weak return flow and the type of vortex shedding is depicted through direct response effects. A channel scale model showing the integration of LRE shedding structures and LS coherent flow structures by is presented in Figure 2.29. The different types of shedding behaviour associated with the passage of low- or high-speed wedges is depicted (along with boundary layer ejections). This conceptual model of longitudinal alignment of coherent structure production and dissipation units is similar to that proposed by *Yalin* [1992]. The *Buffin-Bélanger et al.* [2001b] model highlights the temporal and spatial variability in coherent structure production and interaction dependent on the position and geometry of LREs within the channel. The complex interactions between coherent structures limit the ability to identify and characterise individual coherent flow structures either visually or extracted velocity time series [*Buffin-Bélanger et al.*, 2001b].

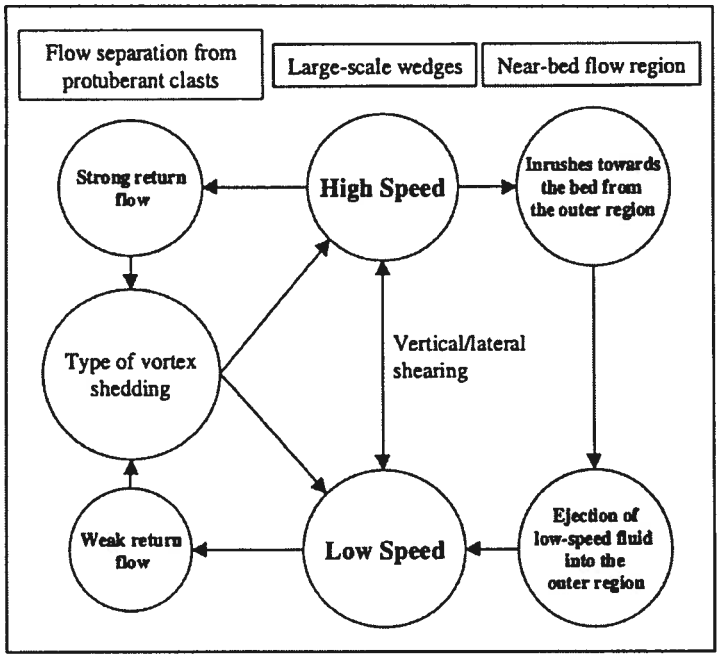

Figure 2.28. The centrality of flow wedges in the dynamics of flow in a gravel-bed river [*Roy and Buffin-Bélanger*, 2001].

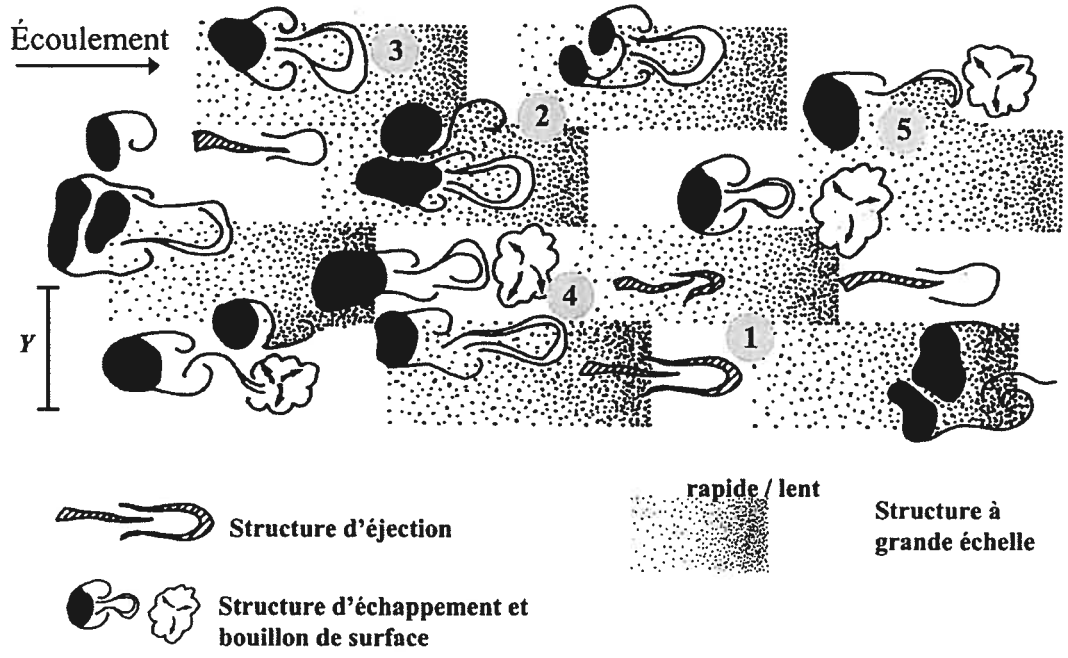

Figure 2.29. Integrated channel scale model presenting the interaction between LS flow structures, ejections and shedding structures [*Buffin-Bélanger et al.*, 2001b].

LREs are the most commonly found microtopographic unit in gravel-bed rivers yet there remain many questions regarding their hydrodynamic effect and apparent random spatial distribution throughout the channel. The shear layer structures shedding from roughness elements must play a critical role in the generation of turbulence in gravel-bed rivers but the relationships of these meso-scale flow structures with LS flow structures remain unclear. The under appreciation for the hydrodynamic effects of LREs may have caused some confusion among aquatic biologists and scientists on the implications of LREs of aquatic biota. A review of the known relationships between LREs and their hydrodynamics and aquatic biota is presented in the following section, as it is hoped that the results of this thesis will be of use to fish scientists and stream managers.

2.4. Large roughness elements and aquatic biota

One of the main applications of a proper characterisation of the hydrodynamics around *in situ* roughness elements is in defining relationships between large roughness elements and aquatic biota. Aquatic biota have different adaptation strategies either avoiding highly turbulent zones or using them to provide cover from less adapted predators. The following three sections outline current research on the links between the hydrodynamics generated by LREs and periphyton, benthic invertebrates and fish.

2.4.1. Periphyton

All aquatic environments sustain periphyton communities attached to stones and soft sediments [*Hondzo and Wang*, 2002]. Periphyton communities form the primary energy source for higher trophic levels in rivers. Periphyton growth and stream hydrodynamics are linked together as stream flows provide the mass and momentum transfer which can either aid periphyton growth or erode periphyton. Under laboratory conditions *Handzo and Wang* [2002] found periphyton growth to be minimal under stagnant conditions, to increase to a maximum density with increasing velocity and turbulent stress and subsequently decrease as the stress became strong enough to detach the periphyton filaments from the wall. This relationship is shown in Figure 2.30 from *Handzo and Wang* [2002] which presents periphyton biomass as a function of shear velocity. In turn, periphyton has been found to influence the local hydraulics. *Nikora et al.* [2002b]

reported that under the presence of periphyton the origin of the logarithmic velocity profile shifts to the top of the filaments, and mean velocity, turbulence intensity and turbulent stresses below the top are suppressed.

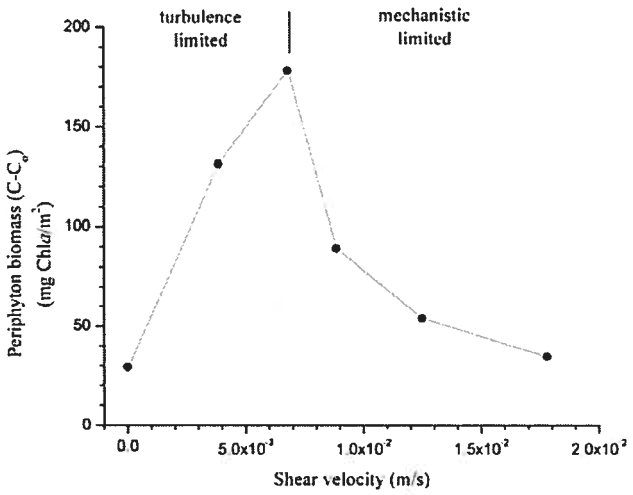

Figure 2.30. Periphyton biomass versus shear velocity, u_*, at the sediment-water interface [*Hondzo and Wang*, 2002].

Quinn et al. [1996] conducted an *in situ* experiment examining the effect of different sized roughness elements on periphyton density and benthic invertebrate density and richness. A positive relationship was found between periphyton chlorophyll *a* density and the size of upstream placed LREs with the exception of the largest size LREs investigated where periphyton density was found to decrease significantly. These results corroborate the study by *Hondzo and Wang* [2002] indicating that the turbulence generated by the roughness elements provides an effective mass transfer of nutrients, yet at a critical LRE size the turbulent stresses generated are sufficient to detach the periphyton from the substrate (Figure 2.30). In *Hondzo and Wang*'s [2002] flume experiments, the only growth-limiting parameter was water velocity; all the other environmental conditions, such as water depth, light, temperature, and nutrients were not limiting growth. The experiments were run for six different velocities which ranged from $\overline{U}$ = 7.4 to 68 cm s^{-1} at a constant flow depth of 0.15 m.

2.4.2. Benthic invertebrates

Some benthic invertebrates have adapted to living in turbulent rivers and have evolved morphologies which reduce drag [*Smith and Dartnall*, 1980; *Statzner and Holm*, 1982]. Black fly larvae have been known to align along separation zones to take advantage of the negative pressure in the recirculation zone [*Lacoursiere*, 1992]. On the other hand, many lotic zoobenthos are not well adapted to minimize drag forces and the spatial distribution of these insects can be directly related to the hydrodynamics and turbulent exposure [*Statzner et al.*, 1988]. Research investigating the generalized effect of the complex flow patterns around LRE on macro invertebrate community density and structure has provided varied and somewhat conflicting results.

Through a very fine-scale instream study, *Hart et al.* [1996] measured the u component velocities at vertical heights of z = 0.001 – 0.01 m from the top surface of five stones selected on the river bed and compared the estimated values of $\overline{U}$ and u' to the distribution of filter feeding invertebrate larvae. *Hart et al.* [1996] were able to show a significant dependence (r^2 = 59%) of larvae abundance to the local $\overline{U}$ measured at z = 0.002 m strongly suggesting that the larvae actively select sites depending on local flow conditions. *Hart et al.* [1996] found that $\overline{U}$ values measured at 0.01 m above the stones (all sites) were not significant predictors of $\overline{U}$ estimated at z = 0.002 m, explaining only r^2 = 1% of the variance, suggesting the importance of obtaining velocity measurements at heights relevant to the aquatic biota studied [*Statzner et al.*, 1998; *Hart and Finelli*, 1999]. The lack of correlation for $\overline{U}$ estimated at z = 0.002 m and at 0.01 m is somewhat surprising considering the strong correlation between velocity signals at different vertical heights observed in other studies [*Buffin-Bélanger et al.*, 2000; *Roy et al.*, 2004]. *Hart et al.* [1996] found u' at z = 0.01 m explained a much smaller percentage of the variance in larval abundance (r^2 = 5%) than for u' at z = 0.002 m (r^2 = 12%). The authors therefore proposed that the variation observed in u' was not related to any immediate (or local) hydrodynamic effect, but was rather due to flow disturbances induced by upstream LREs. A minimal and negative influence of turbulence on benthic invertebrate communities was found by *Robson et al.* [1999] and *Quinn et al.* [1996], respectively, where both experiments involved artificially augmenting turbulent intensities over test patches using upstream positioned LREs. Conversely, *Bouckaert and Davis* [1998]

found benthic invertebrate communities in the immediate stoss and lee zones of LREs to be highly structured by turbulence variables such as k_e and $-\rho\overline{uw}$. Benthic invertebrate communities were significantly richer and more abundant in the wake zone and were distinguished from front communities, while mean velocities close to the bed in both zones were relatively similar. *Bouckaert and Davis* [1998] suggested that the high dependence on turbulence variables was due to their secondary effects such as the increased deposition of particulate organic matter and dissolved oxygen exchange in the wake zone. While *Hart et al.* [1996] suggested the turbulent dynamics originate from other LREs upstream, *Bouckaert and Davis* [1998] results indicate that LREs self-determine their local hydrodynamics and community structure within their immediate surrounding. The question remains open to this date.

2.4.3. Fish

The relationships between fish habitat preference and mean u component velocity have been the focus of numerous studies. While fish preference is dependent on other factors such as cover, mean flow depth and substrate size, species preference for particular velocities has been published and used extensively [*Bovee*, 1978; *Hogan and Church*, 1989]. It has only been relatively recently that researchers have investigated the effects of turbulence on fish density and behaviour. Current research is somewhat divided on these relationships and the relative benefits of LREs. *Liao* [2007] conducted a recent review of fish swimming mechanics and behaviour in the wake of LREs. While the review concentrates on laboratory experiments with simple surface protruding objects at relatively low to moderate *Re* (which may not be applicable to natural environments such as in gravel-bed rivers), the review does suggest that fish are able to negotiate complex flow environments using multi-modal sensory inputs such as vision and hair cells of the lateral line system. An often cited study by *Enders et al.* [2003] investigated the physiological response of juvenile Atlantic salmon (JAS) to increased turbulent intensity. Their respirometry flume experiments differentiated between the effects of $\overline{U}$ and turbulence. At a lower mean velocity (0.18 m s^{-1}) they observed a modest (factor of 1.3) increase in swimming costs when turbulence was increased from u' = 0.05 m s^{-1} to u′ = 0.08 m s^{-1}. For a faster flow ($\overline{U}$ = 0.23 m s^{-1}) a similar increase in turbulence

resulted in a (factor of 1.8) rise in swimming costs. While their work was exploratory in its scope (only 5 individuals studied), it clearly indicates a positive relationship between JAS stress and turbulent intensity.

Many studies have found a positive relationship between the addition or presence of LRE such as boulders and fish density in streams [*Van Zyll de Jong et al.,* 1997; *Mitchell et al.*, 1998; *Armstrong et al.*, 2003; *Vehanen et al.*, 2003; *Coulombe-Pontbriand and Lapointe*, 2004]. *Van Zyll de Jong et al.* [1997] found boulders to be the most effective treatment structured in a forestry impacted stream and noted a significant increase in brook trout and JAS density particularly associated with boulders. *Coulombe-Pontbriand and Lapointe* [2004] noted a significant positive relationship between JAS and boulder abundance on both reach and segment scale (compilation of multiple reaches). The addition of LRE can increase the availability and diversity of habitat, provide protective cover for juveniles and increase the amount of stable substrate for settlement by benthic invertebrates [*Mitchell et al.*, 1998]. Furthermore LRE such as pebble clusters have copious interstitial spaces and crevasses for invertebrates (and fish) to dwell and their stability during flood events is recognized [*Biggs et al.*, 1997]. *Mitchell et al.* [1998] found JAS used the treatment boulders more during higher flows and attributed the preference to an increase in flow complexity (enhancing habitat diversity) and increased cover through visual isolation due to turbulence at the water surface. *Bachman* [1984] observed brown trout to typically select submerged LREs as foraging sites where they would position themselves on the downward-sloping rear surface of the LRE. In this position, the fish avoided high velocity zones overhead and were observed to have minimal tail beat frequencies. While the potential importance of boulders in determining productivity of JAS and other species is widely understood, few studies have elucidated the mechanisms involved in the linkage between boulder presence and salmon productivity [*Kemp et al.*, 2005]. Recent studies by *Dolinsek et al.* [2007a;b] have suggested visual isolation as the determining factor for high densities of juvenile Atlantic salmon (JAS) around LREs. Visual isolation theory was originally proposed by *Kalleberg* [1958] suggesting that increased bed heterogeneity results in higher population density of territorial fish species because fish do not see as much of each other. While visual isolation is likely to be a

factor for territorial fish species, it is difficult to separate the effects of visual isolation from other physical and biological variables such as water velocity, turbulence and abundance of drift.

For the most part fine-scale hydrodynamics and fish behaviour studies investigating the correlations between turbulence generated by LRE and fish preference have been conducted in the laboratory with somewhat divergent results. A novel investigation by *Liao et al.* [2003a, 2003b] looked at the swimming patterns of juvenile rainbow trout under the influence of vortices shed by a surface protruding D-section upstream cylinder. Figure 2.31 shows the distinctive "Kármán gait" adopted by the trout superimposed on the PIV images obtained in subsequent experiments used to confirm the presence of shedding vortices. The fish were seen to "slalom" through the vortices. This behaviour was found to minimize energy expenditure as indicated by lower muscle activity and tail beat frequency. The authors argued that the trout were taking advantage of the return flow portions of shedding vortices and essentially "drafting" behind the D-shaped cylinders. The recent review by *Liao* [2007], focussing on the author's previous laboratory work [*Liao et al.*, 2003a; 2003b; *Liao*, 2006], further emphasized the use by fish of periodic shedding vortices from upstream obstacles to minimize energy expenditure.

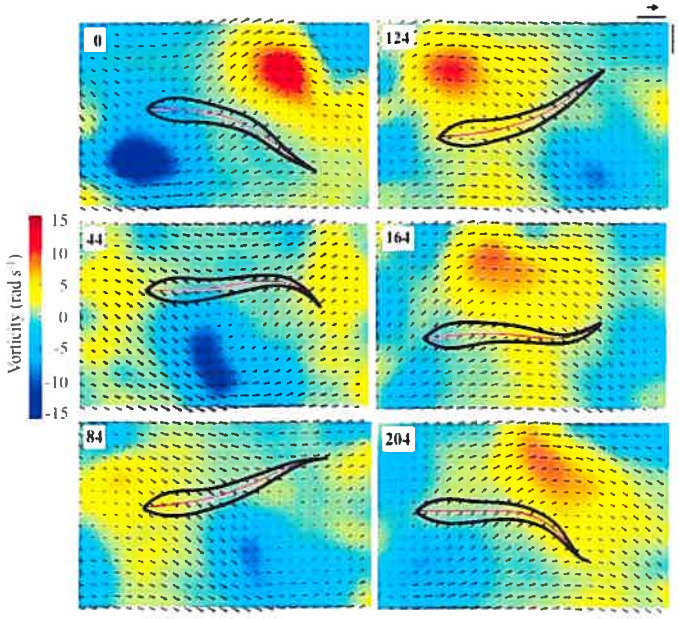

Figure 2.31. Time series (ms) of trout body outlines superimposed onto vorticity and velocity vector plots of the cylinder wake [*Liao et al.*, 2003b].

Some caveats of the *Liao et al.* [2003a] experiments are that they were conducted at low to moderate particle Reynolds numbers $Re_{\emptyset}$ = 5 600 – 20 000; the fish behaviour and instantaneous velocity fields were not sampled concurrently and the cylinders were relatively narrow ($\emptyset_s$ = 0.025 – 0.05 m) and surface protruding. *Liao* [2007] argued that fish are attracted to turbulent flows if their mechanisms of stability are sufficient for a given hydrodynamic environment. The author proposed that only altered flows (such as flows downstream of an obstacle) that remain steady or maintain an aspect of predictability can be exploited by swimming fish, while flows with unpredictable, wide fluctuations in velocity tend to be avoided by fish. This is a key point for the applicability of the findings by *Liao* [2007] to gravel-bed rivers. Depending on LRE size, $Re_{\emptyset}$ can be an order of magnitude greater than in the studies of *Liao et al.* [2003a]. The previous shear layer discussion in this chapter have shown shedding properties to be highly dependent on $Re_{\emptyset}$. At higher $Re_{\emptyset}$, the Karman vortex street stressed by *Liao* [2007] breaks down becoming non-periodic in the near-wake. Other modes of interaction between initial shear layer vortices exist such as fractional pairings and tearings and individual structures can vary unpredictably in shape, size orientation and convection velocity [*Hussain and Zaman*, 1985]. Surface mounted LREs, likely undergo further nonperiodicity due to the dynamics of the reattaching shear layer [*Rubin and McDonald*, 1995]. Furthermore in gravel-bed rivers, the high *Re* and turbulence results in a complex environment where vortices at many scales exist and potentially interact which the structures shedding from LREs enhancing their non-periodicity. Due to the high *Re* associated with gravel-bed rivers, fish behaviour around LREs may be quite different than as proposed by *Liao* [2007].

Kemp et al. [2005] conducted outdoor flume experiments testing for the effects of feeding rates and holding positions of JAS 'complex' and 'simple' habitats. Both habitats had gravel beds, and boulders and cobbles were added to the complex treatment resulting in a range of relative submergence values, Z/h_s, from submerged to surface protruding conditions. The authors found a significant decrease in feeding rates and a significant increase in holding time in the water column in the complex habitats. *Kemp et al.* [2005] did not observe the JAS to be taking advantage of shedding vortices as in

Liao et al. [2003a], and instead interpreted the increased holding as a net cost incurred by the added flow complexity and presumably turbulence intensity.

Detailed velocity and turbulent measurements around the nose velocity of rainbow and brown trout have indicated that fish select focal positions near cover with low average velocities and low turbulence values. Fish avoid low-velocity, high-turbulence locations [*Smith et al.*, 2005; *Cotel et al.*, 2006]. *Smith et al.* [2005] sampled nose velocities 0.02 m from the bottom of the channel and found that while the juvenile rainbow trout preferred the locations with submerged LREs (bricks) at higher flows (Figure 2.32) the turbulence (determined by k_e, $-\rho\overline{uv}$ and $-\rho\overline{uw}$) at the fish focal locations was lower than average. This would indicate that the trout in this experiment while remaining very close to the LREs are avoiding the high turbulent lateral shear layer eddies described by *Liao et al.* [2003a]. For the two flow cases presented in Figure 2.32, there is an order of magnitude increase in *Re* at the low to the high flow condition (*Re* = 1.8 x 10^4 to *Re* = 1.1 x 10^5, respectively). The study by *Smith et al.* [2005], suggests that fish behaviour and preferred holding location is influenced by the *Re* number flow conditions and lends support to the previous discussion on the applicability of laboratory results (such as those of *Liao et al.* [2003a]) to natural river environments.

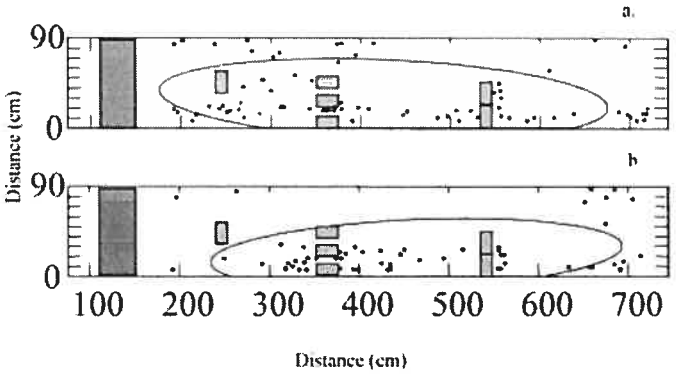

Figure 2.32. Fish locations relative to the locations of bricks for discharges of (a) 0.030 and (b) 0.111 $m^3 s^{-1}$. Flow is from left to right [*Smith et al.*, 2005].

Smith et al. [2006] conducted a more generalized study investigating the volitional density of rainbow trout and their ability to hold position in three test channels with no cover, moderate cover and full cover. They determined that $\langle k_e \rangle$ averaged from 72 spatially distributed measurements was a better predictor of fish density than mean velocity and suggested that $\langle k_e \rangle$ combined the effects of discharge and LREs together.

The apparent contradictions in research results investigating LREs, turbulence and fish (even by the same author as is the case of *Smith et al.* 2005 and 2006 studies) suggest that these relationships are highly complex. There is some indication, at least for *Smith et al.* [2005, 2006], that instantaneous velocity sampling locations can significantly influence the results. A similar result can be concluded from *Hart et al.* [1996] who found no significant correlation between $\overline{U}$ measured at vertical distance of z = 0.01 m and z = 0.002 m from the LRE surface. Another main difficulty with incorporating fish in turbulence studies is that they are autonomous organisms and may make compromises among many interacting physical and biotic factors when choosing a location [*Cotel et al.*, 2006]. These compromises may vary amongst individuals as shown by *Ovidio et al.* [2007].

3. OBJECTIVES AND METHODOLOGY

3.1. Problem Statement

Several fundamental questions remain on the influence of large roughness elements (LREs) on the hydrodynamics of gravel-bed rivers at the local and reach scale, such as: i) what are the local hydrodynamics affecting LRE disposition?; ii) what determines the spatial distribution of LREs within river reaches?; and iii) what is the impact of LRE hydrodynamics on aquatic biota habitat? In order to address these questions, it is critical to characterise and quantify the fine-scale three-dimensional (3D) hydrodynamics surrounding LREs *in situ*. The physical *in situ* processes involved with the shear layer and vortex shedding from LREs need to be resolved as well as the spatial influence LREs have on the local hydrodynamics in the longitudinal, lateral and vertical dimensions. To understand the interactions between submerged LREs and the role they play in instream habitat, sampling schemes need to be spatially distributed at a high enough resolution to capture in detail the physical flow processes associated with LREs. Two-dimensional (2D) *in situ* velocity measurements have proven valuable for investigating turbulent characteristics associated with LREs in the longitudinal-vertical (x-z) centerline plane, yet by incorporating lateral velocity component measurements over longitudinal-lateral (x-y) planes, a fuller 3D characterisation of the effect of LREs can be achieved. A more holistic understanding of the role of LREs in gravel-bed rivers can only be obtained by considering the effect of varied flow conditions (stage and mean velocities) and varied LRE geometries. In order to determine which of these independent variables is dominant in structuring the numerous turbulence statistics (and at which scales) a multivariate statistical approach is advantageous. Such an approach would as well allow the variation in the turbulence statistics to be partitioned in order to isolate the effects of one independent variable over another (i.e., velocity and water depth) or of scale (small- vs. large-scale patterns).

Large-scale (LS) coherent flow structures are a predominant feature of flow in gravel-bed rivers. Research suggests that the sweep and ejection components of LS structures play a key role in near-bed stresses and sediment transport. Based on limited data sets and exploratory field techniques, preliminary *in situ* flow visualization and

velocity measurement studies have suggested a link between LS flow structures and shear layer expansion and contraction, but supporting evidence is needed in order to generalize these observations. It has as well been hypothesised that LS coherent flow structures originate or are maintained through interactions with smaller scale flow structures shedding from LREs. Very little is known of the effect of the shedding vortices on the LS flow structures or the role they play in the maintenance of the larger flow structures. Previous techniques to investigate the interaction between shedding flow structures and LS flow structures have included concurrent *in situ* flow visualization and velocity measurements, yet these studies have been somewhat hampered due the low resolution video technology available at the time, available intrusive 2D instrumentation and the difficulty to synchronize the video and 2D velocity measurements at small time steps [*Roy et al.*, 1999; *Buffin-Bélanger et al.*, 2001a]. With the advent of non-intrusive 3D instrumentation (e.g., ADV) and high resolution digital video it is now possible to obtain very clear underwater images synchronized with 3D high frequency velocity measurements. Flow visualization has been shown to be an invaluable technique for identifying coherent flow structures and with *in situ* sampling advancements a much more detailed characterization of LRE shear layer behaviour is now possible.

With the exception of one recent study on protruding boulders, there are no other *in situ* studies (to our knowledge) on the 3D spatial distribution of turbulent flow parameters around LREs in gravel-bed rivers. A small number of laboratory studies have investigated more complex bedforms and bed topography [e.g., *Lawless and Robert*, 2001a;b; *Buffin-Bélanger et al.*, 2006], yet most flume based hydrodynamic studies focus on simple beds and object morphometries such as isolated hemispheres or 2D backward facing steps and dunes. Many of these flume studies have focused on the longitudinal and vertical turbulent flow field only. Field investigations of fine-scale hydrodynamics around LREs are rare due to the logistics and difficulties involved with obtaining high frequency velocity measurements at precise locations of a spatial discretized grid, a lack of robust field instrumentation, and unpredictable flow conditions. Even though flume experiments present several advantages (e.g., replicability and control of flow conditions allowing for the isolation of a particular variable or variables), they also suffer from several potential limitations. The most

constraining is the flow width/depth ratio which must be kept greater than 5 in order to avoid 3D flow effects [*Kironoto and Graf*, 1994] which can severely bias turbulence statistics such as Reynolds stresses. This limits the size of bed roughness, LREs, and the relative submergence which can be investigated. Furthermore the flume inlet must be a sufficient distance away from the experimental section to allow for the boundary layer to fully develop – *Ranga Raju et al.* [2000] have suggested distances of $x > 40Z$. There is also a problem of generating a water worked gravel bed. These limitations, if not properly addressed can make it difficult to transfer knowledge gained from flume studies to gravel-bed rivers. Flow dynamics around smaller scaled models of bedforms in controlled flume studies may be quite different and not represent the hydrodynamics around full-scale LREs due to the limits on maximum obtainable *Re* values. Gravel-bed rivers present highly turbulent ($Re > 10^5$) complex environments and some flow processes and coherent flow structures may be difficult to replicate in flume.

The dearth of knowledge on the turbulent processes around *in situ* submerged LREs has potentially led to much of the inconsistency between studies of aquatic biota around LRE. The hydrodynamics around *in situ* LRE can be quite complex, and with inadequate spatial and temporal coverage, turbulence measurements may give conflicting results due to sampling locations being within or outside of the shear layer or wake zone. Generalized descriptions of the 3D turbulent hydrodynamics around *in situ* LRE need to be available to biologists and ecologists in order that they may obtain representative turbulence measurements on the scales and locations relevant to the aquatic biota being investigated.

3.2. Objectives

The overall objective of this thesis is to advance our understanding of the turbulent flow field around boulders and pebble clusters in gravel-bed rivers. Through detailed fine-scale measurements and a multifaceted approach incorporating various sampling techniques and statistical analyses, the turbulent characteristics and processes associated with LREs can be quantified and understood. The thesis is organised around the following specific objectives:

1. identify and quantify the spatial scale-dependence of turbulent flow variables in a 2D *x-z* plane crossing over a LRE and to investigate the scale-dependent correlations between turbulence variables.

2. characterise the *in situ* 3D turbulent flow field with and without an isolated submerged LRE and investigate the hydrodynamic effect of LREs on LS turbulent flow structures advecting from upstream;

3. describe and quantify the very fine scales of the shear layer and associated shedding processes around an *in situ* isolated submerged LRE and the behaviour of mesoscale shedding structures under the influence of LS flow structures advecting from upstream;

4. determine the effect of varied flow conditions (stage and mean *u* component velocity) and of LRE geometries (shape, size, orientation) on the *in situ* 3D turbulent flow field and turbulent momentum exchange.

This thesis will provide insights on the general influence of LREs on the turbulent flow field which could lead to the development of guidelines for aquatic biologists or fish managers. The results will also contribute to a more complete view of gravel-bed river hydrodynamics and the role of LREs in maintaining the turbulent structure of the flow. Each objective was investigated in turn and the results are presented in each of the four article chapters (Chapter 4 – 7). The objectives of this thesis and how they relate to the grey areas of knowledge associated with LRE hydrodynamics is summarized in Figure 3.1.

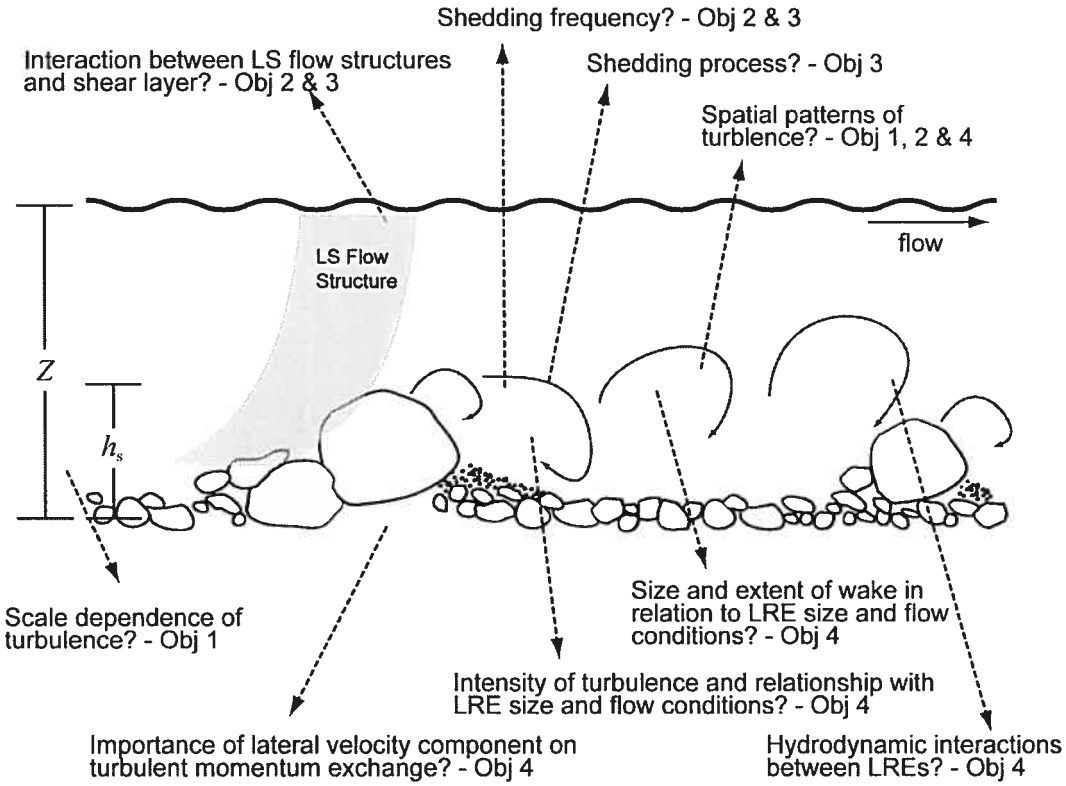

Figure 3.1. Schematic of gaps in knowledgebase (unanswered questions) regarding LRE hydrodynamics and the respective objectives of this thesis used to answer these questions. For simplification a 2D schematic is presented here, however the 3D flow field was predominantly investigated in this thesis.

3.3. Approach and General Methodology

This thesis focuses on the spatial characterisation of turbulence around instream submerged LREs and four chapters of substantive results will give together a more complete and detailed picture of the hydrodynamic effects of LREs in gravel-bed rivers. The spatial characterization integrates the use of multi-scale multivariate statistical analyses of turbulence statistics, flow visualization and quasi-3D reconstruction of the flow field around LREs. The flow field reconstruction relies on maps of the spatial distribution of turbulence statistics derived from fine-scale 3D instantaneous velocity measurements using multiple acoustic Doppler velocimeters (ADVs). The use of multiple ADVs recording simultaneously allowed for the identification of turbulent coherent structures through space-time correlation analysis and the upstream detection

of LS events before they convected overtop of the LREs. High frequency velocity measurements were obtained on horizontal or vertical planes crossing overtop of LREs. A combination of turbulent indicators were estimated including turbulent kinetic energy, mean Reynolds shear stresses, integral time scales, space-time correlations, and conditional events.

The objectives of the thesis are met through experiments carried out in field. The results of these experiments are presented in the following four chapters (Chapters 4 through 7). Each chapter is written as a research article published or submitted to refereed international journals and focuses on one or several of the specific objectives. In Chapter 4, multivariate statistical techniques are used to investigate the spatial-scale dependence of turbulent flow variables. We revisit the 2D turbulent flow data set reported by *Buffin-Bélanger and Roy* [1998] estimated in an *x-z* plane crossing over an *in situ* pebble cluster. This 2D data was used as it provides the most fine-scale *in situ* measurements over a LRE available to date (prior to this thesis) and offers a unique opportunity to properly test the statistical techniques (PCNM and RDA) and establish their potential for extracting the main features of the turbulent flow at various spatial scales. While *Buffin-Bélanger and Roy* [1998] conducted a thorough turbulence analysis on their data set, they were unable to quantify the spatial scale dependence. The PCNM method of extracting scale dependent spatial patterns is a recently developed powerful analysis technique allowing for the quantification of spatial or temporal scale dependence in data sets. Its use in Chapter 4 represents a first time application of this method in water resources sciences. For this first time application to turbulence data, a 2D data set was preferred over a 3D data set, in order to clearly show the benefits of the multivariate statistical technique in straightforward 2D spatial plots. The conceptual model developed by *Buffin-Bélanger and Roy* [1998] is the best available so far and through our additional analysis a greater understanding of the spatial structure of turbulence around LREs is obtained. Given the favourable results and usefulness of RDA for analysing large turbulent data sets, RDA is re-used in Chapter 7 to assess the dependence of turbulent wake variables on mean flow and LRE morphometric parameters.

Chapters 4 to 6 investigate the 2D or 3D turbulent flow field around *isolated* LREs to quantify the physical processes and associated mean and turbulent flow structure around a single LRE. The effects of a LRE on the flow field are made evident in Chapter 5 as this experiment involved obtaining detailed velocity measurements over two horizontal planes with a LRE in place and subsequently removing the LRE and resampling at the same measurement points. Thus any changes in the hydrodynamics could be directly related to the LRE. In Chapter 6, synchronous flow visualization and instantaneous velocity measurements were recorded to further characterise LRE lee-side shedding processes identified by the results of Chapter 5. The synchronous video recordings were essential for observing the behaviour of the shear layer and shedding structures to passing LS coherent structures originating upstream. Using instantaneous velocity measurements obtained from two intersecting planes, the fine-scale 3D characteristics of the shear layer and wake zone are characterised. In Chapter 7, we conducted experiments where 3D velocity measurements were obtained from some sites with *multiple* LREs under varied flow conditions with the aim of investigating LRE geometrical effects, their interaction and the dependence of these hydrodynamics on mean flow conditions. The results from Chapters 5 and 6 are invaluable in interpreting the spatial turbulent patterns observed in Chapter 7. The underlying relationships between mean flow conditions and LRE morphometrics, and time-averaged turbulent wake parameters are determined using RDA. This multivariate statistical technique had been assessed and proven invaluable in Chapter 4 for describing the spatial-scale relationships among turbulence statistics.

The approach used in this thesis allows for a much more complete understanding of the hydrodynamics associated with LREs in gravel-bed rivers and the physical processes associated with the shear layer. The investigation of multiple LREs at multiple river stages allows for some degree of generalization of the results to other gravel-bed river systems. The comprehensive description of spatially distributed turbulence statistics highlights the 3D hydrodynamic effects of LREs in gravel-bed rivers which have important implications for the distribution of LRE in the river channel, sediment transport and fish habitat. The multivariate statistical and variance partitioning procedure allows for the identification of the dominant flow and morphometric variables

responsible for the generation of turbulence in the wake of LREs. Knowledge of the main parameters structuring turbulence in LRE wakes will be of interest to fluvial geomorphologists and fish managers designing optimum fish habitat structures.

3.3.1. *In situ* velocity measurements

Because the turbulent nature of the flow is at the center of this thesis, the analysis relies on velocity measurements at high temporal resolutions and on flow visualization. Except for the data gathered by *Buffin-Bélanger and Roy* [1998] (Chapter 4), all instantaneous velocity measurements used in this thesis were collected with multiple acoustic Doppler velocimeters (ADVs) manufactured by SonTek. The ADVs used are 10 MHz field probes with the sampling volume located 0.1 m below the transducer tip. The sampling volume as specified by the manufacture is cylindrical with dimensions of 6 mm diameter and 9 mm in height. For the experimental deployments used in Chapters 5 and 6, the multiple ADVs were used in order to obtain spatial correlations over the flow field. This involved having one (or two) designated fixed upstream probe(s) and systematically changing the distance of the roving downstream probes. In order to support the ADVs during data collection, a field deployable aluminium frame, 1.5 m x 1.5 m (width by length) was designed. The frame was constructed by Richard Allix (senior machine shop technician) of Concordia University. The ADVs were attached to movable graduated cross-member bars allowing for samples to be obtained at any desired longitudinal, lateral and vertical (x,y,z) location within the square frame (Figure 3.2). The frame also served to support the underwater digital video camera used for the fine-scale investigation of the shear layer behaviour (Chapter 6).

All field work was performed on the Eaton North River which is located in Eastern Townships, Quebec Canada. The Eaton North is a gravel-bed river with a median grain size of approximately D_{50} = 0.035 m, a slope of approximately 0.005 m m^{-1} and a bankfull width of approximately 28 m. The estimated bankfull discharge is approximately 30 m^3 s^{-1}. Several large clast sediments (> 0.20 m) are scattered sporadically throughout the reach some of which form the keystones of pebble clusters and LREs [*Lamarre and Roy*, 2001]. Each article chapter investigated a different LRE of varying size and morphometry (multiple LREs, 10 sites, were investigated in Chapter 7).

For each experimental set-up, the support frame was placed overtop of selected LREs and was aligned with the mean-flow paths using tracer ribbons. The adjustable rebar legs of the frame were hammered into the river bed and the frame was adjusted to horizontal using a carpenter's level. River stage was monitored during each sampling event and did not change appreciably (<5%) throughout each experimental set-up.

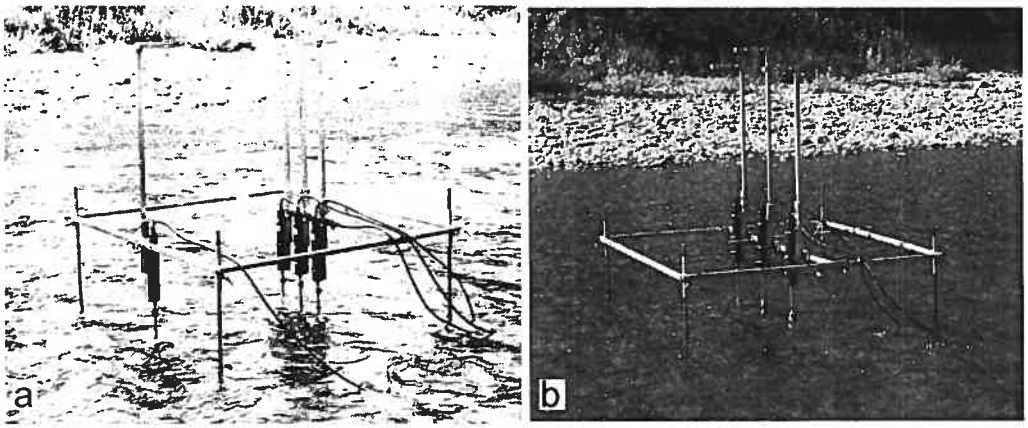

Figure 3.2. Support frame and ADV configurations for the experiments conducted in a) Chapter 5 and b) Chapter 7. Flow is from left to right.

Velocity measurements for all field experiments were obtained using multiple ADVs and specific sampling strategies were used depending on the particular chapter objectives. For Chapter 5, a stationary ADV was positioned upstream along the centerline of a LRE while downstream roving probes were arranged in a lateral array which was shifted to the desired sampling locations (Figure 3.2a). A similar sampling strategy was used in Chapter 7, but without the upstream stationary probe (Figure 3.2b). The added benefit of using multiple ADVs was that it augmented the number of sampling locations which could be measured per day. Velocity sampling schemes consisted of obtaining high density sampling locations within the limits imposed by the support frame's horizontal dimensions which were 1.5 m x 1.5 m. The total number of velocity measurement locations which could be sampled in a single day was restricted due to the involved *in situ* experimental set-up and the remote site location. The frame set-up had to be dismantled at the end of each sampling day in case of flash floods on the river and/or vandalism at night. The support frame provided a fixed reference level over the uneven heterogeneous bed and facilitated a sampling protocol involving measurement locations distributed over level horizontal planes. Even with multiple

ADVs, the total number of sampling locations measurable per day was approximately 140 and it was felt that a minimum density of approximately 70 sampling locations per plane was required to properly characterise the flow field (and the lateral extent of the LRE hydrodynamic influence). Hence, only two horizontal measurement planes (an upper and lower plane) could be sampled at each experimental site. For Chapters 5 and 7, the upper measurement plane was located in the intermediate flow region at approximately $z/Z = 0.45$ and the lower plane was located below the top of the site's largest LRE at approximately $z/Z = 0.25$. We wished to stay away from the bed ($z \geq 0.07$ m) for two reasons: 1) to ensure that the velocity measurements were related to the LRE investigated and not due to smaller bed heterogeneities (i.e., other protruding grains); and 2) to avoid poor signal correlations which were often obtained when near-bed measurements were recorded.

The sampling strategy for Chapter 6 was somewhat different given the focus of the experiment on the fine-scale characterisation of the shear layer and its behaviour to the passage of LS coherent flow structures. Part of the experiment involved concurrent ADV and flow visualization recordings (outlined in detail in Section 3.3.2). For this, the ADVs were aligned in a longitudinal array crossing overtop of the LRE as presented in Figure 3.3. Five concurrent recordings were made while adjusting the position of the third in-line probe sequentially downstream. To supplement the concurrent ADV and flow visualization recordings, further ADV measurements were recorded over a horizontal and a vertical plane centered on the expected shear layer location in the lee of the LRE.

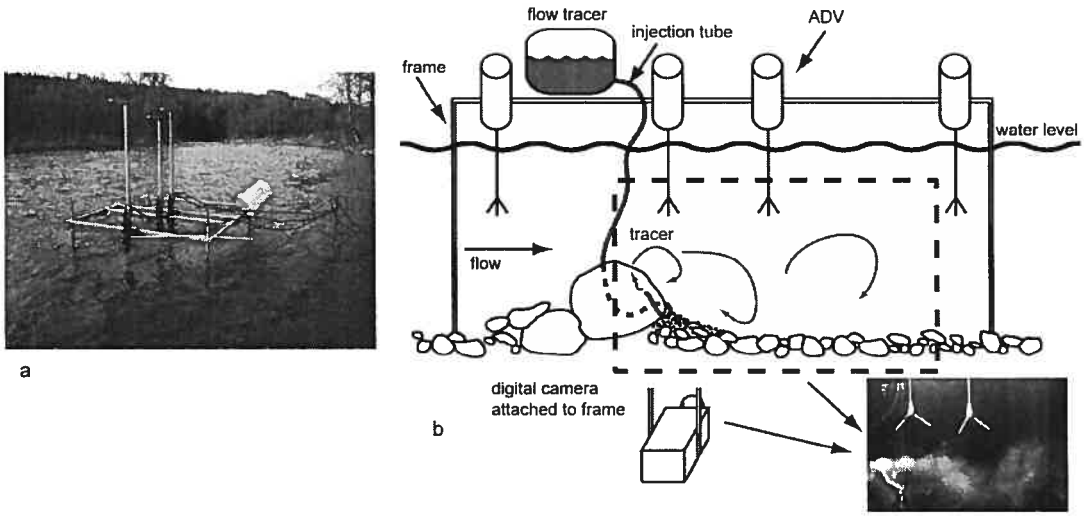

Figure 3.3. a) ADV and underwater digital camera aluminium support frame, 1.5 m x 1.5 m; b) schematic of experimental set-up for synchronous visualization and velocity measurements [*Lacey and Roy*, 2007b].

In order to determine the relationships between the shear layer characteristics in the lee of a LRE and the LS turbulent coherent flow structures advecting from upstream it is necessary to simultaneously sample velocities upstream and downstream of the LREs. The upstream probe was used to estimate space-time cross-correlations (STC) between it and any velocity measurements recorded simultaneously downstream. STC analysis is commonly used to characterising the scales and shapes of turbulent flow structures in laboratory settings [*Grant*, 1958; *Nakagawa and Nezu*, 1981; *Cenedese et al.*, 1991; *Kadota and Nezu*, 1999], but has been rarely used in natural rivers (e.g., *Roy et al.* [1996]; *Rhoads and Sukhodolov* [2004]; *Roy et al.* [2004]). STC analysis relies on the assumption that a strong correlation between simultaneous velocity time series measured at different locations is indicative of coherence within the flow. Analysis of the simultaneous spatial and temporal variability within the velocity field allows for the characterization of the time-averaged behaviour and flow patterns of the turbulent coherent structures. Using this technique, the size and behaviour of LS coherent structures as they pass overtop of LREs can be estimated and any disruptions in the coherent structures due to the LRE shear layer may be observed. The upstream probe was as well used to detect the LS turbulent flow structures before they pass over the LRE and are potentially modified due to the interaction. The reaction of the shear layer to the anticipated passing of the LS structures was thereby observed. For the

experiments where the objectives included characterising the relationships between LS flow structures and LRE shear layers (Chapter 5 and 6) the sampling schemes incorporated a simultaneous fixed upstream probe.

3.3.2. Measurements of instantaneous velocities synchronous with digital video recordings

A major component of the fine-scale shear layer study presented in Chapter 6 was the visual characterization of shear layer processes and the response of the shear layer to the passage of LS flow structures advecting form upstream. The following describes the methodology (the details of which are omitted from Chapter 6) used for the visualization study and how the digital images were synchronized with the simultaneously recorded ADV measurements.

A neutrally buoyant flow tracer was made *in situ* in a 10 L canister by mixing river water with small quantities < 0.2 L of non-toxic white latex paint. The canister was placed on top of the aluminium support frame and the tracer was injected by gravity, through a tube, into the recirculation zone in the lee of the LRE where it could be passively entrained into the shear layer (Figure 3.2b). The end of the injection tube was held in place by a 0.2 m steel nail secured to the bed against the lee side of the cluster. Care was taken to ensure that the tracer be injected directly below (in line with) the ADV probes. The tracer was injected at a rate of approximately 0.02 litre s^{-1}. The Sony digital video camera (model DCR-TRV18), housed in an underwater case, was secured to the support frame and positioned at a vertical distance of $z = 0.1$ m from the bed and a lateral distance of $y = 0.6$ m from the centreline transect providing an x-z plane of view. This side view was centred on the pebble cluster wake and included the back side of the pebble cluster, the injection tube, and the two middle ADVs (Figure 3.2b). The digital video camera was connected to a laptop on the bank via an underwater cable which ensured the proper positioning of the camera in real-time. The digital video camera and the ADVs recorded simultaneously at 30 Hz and 25 Hz, respectively, as the tracer was injected for approximately 4 minutes. A rough *in situ* synchronization between the videos and the ADVs was performed by touching the ADV transmitter during recording – the hand could be observed in the video and resulted in noticeably erroneous spikes in the ADV velocity time series.

Blue and red hue saturation values, HSV, were extracted from each digital image at the estimated ADV sampling volume locations (for the two probes captured by the digital videos (Figure 3.2b). Image intensity time series, I_n, were determined by I_n = HSV_{blue} + HSV_{red} for each frame. I_n has been found to give a good contrast between presence and absence (ambient flow conditions) of tracer in natural river experiments [*Marquis and Roy*, 2006b]. Cross-correlation coefficients, $R_{u_i I_n}$, were estimated between the extracted I_n time series and instantaneous velocity time series (for the two ADVs located within the field of view of the digital images).

$$R_{u_i I_n}(\Delta t) = \frac{\frac{1}{N}\sum_{k=1}^{N} u_i(t_k) \cdot I_n(t_k + \Delta t)}{u_i' I_n'} \tag{3.1}$$

where I'_n is the standard deviation of I_n, i is a velocity component index, u'_i is the standard deviation of u_i, and Δt is the time step. The I_n and u_i time series were synchronized given Δt where maximum $R_{u_i I_n}$ occurs. Using the above procedure, the ADV velocity data and the digital videos were synchronized to within one time-step (Δt = 0.04 s) which is a large improvement on previous synchronization efforts [*Roy et al.*, 1999]. While significant information on turbulent flow structures is obtained independently by the two measurement techniques (ADV and flow visualization), through precise synchronization we were able to visually identify and characterise events estimated using the velocity measurements allowing for a much greater understanding of flow events.

3.4. Conclusion

Many laboratory studies have investigated the fine-scale hydrodynamic around bluff bodies and simple bedforms (a few have investigated pebble clusters). While these studies offer important insights into flow separation and the shedding processes around instream objects, they are conducted under controlled conditions, low to moderate *Re* and often leave out the lateral turbulent component. There are no studies to date (to our knowledge) which have investigated the *in situ* fine-scale three-dimensional hydrodynamics around submerged large roughness elements in gravel-bed rivers. Integrating multiple techniques of turbulence analysis, the approach used in this thesis to

investigate the fine-scale hydrodynamics around LREs will shed light on many grey areas of knowledge such as: the scale-dependence of turbulence; the interrelationship between flow and LRE morphometrics and turbulent wake parameters; the importance of the lateral velocity component in turbulent momentum exchange; the processes involved in shear layer shedding; and the interrelationship between LS coherent flow structures and shedding structures. The lack of knowledge in these areas has led to conflicting studies on the apparent randomness of their channel scale spatial distribution and the benefits they impart to aquatic biota. The fine-scale 3D hydrodynamics spatially characterised in this thesis will help to resolve some of the inconsistencies between these studies and give rise to a better understanding of the role LREs play in the generation of turbulent coherent structures in rivers.

Linking Paragraph A

Many studies conducted in laboratory flumes or *in situ* investigating turbulent flow over topographic features such as dunes or large roughness elements (LREs) have been interested in identifying the spatial patterns of turbulence within their data sets. Subjective, qualitative descriptions are often given on the spatial extent and scale of patterns observed in the time-averaged turbulence statistics without rigorous quantification. Multi-scale dependence and quantification of spatial patterns within spatially distributed data sets is currently of great interest to researchers in many fields such as ecology and water resources. In the following chapter[1], the spatial structures within turbulent flow data were investigated through the use of a new multivariate variation partitioning analysis technique involving principal coordinates of neighbour matrices (PCNM). We revisit the 2D spatially distributed turbulence data reported by *Buffin-Bélanger and Roy* [1998] estimated from instantaneous velocities in an *x-z* plane crossing over an *in situ* pebble cluster. This data set was used due to its exceptionally high density of sampling points measured *in situ* and to show the additional knowledge gained on the turbulent flow field through a multi-scale spatial analysis by comparing with the more traditional analysis presented by *Buffin-Bélanger and Roy* [1998]. The analysis revealed a significant ($\alpha = 0.01$) spatial dependence, 58%, for the mean and turbulent flow variables. Using the orthogonal property of the PCNM variables, the explained variation was partitioned over four significant ($\alpha = 0.01$) spatial scales: very-large (VL, 17%), large (L, 24%), meso (M, 6%) and fine (F, 2%). Nearly 75% of the variance of the main turbulent flow indicators, such as u', w' and $-\rho\overline{u'w'}$ was explained by the VL- and L-scale PCNM submodels, which have longitudinal and vertical length scales of the order of $\Delta x = 5.3Z - 2.6Z$ and $\Delta z = 1.0Z - 0.5Z$ (or alternatively $\Delta x = 10h_s - 5h_s$ and $\Delta z = 2h_s - 1.0h_s$) respectively. Through a multivariate mapping procedure, clear spatial patterns within the explained flow variables emerge around the cluster. The application of PCNM analysis on the turbulent flow field shows the power of the technique to resolve the relevant spatial scales and patterns, and demonstrates its potential use in a variety of water resources studies.

---

[1] Lacey, R.W.J., Legendre, P. and A.G. Roy (2007) Spatial scale partitioning of in situ turbulent flow data over a pebble cluster in a gravel-bed river, *Water Resources Research*, *43*, W03416, doi:10.1029/2006WR005044 (reprinted with permission from AGU).

4. SPATIAL SCALE PARTITIONING OF *IN SITU* TURBULENT FLOW DATA OVER A PEBBLE CLUSTER IN A GRAVEL-BED RIVER

4.1. Introduction

A recent trend in turbulent flow research is to attempt to identify and characterize the temporal and spatial scales of coherent flow structures over smooth as well as rough beds [*Adrian et al.*, 2000; *Liu et al.*, 2001; *Shvidchenko and Pender*, 2001; *Chen and Hu*, 2003; *Roy et al.*, 2004]. Space-time correlations of high frequency velocity time series have shown the existence of large depth-scaled coherent flow structures consisting of high- and low-speed wedges [*Nakagawa and Nezu*, 1981; *Buffin-Bélanger et al.*, 2000; *Roy et al.*, 2004]. An alternative method of investigating the spatial scales of turbulence is through the analysis of the spatial distribution of the mean turbulent parameters of interest. Following this approach, a few studies have investigated the spatial distribution of turbulence properties over and around large roughness elements such as isolated clasts or pebble clusters [*Brayshaw et al.*, 1983; *Paola et al.*, 1986; *Buffin-Bélanger and Roy*, 1998; *Lawless and Robert*, 2001; *Shamloo et al.*, 2001; *Tritico and Hotchkiss*, 2005]. In natural gravel-bed rivers, the bed is made up of poorly sorted clasts ranging in size from very coarse to fine grains, which results in abrupt roughness transitions [*Robert et al.*, 1992]. These rapid changes in roughness have a direct effect on the turbulent length scales and on the spatial patterns of the mean and turbulent flow properties [*Buffin-Bélanger and Roy*, 1998]. The mechanism responsible for these changes is the shedding of vortices in the lee of protuberant particles. Such vortices have a range of sizes and frequencies [*Kirkbride*, 1993]. This suggests a high dependence of the spatial pattern of turbulent flow structures on the distribution of large clasts and of bedforms such as clusters on the heterogeneous bed.

The relationships between spatial patterns of turbulent structure and large roughness elements on the bed were investigated by *Buffin-Bélanger and Roy* [1998]. Through an intense measurement scheme around a pebble cluster, they were able to delineate six characteristic regions of the flow field (acceleration, recirculation, shedding, reattachment, upwelling and recovering flow), and showed the relationships

between these regions and the protuberant clasts. While their study provided qualitative descriptions of numerous flow variables and of their spatial patterns, it did not attempt to quantitatively explain the dependence of the flow variables on the spatial structure, and did not estimate the proportion of the variation within the flow variables explained by the spatial structures.

In ecological studies, quantification of spatial structure is often obtained through trend surface analysis. This is a standard method used to explain the variance associated with spatial trends in variables measured at points in space through polynomial regressions [*Legendre and Legendre*, 1998]. The higher the polynomial order, the finer the spatial structures which can be explained. Yet, the terms within the polynomial are often highly correlated with one another, which prevents the modeling of linearly independent structures at different scales [*Borcard and Legendre*, 2002]. Furthermore, trend surface analysis is devised to model large-scale spatial structures with simple shapes and cannot adequately model finer structures [*Borcard and Legendre*, 2002; *Borcard et al.*, 2004].

Borcard and Legendre [2002] have recently developed a new statistical spatial modeling method: principal coordinates of neighbour matrices (PCNM). The method, the theory for which has been further explored by *Dray et al.* [2006], is a form of distance-based eigenvector maps (DBEM), and has been successfully applied in aquatic ecological studies to describe the dominant spatial scales at which species variation occurs [*Borcard et al.*, 2004; *Brind'Amour et al.*, 2005]. PCNM analysis resembles Fourier analysis and harmonic regression, but has the advantage of providing a broader range of signals and can also be used with irregularly-spaced data [*Borcard and Legendre*, 2002]. PCNM analysis is based on the orthogonal spectral decomposition of the relationships among the spatial coordinates of a sampling design [*Borcard et al.*, 2004]. The orthogonal property of the PCNM technique allows an exact partitioning (no intercorrelation) of the explained variance over different spatial scales. PCNM analysis is used in conjunction with multiple regression to study the spatial structure of a single variable, or with canonical redundancy analysis (RDA) when studying the spatial structure of multiple variables. RDA is an extension of multiple regression used to model multivariate data. It is based on the eigenvalue decomposition of the table of

regressed fitted values, which reduces the large number of associated (linearly correlated) fitted vectors to a smaller composite of linearly independent variables [*Legendre and Legendre*, 1998]. With eigenvalue decomposition, most of the variability is often summarized in the first few dimensions, which facilitates interpretation. Eigenvalue analysis has been used to study turbulent coherent structures through proper orthogonal decomposition (POD) [*Liu et al.*, 2001], and is used extensively in ecology with data sets which include large numbers (hundreds, thousands) of interrelated variables.

PCNM analysis bears some similarity with POD. For POD, the eigenvalue decomposition is performed directly on a two-point correlation coefficient matrix of the flow variable under investigation using Fourier modes which are sinusoidal (quasi-trigonometric) eigenvectors termed eignenfunctions [*Moin and Moser*, 1989; *Berkooz, Holmes and Lumley*, 1993]. As POD is a direct eigenvalue decomposition of the flow variable correlation matrix, the sum of the eigenvalues is equal to the total variance of the flow variable matrix. PCNM analysis is a regression technique which identifies only the fraction of the total variance in a response variable that is spatially dependent. An advantage of the PCNM technique is that the PCNM variables represent the eigenvalue decomposition of the relationships of a specific sampling grid, and can be used to analyze irregularly-spaced data with non-rectangular boundaries. PCNM analysis is, as well, a multivariate regression technique; it offers the added advantage over POD (which can only analyze a single variable at a time), of allowing the analysis of all response variables at once.

Buffin-Bélanger and Roy [1998] investigated each flow parameter, or ratio of flow parameters individually, an approach common in studies investigating the turbulent structure of flows [*Bennett and Best*, 1995; *Lawless and Robert*; 2001]. This approach used for investigating spatial patterns of flow structure could be greatly improved using PCNM and RDA, which can identify and quantify the spatial dependence of all flow parameters at once, thus providing an efficient means of summarizing and interpreting the spatial patterns. This paper examines the potential use of PCNM analysis as a statistical tool for investigating the spatial-scale dependence of turbulent flow processes as a complement to traditional analyses. The paper revisits the turbulent flow data

reported by *Buffin-Bélanger and Roy* [1998] adjacent to and overtop of a pebble cluster in a gravel-bed river. Our study furthers the previous work by explaining and partitioning the variance of the flow parameters over four spatial scales, providing a quantification of the spatially explained variance, and indicating the intercorrelations among the turbulence variables at each scale. This leads to new insights into the turbulent flow field around clusters and protuberant clasts in rivers by suggesting the appropriate scale dependence of the turbulent flow variables, and demonstrates the potential use of PCNM analysis for a wider field of application in water resources studies.

4.2. Field Measurements and Turbulence statistics

The collection and processing of the instantaneous velocity measurements used in our study was described in detail by *Buffin-Bélanger and Roy* [1998] and are briefly summarized here. Velocity measurements were collected from the Eaton North River, Quebec, Canada, on a longitudinal, x, – vertical, z, transect plane with a mean height extending to the water surface (Z = 0.38 m) and a longitudinal length of 4.0 m. The x-z plane crosses through the centre of a naturally formed pebble cluster. The crest of the cluster is located at x = 0.77 m (Figure 4.1) and has a height (h_s) of 0.20 m. Electromagnetic current meters (ECMs) were used to collect instantaneous longitudinal, U, and vertical, W, velocity measurements at a sampling frequency of 20 Hz. The present study consists of 29 vertical profiles (the two most upstream profiles of the original 31 were omitted due to their inconsistent separation distances). Each profile contains 6 to 13 vertical measurement locations (Figure 4.1). In total, the data set consists of 340 velocity time series of 60 seconds duration. Each time series corresponds to a point on the sampling grid of Figure 4.1. The spacing between measurements along the vertical profiles is 0.02 m (with the exception of two offset grid points at x = 1.1 m), while spacing in the longitudinal direction varied from 0.1 m to 0.15 m.

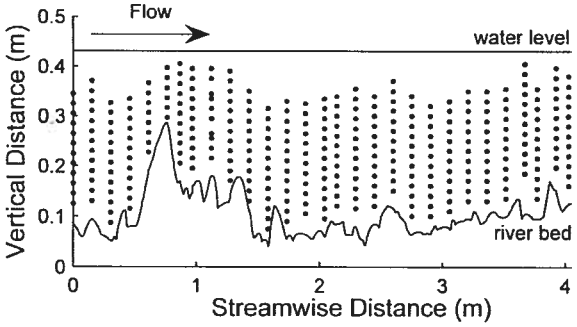

Figure 4.1. Sampling *x-z* transect plane with velocity measurement locations (dots). Modified from *Buffin-Bélanger and Roy* [1998].

The mean downstream velocity ($\overline{U}$), where the overbar represents averaging over time, for the *x-z* plane is 0.28 m s^{-1} resulting in a Reynolds number, *Re*, of 8.0 x 10^4 which indicates a fully turbulent regime. *Buffin-Bélanger and Roy* [1998] investigated and presented a set of 22 flow variables. These consisted of mean and turbulence statistics, and ratios between some of the flow variables. For the current study, we selected a subset of 15 variables to be used as response variables in the PCNM analysis. This subset was selected on the basis that they covered a range of spatial patterns and scales in order to properly test the PCNM method without introducing excessive redundancy between the variables. As such, the flow variables included: mean flow statistics ($\overline{U}$, $\overline{W}$); second order moment statistics (root mean square values, u' and w') which are a measure of the turbulent intensity and had been shown by *Buffin-Bélanger and Roy* [1998] to exhibit broad scale spatial patterns; and the third order moment (skewness, Sk_u and Sk_w). Skewness is a measure of the asymmetry of the velocity distribution, and it reveals the presence of high-magnitude events within the velocity signal [*Buffin-Bélanger and Roy*, 1998]. For example, a positive Sk_w indicates intermittent, infrequent events of vertical velocity directed towards the surface. Previous boundary layer studies have observed near-bed velocity distributions to be positively skewed [*Grass*, 1971].

We have also included the average statistics of turbulent events such as the percent of time (T) and the frequency (f) of low-speed flow ejections and high-speed sweeps. Event statistics are estimated by conditionally sampling the fluctuating component of the velocity signals following *Lu and Willmarth* [1973]. Ejections (quadrant 2) are defined

by negative u and positive w excursions from the mean, while sweeps (quadrant 4) are defined by positive u and negative w excursions. Following *Lu and Willmarth* [1973], a threshold hole size, $T_h = |uw|/u'w$, was used to distinguish between stronger, more energetic, events ($T_h = 2$) and all events ($T_h = 0$). The terminology for "hole" corresponds to the more quiescent contributions which are obtained by subtracting events estimated with $T_h = 2$ from those estimated with $T_h = 0$. Ejections and sweeps are a common feature of turbulent flows over smooth and rough boundaries [*Grass*, 1971], and contribute to the bulk of the positive Reynolds shear stress [*Williams et al.*, 1989]. The event statistics displayed a more localized spatial pattern than the mean turbulence statistics previously mentioned. Mean Reynolds shear stress ($-\rho\overline{uw}$) and integral time scale (ITS_u, ITS_w) obtained from the autocorrelation functions of the longitudinal and vertical velocity time series were also included. The mean shear stress is a measure of the mean turbulent momentum exchange at a sampling location, and ITS is a rough measure of the interval over which velocities are autocorrelated, giving an estimation of the size of turbulent coherent structures.

The spatial mean values for the time-averaged turbulence statistics, event statistics and integral time scales are presented in Table 4.1. Further details on the methods for estimating these variables are presented in *Buffin-Bélanger and Roy* [1998]. The spatial distributions of the standardized values (z-scores) of the 15 flow variables are presented in Figure 4.2. By investigating each subfigure as in *Buffin-Bélanger and Roy* [1998], clear spatial patterns emerge. For instance large patches of high u' and w', $-\rho\overline{uw}$ are observed in the wake of the pebble cluster. The spatial patterns of $T_{Q4}T_{h0}$ and $T_{Q2}T_{h2}$ are patchier, with some better defined trends showing higher values in the wake of the cluster advecting towards the water surface with distance downstream from the cluster increases. While these and other general spatial patterns were described by *Buffin-Bélanger and Roy* [1998], they remain qualitative observations, and investigating each variable sequentially is cumbersome, and does not lead to a global view where the interactions between the variables are fully exploited. To do so requires a multivariate approach that can deal simultaneously with the interrelations between the flow variables, as well as with the spatial components of the data.

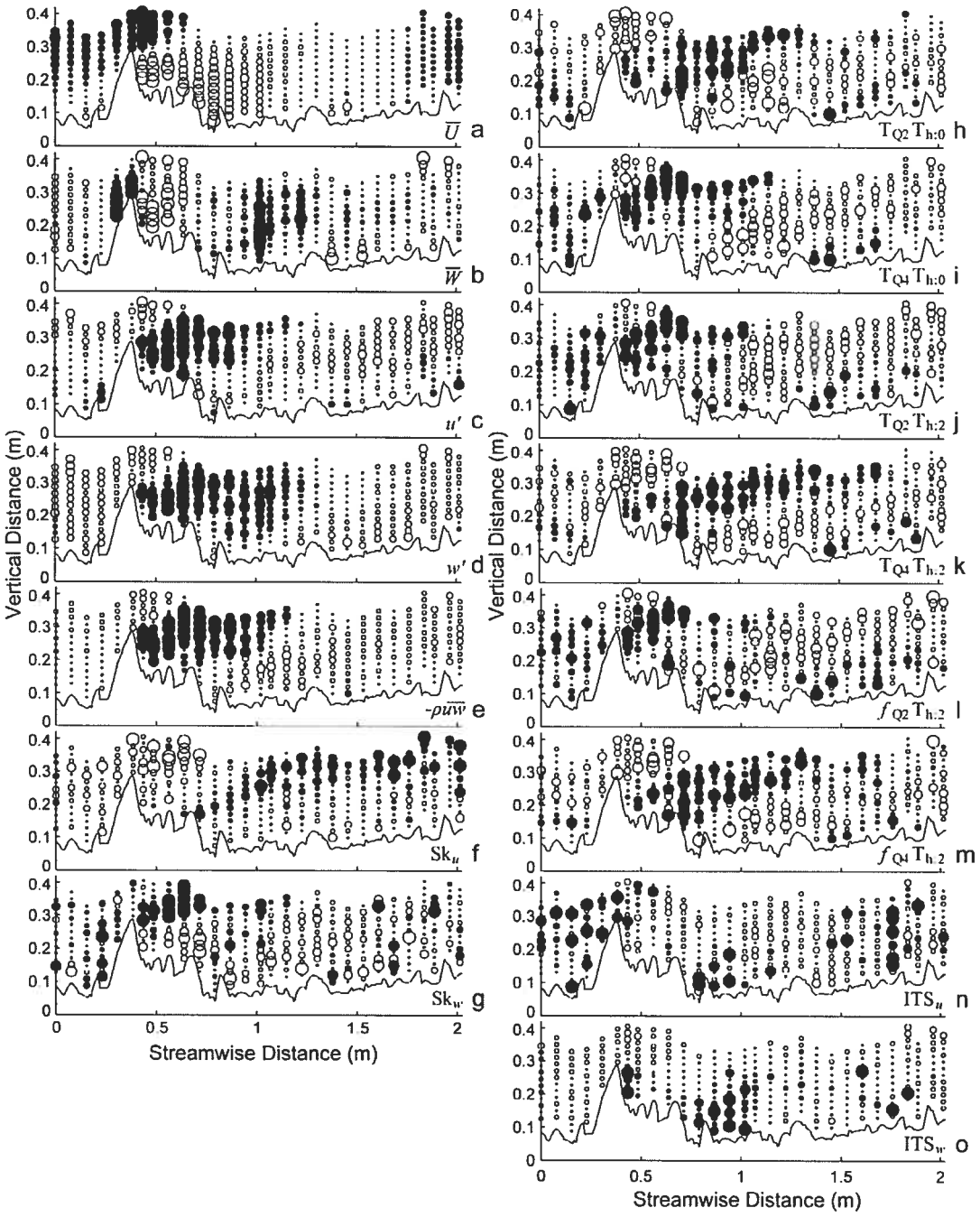

Figure 4.2. *x-z* transect plot of standardized values (z-scores) of the mean and turbulent flow statistics: a) $\overline{U}$ b) $\overline{W}$ c) u' d) w' e) $-\rho\overline{uw}$ f) Sk_u g) Sk_w h) $T_{Q2}T_{h:0}$ i) $T_{Q4}T_{h:0}$ j) $T_{Q2}T_{h:2}$ k) $T_{Q4}T_{h:2}$ l) $f_{Q2}T_{h:2}$ m) $f_{Q4}T_{h:2}$ n) ITS_u o) ITS_w. Positive values are represented by filled bubbles, negative values by empty bubbles. Bubble size indicates relative magnitude. Flow is from left to right. Modified from *Buffin-Bélanger and Roy* [1998].

Table 4.1. Spatial means and standard deviations of the flow variables.

Variable	Mean	Std
$\overline{U}$ (m s^{-1})	0.28	0.11
$\overline{W}$ (m s^{-1})	0.00	0.01
u' (m s^{-1})	0.05	0.01
w' (m s^{-1})	0.04	0.01
$-\rho\overline{u'w'}$ (N m^{-2})	0.60	0.66
Sk_u (m^3 s^{-3})	0.15	0.38
Sk_w (m^3 s^{-3})	0.02	0.27
$T_{Q2}T_{h,0}$ (%)	29.62	3.44
$T_{Q4}T_{h,0}$ (%)	28.58	3.82
$T_{Q2}T_{h,2}$ (%)	2.62	1.42
$T_{Q4}T_{h,2}$ (%)	2.95	1.27
$f_{Q2}T_{h,2}$ (s^{-1})	0.34	0.13
$f_{Q4}T_{h,2}$ (s^{-1})	0.40	0.13
ITS_u (s)	0.79	0.46
ITS_w (s)	0.31	0.20

4.3. PCNM statistical analysis

The PCNM technique is used to explain the spatial dependence and patterns of distributed variables over a sampling grid. The advantage of the PCNM technique is that the explained variance can be explicitly estimated for each spatial scale. The PCNM variables (PCNMs) are obtained by principal coordinate analysis (PCoA) of a truncated pair-wise geographical Euclidian distance matrix among the sampling points. PCNM variables are thus orthogonal to one another (null scalar product). PCNMs are sinusoidal and of decreasing periods, and as such, they can be grouped into submodels corresponding to different scales. Selecting the number of submodels to use and the scale associated with each one (i.e. large, meso, and fine) is a subjective process based on the objectives of the analysis (the level of detail desired) and the similarity between the significant PCNM periods. Once the submodels are constructed, they are used as explanatory variables in RDA. The sinusoidal property of the PCNM variables bears some resemblance to spectral analysis using a Fourier transformation of the autocorrelation function and wavelet analysis. Wavelet analysis is often used to decompose time series into time-frequency space to determine both the dominant modes of variability and how those modes vary in time. Similarly, PCNM analysis fits the grouped sinusoidal PCNM variables to response variables. Here spatial data is used, obtaining a decomposition describing the dominant modes of variability, as well as their spatial variation. Furthermore, PCNM analysis quantifies the fit by an R^2 statistic within

each scale. RDA is more interesting than multiple regression because it can analyze several response variables in a single analysis, and display graphically their regressed interrelationships. In RDA, each canonical ordination axis corresponds to a direction in the response variable space that is maximally correlated to a linear combination of the explanatory variables. The orthogonal nature of the PCNM variables means that the variance explained by each PCNM submodel is unique and additive. The total explained variance can therefore be partitioned among the different PCNM submodels, or spatial scales.

The main constraint for applying a PCNM analysis is that best results are obtained when using a uniform sampling grid with equally spaced x and z. Small irregularities in the sampling grid result in an inability to explain the finer-scale spatial structures. As the variation between sampling point distances increases, the ability of the PCNM technique to resolve the finer-scale spatial structures is compromised (i.e. increases in the sample grid irregularities result in an inability to explain larger and larger fine-scale spatial structures). In the present analysis, the vertical heights were multiplied by a factor of 7.65 to achieve a roughly regular grid pattern between the longitudinal and vertical sampling points. This adjustment allowed the finer-scale variation measured in the vertical dimension to be retained and analyzed. Irregularities at the sampling grid boundaries due to the nonhomogeneous bed and the pebble cluster could not be avoided, and resulted in a loss of fine-scale spatial explanation.

Figure 4.3 illustrates the various steps involved in producing the PCNM variables from the x-z sampling points following PCNM analysis theory [*Borcard and Legendre*, 2002]. A Euclidean distance (D_1) matrix was calculated for all possible distances between sampling locations (Figure 4.3a,b) using the modified coordinates. The D_1-matrix was truncated at a threshold distance (d_t) which was equal to or larger than the minimum between-site connection distance corresponding to the distance that kept all sampling locations connected together in a network. Using hierarchical, single-linkage, agglomerative cluster analysis, the appropriate d_t was estimated to be 0.17 m. Unfortunately, due to the inherent irregularities in the x-z sampling grid that were imposed from the irregular bed topography, truncating the D_1-matrix at 0.17 m resulted in highly disrupted and distorted PCNM variables. This distortion influenced the

amplitude, phase and period of the sinusoids, thereby complicating their interpretation as the PCNMs bear structures at several scales [*Borcard and Legendre*, 2002]. The distortion decreased as d_t was increased, but by increasing d_t, the explanation of fine-scale variability was compromised, because inherently PCNM variables are unable to explain any spatial variance at scales less than d_t [*Legendre and Borcard*, 2006]. The minimum value which produced the fewest singularities was d_t = 0.35 m, a value approximately twice as large as the d_t calculated with the cluster analysis. Consequently, any spatial structure occurring in the flow variables at scales below this threshold (Δx < 0.35 m and Δz = 0.046 m) could not be explained by our analysis, where Δx and Δz represent the physical length scales in the longitudinal and vertical directions, respectively. This constraint should be kept in mind when designing new studies.

Distances between sampling points above d_t were set to a value (d_m = 1.4 m), which is four times higher than d_t (Figure 4.3c), in order to retain only the distances smaller than d_t between neighbouring sites (sampling points) within the D_1 matrix [*Borcard et al.*, 2004]. The eigenvalues and principal coordinates (eigenvectors) of the truncated D_1-matrix were obtained using PCoA (Figure 4.3d). Of the 340 eigenvalues obtained, 180 were positive. A forward selection permutation procedure from the CANOCO program [*ter Braak and Smilauer*, 2002] was used to determine which PCNMs explained a significant (α = 0.01) level of variation in the flow variables. Twenty-nine significant PCNMs were identified, and they were subjectively classified into four submodels according to the scales of their respective periods: very large-scale (VL), large-scale (L), meso-scale (M), and fine-scale (F). One PCNM from each class is presented in Figure 4.3e. The PCNMs can be seen as a series of 2D sinusoidal curves of decreasing periods.

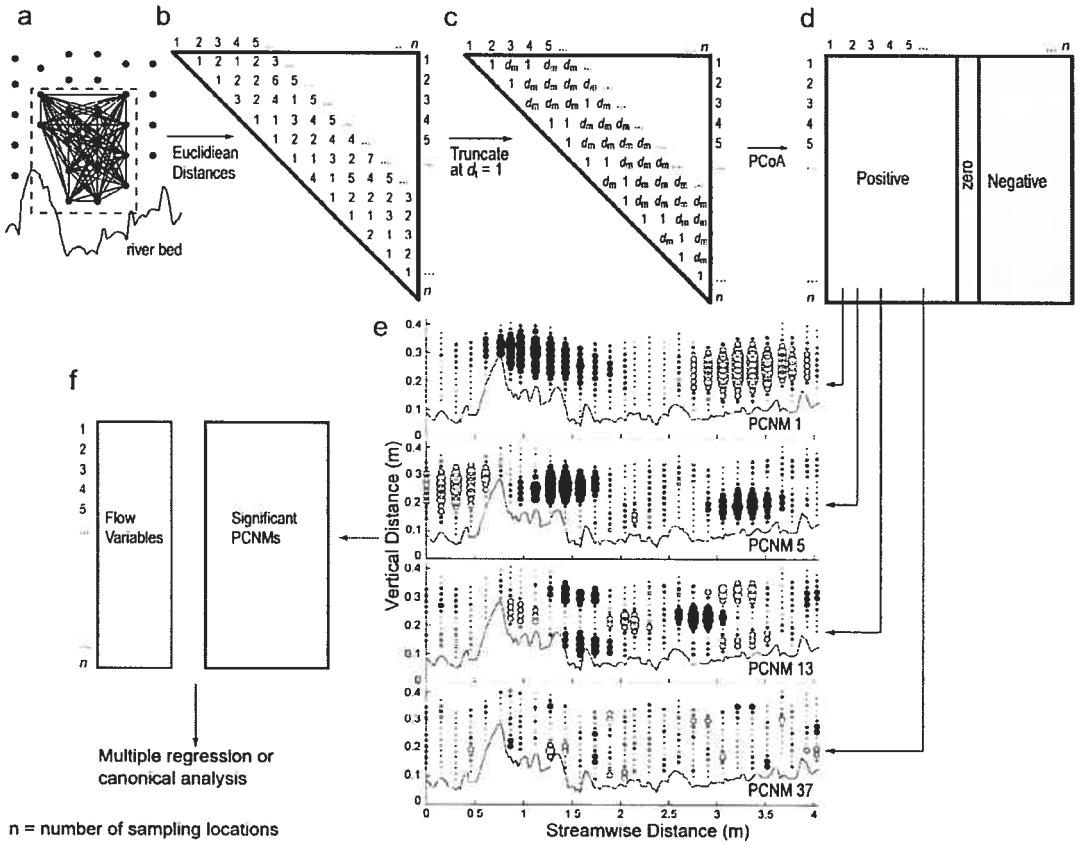

Figure 4.3. Methodology for developing PCNM variables. a) Example of sampling locations with Euclidian links between coordinates; b) Euclidian distance (D_1) matrix; c) truncated D_1 matrix (neighbouring matrix) truncated at d_t = 1.0 by d_m; d) principal coordinate (eigenvector) matrix, indicating positive, zero and negative eigenvalues; e) examples of PCNMs (positive eigenvalued principal coordinates) representing very-large (PCNM 1), large (PCNM 5), meso (PCNM 13) and fine (PCNM 37) scales. The size of the bubbles is proportional to the magnitude of the PCNM variable values (positive values filled). Flow is from left to right. f) Response (flow) matrix and explanatory (PCNM) matrix used in multiple regression and canonical analysis. Modified from *Borcard and Legendre* [2002].

The largest detectable scale, which is linked to the period of the first PCNM, is dictated by the spatial extent of the furthest sampling locations. For instance, when computed from a distance matrix corresponding to n equidistant objects arranged as a straight line, the largest period is equal to n+1 [*Borcard and Legendre*, 2002]. From Figure 4.3e, the longitudinal period of PCNM #1 can be estimated as $x \approx 4$ m, while the period of PCNM #13 is $x \approx 0.6$ m. The physical length scales, Δx and Δz, associated with each PCNM class were estimated from the mean half-period of the grouped PCNMs. Δx

and Δz are presented in Table 4.2 along with the range and number of PCNMs included per class. As indicated in Table 4.2, the maximum longitudinal scale is around $5.3Z$, and the minimum longitudinal scale is equivalent to the flow depth ($1.0Z$); the mean flow depth is $Z = 0.38$ m. Any longitudinal spatial variation in the data occurring at scales above and below these thresholds could not be resolved by our analysis.

Table 4.2. Scale classification of the significant PCNM variables.

Scale	PCNM range	No. of PCNMs	Physical scale (m)	
			$\Delta x/Z$	$\Delta y/Z$
Very Large (VL)	1 – 2	2	5.3	1.0
Large (L)	3 – 10	8	2.6	0.5
Medium (M)	11 – 21	10	1.6	0.3
Fine (F)	22 – 58	9	1.0	0.14

Note: $Z = 0.38$ m is the mean flow depth

The PCNM submodels were used as explanatory (independent) variables in multiple regressions and canonical RDA (Figure 4.3f) for the turbulent flow data obtained from *Buffin-Bélanger and Roy* [1998] and listed in Table 4.1. The flow variables were standardized and both the multiple regressions and the RDA were computed using the CANOCO program [*ter Braak and Smilauer*, 2002]. The global model (containing 180 PCNMs) and all canonical axes of the submodels were tested for significance ($\alpha = 0.01$) using 999 Monte Carlo unrestricted permutations. The significant "fitted site scores" from each submodel were plotted on the sampling point coordinates thus providing a means to interpret the spatial patterns of the results at each scale. The "fitted site scores" are the values obtained from the RDA. The term "fitted site scores" is commonly used in canonical analysis; it designates the principal components of the table of fitted values of the multiple regressions. "Fitted site scores" are calculated by multiplying the canonical eigenvectors by the fitted response variables. The spatial patterns and relative magnitude of each correlated flow variable can be directly interpreted from these plots. Biplots of the RDA eigenvectors focusing on the correlations between the fitted response variables are also presented to give information on the correlations between the turbulence statistics at each submodel scale.

The contribution of the independent variables (global PCNM model or PCNM submodels, in the present study) to the explanation of the response variables is given by the bimultivariate redundancy statistic (or canonical R^2) and its adjusted form, the

adjusted bimultivariate redundancy statistic (or adjusted canonical R^2, R_a^2). The adjusted form is corrected for the explanation that would be provided by the same number of random explanatory variables measured over the same number of observation points. The correction formula is the same as for the adjusted coefficient of multiple determination in multiple regression [*Ezekiel*, 1930]. The canonical R^2 can also be computed as the sum of the RDA canonical eigenvalues divided by the total variance in the array of standardized response variables. Due to the adjustment, the sum of the submodels R_a^2 does not equal the R_a^2 of all PCNM variables.

4.4. Results

In the following, results of the RDA performed on the global model using all 180 PCNMs (positive eigenvalues) are discussed and compared to the explained variance obtained using a more traditional trend surface analysis. The RDA and the multiple regression results performed on the four submodels are presented. The spatial decomposition of the explained variance is presented by plotting the "fitted site scores" of each significant RDA canonical axes. The correlations between flow variables for each submodel are discussed using eigenvector scatter plots.

4.4.1. Global PCNM model RDA

The global RDA based on 180 PCNMs explains a significant portion of the variance of the mean and turbulent flow statistics. The adjusted bimultivariate redundancy statistic, R_a^2, is $R_a^2 = 0.58$ with an F-statistic of 3.64 and an associated $p < 0.001$. The significantly large portion of the explained global variance indicates clearly the spatial dependence of the flow field parameters. For comparison purposes, an RDA was performed on the flow variables using a third-order polynomial created from the x-z sampling location coordinates. While the explained variance of the trend surface analysis was much lower ($R_a^2 = 0.34$, $F = 20.5$, $p < 0.01$) than for the PCNM analysis, this technique was still able to demonstrate the presence of a large-scale spatial pattern. Yet further interpretation is limited due to the highly correlated terms which prevent the modeling of independent structures at different scales [*Borcard and Legendre*, 2002].

4.4.2. PCNM submodels RDA

The results of the RDA performed using the four PCNM submodels indicate an unequal partitioning of the global variance between scales: VL, $R_a^2 = 0.17$; L, $R_a^2 = 0.24$; M, $R_a^2 = 0.06$; and F, $R_a^2 = 0.02$. All submodels were significant at $\alpha = 0.01$. The partitioned R_a^2 values indicate that a substantial portion of the variation of the mean and turbulent flow statistics is explained by the models at very-large and large spatial scales; these scales are of the order of $\Delta x = 5.3Z - 2.6Z$ and $\Delta z = 1.0Z - 0.5Z$. The meso- and fine-scale submodels explain much smaller portions of the variation. These results are perhaps related to previous observations indicating that turbulent flow in gravel-bed rivers organizes itself into large depth-scaled coherent structures [*Shvidchenko and Pender*, 2001; *Roy et al.*, 2004] which are surrounded by small-scale isotropic random eddies [*Townsend*, 1976]. Our results suggest that the turbulent flow variables contain a high spatial dependence, while at smaller scales the turbulent flow variables are more randomly distributed. The lack of spatial structure in the finer-scale submodels may also be caused by the poor resolution of finer scales due to the irregular sampling grid and the d_t used. While depth is a more commonly used variable for scaling turbulent coherent structures, the VL- and L- scale spatial scales could also be scaled by roughness element height (h_s) $\Delta x = 10h_s - 5h_s$ and $\Delta z = 2h_s - 1h_s$. The simple relationship between the VL- and L- scales and roughness element height supports previous work by *Kirkbride* [1993] suggesting the dependence of the shedding spatial patterns on bed roughness elements.

4.4.3. PCNM submodel multiple regressions

A multiple regression was conducted on each flow variable in order to isolate the response of individual flow variables by submodel. The unadjusted coefficient of multiple determination (R^2) represents the explained variation of the response variables by the PCNM submodel and provides a global account of the fit of each model. Details about the variance explained by each PCNM submodel, for each individual flow variable, are presented in Figure 4.4. The PCNM analysis summed over all scales explains nearly 80% of the spatial variation in $\overline{U}$, u', w', and $-\rho\overline{u'w'}$, with 75% being explained by the VL- and L-scale submodels. In other words, large-scale flow patterns

are responsible for 75% of the variance in $\overline{U}$, u', w', and $-\rho\overline{u'w'}$. This finding is comparable with *Liu et al.* [2001] who found, through POD, that large-scale motions with length scales, $\Delta x > 1.6Z$ and $\Delta z = 0.3Z - 2Z$, contained 50% of the total turbulent kinetic energy and two-thirds to three-quarters of the Reynolds shear stress at $Re = 5300 - 30\,000$. Their laboratory experiments were conducted on a smoothed wall rectangular channel and demonstrated the similarities of large-scale motions over smooth- and rough-walled flows. The R^2 for $\overline{U}$ is more than twice as large as that of $\overline{W}$. This is perhaps due to the influence of the pebble cluster on the w component velocity which generally has weaker spatial correlations than the u component [*Nakagawa and Nezu*, 1981]. The variance in $\overline{W}$ is explained in approximately equal portions by the VL-, L- and M-scales; indicating an equal superposition of scales within the x-z plane. Slightly more variance is explained for w' than is for u' and similarly more variance is explained for ITS_w than for ITS_u. This is seen in the z-score plots, as well, (Figure 4.2) where the spatial patterns of w' and ITS_w are more regular than those of u' and ITS_u, respectively. While this result is counterintuitive, given the w component's weaker spatial correlations, it indicates that the w component turbulence statistics are influenced in a more spatially uniform manner by the pebble cluster than their u component counterparts.

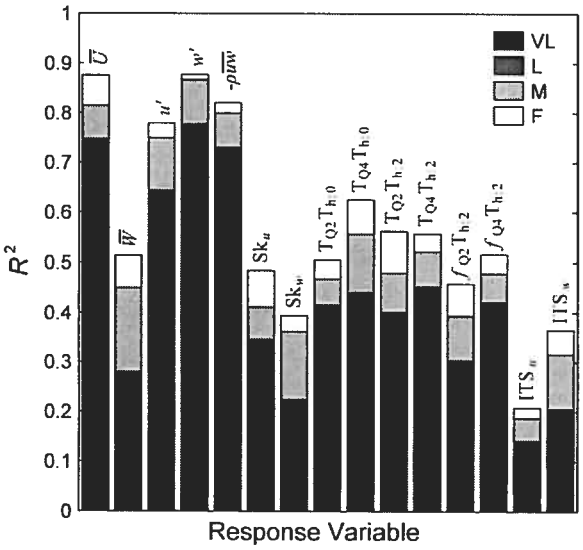

Figure 4.4. Fraction of explained variance (unadjusted coefficient of multiple determination, R^2) for individual mean and turbulent flow variables, for each significant PCNM submodel ($p < 0.05$): very-large (VL), large (L), meso (M) and fine (F) scale.

We expected the meso- and fine-scale submodels to explain a greater percentage of their variability, given that we specifically included turbulence statistics of higher moments (i.e. Sk_u) and of more localized variability (ITS_u) in our flow parameter data set. The R^2 values for the M- and F-scale submodels are inconsistently distributed between these turbulence variables, and do not explain as much of the variability as the larger-scale submodels. It is possible that the resolution of the F-scale PCNMs was too coarse to pick up the fine-scale details where structures had periods too short to be represented. The higher minimum truncation distance and irregular sampling grid may have resulted in the distortion of the finer-scale PCNM variables resulting in a loss of fine-scale resolution.

4.4.4. Spatial decomposition and intercorrelation of PCNM submodel flow variables

Using the multivariate analysis of all flow variables, we mapped the "fitted site scores" of each significant canonical axis for the four submodels investigated (Figure 4.5). All canonical axes presented are significant at $\alpha = 0.01$ with the exception of the M-scale canonical axis 2 which is significant at $\alpha = 0.05$. These maps provide a spatial decomposition of the explained variance for each axis and allow for the perception of spatial patterns within the data. The R_i^2 bar graphs included on the right-hand side of Figure 4.5 indicate the unadjusted fraction of variance explained for each response variable. Since the canonical axes are orthogonal, the fractions of variation they express (R_i^2, where i is the canonical axis index) are linearly independent of one another. Table 4.3 provides a summary of the unadjusted R_i^2 values for each flow variable expressed by the significant canonical axes of each submodel. The unadjusted coefficients of multiple determination, R^2, obtained from all 29 significant PCNMs are, as well, included in the far right hand column of Table 4.3.

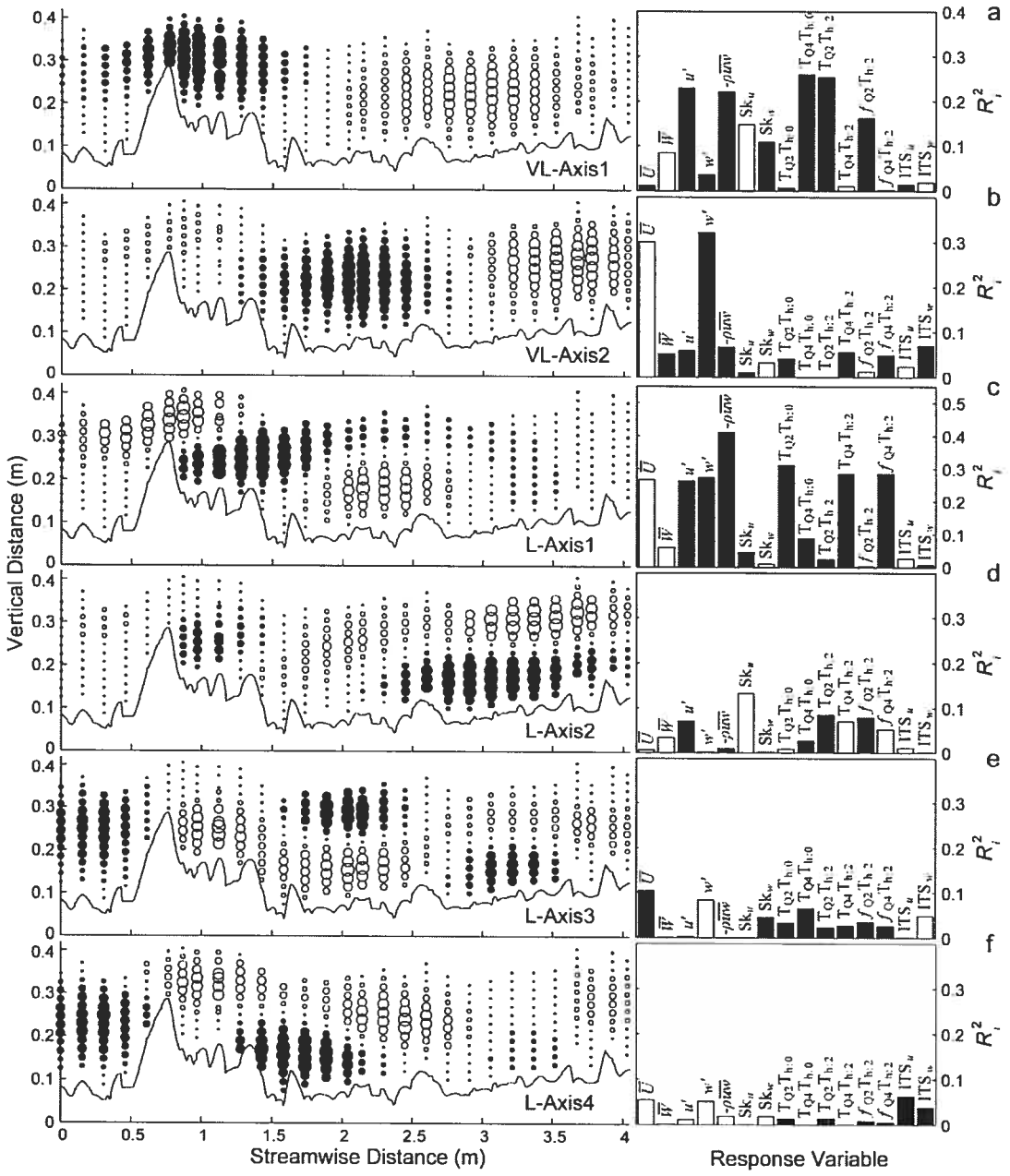

(**Figure 4.5.** see facing next page for caption)

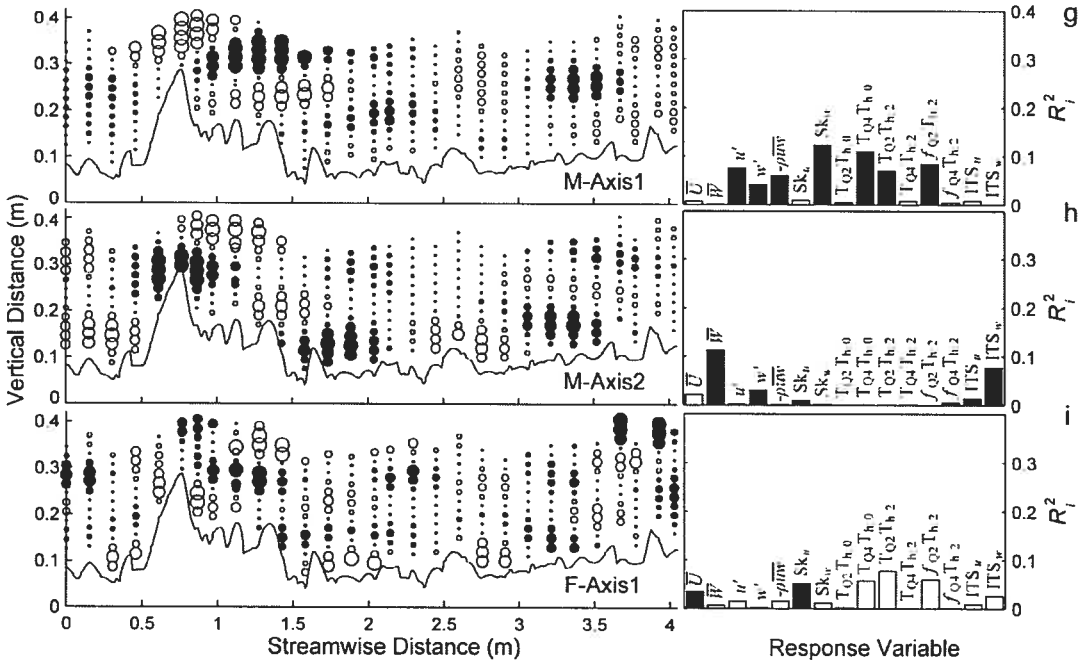

Figure 4.5. Significant canonical axes of the "fitted site scores" ($p < 0.05$) plotted on the sampling location coordinates. a) VL-axis1; b) VL-axis2; c) L-axis1; d) L-axis2; e) L-axis3; f) L-axis4 g) M-axis1; h) M-axis2; i) F-axis1. Positive values are represented by filled bubbles. The right-hand bar graphs present the fraction of variance for each flow variable explained by the canonical axes (empty = negative correlations, filled = positive). Flow is from left to right.

4.4.4.1. Very-large-scale submodel

The "fitted site score" plots of the VL-scale submodel, Figure 4.5a and b, display a depth-scale spatial pattern of $\Delta x = 5.3Z$ and $\Delta z = 1.0Z$ within the turbulent flow variables. These scales are strikingly similar to the large-scale flow structures found in previous studies [*Shvidchenko and Pender*, 2001; *Roy et al.*, 2004]. Values of u', $-\rho\overline{uw}$, Sk_u, Sk_w, $T_{Q4}T_{h:0}$, $T_{Q2}T_{h:2}$, and $f_{Q2}T_{h:2}$ are strongly expressed by the first canonical axis (Figure 4.5a) while $\overline{U}$ and w' are strongly expressed by the second canonical axis (Figure 4.5b). The first canonical axis indicates that high values of u', $-\rho\overline{uw}$, Sk_w, $T_{Q4}T_{h:0}$, $T_{Q2}T_{h:2}$, and $f_{Q2}T_{h:2}$ and low magnitude Sk_u occur in a large region above and adjacent to the cluster between $x = 0.35$ m and 1.5 m; the inverse trend occurs farther downstream between $x = 2.1$ m and 3.7 m. The second canonical axis reveals a zone of low $\overline{U}$ and high w' between $x = 1.3$ m and 2.6 m. Farther downstream between $x = 2.6$ m and 4.0 m, this trend is reversed. Differences between u' and w' indicate that u'

is of greater magnitude near the pebble cluster, while w' is larger farther downstream. The elevated $f_{Q2}T_{h:2}$, positive Sk_w and negative Sk_u in the near-wake are an indication of ejecting structures, while downstream, the reverse skewness trend indicates high-speed sweeps in the $x = 2.1$ m to 3.7 m range.

Table 4.3. Estimated fractions of unadjusted variance (R_i^2) of flow variables expressed by significant canonical axes (Only significant canonical axes of each submodel are presented). The bottom row presents the unadjusted canonical eigenvalues (λ_i) of each significant axis (λ_i are estimated as the mean R_i^2 value for all 15 response variables); and the far right column presents the unadjusted coefficients of multiple determination (R^2) using all 29 significant PCNMs. Monte Carlo significance test (999 unrestricted permutations).

	VL		L				M		F	All Scales
	R_1^2	R_2^2	R_1^2	R_2^2	R_3^2	R_4^2	R_1^2	R_2^2	R_1^2	R^2
$\overline{U}$	0.01	0.30	0.27	0.01	0.10	0.05	0.01	0.02	0.03	0.88
$\overline{W}$	0.08	0.05	0.06	0.03	0.00	0.00	0.00	0.11	0.01	0.51
u'	0.23	0.06	0.26	0.07	0.00	0.01	0.08	0.00	0.02	0.78
w'	0.04	0.32	0.27	0.00	0.08	0.05	0.04	0.03	0.00	0.88
$-\rho\overline{uw}$	0.22	0.07	0.41	0.01	0.00	0.02	0.06	0.00	0.02	0.82
Sk_u	0.15	0.01	0.04	0.13	0.00	0.00	0.01	0.01	0.05	0.48
Sk_w	0.11	0.03	0.01	0.00	0.04	0.02	0.12	0.00	0.01	0.39
$T_{Q2}T_{h:0}$	0.01	0.04	0.31	0.01	0.03	0.01	0.00	0.00	0.00	0.51
$T_{Q4}T_{h:0}$	0.26	0.00	0.09	0.03	0.07	0.00	0.11	0.00	0.06	0.63
$T_{Q2}T_{h:2}$	0.25	0.00	0.02	0.09	0.02	0.01	0.07	0.00	0.08	0.56
$T_{Q4}T_{h:2}$	0.01	0.05	0.29	0.07	0.03	0.00	0.01	0.00	0.00	0.56
$f_{Q2}T_{h:2}$	0.16	0.01	0.00	0.08	0.03	0.01	0.08	0.00	0.06	0.46
$f_{Q4}T_{h:2}$	0.00	0.05	0.28	0.05	0.03	0.01	0.00	0.01	0.00	0.52
ITS_u	0.01	0.02	0.03	0.01	0.00	0.06	0.01	0.01	0.01	0.21
ITS_w	0.02	0.07	0.01	0.00	0.05	0.04	0.00	0.08	0.03	0.36
Canonical Eigenvalue	0.10**	0.07**	0.16**	0.04**	0.03**	0.02**	0.04**	0.02*	0.02**	

* $p \leq 0.05$, ** $p \leq 0.01$

The eigenvectors for the VL-scale (Figure 4.6a) reveal high correlation between u' and $-\rho\overline{uw}$, and $T_{Q4}T_{h:0}$ and $T_{Q2}T_{h:2}$. $\overline{U}$ is negatively correlated with $\overline{W}$, and displays a near zero correlation with u' and $-\rho\overline{uw}$. The inhomogeneous bed and the turbulence generated in the recirculation and shedding zones in the near-wake of the pebble cluster [*Buffin-Bélanger and Roy*, 1998] are likely responsible for disrupting the large-scale spatial correlation between $\overline{U}$ and u'.

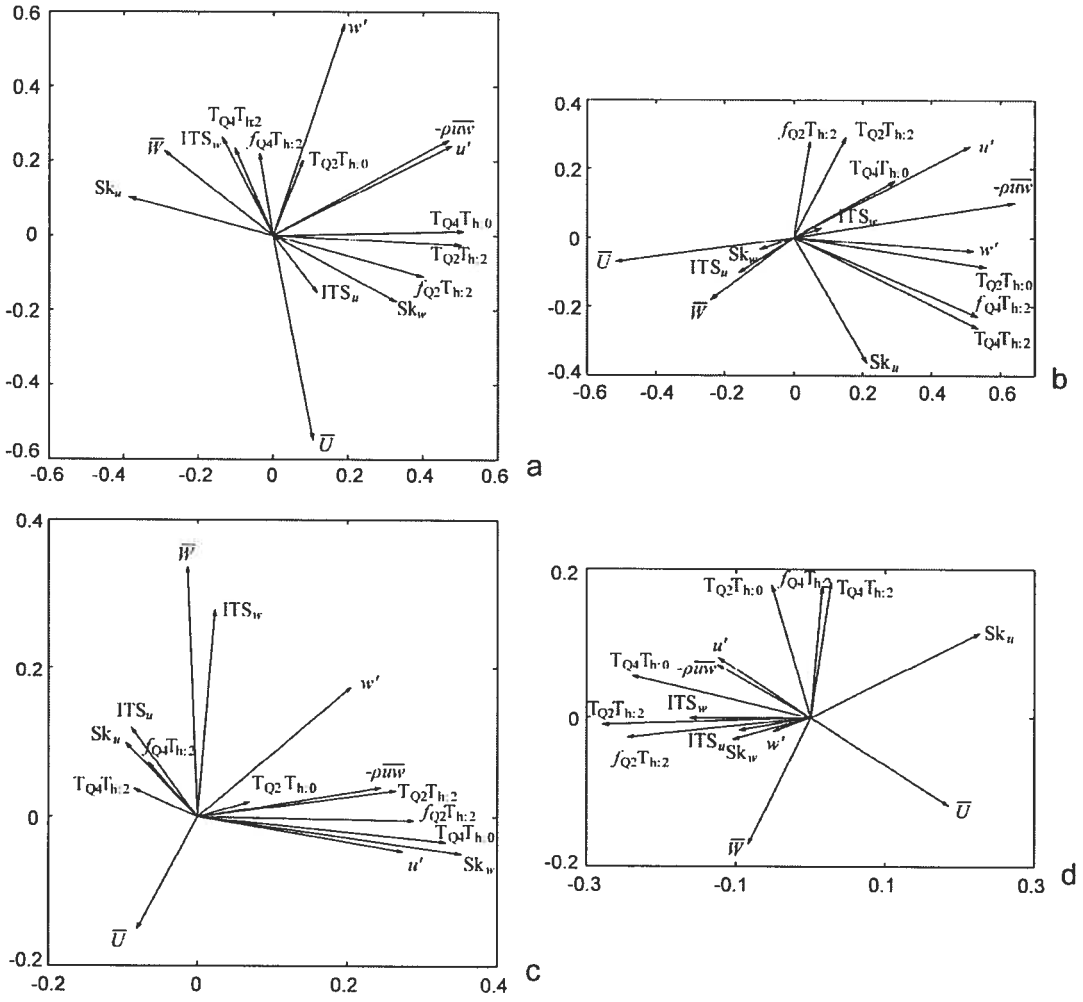

Figure 4.6. Eigenvector scatter plots. Canonical axis 1 is the abscissa while canonical axis 2 is the ordinate. a) VL-scale b) L-scale c) M-scale d) F-scale.

4.4.4.2. Large-scale submodel

The large-scale PCNM submodel explains the greatest fraction of the variance in the flow data. The physical scale of this submodel $\Delta x = 2.6Z$ and $\Delta z = 0.5Z$ is still within the range of sizes described as large-scale structures in previous studies [*Liu et al.*, 2001; *Nakagawa and Nezu*, 1981]. Most of the explained variance is expressed by the first canonical axis ($R_1^2 = 0.16$). The fraction of R_1^2 expressed by individual flow variables (Figure 4.5) differs slightly from the VL-scale submodel. $\overline{U}$, u', w', $-\rho\overline{uw}$, $T_{Q2}T_{h:0}$, $T_{Q4}T_{h:2}$, and $f_{Q4}T_{h:2}$ are strongly expressed by the first axis. Sk_u and $\overline{U}$ are strongly

expressed by the second (R_2^2 = 0.13) and the third (R_3^2 = 0.1) canonical axes, respectively. The PCNMs of the L-scale submodel vertically discriminate scales of 0.5*Z*, and as such, are better able to distinguish spatial patterns which bisect the water column. Conversely, the VL-scale submodel was restricted to investigating depth-scale structures ($\Delta z = 1.0Z$).

The maps of the "fitted site scores" of the first canonical axis (Figure 4.5c) show zones of increased magnitude $\overline{U}$ and positive $\overline{W}$ overtop (stoss side) of the pebble cluster and in the far-wake (x = 0.7 m – 2.8 m). In the upstream zone, the flow constriction induced by the pebble cluster causes a suppression of the turbulence statistics as flow is forced overtop of the cluster [*Buffin-Bélanger and Roy*, 1998]. The far-wake is characterized by fluid upwelling [*Buffin-Bélanger and Roy*, 1998]. These characteristic zones were discussed by *Buffin-Bélanger and Roy* [1998], and through the current analysis, are related to large-scale turbulent flow structures. Between these two zones lies the near-wake region (x = 0.8 m to 2.2 m) which consists of a recirculation and eddy shedding zone [*Buffin-Bélanger and Roy*, 1998]. The recirculation zone is found here to be characterized by large-scale patterns of low magnitude $\overline{U}$, high magnitude u', w', $-\rho\overline{u'w'}$, and a dominance of smaller magnitude ejections ($T_{Q2}T_{h\cdot0}$) and high magnitude sweeps ($T_{Q4}T_{h\cdot2}$). The PCNM technique was able to clearly show the division (shearing) caused by the shedding/recirculation zone and the overlying fluid. The shear layer is initiated at the crest of the pebble cluster and is inclined towards the water surface. The second axis (Figure 4.5d) explains much of the variance in the distal downstream portion of the *x*-*z* transect, where high magnitude Sk_u occurs in the upper water column, indicating infrequent events of accelerated fluid which coincide with the high magnitude sweeps (Q4 events) also indicated by the analysis. The trend is reversed closer to the bed in the distal zone. Canonical axis 3 indicates elevated $\overline{U}$ upstream of the cluster and higher in the water column, and all variables are only weakly explained by canonical axis 4. The between variable correlations (Figure 4.6b) are similar to those discussed for the VL-scale. While the VL-scale plot indicates a much higher correlation between u' and $-\rho\overline{u'w'}$ than between w and $-\rho\overline{u'w'}$, the L-scale plot shows a near equal correlation between u'/ w' and $-\rho\overline{u'w'}$.

4.4.4.3. Meso-scale submodel

The PCNMs of the meso-scale submodel have multiple periods over the *x-z* transect plane in the longitudinal and vertical directions, producing a "checker board" pattern. The variance explained by this scale is between $\Delta x = 1.6Z$ and $\Delta z = 0.3Z$. The R_t^2 expressed by individual flow variables is much smaller than for the two larger scales; only two variables, Sk_w and $T_{Q4}T_{h:0}$, are moderately expressed (Figure 4.5g). The shedding/recirculation zone identified at the larger scales is further subdivided into two distinct zones. The overlying shedding zone with elevated meso-scale turbulence statistics (positive Sk_w and elevated $T_{Q4}T_{h:0}$) initiates at the tip of the pebble cluster, while the recirculation zone below is characterized by decreased turbulence statistics at the meso-scale. The second canonical axis explains pockets of elevated $\overline{W}$ and ITS_w directly above the pebble cluster (Figure 4.5h). These two variables are also highly correlated at the meso-scale, as shown by the eigenvector plot (Figure 4.6c). The plot also indicates a tighter grouping of turbulence statistics than for the two larger scales, where u', Sk_w, $-\rho\overline{uw}$, $T_{Q2}T_{h:2}$, $T_{Q4}T_{h:0}$, and $f_{Q2}T_{h:2}$ are closely correlated.

4.4.4.4. Fine-scale submodel

All flow response variables are weakly expressed at the F-scale (Figure 4.5i), perhaps indicating that the resolution of the F-scale PCNMs (constrained by the selected d_t) is too coarse to pick up the fine-scale details. The larger residual variance in the higher moment and more localized turbulence statistics supports this point. The pattern of scatter in the plotted "fitted site scores" for the F-scale submodel (Figure 4.5i), which we include for completeness, is difficult to interpret. The effects of the irregular sampling grid preferentially distort the smaller scale PCNMs and could be a factor for the apparent random patchiness. On the other hand, the random patchiness observed, may have a physical basis in terms of turbulence theory, where, at small-scales, turbulent motion tends towards local isotropy [*Townsend*, 1976]. The apparent randomly scattered values of Figure 4.5i may represent fine-scale random autocorrelation between neighbouring sampling locations.

4.5. Discussion

Herein, the PCNM method provides a powerful means of describing multivariate spatial patterns within the turbulent flow data. The turbulent flow field over very rough boundaries appears to be well organized at a range of scales identified and quantified by the PCNM analysis. The technique was able to decompose and summarize the complex interrelations of the flow variables over a range of scales. The explanation of 75% of the variation in the standard turbulent parameters u', w', and $-\rho\overline{u'w'}$ by spatial descriptors of $\Delta x = 5.3Z - 2.6Z$ and $\Delta z = 1.0Z - 0.5Z$ indicates that the turbulent energy and shear stress form consistent, large-scale spatial patterns under the influence of a pebble cluster. The relative importance of the large-scale modes is consistent with previous smooth-walled POD studies [*Liu et al.*, 2001], and highlights the similarities between smooth- and rough-walled flows. Previous studies comparing smooth and rough-wall boundary layers have shown that in the outer boundary layer, $z/Z > 0.2$, turbulent intensities and macro-length scales are weakly affected by roughness size [*Grass*, 1971; *Nezu and Nakagawa*, 1993]. Both smooth and rough boundary layers produce sweep and ejection events, irrespective of the surface roughness, even though their generation mechanisms close to the bed are different (as no viscous sublayer is present in rough boundary layers) and it has been found that both types of boundary layers are scaled by roughness size [*Grass and Mansour-Tehrani*, 1996; *Smith*, 1996]. Large-scale coherent structures are a common feature of turbulent flows [*Shvidchenko and Pender*, 2001; *Roy et al.*, 2004], and have been found to be little affected by the shedding vortices of large roughness elements [*Lacey and Roy*, 2007a].

The large-scale patterns observed in our study are determined from the spatial distribution of time-averaged flow parameters, and as such, are not equivalent to the depth-scale, time-dependent, coherent flow structures reported in previous studies based on the analysis of turbulent events [*Shvidchenko and Pender*, 2001; *Roy et al.*, 2004]. Yet the similar scaling suggests that flow depth is the limiting scale for both the spatial patterns of turbulent properties and the large-scale coherent turbulent structures. The dependence of the spatial patterns of the flow parameters on the heterogeneous bed is implied by the simple relationship of the VL- and L-scale PCNM submodels with pebble cluster height ($\Delta x = 10h_s - 5h_s$ and $\Delta z = 2h_s - 1.0h_s$). The longitudinal spatial extent of

the L-scale submodel is equal to the distance estimated in experiments by *Best and Brayshaw* [1985] from their roughness element to the reattachment point. The high level of explanation of the variance in the flow variables at the L-scale is perhaps due to the clear distinction between patterns occurring within and outside of the pebble cluster wake zone. The direct cluster height scaling supports the view that the general flow structure can be linked to the spatial distribution of roughness elements on the river bed [*Clifford et al.*, 1992].

The observations made from the "fitted site scores" regarding the spatial differences between u' and w', and the inverse relationship between Sk_w and Sk_u, were similarly interpreted by *Buffin-Bélanger and Roy* [1998] and can be seen to some degree in the z-score turbulent flow plots (Figure 4.2c, d, f and g). *Buffin-Bélanger and Roy* [1998] gave general descriptions of the turbulent flow variable spatial patterns, but were unable to give scale-dependent, quantitative results. Through PCNM analysis, we are able to estimate the proportion of variances (R_1^2) associated with each flow variable at each spatial scale. The L-scale PCNM submodel clearly shows the division caused by the shedding/recirculation zone and the overlying fluid, and the M-scale PCNM submodel provides further detail on the shedding/shear layer. While similar spatial patterns were observed by *Buffin-Bélanger and Roy* [1998], PCNM analysis quantifies and efficiently summarizes the dependent turbulent parameters associated with these spatial patterns (i.e. high u', w', $-\rho\overline{uw}$, $T_{Q2}T_{h:0}$, $T_{Q4}T_{h:2}$, and $f_{Q4}T_{h:2}$ at the L-scale (Figure 4.5c), and high Sk_w and $T_{Q4}T_{h:0}$ at the M-scale (Figure 4.5g)).

Plotting the "fitted site scores" is an advantage of this multivariate analysis, because it provides an effective means of summarizing the numerous flow variables into a single plot (at each scale), as well as, providing a means of determining which variables are strongly or weakly expressed. Large-scale spatial patterns of the strongly expressed variables can be readily identified from the "fitted site scores" plots. These large-scale patterns are, in some instances, difficult to distinguish on the z-score plots (Figure 4.2) due to the superposition of smaller-scale turbulent patterns. An additional advantage of the PCNM technique is that correlations between flow variables at each scale can be investigated through eigenvector scatter plots (Figure 4.6). These correlations are related to the entire study area and do not differentiate between different

flow regions (i.e. upstream and downstream of the cluster), yet still give valuable information on the relationships between flow variables over different scales. For example, the VL-scale submodel revealed high correlation between u' and $-\rho\overline{u'w'}$, while the L-scale and M-scale submodels estimated similar correlations between u' and $-\rho\overline{u'w'}$, and w' and $-\rho\overline{u'w'}$. While correlations do not indicate a causal link, these results do indicate that, at the largest scales, the Reynolds shear stress and the u component turbulent energy show a much stronger interdependence than for the w component.

The main drawback with the PCNM method is the dependence of the PCNM variables on the uniformity of the sampling grid (i.e., the greater the inconsistency within the sampling grid, the greater the loss of fine-scale structure explanation). When large inconsistencies are present in the sampling grid, the PCNMs are still orthogonal and properly describe the sampling space; yet, instead of containing regular sinusoidal waves, individual PCNMs are composed of sinusoidal waves of multiple scales [*Borcard et al.,* 2004]. This makes it difficult to partition the PCNMs into different scales. In our study, a larger truncation distance was selected to avoid PCNM inconsistencies, and as a result, the explanation of fine-scale variability was limited. The more localized, higher moment and event statistics were much less explained (higher residual variation) than the larger-scale core turbulence statistics. Understanding this constraint will help us design future studies.

The PCNM technique illustrated here, using the characterization of the turbulent flow field, is a powerful statistical tool with a much broader application in fluvial geomorphology. Considering the recent interest in reach-scale, spatial attributes and patterns [*Emery et al.*, 2003; *Clifford et al.*, 2005], PCNM analysis could provide a new way of looking at the ecological and physical environmental variables on a scale basis. For instance, research investigating the spatial scales and patterns over which physical habitat units and ecological (biotic) units interact, could profit from the use of PCNM analysis. Proposed hierarchical models group physical habitat units such as "river styles" [*Thomson et al.,* 2001] and "physical biotopes" [*Newson and Newson*, 2000] at different scales. These classifications, such as the "river styles" geomorphic channel classification system [*Thomson et al.,* 2001], can be quite cumbersome due to the number of

parameters required to place rivers into the correct unit at each scale. Physical units or flow parameters, which are relevant at one scale, are not necessarily important to biota at other scales. Hierarchical cluster analysis has been used as a spatial statistical tool to define physical units, yet lacks the differentiation of patterns between scales [*Emery et al.*, 2003]. PCNM analysis is a much more powerful technique to provide spatially explicit and scale dependent relationships between flow variables and aquatic species data. These scale-dependent (hierarchical) spatial patterns could be used to determine the habitat units important for geomorphologists and ecologists. Similarly to *Clifford et al.*, [2005], conducting PCNM analysis on the high resolution velocity and depth data estimated by a hydrodynamic model would provide a powerful appraisal tool for river rehabilitation projects.

4.6. Conclusions

PCNM analysis successively partitioned the variance (according to characteristic spatial scales) associated with the mean and turbulent flow variables calculated from instantaneous velocities measured over an *in situ* turbulent flow field in the presence of a pebble cluster in a gravel-bed river. The variation was partitioned over four spatial scales: very-large, large, meso and fine. The full model significantly explained 58% of the variance in the data (R_a^2), while the submodels VL, L, M, and F explained significant ($\alpha = 0.01$) portions of the variance (17%, 24%, 6%, and 2%, respectively). The PCNM analysis was able to demonstrate a high spatial dependence within the flow variables and to quantify the dominant spatial scales and patterns of the core turbulence variables in the mean and turbulent flow data. The VL- and L-scales explained 75% of the variance of the main turbulent flow indicators u', w', and $-\rho\overline{u'w'}$. The L-scale submodel explained the largest percentage of the variance throughout most of the flow variables. Our results suggest that flow depth and roughness element height are appropriate scales for the time-averaged spatial patterns which were observed.

The usefulness of the PCNM statistical technique is that it quantifies the spatial dependence of individual response variables over a user-defined range of spatial scales. The method provides a spectral decomposition for spatially irregular sampling locations which is much more powerful than currently-used methods of quantifying spatial

structure (i.e. trend surface analysis). In our study, the mapped "fitted site scores" of the PCNM submodels not only provided similar information to the z-score flow parameter plots, but also allowed for the quantification of the explained variance and for the identification of scale differences within the flow variables. PCNM analysis by canonical RDA was able to summarize the core spatially dependent variables in only a few plots, allowing for a rapid analysis and quantification of spatial patterns. The intercorrelations among individual response variables at each spatial scale are illustrated through eigenvector scatter plots. This allows researchers to refine their analysis and to examine in detail the structure of the data. This is a considerable advantage over the practice often followed in analyses of spatial structures in hydrodynamics, where plots of each flow variable are investigated in turn. The PCNM technique is a powerful tool to understand the spatial relations among complicated sets of variables. The present application to turbulent flow dynamics around a pebble cluster, a problem of great complexity, illustrates the power of the method and its potential for a broad range of applications in water resources and the earth sciences.

Linking Paragraph B

The previous chapter shows that the time-averaged turbulence variables overtop and downstream of a LRE are well structured over large spatial scales: $\Delta x = 2.6Z - 5.3Z$ and $\Delta z = 0.5Z - 1.0Z$ or alternatively $\Delta x = 5h_s - 10h_s$ and $\Delta z = 1.0h_s - 2h_s$. More specifically, the majority of the explained variation in u', w', and $-\rho\overline{u'w'}$ is by $\Delta x = 5h_s$ and $\Delta z = 1.0h_s$ spatial scales. These results pertain to the spatial patterns of turbulence for a 2D vertical plane crossing over the centerline of a LRE, yet due to the experimental set-up the lateral hydrodynamic effect of the LRE could not be addressed. The next thesis chapter[2] provides complementary results on the spatial distribution and patterns of turbulence by measuring 3D instantaneous velocities over two horizontal planes with and without a LRE present. The 3D processes and spatial patterns of the turbulent flow around a naturally formed *in situ* pebble cluster are specifically addressed as well as the effect of the pebble cluster on LS coherent flow structures. Instantaneous high frequency velocities were measured using the simultaneous deployment of four acoustic Doppler velocimeters, with the pebble cluster and after the cluster was removed. Results indicate a slight (10%) increase in turbulent kinetic energy over the sampling area when the pebble cluster is present. Individual velocity spectra in the wake of the pebble cluster differ greatly from those when the cluster is removed. The vertical velocity spectra contain a marked peak which decreases in frequency from 1.8 Hz near the cluster to 1.0 Hz further downstream. This peak is associated with eddies shedding from the shear layer in the lee of the cluster and it agrees well with the values estimated using U-level event analysis and those estimated using a Strouhal number of 0.18. Space-time correlations indicate the presence of coherent depth-scale macroturbulent flow structures. These structures in the intermediate flow region are relatively unaffected by eddies shedding from the pebble cluster. The results suggest the effects of the pebble cluster on the surrounding flow dynamics are quite localised and limited to the near-bed region.

---

[2] Lacey, R.W.J., and A.G. Roy (2007a) A comparative study of the turbulent flow field with and without a pebble cluster in a gravel-bed river, *Water Resources Research*, *43*, W05502, doi:10.1029/2006WR005027 (reprinted with permission from AGU).

5. A COMPARATIVE STUDY OF THE TURBULENT FLOW FIELD WITH AND WITHOUT A PEBBLE CLUSTER IN A GRAVEL-BED RIVER

5.1. Background

Large-scale coherent flow structures appear to be ubiquitous in poorly sorted gravel-bed rivers [*Kirkbride and Ferguson*, 1995; *Roy et al.*, 1996; *Roy et al.*, 2004]. These structures consist of depth scaled intermittent fronts of high-speed fluid which are mainly directed towards the bed and of low-speed fluid that predominantly move towards the free surface. The origin of these structures is not fully understood. It is likely that they originate at the inner layer of the bed as hairpin vortices and expand upward coalescing into larger and larger structures [*Kline et al.*, 1967; *Perry et al.*, 1986; *Yalin*, 1992; *Nezu and Nakagawa*, 1993; *Smith*, 1996]. These macro-structures exist under highly variable bed roughness conditions from smooth wall laboratory studies [*Falco*, 1991] to very rough wall gravel-bed river studies [*Buffin-Bélanger et al.*, 2000; *Roy et al.*, 2004]. Recent visualization studies by *Shvidchenko and Pender* [2001] have related high- and low-speed wedges to depth-scale eddies advecting downstream at the bulk flow velocity. These depth-scale vortical movements (downward and upward vorticity) were responsible for generating alternating high- and low-speed zones and play a critical role in the mechanism of the open-channel turbulence and bed particle transport.

Macro-scale coherent flow structures advect overtop of large bed roughness elements such as pebble clusters which themselves have been found to shed meso-scale structures [*Best and Brayshaw* 1985; *Acarlar and Smith*, 1987] that scale with the roughness element height near the point of shedding [*Duncan*, 1970]. Common shedding features include: the positioning of a standing hairpin vortex initiating upstream, with flanking rotating legs trailing downstream, and an intermittent shedding wake vortex caused by a leeside separation shear zone [*Best*, 1996]. These shedding properties have yet to be characterised *in situ*. Roughness elements such as pebble clusters form naturally in gravel-bed rivers and constitute the most frequent microtopography present in poorly sorted gravel-bed rivers [*Brayshaw*, 1984]. It has been suggested that their spatial arrangement maximizes flow resistance [*Hassan and Reid*, 1990] and is

determined by their turbulent wake dynamics [*Clifford et al.*, 1992]. Boulder clusters have been found to play a significant role for fish habitat [*Van Zyll de Jong et al.*, 1997].

Previous studies of the interactions between macro-turbulent flow structures and pebble clusters are based on two-dimensional (2D) high resolution velocity measurements and flow visualisation [*Buffin-Bélanger and Roy*, 1998]. These studies suggest a feedback mechanism in which the meso-structures shed from pebble clusters are affected by the passage of high- and low-speed wedges [*Buffin-Bélanger and Roy*, 1998; *Buffin-Bélanger et al.*, 2001a]. The shedding motion seems to expand vertically as a low-speed wedge flows over top of the cluster and it is suppressed during the passage of a high-speed wedge. The question remains, however, if the turbulent flow structure in a gravel-bed river is much affected by the presence of pebble clusters. In order to determine the relative importance of roughness elements on flow hydraulics from both a physical and a biological point of view, it is necessary to understand the three-dimensional (3D) interaction between large-scale flow structures and meso-scale structures shed from roughness elements.

This study examines the detailed *in situ* 3D turbulent flow processes around a pebble cluster and the interactions between macro- and meso-scale turbulent coherent flow structures in a gravel-bed river. The experiment was conducted with and without the presence of an isolated, naturally formed, pebble cluster. We focused on the characterization of physical processes associated with a single, submerged roughness element in order to isolate its effects on the turbulent flow field. While the specific turbulence statistics are dependent on the roughness element geometry selected, the *in situ* physical processes investigated such as the shedding structures from the shear layer and their interaction with macro-scale structures can be generalized to other situations where shear flow occurs overtop of roughness elements.

The approach of the study rests on the use of spectral analysis and space-time correlations between velocity fluctuations measured simultaneously at various points in the flow. Space-time correlation (STC) analysis has proven very useful in characterising the scales and shapes of turbulent flow structures in laboratory settings [*Grant*, 1958; *Nakagawa and Nezu*, 1981; *Kadota and Nezu*, 1999], in gravel-bed rivers [*Roy et al.*, 1996; *Roy et al.*, 2004] and at channel confluences [*Rhoads and Sukhodolov*, 2004]. The

analysis relies on the assumption that a strong correlation between simultaneous velocity time series measured at different locations is indicative of coherence within the flow. Analysis of the simultaneous spatial and temporal variability within the velocity field allows us to characterise the time-averaged behaviour and flow patterns of the turbulent coherent structures as they advect past the pebble cluster. The analysis of spatial patterns of the turbulent flow field around naturally occurring large roughness elements such as boulders and pebble clusters in rivers has been the focus of only a few studies [*Buffin-Bélanger and Roy*, 1998; *Tritico and Hotchkiss*, 2005].

5.2. Field Measurements

The study site is located on the Eaton North River in the Eastern Townships, Quebec, Canada (Figure 5.1a). The bankfull width at the sampling location is approximately 28 m while the wetted width at the time of sampling was 16 m. The Eaton North is a gravel-bed river with a D_{50} = 0.035 m. Several large clast sediments (> 0.20 m) are scattered sporadically throughout the reach some of which form the keystones of pebble clusters [*Buffin-Bélanger and Roy*, 1998; *Lamarre and Roy*, 2001]. An aluminium square frame with dimensions 1.5 m x 1.5 m (designed specifically to support four SonTek acoustic Doppler velocimeters (ADVs)) was positioned overtop of a naturally occurring isolated pebble cluster (Figure 5.1b and Figure 5.1c). The upstream side of the frame was perpendicular to the longitudinal flow direction and was positioned approximately 0.20 m upstream of the pebble cluster. Care was taken to level the frame and to insure that it was aligned with flow using tracer ribbons. This method proved insufficient, however, as the frame was slightly misaligned with flow streamlines and a rotation of the velocity measurements was necessary. The mean water depth (Z) within the sampling area was 0.35 m. The pebble cluster consisted of six imbricated stones (Figure 5.1c) with a maximum protrusion (h_s) of 0.1 m, resulting in a relative roughness of h_s/Z = 0.3. Five smaller cobbles (D_{50} = 0.08 m) were imbricated on the stoss side of the cluster with course sand in the lee - recirculation zone. The size and relative roughness of the pebble cluster is typical of the many submerged isolated cobbles and boulders present in our study reach and is approximately the same width and half the height of a pebble cluster investigated by *Buffin-Bélanger and Roy* [1998] on the Eaton North River. The

dimensions of the keystone (obstacle clast) once removed were 0.33 m, 0.18 m, and 0.07 m for the A, B and C orthogonal axes, respectively. The bed topography (with cluster) was measured in detail using a Trimble series 5000 total station and the bed was photographed underwater with a Nikon Coolpics digital underwater camera which has a resolution of 5.0 megapixels and a focal length of 28 mm. The photographs provided information on the spatial arrangement of bed particles and their relative size within the study area. All large cobbles and boulders (< 3.0 m upstream of the site) which protruded noticeably into the flow were removed prior to the experiments in order to assure that upstream flow conditions would not influence the experimental site.

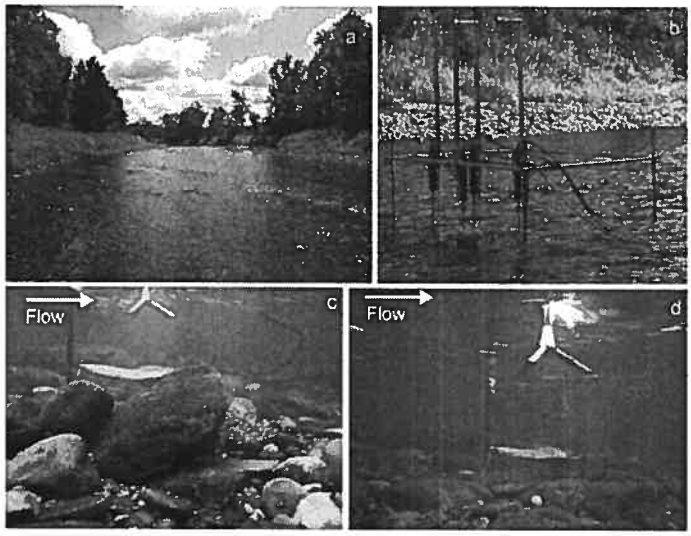

Figure 5.1. a) Upstream view of the Eaton North River; b) Aluminium support frame with 4 ADVs (flow is from left to right); c) Side view of pebble cluster; d) Same view as in (c) after the pebble cluster has been removed.

The 3D instantaneous longitudinal (U), lateral (V), and vertical (W) velocities were measured using the simultaneous deployment of four ADVs over a two day period. The river stage dropped by 0.015 m (4.3%) over the two days. Measurements were made with the cluster (Figure 5.1c) and after the pebble cluster was removed (Figure 5.1d). Figure 5.2 presents a schematic of the support frame and sampling locations. The upstream probe was kept stationary throughout both sets of measurements, while the three downstream roving probes were shifted along the frame to specific grid locations. Velocities were sampled over two horizontal planes at a lower relative height of z/Z = 0.2 and an upper relative height of z/Z = 0.4. These heights were selected so as to

characterise the inner and intermediate flow regions and to insure the hydrodynamic effects of the pebble cluster would be properly represented. Three series of measurements were required to cover 71 points in each plane. During the first series, the three roving probes were laterally separated by 0.17 m and were shifted downstream sequentially as indicated in Figure 5.2. The lateral separation distance between the roving probes was increased to 0.27 m and 0.47 m, for the second and third series respectively. We were restricted, in this study, to sample at a frequency of 12 Hz due to the maximum data transfer capability of the system. Instantaneous velocities were measured for 3.5 minutes resulting in 2500 measurements per time series. This record length was slightly more conservative than the optimal time series length suggested by *Buffin-Bélanger and Roy* [2005].

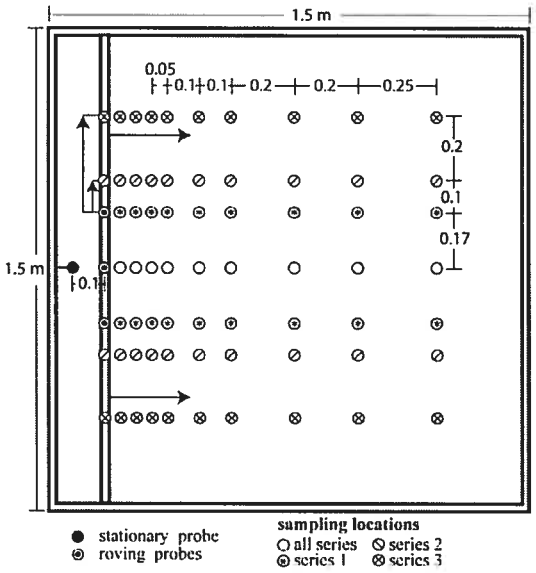

Figure 5.2. Plan view of the frame and of the sampling locations. The sampling strategy of the velocity fluctuation measurements used four ADVs simultaneously. It consisted of three series of measurements at two different sampling planes at relative heights of z/Z = 0.2 and z/Z = 0.4 respectively. A probe remained stationary at the front of the cluster during all three series at a given height above the bed while the three other probes were located systematically further downstream. All indicated distances on the diagram are in metres. Flow is from left to right.

5.3. Data Treatment and Analysis

Velocity time series were visually inspected for obvious abnormalities. Following the suggestion of the ADV manufacturer and *Lane et al.* [1998], entire velocity series with

time averaged signal correlations below 70% were removed from further analysis. The ADV signal correlation is a quality control parameter which indicates the spectral width between dual pulse-pair velocity estimates. In this study, the signal correlation was found to decrease primarily as a result of three reasons: low seeding due to the clear water of the river; interference between adjacent ADVs when the separation distance was less than 0.2 m; and excessive bottom echo noise arising from the pulse signals rebounding off the heterogeneous gravel bed. Spectral analysis was used as a secondary means of detecting noise in the velocity signals. The slope of the power spectra within the inertial subrange was compared to the Kolmogorov -5/3 law. Noisy signals which exhibited a generally flat slope were removed from further analysis. This screening process resulted in the rejection of 12% of the measured time series.

Individual low signal correlations associated with large spikes in the velocity series were detected using the phase-space thresholding filter [*Goring and Nikora*, 2002]. On average 0.4% of samples within a time series were detected and replaced with interpolated values from adjacent time-steps. Application of the phase-space thresholding filter resulted in little change in the velocity spectra, with the exception of relatively spiky data where the removal of the spikes resulted in a slight increase in the slope of the spectra and a slight decrease in spectral power over high and low frequencies. Doppler noise, considered as a white noise, is an inherent characteristic of Doppler-based backscatter measurement systems and is present over all frequencies [*Nikora and Goring*, 1998]; yet it is important to remove its influence at high frequencies to avoid aliasing errors due to the folding back of frequencies above the Nyquist frequency. Low-pass filters are recommended to avoid aliasing errors [*Bendat and Piersol*, 1986; *Lane et al.*, 1998] and are still a common method of removing aliasing effects when sampling with ADVs [*Venditti and Bauer*, 2005]. Failure to remove the Doppler noise at high frequencies may result in biases in the estimation of turbulence statistics (especially for higher order moments) [*Lane et al.*, 1998] and aliasing errors may result in misinterpretation of spectral trends. The time series were therefore filtered with a 3rd order Butterworth filter where the half-power frequency (f_{50}) was set to $f_D/2.93 = 4.1$ Hz (where $f_D = 12$ Hz is the sampling frequency). This f_{50} was suggested by *Roy et al.* [1997] and leaves only 9.2% of the variance above $f_n = 6$ Hz.

The f_{50} selected is similar to that used by *Venditti and Bauer* [2005] (f_{50} = 5 Hz) whose study investigated the *in situ* turbulent hydrodynamics over dunes and suggest that little spectral energy left above 2 Hz.

The aluminium ADV support frame facilitated the implementation of a Cartesian coordinate system over the study area (the coordinate system origin is located in the upstream/right corner of the frame) with the x axis aligned in the main longitudinal flow direction and the y axis perpendicular to flow. The 3D velocity components (u, v, and w) were measured at specific x-y sampling coordinates. Velocity component orientation followed the right hand rule with positive u in the downstream direction and aligned with the x axis. Given the alignment of the ADV probes, it was expected that spatial averaging of v and w component mean velocities would give values close to zero. The double spatial average, $<<\cdot>>$, for the u, v and w component velocities were estimated by spatially averaging mean velocity measurements over each measurement plane, $<\cdot>$, and subsequently averaging over the two measurement planes. The double spatial average revealed deviations from zero in $<<\overline{V}>>$ and $<<\overline{W}>>$, where the overbar represents time averaged values. These deviations, especially for the v component, were caused by the sensor/frame misalignment with respect to the flow paths. The fixed reference imposed by the support frame insured that any misalignment was consistent for all measurements. Each velocity time series was therefore rotated by approximately 3.2° in the lateral direction and 2.4° in the vertical direction in order to bring $<<\overline{V}>>$ and $<<\overline{W}>>$ close to zero. All treated velocity time series were detrended and were stationary as revealed by a reverse arrangement test at a significance level, α, of 0.05 [*Bendat and Piersol*, 1986].

Turbulence statistics were estimated at each measurement location. These statistics included the root mean squared velocity fluctuations (RMS), u', v', w'; turbulent kinetic energy $k_e = 0.5(u'^2 + v'^2 + w'^2)$; velocity turbulent intensities, $I = u'/\overline{U}$; shear velocity turbulent intensities, $I_* = u'/u_*$. The shear velocity, u_*, was estimated from the lower plane, $z/Z = 0.2$, single-point measurements using $u_* = (C_* k_e)^{0.5}$ as suggested by *Biron et al.* [2004] for complex flow field studies where $C_* = 0.19$ [*Soulsby*, 1983].

Velocity spectra were estimated using discrete fast Fourier transforms (fft) of each data series given by:

$$S_{uu}(\omega) = \frac{1}{Tn}\left|\sum_{t=1}^{n} x_t e^{-j\omega t}\right|^2 \tag{5.1}$$

where T is the sampling interval, n is the number of velocity measurements in the series, x_i is the time domain signal and ω angular frequency. Individual velocity spectra were smoothed using the averaging method developed by Welch (1967) with 10 nonoverlapping rectangular windows. 95% confidence intervals, *CI*, for individual power spectra were calculated based on a χ^2 distribution with 20 degrees of freedom per velocity spectra [*Bendat and Piersol*, 1986]. Non-smoothed velocity spectra were spatially averaged over each measurement plane and converted to wavenumber, k, domain given $S_{uu}(k) = S_{uu}(f)\overline{U}/2\pi$ and $k = 2\pi f/\overline{U}$ and scaled by u_* and z in order to determine general trends influenced by the pebble cluster. 95% confidence intervals for the spatial averaged spectra were estimated by assuming a normal distribution of power spectra densities at each wavenumber:

$$CI = < S_{uu}(k) > \pm 1.96 \cdot \frac{S_{uu}(k)'}{\sqrt{N}} \tag{5.2}$$

where $< S_{uu}(k) >$ is the spatially averaged power spectral densities, $S_{uu}(k)'$ is the standard deviation of N power spectral densities (i.e. the standard error) over the measurement plane at a given wavenumber. The *CI* calculated by Equation 5.2 does not include the standard error associated with the estimation of individual spectra which would necessarily increase the size of the *CI*. The conversion from the frequency, f, to the k domain requires the assumption that the data series meet the Taylor frozen-turbulence hypothesis (FTH) which is generally the case when $I << 1.0$ [*Townsend*, 1976]. According to the FTH, velocity fluctuations in time at a point are the same as the instantaneous distribution of spatial fluctuations in the mean flow direction. High I is an indication that structures could quickly distort by displacements of vortex centres or by vortex growth, stretching, splitting, or pairing. In our study, high I values are anticipated in the wake of the pebble cluster due to the reduced longitudinal velocities and elevated turbulent energy.

The autocorrelation coefficient, R_{ii}, between values of a velocity component, v_i, where i is an index representing one of the three velocity components, at two different times, t and $t + \Delta t$, where Δt is the time step, is estimated by:

$$R_{ii}(\Delta t) = \frac{\frac{1}{n}\sum_{k=1}^{n} v_i(t_k) \cdot v_i(t_k + \Delta t)}{(v_i')^2} \tag{5.3}$$

The temporal autocorrelation function, ACF, is obtained by incrementally increasing Δt in Equation 5.3. Integrating the ACF over the time steps gives the integral time scale, ITS_i, which is a rough measure of the interval over which v_i is correlated with itself:

$$ITS_i = \int_0^{t_1} R_{ii}(\Delta t)\, dt \tag{5.4}$$

where t_1 is the time step for the first zero crossing or for which the correlation is not significantly different than zero at $\alpha = 0.05$. Herein, the permutation procedure presented by *Buffin-Bélanger et al.* [2001a] was used to determine the confidence intervals associated with the autocorrelation of the filtered velocity signals. The macro-scale eddy size or integral length scale, L_i', is obtained by (assuming the FTH is applicable):

$$L_i' = \overline{U}_c \cdot ITS_i \tag{5.5}$$

where the superscript 't' specifies the length-scale as a time derived value and $\overline{U}_c$ is the mean advective velocity of the flow structures in the longitudinal direction:

$$\overline{U}_c = \frac{\Delta x}{\Delta t_{max}} \tag{5.6}$$

where Δt_{max} is the time step for which maximum correlation occurs over a longitudinal separation distance of Δx. Physically, the estimated L_i' is an average length scale over all eddy sizes [*Townsend*, 1976].

Spatial time correlations over the horizontal xy-plane are estimated from correlations between the velocities measured by the upstream fixed probe and the roving downstream probes. The time-shifted cross-correlation coefficient, R_{ij}, or space-time correlation (STC) [*Grant*, 1958] is estimated from:

$$R_{ij}(\Delta x, \Delta y, \Delta t) = \frac{\frac{1}{n}\sum_{k=1}^{n} v_i(x, y, t_k) \cdot v_j(x + \Delta x, y + \Delta y, t_k + \Delta t)}{v_i' v_j'} \tag{5.7}$$

where v_i and v_j, represent the i and j velocity components for time series measured at x,y and $x+\Delta x,y+\Delta y$, respectively. Δx and Δy are the longitudinal and lateral separation distances, respectively. The two-dimensional space-time correlation function, STCF, over the measurement plane for a given time step Δt, is obtained by calculating R_{ij} for all values of Δx and Δy. STC analysis gives a measure of the spatial extension of the time-averaged turbulent structures in a given direction [*Uijttewaal and Tukker*, 1998] and provides a quantitative estimate of the mean life-time of individual eddies as they advect downstream [*Townsend*, 1976].

The spatial cross-correlation along the centreline of the sampling area is obtained by setting $R_{ij}(\Delta x,\Delta y=0,\Delta t=0)$ in Equation 5.7, and calculating $R_{ij}(\Delta x)$ for all values of Δx. The turbulent macro-scale, L_i, can be estimated directly by integrating $R_{ij}(\Delta x)$ from $\Delta x \approx 0$ to $\Delta x = x_1$ at which the correlation distance is not significantly different than zero ($\alpha = 0.05$). The estimated ACFs and time derived L_i' (Equations 5.2 – 5.4) for the upstream probe were compared with the centreline spatial cross-correlations and L_i to investigate the validity of the FTH. This method has been previously used to test the applicability of the FTH in plain boundary layers [*Cenedese et al.*, 1991]. The method has as well been applied to free-surface shear layers and associated coherent structures where a good agreement was found between ACFs and spatial cross-correlation functions [*Uijttewall and Tukker*, 1998; *Rhoads and Sukhodolov*, 2004].

The frequency of high-speed (HS) and low-speed (LS) events within each u component velocity signal was estimated using the U-Level technique. This is a conditional sampling method that calculates the frequency and duration of velocity excursions higher and lower than the mean. *Luchick and Tiederman* [1987] have introduced a threshold based on the standard deviation of the velocity time series (u') for the detection of an event. The threshold used in this study was $|u| > 1.3u'$ to determine the beginning of an event, while the end of an event was set at $|u| < 0.25u'$. These threshold values are suggested by several studies [*Bogard and Tiederman*, 1986; *Luchick and Tiederman*, 1987; *Roy et al.*, 2004].

The interpolation procedure for the spatial distribution plots (i.e., site topography and turbulence variables) is based on a Delaunay triangulation of the spatially distributed measured points. The interpolated surface is subsequently smoothed using a

shape-preserving piecewise cubic Hermite interpolation method [*Fritsch and Carlson*, 1980]. The cubic interpolation method has the added benefits over more commonly used cubic splines as it has no local overshoots and less oscillation for irregular data.

5.4. Results

The bed topography, in the area delimited by the velocity measurement locations is presented in Figure 5.3a. The pebble cluster is clearly delineated by the high elevation contours. Two distinct zones of deposition were observed around the cluster: fine sediment deposition in its wake and larger clast deposition (D_{50} = 0.075 m) imbricated on its stoss side. This distinctive size sorting is consistent with the typical characteristics of pebble clusters [*Brayshaw*, 1984]. Downstream of the pebble cluster the bed elevation decreases by approximately 0.06 m. This drop in elevation is possibly due to the wake in the lee of the cluster where vortices may impinge on the bed in the reattachment zone [*Best and Brayshaw*, 1985]. The location of reattachment is dependent on *Re* [*Kadota and Nezu*, 1999] and is difficult to predict without near-bed velocity measurements. Previous laboratory studies indicate that reattachment occurs at about $5h_s$ downstream from the protruding element [*Best and Brayshaw*, 1985; *Kadota and Nezu*, 1999] which corresponds to an x coordinate of about 0.8 m (Figure 5.3). Figure 5.3b presents the photo composite of the bed compiled from 130 underwater digital photographs. Individual image distortion produce compound uncertainties on the position of individual stones with respect to the velocity sampling locations (black dots). Yet, the composite photo gives a good view of the pebble cluster (center left) and the surrounding bed characteristics. The bed surface has an armoured layer with many interlocking roughness elements. Large imbricated particles aligned in a longitudinal direction are observed on the stoss side of the pebble cluster. From Figure 5.3 we can discern zones of different bed particle sizes. A large zone of relatively smaller particles can be seen in Figure 5.3b to the left of the pebble cluster (looking downstream) from x = 0.0 m – 1.0 m while to the right of the cluster the bed particles are relatively larger. The higher elevations measured at x = 0.6 m – 0.75 m (Figure 5.3a) are due to two large well imbricated cobbles (Figure 5.3b). Similarly the small high elevation circular area

measured at x = 0.25 m (to the right of the cluster) represents a protruding pebble (Figure 5.3b).

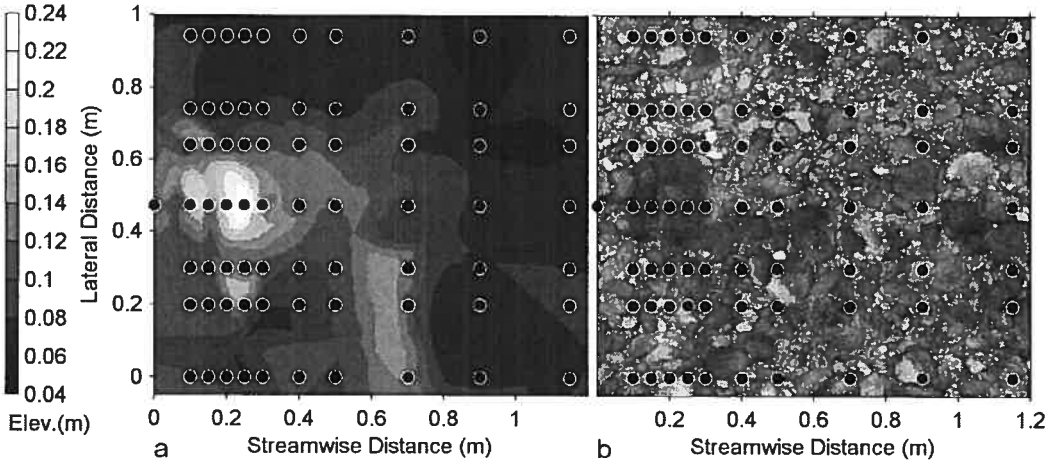

Figure 5.3. a) Bed topography elevations; b) Photo composite of the bed. The pebble cluster can be seen in the central left portion of both images. Black dots represent sampling locations of the velocity measurements. Flow is from left to right.

5.4.1. Turbulence statistics

The spatial average and standard deviations of the mean and turbulent flow statistics are summarized in Table 5.1. In this experiment, the Reynolds numbers (based on mean depth and spatially averaged mean velocities) are around 2.0 x 10^5. Mean longitudinal velocities decrease from about 73 cm s^{-1} to 58 cm s^{-1} as we move from the upper to the lower measurement plane. The spatial mean of u', v' and w' show two general trends: $\langle u' \rangle$ is greater than $\langle v' \rangle$ which is greater than $\langle w' \rangle$ and RMS increases in all three components close to the bed ($z/Z = 0.2$). This is consistent with previous studies [*Nezu and Nakagawa*, 1993; *Nikora and Goring*, 2000; *Lawless and Robert*, 2001; *Roy et al.*, 2004] and is characteristic of turbulence generation over a rough boundary. The standard deviation of $\overline{U}$ is doubled when the cluster is present for z/Z =0.2 while little difference is observed between <RMS> with and without the pebble cluster. The variability induced by the pebble cluster is better identified when investigating the spatial distribution of u', v' and w' for each measurement plane (Figure 5.4). Large zones of high u', v', and w' values are seen in the wake of the cluster. This is most notable for w' as it doubles in magnitude to a distance of $x/h_s \approx 4.0$ downstream from the lee edge of the cluster. Without the cluster, RMS values vary little in space

with isolated patches of slightly higher or lower RMS. These patches can be attributed to the heterogeneous bed. The RMS values are relatively lower to the right of the pebble cluster where the large zone of relatively smaller bed particles was observed (Figure 5.3b). Patches of higher RMS may be associated with isolated roughness elements such as the protruding pebble previously mentioned at $x = 0.25$ m (Figure 5.3a and 3b).

Table 5.1. Spatial averages (and standard deviations) of the mean and turbulent flow parameters for each plane of measurements and in the case of the cluster being present or removed.

		$<\overline{U}>$ cm s^{-1}	$<\overline{V}>$ cm s^{-1}	$<\overline{W}>$ cm s^{-1}	$<u'>$ cm^2 s^{-2}	$<v'>$ cm^2 s^{-2}	$<w'>$ cm^2 s^{-2}	$<k_e>$ cm^2 s^{-2}	$<u'/2k_e>$	$<v'/2k_e>$	$<w'/2k_e>$
Up	present	73.7 (5.8)	0.0 (3.7)	-0.2 (2.4)	11.3 (1.1)	7.7 (0.7)	5.3 (0.8)	109.4 (23.8)	0.59 (0.03)	0.28 (0.03)	0.13 (0.02)
	removed	70.6 (5.7)	-0.6 (2.0)	0.1 (1.3)	10.8 (0.6)	7.6 (0.4)	5.0 (0.4)	100.3 (10.3)	0.59 (0.03)	0.29 (0.02)	0.13 (0.01)
Lw	present	57.9 (12.2)	0.0 (3.2)	0.3 (3.6)	12.2 (1.1)	8.6 (1.0)	5.9 (1.4)	130.1 (24.3)	0.58 (0.07)	0.29 (0.04)	0.13 (0.05)
	removed	57.9 (6.1)	0.6 (1.9)	-0.1 (1.8)	12.4 (1.1)	8.6 (0.6)	5.4 (0.6)	129.4 (19.5)	0.60 (0.03)	0.29 (0.03)	0.11 (0.02)

Parentheses ( ) represent the standard deviation about the mean

The spatial distribution of k_e and I for each plane is presented in Figure 5.5. The spatially averaged k_e and I values with and without the cluster are presented in Tables 5.1 and 5.2. $<k_e>$ increases by 10% in the upper plane of measurement when the cluster is present while $<k_e>$ values for the lower plane ($z/Z = 0.2$) are similar to the upper plane ($z/Z = 0.2$). Conversely k_e values in the cluster wake double in magnitude from about 100 cm^2 s^{-2} to about 200 cm^2 s^{-2} (Figure 5.5a). The spatially averaged energy distributions for all three flow components, $<u'^2/2k_e>$, $<v'^2/2k_e>$, and $<w'^2/2k_e>$ are around 0.59, 0.28, and 0.13, respectively. These values are consistent with the empirically derived values of *Nezu and Nakagawa* [1993] for the intermediate region 0.55, 0.28 and 0.17, respectively, and with studies on ambient flow (straight river) measurements [*Sukhodolov and Rhoads*, 2001]. As seen in Table 5.2, $<I>$ increases with proximity to the bed regardless if the cluster is present or removed, yet the variability around $<I>$ (as determined by the standard deviation) is an order of magnitude greater with the cluster than without it for the plane at $z/Z = 0.2$. Local values of I, presented in Figure 5.5b, are seen to exceed 0.4 and in fact exceed 1.0 in the wake of the cluster due to near zero $\overline{U}$. The spatial influence of the cluster is readily seen in Figure 5.5 and important differences are observed when I and k_e values with and without the cluster are compared. Spatially averaged I. for the three velocity components presented in Table 5.2 slightly

increase with proximity to the bed in both cases, with and without the pebble cluster. This is consistent with the findings of *Nezu and Nakagawa* [1993]. For the inner flow region (z/Z=0.2), $<u'/u_*>$, $<v'/u_*>$, and $<w'/u_*>$ are *about* 2.5, 1.7, and 1.1 respectively which are very close to values reported by *Monin and Yaglom* [1971] of $u'/u_* = 2.3$, $v'/u_* = 1.7$, and $w'/u_* = 0.9$. These values were proposed for large Reynolds shear numbers, Re_*, where $Re_* = u_* Z/\nu$, and ν is the kinematic viscosity. Spatial mean Re_* values in our study ranged from 13 100 – 13 300.

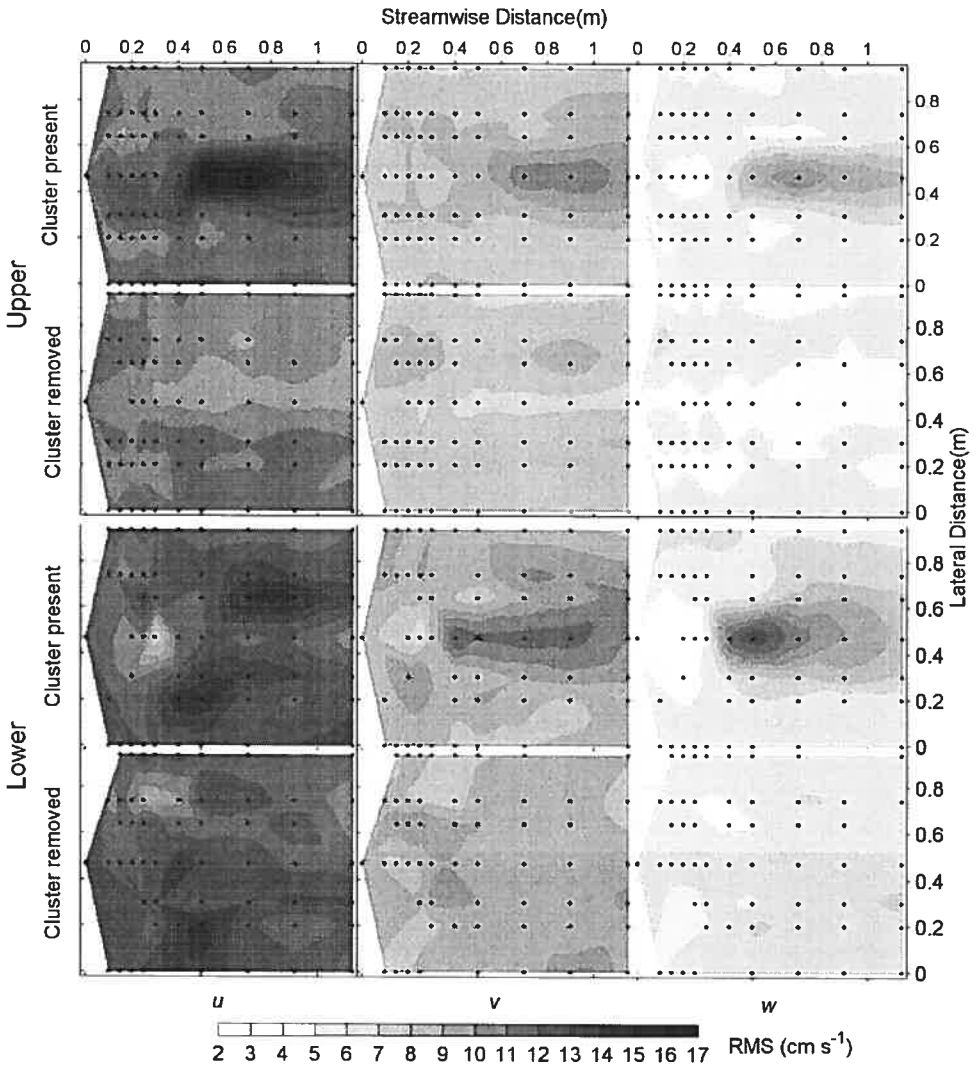

Figure 5.4. Spatial distributions of u', v' and w' values for the planes of measurement and for the cases with and without the pebble cluster. Black dots represent sampling locations of the velocity measurements. Flow is from left to right.

Table 5.2. Spatial averages (and standard deviations) of I and I_{*i} for each plane of measurements and in the case of the cluster being present or removed.

		$\langle I \rangle$	$\langle I_{*u} \rangle$	$\langle I_{*v} \rangle$	$\langle I_{*w} \rangle$
Up	present	0.16 (0.03)	2.30 (0.23)	1.57 (0.14)	1.06 (0.13)
	removed	0.15 (0.02)	2.20 (0.20)	1.53 (0.14)	1.02 (0.12)
Lw	present	0.23 (0.18)	2.46 (0.16)	1.74 (0.11)	1.17 (0.19)
	removed	0.22 (0.04)	2.51 (0.07)	1.74 (0.09)	1.09 (0.08)

Parentheses ( ) represent the standard deviation about the mean

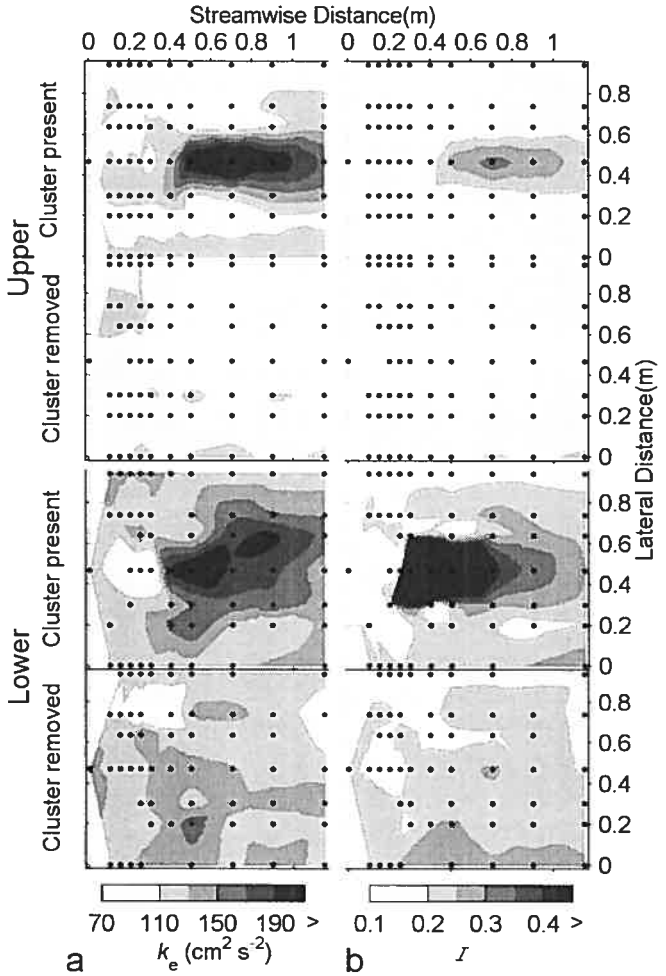

Figure 5.5. The spatial distributions for each measurement plane and for both cases, with and without the pebble cluster, of a) Turbulent kinetic energy, k_e; b) Longitudinal velocity turbulent intensity, I. Black dots represent sampling locations of the velocity measurements. Flow is from left to right.

5.4.2. Spectral Analysis

The wavenumber spectral density functions were spatially averaged over each measurement plane, $\langle S_{ii} \rangle$, and scaled by u_* and z (Figure 5.6). 95% confidence intervals were estimated using Equation 5.2 and the mean value for the u component (averaged over wavenumbers) is presented on each subplot. The $\langle S_{ii} \rangle$ of the upper and lower measurement planes when scaled by u_* and z should reduce to universal forms for each velocity component [*Soulsby*, 1977] and should display inverse power law regions [*Perry et al.*, 1986]. As can be seen in Figure 5.6, the spectra for the u component do collapse at $kz > 0.2$ with and without the cluster as both spectral density functions fall within the confidence interval estimated. The slopes of the spectra show segments of both the intermediate, k^{-1}, and inertial, $k^{-5/3}$, subranges which are typical of turbulent boundary layers [*Perry et al.*, 1986; *Cenedese et al.*, 1991; *Nikora*, 1999]. The slight curvature of $\langle S_{uu} \rangle$ is likely a reflection of the spatial averaging of independent spectra over the heterogeneous bed as the length and boundaries of k^{-1} and $k^{-5/3}$ differ between individual spectra. The lack of a scaled region for the v and w component spectra and the small $k^{-5/3}$ region for the u component spectra are perhaps a reflection of the imposed low cutoff frequency of $kz = 3.1$ and $kz = 4.5$ for the lower and upper planes of measurements, respectively. Previous studies of turbulent flows in a boundary layer suggest that the low cutoff frequency used here would result in an approximate loss in variance of 10% and 40% of the u and w component velocities, respectively [*Soulsby*, 1980]. This suggests that the $k^{-5/3}$ range for the u component and both the k^{-1} and $k^{-5/3}$ ranges for the w component may extend into higher wavenumbers than those observed. The spike observed in Figure 5.6 at higher wavenumbers (u component) spectra for both upper measurement planes is likely due to signal interference between the upstream stationary ADV and the downstream ADVs and/or reflection off of the pebble cluster itself. This spike can be clearly distinguished in several individual u spectra obtained from locations upstream and adjacent to the pebble cluster.

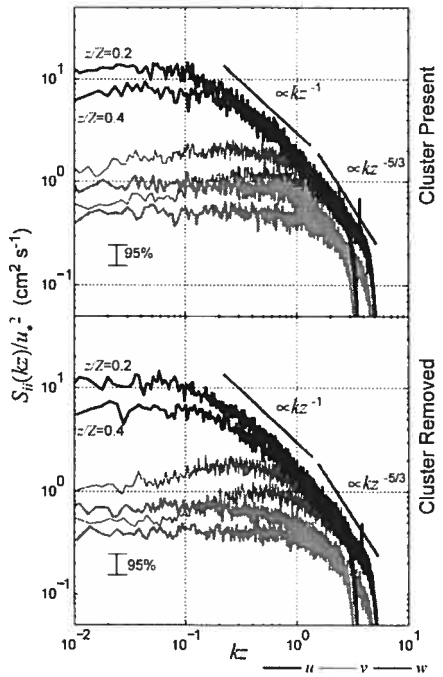

Figure 5.6. Spatially averaged wavenumber spectral density, $<S_{ii}>$, for each measurement plane. The spectra are scaled by u_* and z.

Subtle differences are observed between $<S_{ii}>$ with or without the pebble cluster. A better marked contrast is seen between measurements obtained from the upper and lower planes. A rounded peak is observed at $kz = 1.0$ for the w component when the cluster is present which is not observed when the cluster is removed. In general, the energy associated with the three velocity components, throughout the wavenumbers investigated, is greater when the cluster is present than without the cluster. At low wavenumbers, $S_{uu}(kz)/u_*^2 > S_{vv}(kz)/u_*^2 > S_{ww}(kz)/u_*^2$ suggesting anisotropic conditions while the $<S_{ii}>$ of the three components converge at higher wavenumbers indicating a tendency towards local isotropic turbulence. The discrepancy between the energy contributions from the u and v components at higher wavenumbers and the w component is possibly related to the higher noise level in the horizontal velocity spectrum due to ADV transducer configuration [*Voulgaris and Trowbridge*, 1998]. The noise level associated with the horizontal velocity components for the ADVs used in this study were estimated using the ADV transformation matrices and are on average 31 times higher than that for the vertical component.

The shape and characteristics of the individual spectra, S_{ii}, of all three velocity components obtained in the presence of the cluster differ greatly from those when the cluster is removed. This variability is more pronounced in the proximity of the cluster and it contrasts sharply from the relatively similar spatially averaged spectra presented above. Figure 5.7 shows a sequence of five spectral plots for velocities measured along the centreline close to the bed at distances of x/h_s = 1.0 to x/h_s = 8.5 downstream from the lee edge of the cluster. When the pebble cluster is present, a well defined peak in the S_{ww} is evident from x/h_s = 1.0 to x/h_s = 4.0. Over this distance, the peak decreases in frequency from 1.8 Hz to 1.0 Hz. A smaller peak in S_{vv} occurs from x/h_s = 4.0 to x/h_s = 6.0. At x/h_s = 8.5, the velocity spectra with the cluster resemble those without the cluster and are similar to the spatially averaged spectra shown in Figure 5.6. When the cluster is present u' decreases by 8% and v' and w' increase by 30% and 80%, respectively, over the sequence from x/h_s = 1.0 to x/h_s = 8.5.

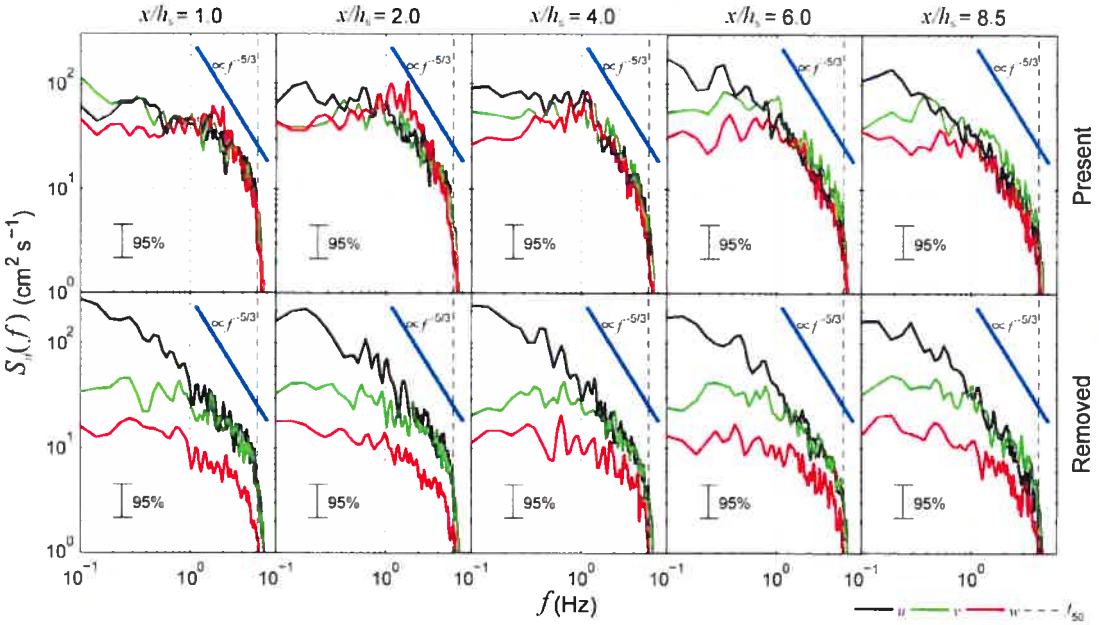

Figure 5.7. Spectral density, S_{ii}, for the measurement plane at z/Z = 0.2, with and without the pebble cluster. The spectral sequence starts downstream of the lee side edge of the pebble cluster and it follows along the centerline.

The presence of a shift in the frequency for the peak S_{ww} is most likely related to the vortices being shed from the separation zone in the lee of the pebble cluster. A shift in frequency with increasing distance from the point of origin of a shear layer has been observed in splinter plate studies for the v component where it was suggested to

represent the coalescence and growth of shedding eddies [*Uijttewaal and Tukker*, 1998]. Shedding frequencies, f = 1.0 Hz to 1.3 Hz, were estimated using the Strouhal number, $S_t = fh_s/\overline{U} \approx 0.18$ as suggested by *Achenbach* [1974]. These expected shedding frequencies are in good agreement with the peak frequencies observed in the velocity spectra (1.0 Hz to 1.8 Hz).

5.4.3. Frozen turbulence hypothesis

The applicability of the FTH was tested by comparing the velocity time series autocorrelation functions, $R_{ii}(\Delta t)$ with the space-time correlation functions, $R_{ij}(\Delta x,\Delta y=0,\Delta t=0.25)$ (Figure 5.8). Space-time correlations were performed between the upstream stationary probe and the downstream roving probe along the centerline with a time lag of 0.25 s. Maximum correlation should occur at Δt=0, yet due to signal interference between sensors at $\Delta x < 0.2$, it was necessary to use a slight time lag of 0.25 s to avoid corruption of the correlation function. In general, the FTH hypothesis seems to hold and there is good agreement between the $R_{uu}(\Delta t)$ and $R_{uu}(\Delta x,y=0,\Delta t=0.25)$ with the exception of z/Z = 0.2 plane when the cluster is present. Here, $R_{uu}(\Delta x, y=0,\Delta t=0.25)$ is severely disrupted by the wake in the lee of the cluster at x = 0.35 m (0.05 m from the lee side edge of the cluster) as shown by the strongly negative correlations. Integral length scales, L_t and L_t' estimated by integrating the STCFs and ACFs, respectively, are presented in the top right corner of each subplot of Figure 5.8. $\overline{U}_c$ values required to estimate L_t' (Equation 5.6) are presented in Table 5.3 and are not significantly different than $<\overline{U}>$ (α = 0.01, Wilcoxon rank sum test) with the exception of the measurements from the z/Z = 0.4 plane when the cluster is present. Both length scales L_u (u component) and L_u' agree well with one another with the exception of the lower plane (z/Z = 0.2) with the cluster. L_v' and L_w' were consistently longer than L_v and L_w in all cases except for the v component where the cluster is removed. Given the relative agreement between L_u and L_u' the use of the FTH over a rough heterogeneous boundary with large I may be adequate with the exception of the measurements taken close to the top of the pebble cluster and in its wake near the bed.

Table 5.3. Mean advection velocity and spatially averaged mean ITS for each plane of measurements and in the case of the cluster being present or removed.

		$\overline{U}_c$ cm s^{-1}	<ITS$_u$> s	<ITS$_v$> s	<ITS$_w$> s
Up	present	64.5* (6.4)	0.33 (0.07)	0.11 (0.01)	0.11 (0.02)
	removed	72.8 (5.0)	0.34 (0.06)	0.11 (0.02)	0.11 (0.01)
Lw	present	57.5 (14.3)	0.31 (0.09)	0.11 (0.02)	0.11 (0.02)
	removed	63.9 (11.1)	0.31 (0.08)	0.11 (0.02)	0.11 (0.02)

* Significantly different from $<\overline{U}>$ at $\alpha = 0.01$

Parentheses ( ) represent the standard deviation about the mean

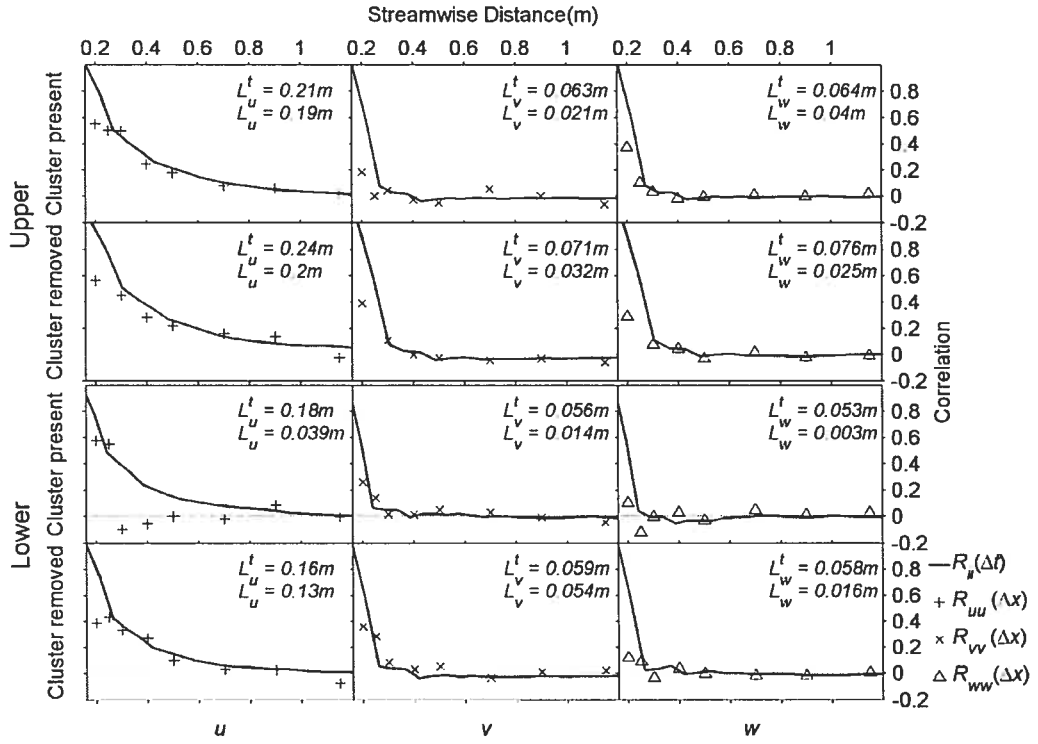

Figure 5.8. Comparison of the length scales obtained from the autocorrelation, $R_{ij}(\Delta t)$, and spatial-time correlation, $R_{ij}(\Delta x,\Delta y=0,\Delta t=0.25)$, analyses for all three velocity components measured at two planes above the bed with and without the cluster.

5.4.4. Length scales, integral time scales and correlation structure lengths

The estimated length scales for L_u and L_w tend to increase with height above the bed: at z/Z =0.2, L_u/Z = 0.37 and L_w/Z = 0.046 while at z/Z =0.4, L_u/Z = 0.57 and L_w/Z = 0.071. These results are in agreement with the hypothesis that eddies scale with height above the bed [*Townsend*, 1976; *Nezu and Nakagawa*, 1993; *Nikora*, 1999] and the estimated

scale values are close to the half-power law for wall and intermediate flow regions [*Nezu and Nakagawa*, 1993]. The estimated L_i values are as well similar to those obtained in laboratory experiments by *Nakagawa and Nezu* [1981] who found $L_u/Z = 0.31$ and $L_w/Z = 0.075$.

Spatial mean *u*, *v* and *w* component ITS values for each plane of measurements are presented in Table 5.3. There is no difference between measurements with the cluster and those without. As shown for the integral length scales, a 3:1 ratio is observed between $<ITS_u>$ and $<ITS_w>$ which is consistent with previous studies in gravel-bed rivers [*Roy et al.*, 1996; *Buffin-Bélanger and Roy*, 1998]. The magnitudes of $<ITS_u>$ are 50% less than in these previous studies, however. This may be due to a number of factors: (i) the inherently smaller sampling volume used by ADVs to estimate velocities [*Roy et al.*, 1996], (ii) the higher mean flow velocities in our experiment (58 cm s^{-1} to 74 cm s^{-1}) compared to 30 cm s^{-1} in *Buffin-Bélanger and Roy* [1998] (iii) the filter type, order and f_{50} used. The spatial distributions of ITS_u are presented in Figure 5.9a. A large zone of low ITS_u values is located in the wake of the pebble cluster. When the cluster is not present, a zone of low ITS_u is not observed and the spatial pattern of ITS_u appears to be less structured. The complex spatial distributed patterns of ITS_u values especially without the cluster reflect the susceptibility of the autocorrelation function to bed irregularities. The results of the U-Level analysis, presented in Figure 5.9b, complement the ITS_u results by indicating the frequency of two types of turbulent events. The frequency for both high-speed (HS) and low-speed (LS) events increases in the wake of the pebble cluster. The zones of higher event frequency are highly correlated with small ITS_u in the lee of the pebble cluster suggesting the shedding of smaller coherent structures. At the lee edge of the pebble cluster, the combined maximum event frequency (HS + LS) for the $z/Z = 0.2$ measurement plane ranges from $f = 1.3$ Hz – 1.1 Hz, which is well within the range of shedding frequencies observed from the power spectra and those estimated using a Strouhal number of 0.18. Without the cluster, the combined event frequencies are much lower with a value around 0.8 Hz.

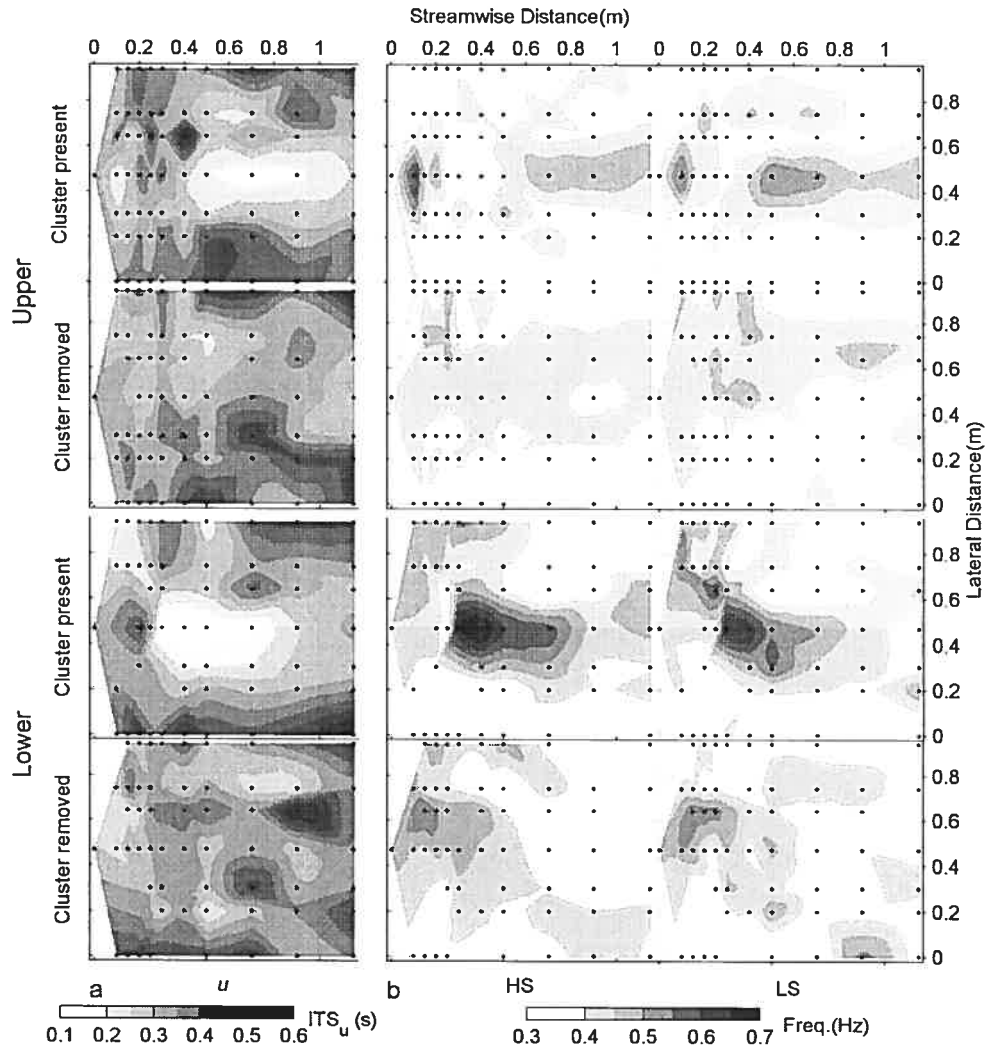

Figure 5.9. a) Longitudinal velocity integral time scale (ITS_u); b) U-level analysis indicating the frequency of high-speed (HS) and low-speed (LS) events. Black dots represent sampling locations of the velocity measurements. Flow is from left to right.

Figure 5.10 shows the STCFs for the three velocity components with and without the cluster over time lags, Δt = 0.25 s, 0.5 s, 1.0 s, 1.5 s, and 2.0 s and gives a quasi-3D picture of the correlations. The spatial pattern of longitudinal velocity component STC, $R_{uu}(\Delta x,\Delta y,\Delta t)$ (Figure 5.10a), is characterized by high positive and negative values in alternating long and narrow streaks. Significant correlations ($\alpha = 0.05$) for $R_{uu}(\Delta x,\Delta y,\Delta t$=0.25) extend over most of the longitudinal length of the sampling zone. The distance from the maximum $R_{uu}(\Delta x,\Delta y,\Delta t$=0.25) to non-significant correlation (upper measurement plane) is 0.8 m. *cor*-$L_{m,n}$ is defined as the length of significant

$R_{ij}(\Delta x,\Delta y,\Delta t)$ (Equation 5.7) in the m direction (x or y) for the n velocity component (u, v or w). For the u component in the x direction, $cor\text{-}L_{x,u}$ = 1.6 m (or 4.6Z), and was estimated by doubling the downstream extent of correlation (0.8 m) to account for the correlation extending upstream. The longitudinal structure width is $cor\text{-}L_{y,u}$ = 1.0Z. Following the sequence of time lags (from left to right in Figure10) the downstream advection of the correlated structures is apparent. The alternating regions of negative and positive correlations strongly suggest the presence of laterally spaced high- and low-speed wedges which form narrow alleys that are side-by-side as those found by *Nakagawa and Nezu* [1981] and *Roy et al.* [2004]. The maximum correlation decreases gradually with advecting distance, and the lack of symmetry of the spatial pattern of correlation values indicates an inhomogeneous flow field [*Cenedese et al.*, 1991]. The similarity between $R_{uu}(\Delta x,\Delta y,\Delta t)$ with the cluster and without the cluster at z/Z = 0.4 is striking. There is no apparent difference between the patterns of correlation in both situations, indicating that they are relatively unaffected by the large roughness element and associated shedding meso-structures. $R_{uu}(\Delta x,\Delta y,\Delta t)$ values without the cluster at z/Z = 0.2 are somewhat smaller than those estimated at z/Z = 0.4 and $\overline{U}_c$ is slower (Table 5.3). In the case of the lower measurement plane with the cluster, the correlated structure appears to deform and split off to the left side of the cluster where the structure width is halved. This splitting or deformation behaviour has been observed in vorticity visualisation studies [*Rockwell*, 1998]. For z/Z =2.0, at x/h_s = 6.0 (downstream from the lee edge of the cluster) the pattern of correlation values regains its original width and is similar in shape and magnitude to that when the cluster is removed. A similar behaviour is observed with $R_{vv}(\Delta x,\Delta y,\Delta t)$ which is disrupted by the pebble cluster, passes to the left side, and redevelops downstream. $R_{vv}(\Delta x,\Delta y,\Delta t)$ patterns are much smaller than for $R_{uu}(\Delta x,\Delta y,\Delta t)$ reflecting flow anisotropy which occurs whether the cluster is present or not. This suggests that preferred directions of the turbulent fluctuations are not affected markedly by the LRE for the upper measurement level.

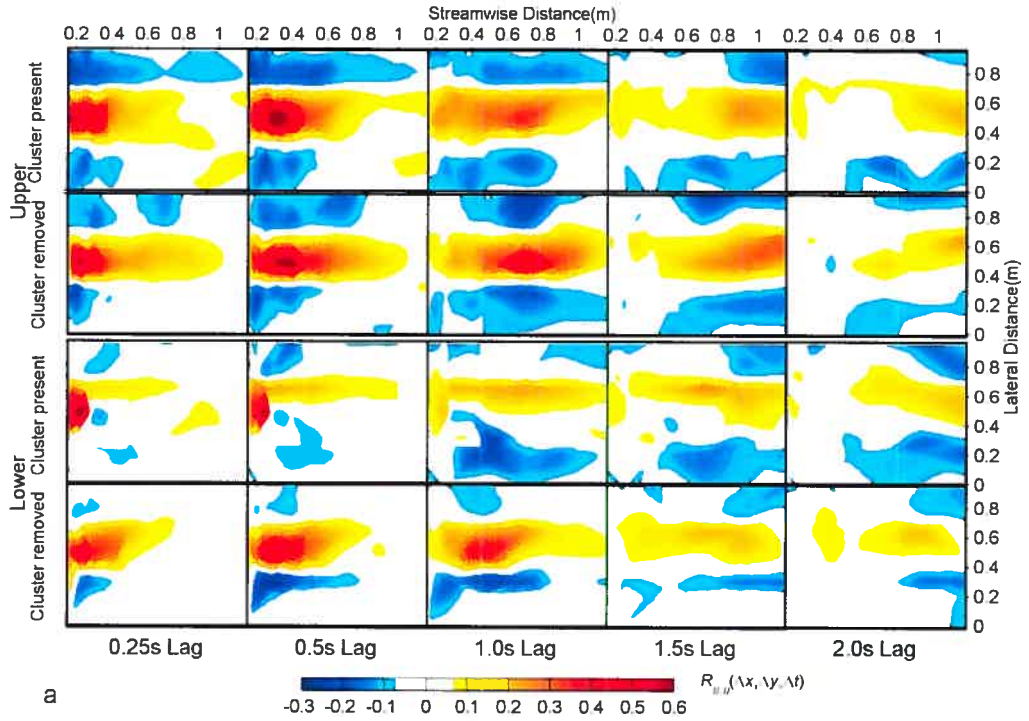
Streamwise Distance(m)
0.2 0.4 0.6 0.8 1
Upper
Cluster present
Cluster removed
Lower
Cluster present
Cluster removed
Lateral Distance(m)
0 0.2 0.4 0.6 0.8
0.25s Lag
0.5s Lag
1.0s Lag
1.5s Lag
2.0s Lag
-0.3 -0.2 -0.1 0 0.1 0.2 0.3 0.4 0.5 0.6
$R_{uu}(\Delta x, \Delta y, \Delta t)$

a

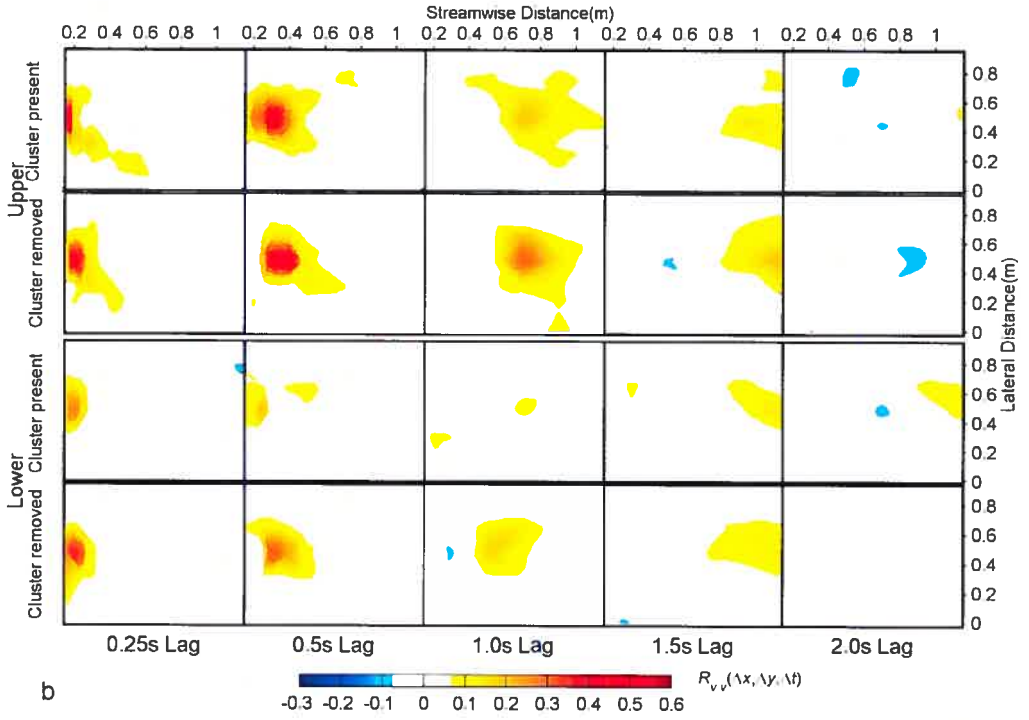
Streamwise Distance(m)
0.2 0.4 0.6 0.8 1
Upper
Cluster present
Cluster removed
Lower
Cluster present
Cluster removed
Lateral Distance(m)
0 0.2 0.4 0.6 0.8
0.25s Lag
0.5s Lag
1.0s Lag
1.5s Lag
2.0s Lag
-0.3 -0.2 -0.1 0 0.1 0.2 0.3 0.4 0.5 0.6
$R_{vv}(\Delta x, \Delta y, \Delta t)$

b

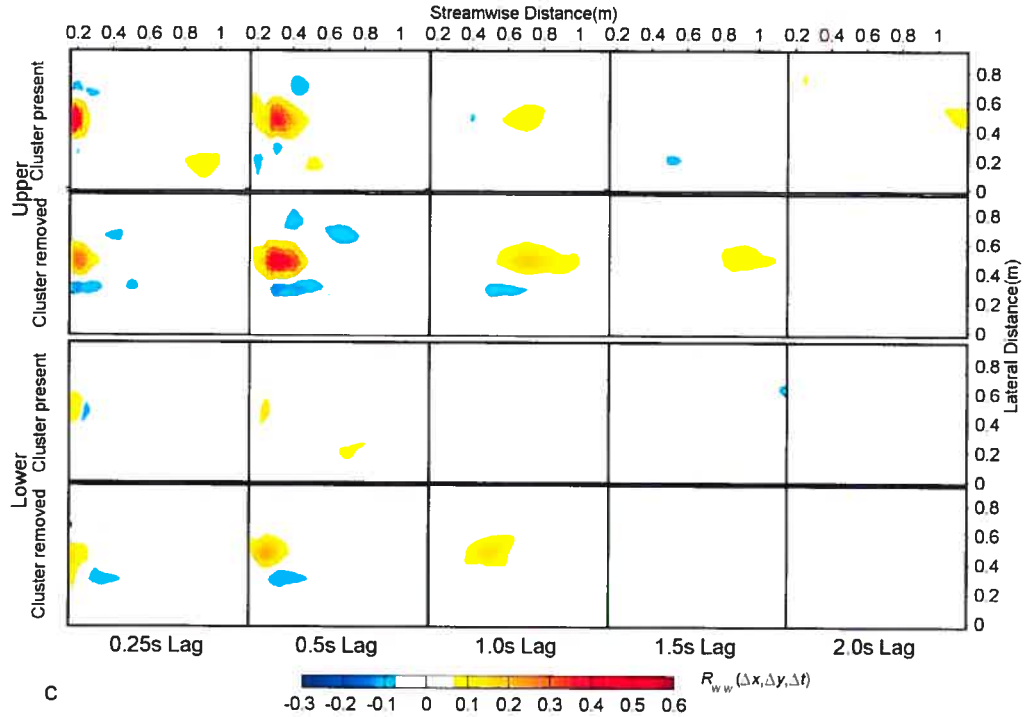

Figure 5.10. Space-time correlation, $R_{ij}(\Delta x,\Delta y,\Delta t)$, function diagrams for the a) longitudinal; b) lateral; c) vertical velocity components at time lags, Δt = 0.25s, 0.5s, 1.0s, 1.5s, and 2.0s. The spatial patterns are given for both measurement planes and for both cases, with and without the pebble cluster. Only significant correlations are represented (α = 0.05). Flow is from left to right in each sub-plot.

5.5. Discussion

There is a lack of marked differences between the spatial mean flow statistics (Tables 5.1 and 5.2) with the cluster and without. This may in part be explained by the relatively small percentage of planar area occupied by the pebble cluster (5%) over the sampling area. The hydrodynamic effects of the cluster appear to be localized and are smoothed out in the spatial mean flow statistics. The only exception is k_e for the measurement plane z/Z = 0.4 which is 10% greater with the cluster, yet this result is highly dependent on the density, distribution and area covered by the measurement locations. Thus the spatial average of k_e over an entire river reach may reveal little noticeable influence. The spatial distributions of u', v', and w' reveal extensive flow modifications and complex 3D dynamics associated with the shedding motions in the wake developed downstream of the pebble cluster. At z/Z = 0.2, high values of u' in zones flanking the cluster may reflect trailing vortices [*Best and Brayshaw*, 1985; *Tritico and Hotchkiss*, 2005], while

the high v' values directly behind the pebble cluster may indicate the convergence of vertical axis vortices [*Lawless and Robert*, 2001]. The high w' values in the wake of the cluster are an indication of the free-shear layer and associated shedding vortices. Locally k_e increases by a factor of approximately 2.0 in the wake of the cluster at both measurement heights.

The observed increased turbulent activity and complex u, v and w interactions stress the importance of the 3D characterization of the system hydrodynamics. The spatially averaged lateral component, which is often ignored in turbulent studies, contributes about 30% of the total energy and v' is locally approximately equal to u' and w' in the cluster wake. The specific values and the extent of local patterns of u', v', and w' are related to the geometry and relative depth of the cluster under investigation, yet their relative contributions to k_e and relative spatial characteristics have been observed in previous laboratory experiments [*Lawless and Robert*, 2001] and may be generalized to other submerged roughness elements. Pebble clusters and large roughness elements act as turbulent energy generation mechanisms where energy is transferred from the mean flow to turbulent eddies in all three velocity components through shedding processes and the dynamics of the flow separation zone in the lee of the cluster. The complex spatial patterns and relative values observed here stress the importance of measuring all three velocity components.

The range of shedding frequencies estimated using the Strouhal number of 0.18, f = 1.0Hz – 1.3Hz, is in good agreement with the range of shedding frequencies in S_{ww}, f = 1.0Hz – 1.8Hz, in the wake of the cluster. To our knowledge this represents the first time that the *in situ* shedding process from a pebble cluster has been recorded using high frequency velocity measurements. The peak shedding frequency decreases as the distance downstream from the cluster increases perhaps as an indication of the coalescence of shedding structures (inverse energy cascade) [*Uijttewaal and Tukker*, 1998]. The peak shedding frequency range is as well in good agreement with combined event frequencies, f = 1.1Hz – 1.3Hz estimated in the cluster wake where ITS_u values decrease by 75%. This suggests that given similar velocity and relative roughness conditions, conditional event analysis could be used as a tool to determine the shedding frequencies of large roughness elements. The shedding behaviour observed here is a

general characteristic of shear layers and should be observable with other submerged roughness and different geometries of pebble clusters, but the peak shedding frequency values we observed are most likely specific to the geometry and *Re* of our study.

The lengths, $cor\text{-}L_{x,u} = 4.6Z$, and widths, $cor\text{-}L_{y,u} = 1.0Z$, of the large-scale turbulent flow structures observed here through the quasi-3D STCF maps conform with observations through flow visualisation in flume studies [*Shvidchenko and Pender*, 2001] and PIV studies [*Liu et al.*, 2001] where structure lengths were estimated as $4.5Z$ and between 2 and $4Z$, respectively. The $cor\text{-}L_{x,u}$ and $cor\text{-}L_{y,u}$ estimated in this study are also in good agreement with previous field studies by *Roy et al.* [1996] and *Roy et al.* [2004] where $cor\text{-}L_{x,u}/2$ are between 2-3Z and $cor\text{-}L_{y,v}$ range between 0.5-1Z. The long, narrow shape of the structures as shown by $R_{uu}(\Delta x,\Delta y,\Delta t)$ was postulated by *Adrian et al.* [2000] to be the result of the longitudinal alignment of many hairpin vortex packets initiating from the bed. The smaller packets are nested within larger packets, creating the appearance of multiple zones of uniform longitudinal momentum. These zones would coincide with high- and low-speed wedges in *Roy et al.* [2004]. *Adrian et al.* [2000] have proposed that large-scale vortices are formed by the agglomeration of small-scale ($z^+ = zu_*/\upsilon = 100$) inner-layer hairpin vortices. Considering that the macro-scale turbulent structures described herein scale with the thickness of the inner layer as $z+ =$ 13 300, a more likely and simpler scaling is with outer variables such as flow depth [*Roy et al.*, 2004]. This supports the notion that channel depth functions in some meaningful way to limit the scale for turbulent eddies in rivers [*Church*, 2007]. *Nezu and Nakagawa* [1993] have speculated that in a flow with high *Re* over rough complex boundaries, where the generation of coherent macro-scale structures is much more complex, the coalescence of bursting motions may occur violently and thus large-scale agglomerations may form high- and low-speed fronts that scale with the outer variables. Studies on rough beds also suggest that shedding vortices have a range of sizes and frequencies due to the assemblage of different grain sizes and shapes of roughness elements [*Kirkbride*, 1993].

While the generation mechanism of large-scale flow structures is still unclear, it is apparent from this study that their characteristics are relatively unaffected by large protuberant bed roughness elements such as pebble clusters. For the upper plane of

velocity measurements at $z/Z = 0.4$, we found very little difference between the large-scale turbulent coherent structures advecting downstream when the cluster is present or absent. Furthermore at $z/Z = 0.2$, the structures are deformed by the cluster yet they regain their coherence over a relatively short distance downstream ($6.0h_s$). Given the estimated eddy shedding frequency and the elevated k_e values observed in the wake of the cluster, the persistence and robustness of the coherent structures is somewhat surprising. It implies that the effects imparted by the pebble cluster on the turbulent flow field are local and are limited to the near-bed region (at least for the relative size of roughness elements observed in our study). In general, our study indicates that roughness elements with relative heights of less than about $h_s/Z = 0.3$ have relatively little influence on the macro-scale coherent flow structures in the intermediate and subsequently free-surface region. On the other hand, the flow visualisation results from a field experiment by *Roy and Buffin-Bélanger* [2001] have suggested that the shedding behaviour of vortices in the lee of protruding clasts is dependent on the passage of high- and low-speed wedges which through either strong or weak return flow from the separation zone determines the spatial extent of shedding into the intermediate flow region. This model is further supported by research suggesting that the intermittent behaviour of shedding vortices is in part influenced by the passage macro-scale flow structures [*Lacey and Roy,* 2006].

5.6. Conclusions

This study supports the presence of tridimensional coherent macro-turbulent flow structures in gravel-bed rivers and gives new insight on their 3D spatial patterns and persistence as they advect past a pebble cluster. The u', v', and w' patterns indicate complex flow around and overtop of the pebble cluster with zones of flow convergence, shearing and shedding. Pebble clusters and large roughness elements may represent an important source of turbulent kinetic energy (10% average increase in our study) in river systems, yet this value is highly dependent on the spatial density of the clusters over the reach. Previous studies have suggested a link between turbulent dynamics and microtopographic bedforms [*Clifford et al.*, 1992], yet the apparent random spatial distribution of pebble clusters in the Eaton North River [*Lamarre and Roy*, 2001],

suggest a lack of dependence of microtopographic bed forms on turbulent wake dynamics.

Peak shedding frequencies identified from spectral analysis in the lee of the pebble cluster agree with frequencies estimated using U-level analysis and those predicted using a Strouhal number of 0.18. The shedding eddies have a localized effect on the overlying flow structure, do not propagate far from the cluster ($x/h_s = 6.0$), and are quickly incorporated into the large-scale coherent flow structures. The spatial distribution of simultaneous velocity measurements allowed for a full *in situ* characterization of the 3D extent and the temporal behaviour of the large-scale coherent flow structures. These structures were found to scale with flow depth and to be long and narrow confirming the results of several previous studies. They are not much affected by the pebble cluster whose shedding eddies are more likely to strengthen the macro-scale flow structures as suggested by *Buffin-Bélanger et al.* [2001a] than to disrupt them. While the large-scale coherent structures were relatively undisturbed by the small-scale bedforms investigated in our study, their behaviour and response to the 3D dynamics of larger-scale bedforms such as pools and riffles could potentially be much different and merits further investigation.

Linking Paragraph C

Through the use of spectral analysis in the previous chapter, peak shedding frequencies in the lee of the LRE were identified. To our knowledge this represented the first time that the *in situ* shedding process from a LREs had been recorded using high frequency velocity measurements. In order to confirm the spectral peaks as shedding shear layer flow structures a new experimental approach was developed based on concurrent flow visualization and 3D velocity measurements which could focus in detail on the wake processes and elucidate their behaviour. Chapter 5 as well showed that LS flow structures were marginally affected by the meso-scale shedding from the pebble cluster, yet the response of the shear layer to the passage of LS could not be investigated. Through the synchronous measurement technique used in the following chapter[3], the effect of LS flow structures on the shear layer and associated flow structures could be shown. Instantaneous 3D velocity measurements were obtained from two intersecting planes in the lee of an isolated pebble cluster. Two vortex shedding modes in the wake of the cluster were identified: a small scale high frequency initial instability mode and a lower frequency mode that scales with cluster height. The lower frequency mode arose from the intermittent interaction and amalgamation of the small-scale instability vortices. Mean Reynolds shear stresses, velocity spectra and coherency squared spectra indicated a dominance of lateral axis shedding vortices in the wake of the cluster. Conditional quadrant analysis revealed that Q2 and Q4 events contributed 80% of the total *uw* component Reynolds shear stress and demonstrated a dominance of ejection events in the wake of the cluster. Our results support previous models suggesting the vertical expansion and contraction of the shear layer with the passage of Q2 and Q4 events, respectively, yet this behaviour is found here to be much more intermittent than previously shown.

---

[3] Lacey, R.W.J. and A.G. Roy (2007c) Fine-scale characterization of the turbulent shear layer of an instream pebble cluster, *Journal of Hydraulic Engineering, in press* (reprinted with permission from ASCE).

6. FINE-SCALE CHARACTERIZATION OF THE TURBULENT SHEAR LAYER OF AN INSTREAM PEBBLE CLUSTER

6.1. Introduction

In gravel-bed rivers, the hydrodynamics are strongly influenced by the heterogeneous topography of the bed, composed of discrete particles, bedforms and roughness elements of various shapes, sizes and orientations [*Kirkbride*, 1993]. The protrusion of these grains and bedforms has a significant influence on the turbulent flow field. The turbulent mixing processes are driven by the shear flow overtop of the protruding elements which result in the production and shedding of vortices in the separation zone in the lee of the protrusion. These vortices entrain and interact with the surrounding fluid. The hydrodynamics in turn govern the dispersion and distribution of sediments, nutrients, and stream biota within the water column. A proper characterization of the shear flow around protruding elements is critical to the understanding of river hydrodynamics and turbulent mixing processes in gravel-bed rivers.

Shear flows have been investigated and characterized in the laboratory over a large variety of conditions such as free mixing layers [*Winant and Browand*, 1974], backward-facing steps and dunes [*Hasan*, 1992; *Bennett and Best*, 1995; *Kadota and Nezu*, 1999] and around bluff bodies [*Taneda*, 1978]. In rivers, the majority of research on shear flows has focused on stream confluences [*Biron et al.*, 1993; *Rhoads and Sukhodolov*, 2004] and relatively few studies have examined shear flows around large roughness elements in rivers [*Buffin-Bélanger and Roy*, 1998; *Buffin-Bélanger et al.*, 2001a; *Tritico and Hotchkiss*, 2005]. Bluff bodies, backward-facing steps and pebble clusters are characterized by a flow separation zone, shear layer instability and the associated shedding vortices. Laboratory studies of shear under fully turbulent flow conditions (where Reynolds numbers, $Re > 10\ 000$), have characterized two distinct modes of instability: the initial instability mode that scales with the momentum thickness at separation and a body mode which scales with the body diameter, h_s [*Hasan*, 1992]. The rolling up of the initial laminar shear layer causes a train of small-scale vortices which steadily broaden downstream and through fluid entrainment and merging processes between eddies give rise to a new set of larger shedding structures

downstream [*Fuchs et al.*, 1980; *Hasan*, 1992]. Under certain conditions, the shift from small to larger scale vortex structures can be the result of vortex pairing and amalgamation which enables the adjustment of the smaller initial scales to the larger scales at a distance equivalent to several h_s downstream [*Winant and Browand*, 1974; *Fuchs et al.*, 1980]. The scarcity of *in situ* investigations of shear flows, especially over roughness elements, is most likely due to the difficulties of obtaining field measurements in fully developed turbulent flows at high Reynolds numbers, typically greater than 1×10^5, to properly characterize the scales of the turbulent motion.

In gravel-bed rivers, large scale (LS) coherent flow structures are a predominant feature of the flow [*Nakagawa and Nezu*, 1981; *Roy and Buffin-Bélanger*, 2001; *Roy et al.*, 2004]. These structures consist of depth scaled intermittent fronts (or wedges) of high- and low-speed fluid. While LS structures are composed of several types of fluid motion, high-speed structures consist mainly of rapid downward motion (sweeps), and low-speed structures are mainly associated with slow upward motions (ejections) [*Roy and Buffin-Bélanger*, 2001]. For the visualisation component of our study, we concentrate on the sweep and ejection portions of the LS coherent structures in order to clearly characterise the response of the pebble cluster shear layer to the passage of LS sweep or ejection events. Following *Paiement-Paradis et al.*, [2003], the detected LS coherent structures have durations of greater than 0.2 s. Sweeps and ejections have been found to contribute to the bulk of the total Reynolds shear stress and as such exert a considerable influence on local sediment dynamics [*Williams et al.*, 1989]. LS structures appear to be little affected by the occurrence of shedding motions from isolated pebble clusters [*Lacey and Roy*, 2007a], yet have been found to exert an influence on shedding motions – where the shear layer was found to expand upwards with the passage of ejection events [*Buffin-Bélanger and Roy*, 1998; *Roy et al.*, 1999; *Buffin-Bélanger et al.*, 2001a].

The purpose of this study was to conduct a detailed investigation of the turbulent processes in the shear layer and turbulent wake region of an isolated instream pebble cluster in a river and to link these processes with the large scale turbulent flow structures. This study is carried out at a fine three-dimensional (3D) spatial scale using instantaneous velocity measurements and simultaneous flow visualization techniques.

We specifically focus on a spatial description of the hydrodynamics in the wake region and the physical processes associated with the shear layer to identify *in situ* the characteristics of shear flows observed in previous laboratory studies such as the frequency and Reynolds shear stresses of the shedding vortices. We also investigated the behaviour of the shear layer under the influence of LS flow events to substantiate the results of previous *in situ* studies. In general, our study brings forth original results on the fine-scale processes of the shear layer and gives visual insights into turbulent events estimated through instantaneous velocity measurements.

6.2. Methods

6.2.1. Field Measurements

Our study was conducted around a naturally occurring isolated pebble cluster in the Eaton North River (Eastern Townships, Quebec, Canada). The Eaton North is a gravel-bed river with a bankfull width of 28 m and a median grain size of 0.035 m at the sampling reach. The grain size distribution is poorly sorted with several large clast sediments (> 0.20 m) randomly distributed throughout the reach some of which form the keystones of pebble clusters [*Lamarre and Roy*, 2001]. The length and width of the pebble cluster were 0.44 m and 0.3 m, respectively. The bed topography of the sampling area was mapped using a Trimble series 5000 total station. The maximum protrusion height, h_s, of the cluster is 0.17 m and the mean water depth (Z) within the sampling zone was 0.43 m resulting in a relative roughness of h_s/Z = 0.4. Reynolds numbers (based on mean flow velocity and Z) were of the order of 3.2×10^5.

Four SonTek acoustic Doppler velocimeters (ADVs), supported by a 1.5 m square aluminium frame, were positioned overtop of the pebble cluster. The frame facilitated the implementation of a Cartesian coordinate system where the longitudinal (streamwise), lateral (cross-stream), and vertical dimensions are defined as x, y and z, respectively. The x coordinate was aligned with the mean streamwise flow direction and the origin (x = 0 m) was located at the lee-side edge of the pebble cluster. The origin of the y coordinate was at the centre point of the cluster and the z origin was defined at the mean bed elevation within sampling area. The coordinate system was non-dimensionlized (x^+,y^+,z^+) by dividing by the cluster protrusion height, h_s = 0.17 m.

Velocity component orientation followed the right hand rule with positive u in the downstream direction, aligned with the x axis

The two upstream ADVs remained in fixed positions throughout the experiment: (x^+,y^+,z^+) = (-2.4, 0, 0.9) and (0.6, 0, 0.9) while the two downstream ADVs were shifted to specific grid locations. As the four ADVs recorded simultaneously, the purpose of the fixed probes was to allow for the estimation of space-time correlations between the upstream and the downstream measurements. Three-dimensional (3D) instantaneous velocities were measured at 40 locations downstream of the cluster over two intersecting orthogonal planes: a horizontal plane at an elevation of $z^+ = 0.9$ above the bed; and a vertical plane along the centerline of the cluster ($y^+ = 0$). The bed topography and sampling locations are presented in Figure 6.1.

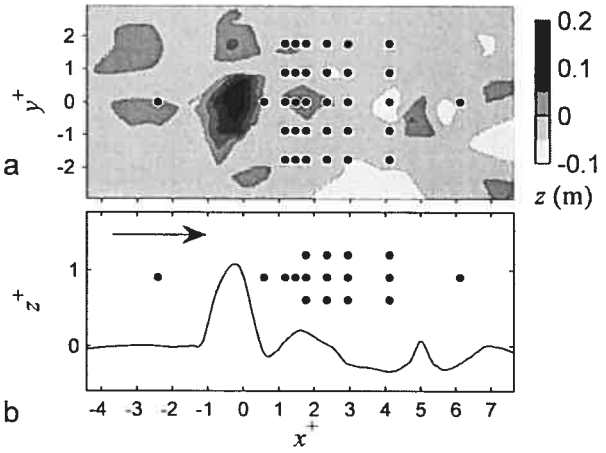

Figure 6.1. Bed topography; (a) Plan view; (b) Side view. Black dots represent sampling locations of the velocity measurements. Flow is from left to right (modified from *Lacey and Roy* [2006]).

The shear layer was further characterized through the simultaneous recording of digital video sequences. A Sony digital video camera housed in a water-proof case was attached to the support frame and positioned underwater at a lateral distance of 0.6 m from the centerline of the cluster. A neutrally buoyant tracer made of non-toxic white latex paint with river water was injected continuously into the recirculation zone directly behind the cluster at x^+,y^+ = (0,0) where it could be passively entrained into the overlying shear layer. The video camera was oriented to give a side view (x-z plane) which included the lee side of the pebble cluster and two probes directly downstream of the cluster. Sets of simultaneous digital film and instantaneous velocities were recorded

for five different longitudinal centerline positions of (x^+,y^+,z^+) = (1.2, 0, 0.9), (1.5, 0, 0.9), (1.8, 0, 0.9), (2.4, 0, 0.9), and (2.9, 0, 0.9).

The sampling frequencies for the ADVs and the digital video camera were 25 Hz and 30 Hz, respectively. Instantaneous longitudinal, U, lateral, V, and vertical, W, velocities were recorded for 100 s, as recommended by *Buffin-Bélanger and Roy* [2005], with the exception of the time series sets recorded simultaneously with the digital videos. These time series ranged between 4 min and 7.5 min in length. Video record lengths ranged between 2 and 6 min.

6.2.2. Data treatment

Instantaneous velocity time series were visually inspected for irregularities and atypical spikes. With the exception of the velocities measured in the near-wake, the majority of the velocity signal correlations were above the recommended cutoff (70%). It has been suggested that failure to remove velocity values with correlation lower than 70%, introduces bias into both mean velocity values and turbulence statistics [*Lane et al.*, 1998]. The velocities measured in the near shear layer had mean signal correlations of between 65% and 70%, most likely induced by the high velocity shear occurring in the ADV sampling volume. These time series were kept for the analysis in spite of having lower signal correlations as these measurements were crucial for characterizing the dynamics of the shear layer. While the velocity spectra of these few signals indicated an adequate fit with the Kolmogorov -5/3 law in the inertial subrange, these near-wake time series may have introduced a bias in our estimated near-field turbulence statistics.

The U, V, and W velocity time series, were back transformed to beam velocities and de-spiked using the *Goring and Nikora* [2002] phase-space thresholding method replacing them with interpolated values based on adjacent time-step velocities. In order to keep the auto- and cross-correlations of the velocity signals non-biased, a low-pass filter was not applied to the time series as is commonly done to remove possible aliasing effects [e.g. *Venditti and Bauer*, 2005]. The detrended velocity time series were tested for stationarity using a reverse arrangement test at a significance level $\alpha = 0.05$ [*Bendat and Piersol*, 1986]. All data series were found to be stationary.

In the field, care was taken to align the support frame and the ADVs with the streamwise flow direction, and therefore time-averaged lateral velocities, $\overline{V}$, measured

at upstream and distal downstream locations (x^+ = -2.4 and x^+ = 6.2) were expected to be close to zero. Nevertheless, $\overline{V}$ was found to be systematically offset by a mean angle of 8.5°. All velocity time series were, therefore, rotated in the lateral plane, using polar coordinates, by an angle of 8.5°.

Image intensity, I_n, time series were obtained by extracting blue and red hue saturation values, HSVs, from each digital image at the estimated ADV sampling volume locations. I_n time series were cross-correlated and synchronized to within one time step of simultaneous velocity measurements following the procedure outlined in *Lacey and Roy* [2006]. The synchronization allowed for a direct comparison between turbulent events estimated in the velocity time series with those observed in the digital films.

Mean turbulence statistics were calculated at each measurement location. These statistics included the root mean squared (RMS), u', v', w'; skewness coefficients, Sk_i, kurtosis coefficients, K_i, (the third and forth statistical moments of velocity); turbulent kinetic energy $k_e = 0.5(u'^2 + v'^2 + w'^2)$; mean Reynolds shear stresses, $-\rho\overline{uv}$, $-\rho\overline{uw}$, and $-\rho\overline{vw}$, where ρ is the water density and u, v and w represent the fluctuating velocity components (e.g. $U = \overline{U} + u$) and the overbar represents time-averaged quantities.

The longitudinal, u, component integral time scales, ITS_u, were estimated by integrating the u component autocorrelation coefficient, R_{uu}, over time:

$$ITS_u = \int_0^{t_1} R_{uu}(\Delta t)\,dt \tag{6.1}$$

$$R_{uu}(\Delta t) = \frac{\frac{1}{n}\sum_{k=1}^{n} u(t_k)\cdot u(t_k + \Delta t)}{(u')^2} \tag{6.2}$$

where t_1 is the time step for the first zero crossing or for which the correlation is not significantly different than zero (α = 0.05) and Δt is the time lag. ITS_u is a rough measure of the interval over which u is correlated with itself and gives an indication of the average duration of turbulent coherent flow structures.

Maximum space-time correlations, $R_{ik}(\Delta x,\Delta y,\Delta z,\Delta t_{max})$, were estimated between the fixed probe locations and all downstream measurement points. The time-shifted cross-correlation coefficient, R_{ik}, or space-time correlation, STC, is estimated by:

$$R_{ik}(\Delta x,\Delta y,\Delta z,\Delta t)=\frac{\frac{1}{n}\sum_{p=1}^{n}\upsilon_i(x,y,z,t_p)\cdot\upsilon_k(x+\Delta x,y+\Delta y,z+\Delta z,t_p+\Delta t)}{\upsilon_i'\upsilon_k'} \tag{6.3}$$

where i, k and p are indices; υ represents the i or k velocity component, for time series measured at x,y,z and $x+\Delta x,y+\Delta y,z+\Delta z$, respectively. Δx, Δy and Δz are the longitudinal, lateral and vertical separation distances, respectively. The variable $R_{ik}(\Delta x,\Delta y,\Delta z,\Delta t_{max})$ is the maximum R_{ik} for all possible values of Δt at each x, y, z location, where Δt_{max} is defined as the time lag where maximum correlation occurs. $R_{ik}(\Delta x,\Delta y,\Delta z,\Delta t_{max})$ functions correspond to the trajectory of time-averaged turbulent coherent structures advecting downstream of the fixed probe locations.

Velocity power spectra, $S_{ii}(f)$, were estimated using discrete fast Fourier transforms (fft) of each data series by:

$$S_{ii}(f)=\frac{2}{Tn}\left|\tilde{\upsilon}_i(f)\right|^2 \tag{6.4}$$

$$\tilde{\upsilon}_i(f)=\int_{-\infty}^{\infty}\upsilon_i(t)e^{(-j2\pi ft)}dt \tag{6.5}$$

where $\upsilon_i(t)$ is the time domain signal of the u, v or w velocity component while $\tilde{\upsilon}_i(f)$ is the frequency domain signal. T is the sampling interval, n is the number of velocity measurements in the series, f is the frequency. Velocity spectra were smoothed using *Welch*'s [1967] averaging method using 20 non-overlapping rectangular windows for the n = 2500 series, and 23 to 45 non-overlapping rectangular windows for the series recorded simultaneously with the digital videos. 95% confidence intervals for individual power spectra were estimated based on a χ^2 distribution with between 40 to 90 degrees of freedom depending of record length [*Bendat and Piersol*, 1986].

Cross-spectra, $S_{ik}(f)$, were used to estimate coherency squared spectra, $\gamma_{ik}^2(f)$. $S_{ik}(f)$ represent the power that the two velocity spectra have in common at specific frequencies while $\gamma_{ik}^2(f)$ is a measure of the cross-correlation between velocity components over specific frequencies:

$$S_{ik}(f) = \frac{2}{Tn}\upsilon_i(f)\upsilon_k(f) \tag{6.6}$$

$$\gamma_{ik}^2(f) = \frac{|S_{ik}(f)|^2}{S_{ii}(f)S_{kk}(f)} \tag{6.7}$$

where i and k are indices for the three velocity components. $\gamma_{ik}^2(f)$ spectra were smoothed with double the number of rectangular windows as for their respective $S_{ii}(f)$ as the windows were overlapped by 50%.

Quadrant analysis was conducted to identify and characterize turbulent events within the velocity time series. The analysis was performed solely on the centerline measurements at y^+,z^+ = (0,0.9) which were recorded simultaneously with the digital videos. Quadrant events were detected using *Lu and Willmarth* [1973]; where outward interactions,Q1 = $\{u > 0, w > 0\}$; ejections, Q2 = $\{u < 0, w > 0\}$; inward interactions, Q3 = $\{u < 0, w < 0\}$; and sweeps, Q4 = $\{u > 0, w < 0\}$. Quadrants were evaluated using two threshold hole sizes, H, where:

$$H = \frac{|uw|}{u'w'} \tag{6.8}$$

Hole sizes of H = 0 and H = 2 were selected in accordance with previous studies [*Bennett and Best*, 1995; *Buffin-Bélanger and Roy*, 1998; *Sambrook Smith and Nicholas*, 2005]. Frequency and duration of events, as well as, the maximum shear stress and the total shear stress per event were estimated.

The interpolation procedure for the spatial distribution plots (i.e., site topography and turbulence variables) is based on a Delaunay triangulation of the spatially distributed measured points which are smoothed based on a shape-preserving piecewise cubic interpolation method.

6.3. Results

6.3.1. Time-averaged mean and turbulence statistics

The unobstructed time-averaged longitudinal velocity , $\overline{U}$, is 80 cm s^{-1} at z/Z = 0.35. $\overline{U}$ decreases by 50% in the near-wake to a value of 46 cm s^{-1} at z^+ = 0.9, and by more than 90% closer to the bed at z^+ = 0.6. The turbulent activity in all three dimensions is well summarized through the turbulent kinetic energy, k_e (Figure 6.2). In the near-wake of the

cluster, $k_e = 830$ cm^2 s^{-2}, which is an increase of a factor of 4 compared with values at $y^+ = \pm 1.8$ (outside of the wake zone). The zone of elevated k_e slopes towards the bed with downstream distance indicating bed values of k_e may be quite high in the wake of the cluster. The spatial distribution of k_e in the x-y plane is mostly symmetric about the centerline x axis and the width of the wake seems to be limited by the dimensions (width) of the cluster. The spatial distribution of k_e, including its increased magnitude towards the bed, is quite similar to that of the uw mean Reynolds shear stress (Figure 6.3). The spatial distribution of the mean Reynolds shear stresses demonstrates the dominance of the $-\rho\overline{uw}$ stress compared with $-\rho\overline{uv}$ and $-\rho\overline{vw}$; $-\rho\overline{uw}$ is 3 to 5 times greater in magnitude in the wake of the cluster than the other two stresses reaching values of 25 N m^{-2} in the near-wake of the cluster at $x^+,y^+ = (1.5,0)$. The lateral extent of the high magnitude $-\rho\overline{uw}$ zone is relatively narrow, is centered behind the cluster and extends towards the bed. While the magnitude of $-\rho\overline{uv}$ is much less than for $-\rho\overline{uw}$, it does show an increase closer to the bed. $-\rho\overline{vw}$ values are relatively small in magnitude, but unlike the other two Reynolds shear stresses, they are relatively symmetric in both the x-y and the x-z planes.

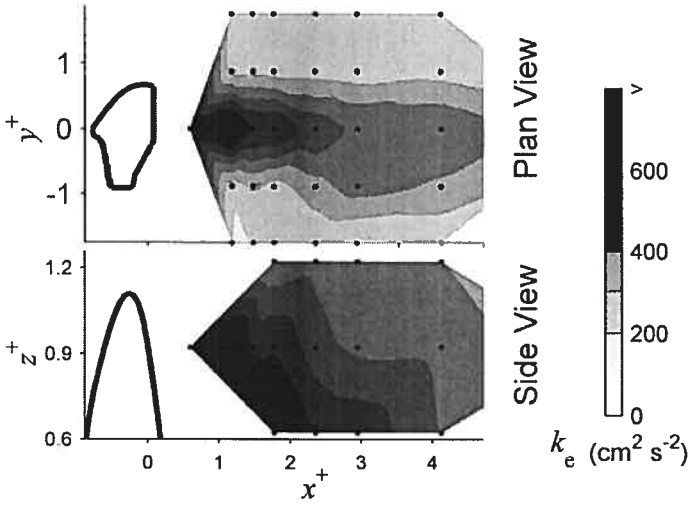

Figure 6.2. Plan and side views of turbulent kinetic energy k_e. Black dots represent sampling locations of the velocity measurements. Flow is from left to right. Cluster location is represented by thick black line.

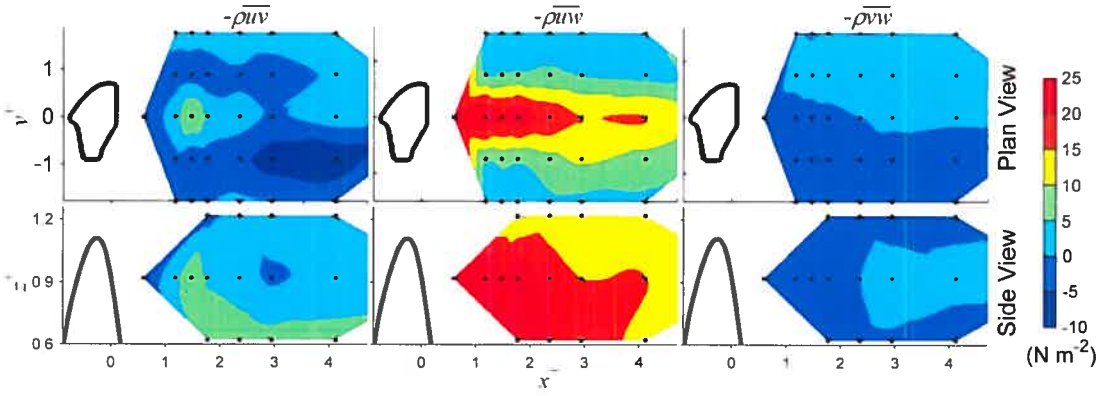

Figure 6.3. Plan and side views of mean Reynolds shear stresses, $-\rho\overline{uw}$. Black dots represent sampling locations of the velocity measurements. Flow is from left to right. Cluster location is represented by thick black line.

6.3.2. Spectral analysis

Details of the pebble cluster wake and shedding behaviour were investigated using spectral analysis. Figure 6.4 presents velocity power spectra, $S_{ii}(f)$, and coherency squared spectra, $\gamma_{ik}^2(f)$, for 5 measurement locations correspond to: an upstream centerline location – representing the unobstructed flow condition (Figure 6.4a-b); two downstream centerline locations (Figure 6.4c-f); and two downstream right side locations (Figure 6.4g-j). All velocity spectra (Figure 6.4a,c,e,g,i) display regions of constant $f^{-5/3}$ slope at higher frequencies indicative of the inertial subrange. At low frequencies, velocity spectral power display similar relationships between velocity components where $S_{uu}(f) > S_{vv}(f) > S_{ww}(f)$. The estimated velocity spectra do not collapse perfectly in the inertial subrange and the slight deviation of slope in the horizontal velocity components is likely due to the presence of Doppler noise which is inherent in acoustic backscatter systems [*Voulgaris and Trowbridge*, 1998]. Due to the ADV transducer configuration, the horizontal velocity components contain significantly higher noise levels than for the vertical component [*Voulgaris and Trowbridge*, 1998].

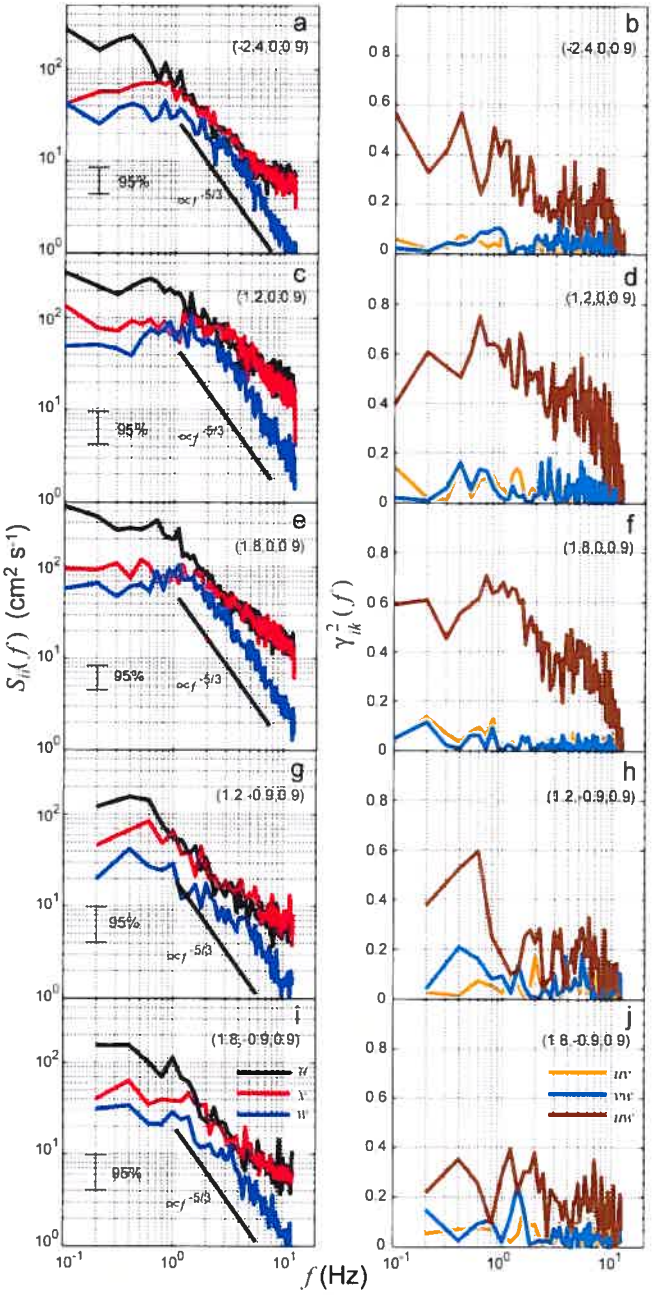

Figure 6.4. Velocity power spectra, $S_{ii}(f)$ and coherency squared spectra, $\gamma^2_{ik}(f)$. The spectra are estimated at x^+,y^+,z^+ measurement locations: (a-b) (-2.4,0,0.9); (c-d) (1.2,0,0.9); (e-f) (1.8,0,0.9); (g-h) (1.2,-0.9,0.9); (i-j) (1.8,-0.9,0.9)

Noticeable differences are seen in Figure 6.4 when comparing upstream spectra (Figure 6.4a-b) with those estimated from downstream locations (Figure 6.4c-j). Along the centerline at x^+,y^+,z^+ = (1.2,0,0.9) and (1.8,0,0.9) peaks in $S_{ww}(f)$ are observed at f = 1.3 Hz, and f = 1.0 Hz, respectively (Figure 6.4c,e). These peaks are less apparent for

$S_{uu}(f)$ and $S_{vv}(f)$. This peak frequency is attributed to vortices shedding from the shear layer caused by the cluster and is consistent with the result with previous submerged pebble cluster studies [*Lacey and Roy*, 2007a]. Along the centreline, the peaks in $S_{ww}(f)$ correspond well with the lower frequency peaks observed in the *uw* component coherency squared spectra, $\gamma^2_{uw}(f)$ (Figure 6.4d,f). The coherency squared spectra in the centerline wake of the cluster indicate a dominance of $\gamma^2_{uw}(f)$ compared with the other two cross-correlation spectra $\gamma^2_{uv}(f)$ and $\gamma^2_{vw}(f)$. This suggests that the vortices shedding from the lee of the cluster at $y^+ = 0$ have predominantly lateral axes and hence that most of the turbulent momentum exchange in the wake of the cluster is driven by lateral oriented "roller" eddies. The $\gamma^2_{uw}(f)$ are distinctly bimodal in the cluster wake, which is very apparent for $\gamma^2_{uw}(f)$ at $x^+ = 1.8$ (Figure 6.4f) where a higher frequency peak also occurs at about $f = 5$ Hz. This higher frequency peak is imperceptible in the $S_u(f)$ (Figure 6.4e). No obvious peaks are observed in the $S_u(f)$ estimated from the velocity measurements obtained along the downstream right side of the cluster at $y^+ = -0.9$ (Figure 6.4g,i). While $\gamma^2_{uw}(f)$ values are not as high as for the downstream centerline measurements, $\gamma^2_{uw}(f)$ still dominates $\gamma^2_{uv}(f)$ and $\gamma^2_{vw}(f)$ over the entire frequency range estimated (Figure 6.4h,j).

6.3.3. Correlation analysis

The *u* component integral time scale, ITS_u, decreases in the cluster wake and displays a complex asymmetric pattern in the *x*-*y* plane (Figure 6.5). Upstream at $x^+,y^+,z^+ = (-2.4, 0, 0.9)$, $ITS_u = 0.25$ s (not shown), while in the near-wake and in proximity to the bed $ITS_u = 0.1$ s. A similar decrease in ITS_u in the wake of a pebble cluster has been previously observed by [*Buffin-Bélanger and Roy*, 1998]. The high ITS_u values estimated to the left of the cluster, $y^+,z^+ = (0.9,0.9)$ downstream at $x^+ = 1.5$, $x^+ = 1.8$ and $x^+ = 2.4$ are perhaps because these measurement points lie just outside of the wake region (as suggested by Figure 6.2) and therefore represent unperturbed ITS_u values.

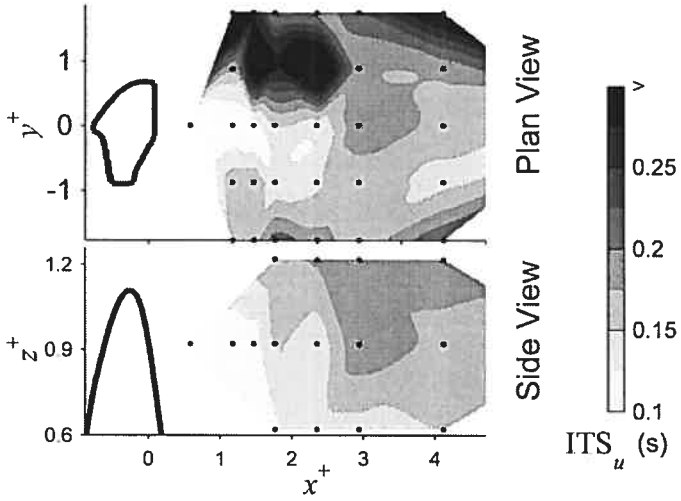

Figure 6.5. Plan and side views of u component integral time scale, ITS_u. Black dots represent sampling locations of velocity measurements. Flow is from left to right. Cluster location is represented by thick black line.

Maximum u component space-time correlations, $R_{uu}(\Delta x,\Delta y,\Delta z,\Delta t_{max})$, were estimated between the two upstream measurement locations, x_o^+,y_o^+,z_o^+ = (-2.4, 0, 0.9) and (0.6, 0, 0.9), and all downstream locations (Figure 6.6). The spatial distribution of $R_{ik}(\Delta x,\Delta y,\Delta z,\Delta t_{max})$ gives a measure of the mean pathways of the time averaged turbulent coherent structures by estimating regions of strongest correlation as the structures advect downstream. A marked asymmetry in the x-y plane is observed in the spatial distribution of $R_{uu}(\Delta x,\Delta y,\Delta z,\Delta t_{max})$ of Figure 6.6a. Similarly to the ITS_u distribution, there is a significant reduction in $R_{uu}(\Delta x,\Delta y,\Delta z,\Delta t_{max})$ in the near-wake of the cluster at $y^+ = 0$, $z^+ = 0.9$ and towards the bed at $z^+ = 0.6$. This reduction is likely due the coherent structures shed from the cluster which dominate the hydrodynamics in the near-wake region. These highly turbulent structures have little coherency with the larger-scale structures advecting from upstream. The asymmetric significant correlation values to the right side of the cluster at $y^+ = 0.9$ is likely a reflection of the specific geometry of the pebble cluster investigated and represent a predominance of flow from the upstream measurement point towards the right side of the cluster. Figure 6.6b presents the $R_{uu}(\Delta x,\Delta y,\Delta z,\Delta t_{max})$ obtained between the measurement location directly downstream of the cluster x_o^+,y_o^+,z_o^+ = (0.6,0,0.9) and all downstream measurement locations. Unlike for the previous cross-correlations (Figure 6.6b), the spatial distribution of $R_{uu}(\Delta x,\Delta y,\Delta z,\Delta t_{max})$ is quite symmetrical in the x-y plane and indicates

that the correlated structures advect predominantly in the longitudinal direction. $R_{uu}(\Delta x,\Delta y,\Delta z,\Delta t_{max})$ values in the x-z plane are practically one dimensional with a strong gradient in the longitudinal direction. The decreasing correlation gradient is caused by the gradually deformation of the velocity fluctuations by the surrounding flow field causing a loss in coherence with the upstream measurement point [*Cenedese et al.*, 1991]. The $R_{ik}(\Delta x,\Delta y,\Delta z,\Delta t_{max})$ values estimated for the v and the w components, while not presented here, show similar spatial patterns and trends as those shown for the u component, yet the magnitude and persistence of the cross-correlations are substantially less with $R_{uu}(\Delta x,\Delta y,\Delta z,\Delta t_{max}) >> R_{ww}(\Delta x,\Delta y,\Delta z,\Delta t_{max}) > R_{vv}(\Delta x,\Delta y,\Delta z,\Delta t_{max})$.

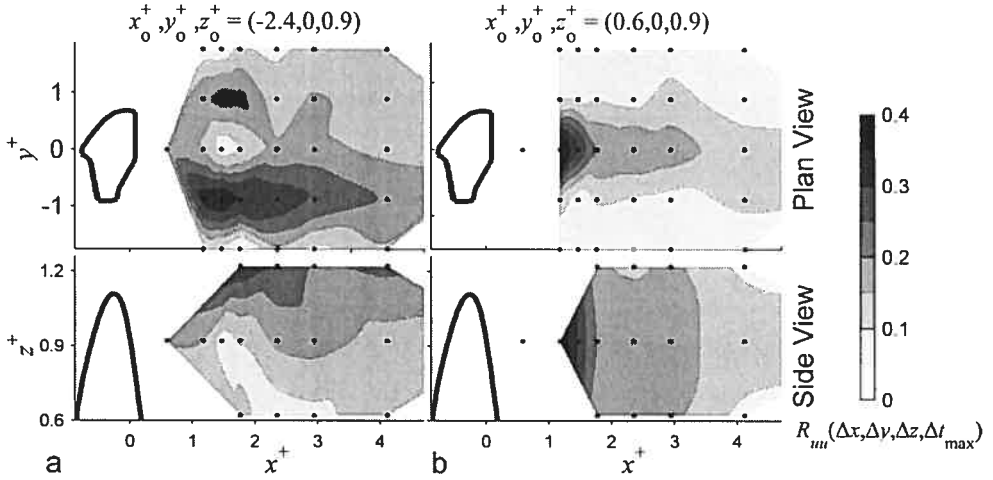

Figure 6.6. Plan and side views of (a) u component maximum space-time correlations, $R_{uu}(\Delta x,\Delta y,\Delta z,\Delta t_{max})$. Between measurements at x = -0.4 m and all downstream measurements and (b) between measurements at x = 0.1 m and all downstream measurements. Black dots represent sampling locations of the velocity measurements. Flow is from left to right. Cluster location is represented by thick black line.

6.3.4. Quadrant analysis

Figure 6.7 shows the fractional contributions of each quadrant to the time-averaged uw component Reynolds shear stress, $-\rho\overline{uw}$, for hole sizes, H = 0 and H = 2 along the centerline at z^+ = 0.9 (z/Z = 0.35). The dominance of Q2 and Q4 events, over Q1 and Q3 events, is clearly shown throughout the centerline transect, where the combined Q2 and Q4 contributions account for approximately 80% of the total Reynolds stress (both positive and negative). More specifically, Q2 events dominate the fractional contribution at both hole sizes investigated for all measurement locations with the exception of the location closest to the lee side of the cluster in the near wake (x^+ = 0.6). The dominance

of Q2 events corroborates laboratory dune studies [*Bennett and Best*, 1995] and rough-wall studies [*Nakagawa and Nezu*, 1977]. Both *Sambrook Smith and Nicholas* [2005] and *Buffin-Bélanger and Roy* [1998] observed more complex relationships between Q2 and Q4 events which were inversed as hole size increased from $H = 0$ to $H = 2$. Our results, on the contrary, demonstrate an insensitivity to the Q2/Q4 ratio with increased hole size.

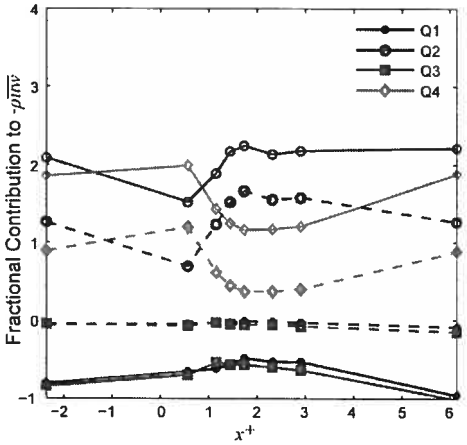

Figure 6.7. Fractional contribution of quadrants to local *uw* component mean Reynolds stress, $-\rho\overline{uw}$, for hole sizes, $H = 0$ (solid lines) and $H = 2$ (dashed lines). Lee edge of cluster is positioned at $x^+ = 0$. Estimates are for eight measurement points along the centerline $y^+ = 0$ at $z^+ = 0.9$ for eight longitudinal locations $x^+ = -2.4$, $x^+ = 0.6$, $x^+ = 1.2$, $x^+ = 1.5$, $x^+ = 1.8$, $x^+ = 2.4$, $x^+ = 2.9$, and $x^+ = 6.2$.

Given the very low fractional contribution of Q1 and Q3 events, the rest of the analysis presented here concentrates on Q2 and Q4 events. The statistical distribution of maximum instantaneous shear stress per event, $-\rho uw_{Max}$, for the centerline measurements was investigated through box-plots for $H = 0$ and $H = 2$ (Figure 6.8). The frequency of events is shown to be highest in the near-wake at $x^+ = 0.6$ and decreases with downstream distance for both Q2 and Q4 events. Similarly to the previous fractional contribution plot, the dominance of Q2 events for both hole sizes investigated is apparent in Figure 6.8. Extreme events are not only much more prevalent for Q2 than for Q4 but they as well have much higher $-\rho uw_{Max}$ than for Q4 events. Some of these Q2 extreme events, specifically in the near-wake at $x^+ = 1.2$ to $x^+ = 1.8$ have double the $-\rho uw_{Max}$ than Q4 extreme events with values reaching 500 N m^{-2}. These extreme events, produced only in the wake of the cluster, are very infrequent, yet incorporate a very large shear stress – more than an order of magnitude greater than median values ($H = 0$).

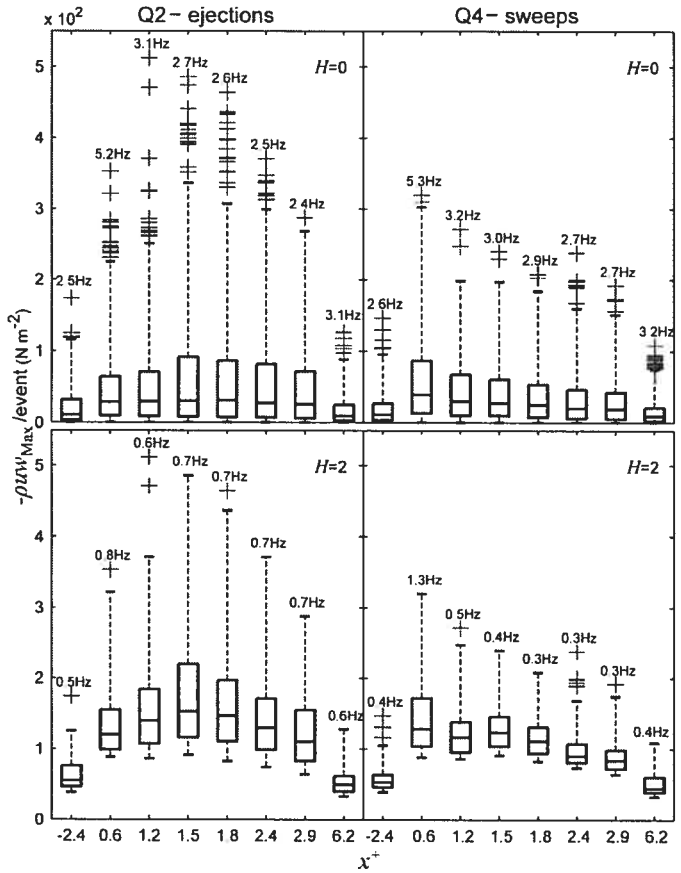

Figure 6.8. Distribution of maximum $-\rho uw$ per Q2 and Q4 event at two hole sizes $H = 0$ and $H = 2$. Box-plots estimate measurement points along the centerline $y^+ = 0$ at $z^+ = 0.9$ for eight longitudinal locations $x^+ = -2.4$, $x^+ = 0.6$, $x^+ = 1.2$, $x^+ = 1.5$, $x^+ = 1.8$, $x^+ = 2.4$, $x^+ = 2.9$, and $x^+ = 6.2$. Cross points represent extreme values beyond 3 times the interquartile range. Frequencies of occurrence are presented at the top of each box-plot.

Previous *in situ* river studies have estimated negative power law relationships between event frequency and duration where less frequent events have a greater duration and visa versa [*Paiement-Paradis et al.*, 2003; *Roy et al.*, 2004]. Figure 6.9a-b shows inverse relationships between $\overline{-\rho uw_{Max}}$ and frequency of event occurrence for six centerline measurement locations. As well, the magnitude of $\overline{-\rho uw_{Max}}$ is higher in the wake of the cluster than at the upstream or distal downstream locations. Figure 6.9c-d presents the sum of $-\rho uw$ for Q2 and Q4 events as a function of event frequency. While Figure 6.9a-b indicates that less frequent (and longer duration) events contain much higher $\overline{-\rho uw_{Max}}$ their contribution to the total $-\rho uw$ is much less than intermediate events (Figure 6.9c-d). Inspection of individual series in Figure 6.9c-d reveal marked

peaks in Σ-ρuw which shift to lower frequencies with distance downstream from the pebble cluster. Particularly clear is the peak Σ-ρuw for the Q4 events at $x^+ = 0.6$ (Figure 6.9d).

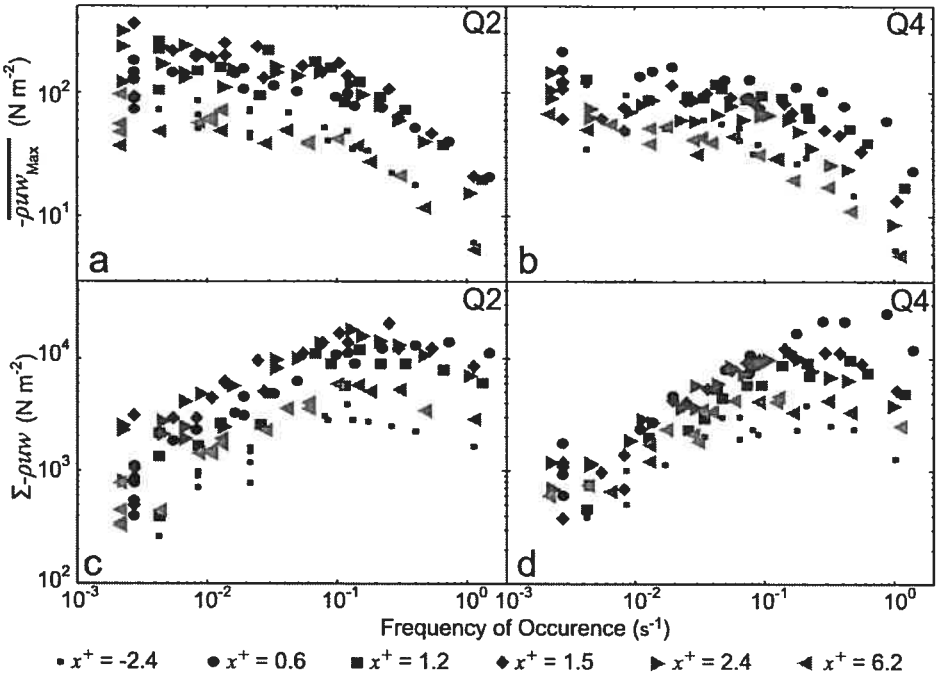

Figure 6.9. -ρuw versus frequency of Q2 and Q4 events.(a-b) Average maximum -ρuw per event, $-\overline{\rho uw}_{Max}$, versus frequency of occurrence. (c-d) Sum of -ρuw per event at each frequency of occurrence. Estimates are for measurement points along the centerline $y^+ = 0$ at $z^+ = 0.9$ for six longitudinal locations $x^+ = -2.4$, $x^+ = 0.6$, $x^+ = 1.2$, $x^+ = 1.5$, $x^+ = 2.4$, and $x^+ = 6.2$.

6.3.5. Skew and kurtosis coefficient analysis

The skewness coefficient is a measure of the symmetry of a probability density function of turbulent fluctuations and provides complementary results to quadrant analysis for characterizing turbulent events. A negative skewness is an indication that, relatively rare, large negative values are more frequent than large positive values (i.e., negative Sk_u indicates that low-speed events are more dominant than high-speed events). A negative Sk_u along with a positive Sk_w indicates the occurrence of strong ejection events within the velocity signal. u, w and uw skew coefficients for centerline measurements $z^+ = 0.9$ are presented in Table 6.1. With the exception of the measurement location at $x^+ = 0.6$, negative Sk_u and positive Sk_w are estimated in the wake indicating the occurrence of strong ejection events. The negative Sk_{uw} shown in the

wake indicates the occurrence of strong *-uw* events. The strength of the skew values increase with distance downstream obtaining maximum values of $x^+ = 1.8$ and subsequently diminish in magnitude with further distance downstream. Skew coefficients estimated from velocity measurements in the wake closer to the bed at $z^+ = 0.6$ were of opposite sign (i.e., positive Sk_u and negative Sk_w) indicating the presence of strong sweep events. Similar spatial trends of skewness in the wake of a pebble cluster have been observed by *Buffin-Bélanger and Roy* [1998]. Positive Sk_u close to the bed and negative Sk_u is as well consistent previous rough-bed studies [*Nakagawa and Nezu*, 1977; *Raupach*, 1981]. The intermittency of turbulence in the wake was investigated by estimating kurtosis coefficients, K_i, and intermittency factors, $\xi = 3.0/K_{uw}$ [*Batchelor*, 1970] for the centerline velocity measurements (Table 6.1). K_u and K_w values along the centerline wake hardly deviate from the Gaussian distribution ($K = 3.0$), yet K_{uw} values show high intermittency. Minimum ξ occurs at $x^+ = 1.8$ where the intermittent large contributions to the Reynolds stress occur 21% of the total time.

Table 6.1. Skewness and kurtosis coefficients and intermittency factors for *u*, *w* and *uw* time series estimated from eight centerline measurement locations at $y^+ = 0$ and $z^+ = 0.9$.

x^+	Sk_u	Sk_w	Sk_{uw}	K_u	K_w	K_{uw}	ξ
-2.4	-0.13	0.09	-1.62	2.73	2.88	8.54	0.35
0.6	-0.05	-0.09	-1.64	2.98	2.58	8.36	0.36
1.2	-0.35	0.33	-2.00	3.04	2.82	12.13	0.25
1.5	-0.52	0.56	-2.37	3.10	3.18	13.35	0.22
1.8	-0.57	0.60	-2.53	3.16	3.19	14.39	0.21
2.4	-0.55	0.56	-2.32	3.08	3.27	12.65	0.24
2.9	-0.48	0.55	-1.98	2.94	3.24	10.41	0.29
6.2	-0.17	0.13	-1.24	2.79	2.88	7.85	0.38

6.3.6. Visualization

Visualization of the shear layer and associated shedding processes provided an invaluable complement to the analysis of instantaneous velocity time series analysis. Two distinct frequency modes of shedding were observed and visually estimated as approximately $f = 5$ Hz and $f = 1$ Hz. These two modes are in good agreement with those estimated through spectral analysis, $\gamma^2_{uw}(f)$ of the downstream centerline measurements (Figure 6.4d,f). The high frequency structures shed from the lee edge of the cluster with a high periodicity, yet once detached from the cluster top their detection and behaviour is intermittent. Figure 6.10a-d presents the two most common behaviours observed.

Figure 6.10a-b shows an example where the small-scale vortices do not interact and advect downstream either parallel to the bed surface or with an up or down trajectory. Figure 6.10c-d presents the situation where the small-scale vortices interact with one another. Here two small-scale vortices can be seen to pair together soon after shedding from the top of the cluster. Both of these behaviours are highly intermittent. The interaction and mixing of the initial instability vortices and the entrainment of the surrounding fluid was seen to give rise to secondary, larger-scaled structures (Figure 6.10e-f). These structures shed downstream at a frequency $f = 1$ Hz which is in good agreement with the shedding frequency ($f = 0.85$ Hz) estimated by $Sr = h_s f / \overline{U}$, where a Strouhal number, $Sr = 0.18$ was used [*Achenbach*, 1974].

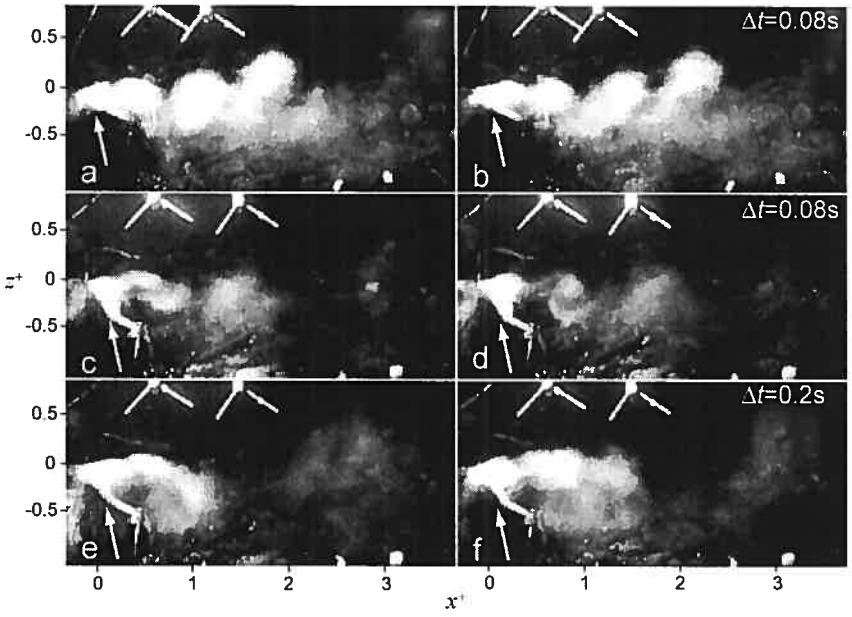

Figure 6.10. Digital image pairs, separated by Δt, presenting characteristic shedding behaviour: (a-b) shedding of individual initial instability vortices, mode 1; (c-d) pairing of two initial instability vortices; (e-f) formation and shedding of h_s scaled structures, mode 2. Flow is from left to right. Arrow indicates tracer injection location.

The behaviour of the shear layer under the influence of large-scale (LS) coherent flow structures advecting from upstream was investigated through the synchronized visualization technique outlined by *Lacey and Roy* [2006]. While the shear layer was found to respond by ejecting upwards under the passage of LS low-speed events, as previously described by *Roy et al.* [1999], on many occasions the response would be mitigated or opposite to the expected behaviour. A sequence of six images

demonstrating the response of the shear layer to two sequential LS low-speed events is presented in Figure 6.11. The second event in the $-\rho uw$ time series (Figure 6.11b) has a peak $-\rho uw$ = 116 N m^{-2} placing it within the top 10 strongest events measured at x^+ = -2.4. The x^+ = -2.4 time axes (abscissa) is synchronized with the x^+ = 0.6 time series by subtracting the mean coherent structure advection time, 0.76 s, between x^+ = -2.4 and x^+ = 0.6 determined through STC analysis. In the first image at t = 0.4 s, the shear layer is parallel to the bed before it expands upward into the outer flow layer at t = 0.7 s under the influence of the LS low-speed (ejection) event advecting from upstream measured at x^+ = -2.4 (Figure 6.11b). The event is identified in both the $-\rho uw$ plots at x^+ = 0.6 and at x^+ = 1.2; but its duration is shortened in these time series by the occurrence of a Q4 event at t = 1 s and t = 1.1 s, respectively. The second exceptionally high magnitude ejection event observed in the upstream time series (x^+ = -2.4) passes overtop of the cluster at t =1.0 s but has little noticeable effect on the shear layer.

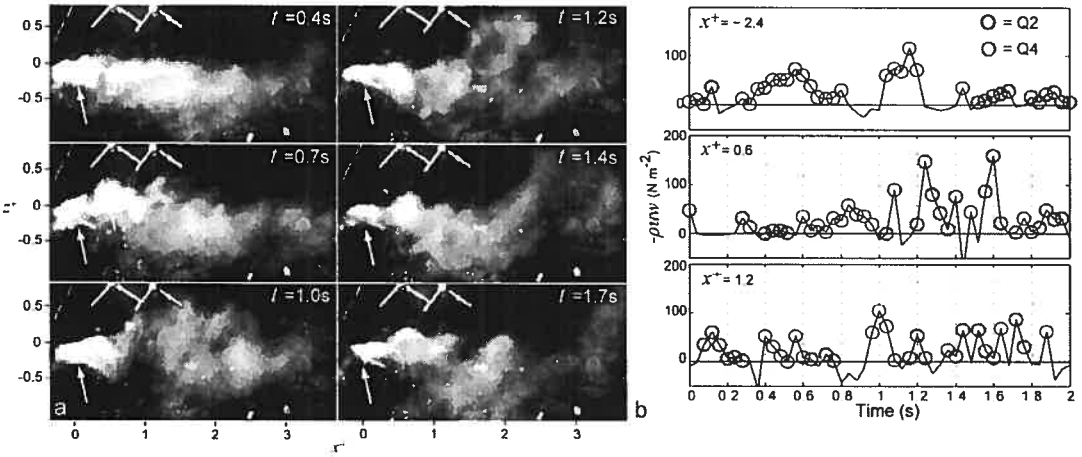

Figure 6.11. (a) Sequence of 6 enhanced images detailing the behaviour of the shear layer with the passage of LS ejection structures advecting from upstream for t = 0.4 s; t = 0.7 s; t = 1.0 s; t = 1.2 s; t = 1.4 s; t = 1.7 s; (b) $-\rho uw$ time series for measurement positions x^+ = -2.4, x^+ = 0.6, and x^+ = 1.2. Quadrant 2 and Quadrant 4 contributions are presented as dark and pale circles, respectively. The x^+ = -2.4 time series, has been synchronized with the x^+ = 0.6 location. Flow is from left to right. Arrow indicates tracer injection location.

A second digital sequence and corresponding $-\rho uw$ time series is presented in Figure 6.12 and demonstrate the behaviour of the shear layer to the passage of a sweep event observed upstream. The $-\rho uw$ x^+ = 1.2 time series includes the 5th strongest Q2 event, $-\rho uw_{Max}$= 325 N m^{-2}, estimated at x^+ = 1.2. The image sequence starts at t = 0.6 s

where a dip in the shear layer associated with the passage of the sweep event is shown. The shear layer then bulges up and curls in the clockwise direction (t = 0.8 s to t = 0.9 s). The high $-\rho uw$ in the x^+ = 0.6 time series seems to be related to the front edge of the rotating structure as proposed by *Shvidchenko and Pender* [2001] for LS coherent structures. The structure itself appears to be an agglomeration of many small-scale vortices. At t = 1.1 s, the structure collapses down towards the bed and is advected downstream. The large ejection event measured at x^+ = 1.2 (t = 1.5 s) does not appear to be related to the sweep event or to the passage of LS low-speed structures from upstream.

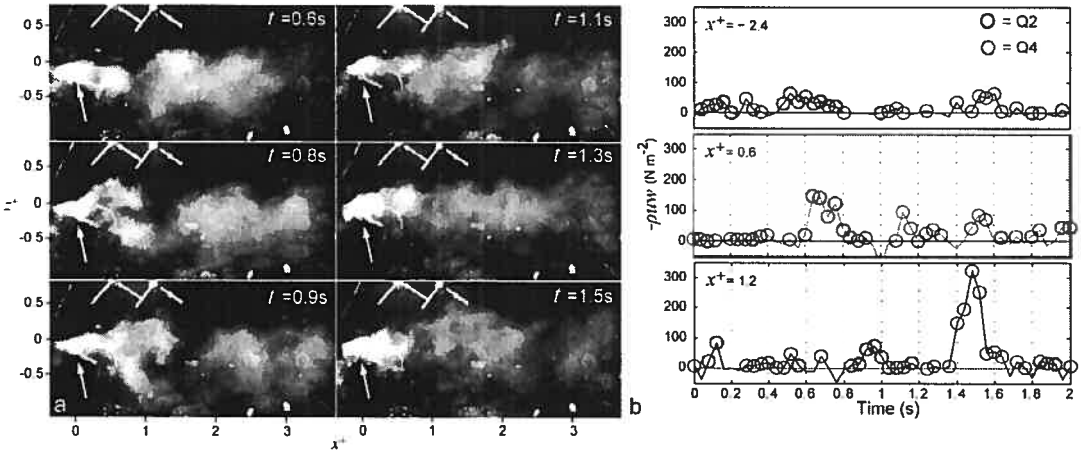

Figure 6.12. (a) Sequence of 6 enhanced images detailing the behaviour of the shear layer with the passage of LS sweep and ejection structures advecting from upstream for t = 0.6 s; t = 0.8 s; t = 0.9 s; t = 1.1 s; t = 1.3 s; t = 1.5 s; (b) $-\rho uw$ time series for measurement positions x^+ = -2.4, x^+ = 0.6, and x^+ = 1.2. Quadrant 2 and Quadrant 4 contributions are presented as dark and pale circles, respectively. The x^+ = -2.4 time series, has been synchronized with the x^+ = 0.6 location. Flow is from left to right. Arrow indicates tracer injection location.

6.4. Discussion

Our study provides a detailed *in situ* characterization of the surrounding flow field and shear layer of an instream pebble cluster. Through flow visualization and analysis of velocity measurements, two shedding modes were identified: a small-scale higher frequency initial instability mode and a meso-scale lower frequency mode which arising through the interaction and mixing of the small-scale vortices and the entrainment of the surrounding fluid. This two-scale model corroborates the observations of *Hasan* [1992]

and is supported by the downstream centerline $\gamma^2_{uw}(f)$ plots (Figure 6.4d,f) which display bimodal $\gamma^2_{uw}(f)$ peaks at similar frequencies to those observed through visualization. The downstream $\gamma^2_{uw}(f)$ plots and the spatial distribution of Reynolds shear stresses indicate that the cluster wake is dominated by *uw* turbulent momentum exchange driven by lateral oriented "roller" eddies. The shedding lateral vortices detected through quadrant analysis (of the instantaneous velocity wake measurements) give an event signature of frequent Q4 and strong Q2 events which dominate the fractional contribution to the local shear stress (Figure 6.7 and 6.8).

The dominance of lateral vortices is remarkable especially in view of the recent studies showing the importance of vertical vortices shedding from instream boulders [*Tritico and Hotchkiss*, 2005]. The apparent contradiction in results is perhaps linked to the relative roughness of the boulder investigated. Unlike the study of *Tritico and Hotchkiss* [2005], who investigated boulders that protruded above the water surface, our study examines a submerged roughness element (with a relative roughness of 0.4). This suggests that the importance of vertical vortices is likely to increase with relative roughness.

The spatial description of k_e and elevated values in the pebble cluster wake is consistent with previous studies [*Lacey and Roy*, 2007a]. The increased k_e towards the bed has been observed in past bedform studies using two dimensional (*u*,*w*) measurements [*Bennett and Best*, 1995; *Buffin-Bélanger and Roy*, 1998]. Similarly with previous laboratory dune studies [*McLean et al.*, 1994; *Bennett and Best*, 1995; *Kadota and Nezu*, 1999] the point of highest magnitude $-\rho\overline{uw}$ occurs further downstream from the point of boundary layer separation and the location of the expected maximum velocity gradient ($d\overline{U}/dz$). In our experiment, the maximum $-\rho\overline{uw}$ occurs at $x^+ = 1.5$ and is due to the more intermediate frequency shedding structures demonstrated by the peaks in the Σ-ρuw plots (Figure 6.9c). The peak Σ-ρuw is shown to shift from higher to more intermediate frequencies with downstream distance supporting the view that the shedding structures are interacting and growing into larger coherent structures.

An estimation of the size of the shedding structures can be obtained by applying the Taylor's frozen turbulence hypothesis (FTH) and multiplying the ITS_u values by the

site specific $\overline{U}$. The applicability of the FTH is certainly in question in our case due to very high turbulent intensity in the wake but does give a rough estimate of the turbulent macro-length scales, L_u. Application of the FTH results in L_u = 0.04 m and L_u = 0.13 m estimated at x^+ = 0.6 and x^+ = 2.9, respectively. These length scales fit well with the length scales of the two shedding modes observed in the digital images (Δx = 0.05 m and Δx = 0.18 m [*Lacey and Roy*, 2007b] and the meso-scale shedding mode is approximately the same size as the cluster height, h_s = 0.17 m.

The fractional contribution to local shear stress estimates indicate a dominance of Q2 events over all centerline measurement locations at both hole sizes with the exception of the near-wake at x^+ = 0.6 where Q4 events dominate. *Bennett and Best* [1995] observed high Q4 contributions in the shear layer close to the lee face of their laboratory dunes and attributed this to topographic forcing and the inrush of high speed fluid towards the bed. Similarly to our results, *Bennett and Best* [1995] also observed higher frequency of Q4 and high magnitude Q2 events in the near wake zone and suggested the interaction and pairing of vortices as one possible mechanism for these energetic events. Qualitative inspection of the digital images and simultaneous velocity time series suggest that the front downward rotating portion of individual shedding eddies is detected as a Q4 event while the tail end of the eddies is detected as a Q2 event. These results are likely dependent on the measurement location (i.e., height above the bed) and would likely result in a dominance of Q4 events closer to the bed as observed by *Bennett and Best* [1995].

The simultaneous digital video and instantaneous velocity measurements enabled us to describe and understand the intermittent behaviour of the shear layer and its interaction with large-scale turbulent flow structures. While the small-scale shedding frequency is quite regular initially, as the structures detach they are influence by the surrounding flow field and undergo a range of morphological and behavioural changes (Figure 6.10). The shedding structures are observed to intermittently occupy much of the *x-z* plane by alternately advecting downstream with upward, parallel and downward trajectories. Reasons for the irregular behaviour are undoubtedly related to the highly complex turbulent flow and high Reynolds number which distort and shear the coherent structures over short distances as seen by the quick dissipation of the injected tracer.

Variability in shear layer response to the passage of LS structures has been previously observed [*Buffin-Bélanger et al.*, 2001a], yet some consistent trends emerge such as the expansion and ejection upwards of the shear layer with the passage of LS low-speed (ejection) events, and the collapse of the shear layer towards the bed with the passage of LS high-speed (sweep) events. The variability in the shear layer behaviour (e.g. extent of expansion and contraction) may be an indication that certain physical processes in this complex flow environment are not fully understood and require further investigation.

6.5. Conclusions

While we present the results of a single submerged cluster, its size and relative roughness is typical of many submerged isolated elements in our study reach and in other gravel-bed rivers. The physical processes we observed are fundamental to shear flows which have general identifiable characteristic structures [*Fuchs et al.*, 1980] regardless of the environment where they are investigated. While *in situ* studies are difficult to undertake, particularly in high *Re* environments, they provide important confirmation of laboratory findings. The highly detailed analysis presented here allowed the *in situ* identification of the bimodal shedding and the dominance of lateral vortices in the wake of submerged roughness elements. The in-depth analysis has also confirmed and further detailed the behaviour of the shear layer under the influence of LS coherent structures. The dominance of longitudinal-vertical turbulent momentum exchange in the wake of the pebble cluster has several implications. For instance, recent studies suggest that fish use vertical vortices for energy conservation [*Liao et al.*, 2003b]. If vertical vortices are intermittent and do not dominate the wake region of submerged large roughness elements, then these zones could not be readily utilized by fish. Furthermore, the wake region in our study is characterized by the highest k_e and uw Reynolds shear stress extending towards the bed. Turbulence is positively correlated with fish bioenergetics (causing fish stress) [*Enders et al.*, 2003] and the high turbulence in the wake of the cluster likely constitutes unfavourable fish habitat. Elevated strong ejection and sweep events are instrumental in the transport suspended and bedload sediments, respectively [*Bennett and Best*, 1995; *Williams et al.*, 1989].

Linking Paragraph D

Each of the previous article chapters in this thesis focuses on the hydrodynamics associated with a single (isolated) LRE. The results of these chapters have provided invaluable information on the (scale dependent) spatial patterns of turbulence around LREs, on shear layer processes and on the interaction between shedding vortices and LS coherent flow structures. While the shear layer processes have some general applicability, the generalization of LRE effects on turbulent structure remains difficult due to a lack of replicate observations. To specifically address this issue, the following final article chapter[4] characterizes the 3D flow field overtop of and around *multiple* instream submerged cobbles, boulders and pebble clusters under varied flow conditions with the specific aim of investigating the LRE geometrical effects, LRE hydrodynamic interactions and the dependence of these hydrodynamics on mean flow conditions. The results from Chapters 5 and 6 were critical for interpreting the spatial patterns of the turbulence variables observed in Chapter 7. Spatially distributed high frequency 3D velocity measurements were recorded *in situ* using acoustic Doppler velocimeters at different flow stages. The spatial distribution of turbulent kinetic energy, k_e, longitudinal component integral time scale, ITS_u and mean Reynolds shear stresses was characterized and is presented for selected sites. The relative importance of longitudinal-vertical, *uw*, Reynolds shear stress was observed to increase with flow stage compared with the longitudinal-lateral, *uv*, and lateral-vertical, *vw*, Reynolds shear stresses and to dominate at the highest flow stages sampled. Canonical redundancy analysis, a technique used in Chapter 4 for describing the spatial-scale relationships among turbulence statistics, was applied to relate roughness element morphometrics and mean flow conditions to the turbulent parameters estimated in the cluster wake (i.e., k_e, mean Reynolds shear stresses and ITS_u). Large roughness element morphometrics such as lateral width explained the highest proportion of the variance in the turbulent wake variables, while mean free-stream velocity explained the second highest proportion of the variance.

---

[4]Lacey, R.W.J. and A.G. Roy (*submitted 03/10/07*), The spatial characterization of turbulence around large roughness elements in a gravel-bed river, *Geomorphology*.

7. THE SPATIAL CHARACTERIZATION OF TURBULENCE AROUND LARGE ROUGHNESS ELEMENTS IN A GRAVEL-BED RIVER

7.1. Background

Large roughness elements (LREs) such as pebble clusters and boulders are considered to be the most prevalent microtopographic feature of poorly sorted gravel-bed rivers and have been found to occupy as much as 10% of the river bed [*Brayshaw*, 1984]. These features enhance bed stability as they interlock and imbricate with the surrounding substrate limiting the availability of readily transportable particles and delaying their incipient motion [*Brayshaw*, 1984]. It has further been suggested that their spatial arrangement tends towards maximum flow resistance [*Hassan and Reid*, 1990]. This occurs when the spatial arrangement (or density) of LREs is such that the length of the turbulent wake is approximately equal to the distance downstream to the next aligned LRE.

Numerous studies have investigated the wake characteristics of isolated hemispheres in laboratory flumes [*Brayshaw et al.*, 1983; *Best and Brayshaw*, 1985; *Paola et al.*, 1986; *Acarlar and Smith*, 1987; *Shamloo et al.*, 2001] while relatively few investigations have been carried out on LREs in natural rivers [*Buffin-Bélanger and Roy*, 1998; *Tritico and Hotchkiss*, 2005; *Lacey and Roy*, 2007a; *Lacey and Roy*, 2007c]. Common characteristics are a flow separation zone, shear layer instability and the associated shedding vortices. *Lacey and Roy* [2007c] showed the presence of intense Reynolds stresses for the longitudinal-vertical, *uw*, velocity components in the wake of an in situ LRE. Through spectral analysis and visualization, they have related the intense turbulent activity to shedding lateral vortices. *Tritico and Hotchkiss* [2005] have characterised the turbulent flow field downstream of three water surface emergent boulders, one of which was sampled at three flow stages. They demonstrated the importance of vertical oriented vortices for surface protruding elements but did not examine in detail the flow stage induced changes. Opposite circulation of vertical vortices downstream of LREs may be identified by zones of positive and negative longitudinal-lateral, *uv*, Reynolds stress [*Tritico and Hotchkiss*, 2005] which may occur

in high magnitude parallel elongated zones to the right and left side of LRE wakes. The studies of *Buffin-Bélanger and Roy* [1998] and *Lacey and Roy* [2007a] provide a detailed spatial characterization of the in situ flow field around isolated cobbles and pebble clusters. The focus of these studies was to isolate the fundamental in situ turbulent processes but a generalization of these results is restricted. This is because only a single roughness element was investigated in each study; the roughness elements were isolated; and each element was subject to a single flow condition.

An important application of a detailed characterisation of the hydrodynamics around in situ roughness elements is to establish relationships between roughness elements and the presence and behaviour of aquatic biota such as fish. Such relationships are helpful to develop guidelines for stream rehabilitation projects. Judging from the inconsistent results between fish preference in the presence of roughness elements and the associated turbulence production, these relationships are complex. Fish density has been found to increase with added boulder clusters [*Van Zyll de Jong et al.*, 1997; *Dolinsek et al.*, 2007a;b] and has been positively correlated with mean turbulent values measured around LREs [*Smith et al.*, 2006]. Conversely, turbulence induces higher swimming costs and causes stress to the fish [*Enders et al.*, 2003]. Fish have also been found to select positions near cover with low average velocities and low turbulence values and to avoid low-velocity, high-turbulence locations [*Smith et al.*, 2005; *Cotel et al.*, 2006]. Laboratory research by *Liao et al.* [2003b] has suggested that fish take advantage of vertical vortices by adapting a specific energy saving swimming pattern synchronized to the shedding vortices. Yet, in situ research on gravel-bed rivers has indicated that lateral vortices are not the dominant form of momentum transfer in the lee of submerged roughness elements and shedding vortices are aperiodic [*Lacey and Roy*, 2007c]. While the wake region of LREs is characterized by high turbulent activity causing fish stress, fish preference for LREs may be due to other beneficial physical or biotic factors which outweigh the negative effects induced by turbulence. For instance pebble clusters have copious interstitial spaces and crevices for invertebrates (and fish) to dwell and their stability during flood events is an asset for the biota [*Biggs et al.*, 1997] and visual isolation induced by added boulders has been shown increase densities for territorial fish species [*Dolinsek et al.*, 2007a;b].

The objectives of this study are to characterise and compare the hydrodynamics of several naturally occurring LREs in a gravel-bed river and to determine the turbulence response to changes in flow stage, mean free-stream longitudinal velocity, and LRE morphometry. A further objective is to identify functional relationships between mean flow variables and LRE morphometrics; and time-averaged turbulent wake parameters through regression analysis. Due to the large number of interrelated variables, a multivariate statistical approach, canonical redundancy analysis (RDA), is used. RDA is a multivariate extension of multiple regression allowing for the simultaneous analysis of many explanatory and response variables. A multivariate regression approach is valuable for our study as it identifies the independent variables (mean flow variables and LRE morphometrics) which explain the greatest amount of variance in the turbulent wake parameters. Based on known physical relationships between explanatory and response variables and aided by a forward selection procedure redundant, highly correlated, variables can be identified and removed. High frequency three-dimensional (3D) velocity measurements were recorded at 10 sites which contained isolated or multiple naturally occurring submerged LREs covering a variety of morphometries. A subset of sites was resampled under several flow conditions. The detailed characterization of turbulent flow patterns around LREs provided here leads to a deeper understanding of their general hydrodynamic effect in rivers and of their potential role in aquatic biota habitat.

7.2. Field Measurements

Ten study sites with large roughness elements (LREs) were selected along a 100 m reach of the Eaton North River in the Eastern Townships, Quebec, Canada. The Eaton North is a gravel-bed river with a bankfull width of approximately 30 m and a median grain size of 35 mm over the sampling reach. The bankfull flow for the river estimated from a gauging station just upstream of the study reach is approximately 30 $m^3 s^{-1}$. The grain size distribution is poorly sorted with several large clasts (intermediate b axis > 0.20 m) distributed throughout the reach. Three SonTek acoustic Doppler velocimeters (ADVs) supported by a rigid aluminium square frame, 1.5 m by 1.5 m, were used to measure instantaneous 3D velocities at the ten sites. The frame was positioned overtop

of selected large roughness elements (LREs) consisting of cobbles, boulders, and pebble clusters. The sites were selected based on our objective to document the effects of flow stage, relative submergence and LRE geometry on turbulent wake characteristics. Of the ten sites investigated, five contained isolated LREs, while the other five contained multiple LREs. Within the multiple LRE set, three sites contained laterally aligned elements. For sites with isolated LREs, the frame was positioned such that the LRE was located in the upstream central portion of the frame. When sites consisted of multiple LREs, the frame was positioned in order to obtain velocity samples from the wake zones of each LRE included within the frame. This relative positioning of the frame was a subjective process and in some instances the extent of the wake zones of certain LREs could not be determined. The flow field of six sites was resampled at different flow stages. Field markers inserted into the riverbed were used to help reposition the frame at the same place on subsequent sampling events. Initial and repositioned frame locations were measured using a Trimble series 5000 total station to quantify the repositioning error. The mean longitudinal, x, and lateral, y, difference between sampled and resampled frame locations is 0.021 m and 0.037 m, respectively. Careful frame repositioning insured that instantaneous velocity measurements were resampled at the same in situ locations (under different flow conditions). The bed topography of each site was mapped using an average 200 total station measurement points. Each LRE was specifically characterized by approximately 25 measurements.

3D instantaneous velocities were measured over two longitudinal-lateral, x-y, planes – an upper and lower plane located above and below the top of the LREs. Due to shallow depths at Site 8, only a lower plane could be measured. For six sites (Site 4-7, 9, 10) velocities were re-sampled at one or two different flow stages. The mean relative height, z/Z, of all the upper measurement planes (averaged over 9 sites and flow stages) is 0.47 while the mean z/Z for the lower level planes is 0.27. For the six resampled sites, the mean z difference in upper level plane measurements is 0.009 m, while the mean z difference for the lower plane measurements is 0.007 m. Instantaneous velocities were measured over a 1.2 m by 1.2 m square grid with a spacing of 0.2 m in both x and y. This sampling density resulted in approximately 49 locations per x-y plane. A total of approximately 1760 three component velocity time series were measured during the

entire experiment. The instantaneous longitudinal, U, lateral, V, and vertical, W, velocities were recorded at a frequency, f, of 25 Hz during 100 s, as recommended by *Buffin-Bélanger and Roy* [2005]. Examples showing the sampling grid for the velocity measurements and the bed topography for six different sites (Sites 2, 3, 5, 7, 8, and 10) are presented in Figure 7.1.

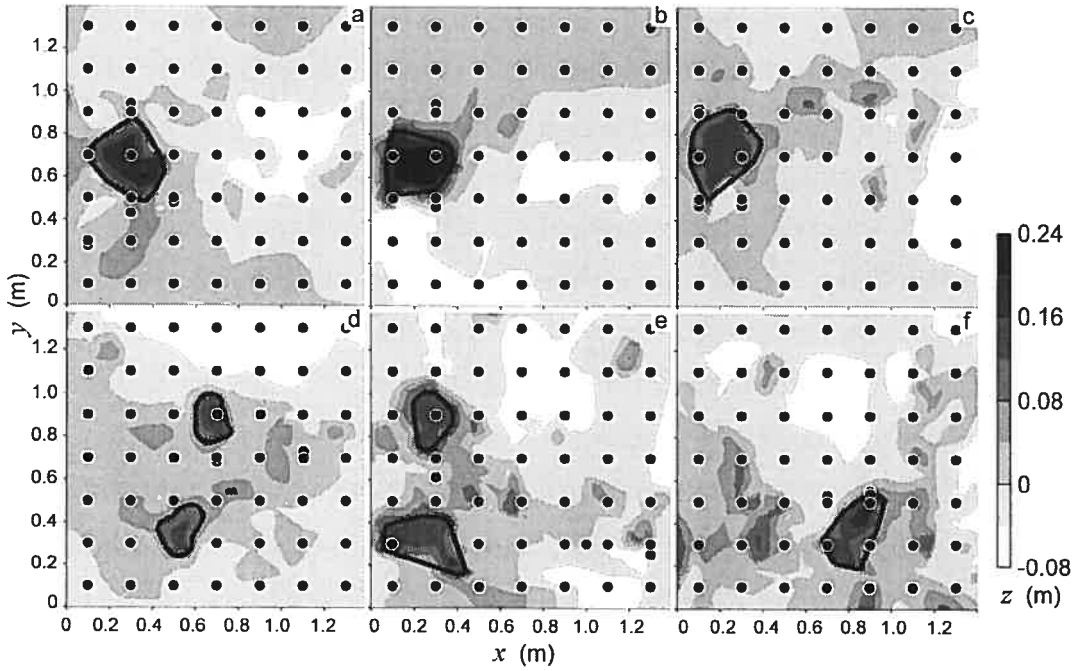

Figure 7.1. Plan view of bed topography: (a) Site 3, (b) Site 5, (c) Site 7, (d) Site 2, (e) Site 8, (f) Site 10. Black dots represent sampling locations of the velocity measurements. Flow is from left to right. LRE x-y cross-section plotted as thick black line.

7.3. Data Analysis and Treatment

Using the support frame as the reference which was aligned with the mean longitudinal streamlines using tracer ribbons, a Cartesian coordinate system x,y,z was defined as the longitudinal (streamwise), lateral (cross-stream), and vertical dimensions, respectively. The x coordinate is aligned with the mean streamwise flow direction and the origin x,y = (0,0) at each site is located at the upstream right-hand corner of the sampling area and the z origin is defined as the mean bed elevation within each sampling area. The orientation of the streamwise, lateral and vertical velocity components followed the right hand rule with positive u in the downstream direction, aligned with the x axis, positive v towards the left bank and positive w towards the water surface.

The digital elevation model (DEM) derived from the topographic measurements was used to estimate morphometrics of the largest roughness element of each site. The interpolation procedure for estimating the DEM (and the spatial distribution plots of the turbulence variables) is based on a Delaunay triangulation of the spatially distributed measured points which are then smoothed using on a shape-preserving piecewise cubic interpolation method. The morphometric measurements included the protrusion height, h_s; lateral width, $\varnothing_s$; lateral projection area (parabolic segment estimation), $A_s = 2/3 h_s \cdot \varnothing_s$ and relative submergence, Z/h_s. h_s was estimated using the mean height of the highest three points measured with the total station on top of the LRE. A mean value was used as it better represents the height of the LRE over the full lateral width instead of at a single isolated point across the irregular LRE surface. $\varnothing_s$ was estimated from the DEMs at the same height as the lower plane ADV velocity measurements (z_{Lw}). The $\varnothing_s$ at this height (outlined in Figure 7.1) was thought to be the most relevant width metric for the lower plane ADV measurements. The DEMs were used to estimate the LRE morphometrics due to the difficulties of accurately measuring the morphometrics underwater using a straight ruler. It was felt that LRE morphometric estimates made from the DEMs would offer more consistent estimates between sites. Sites 2 and 8 contained two large roughness elements of approximately equal size and therefore both were included in the analysis (e.g., 8R1 and 8R2).

Instantaneous velocity time series were visually inspected for irregularities and atypical spikes. All velocity series with average velocity signal correlations below 70% were rejected as it has been suggested that failure to remove velocity values with low correlation, < 70%, introduces bias into both mean velocity values and turbulence statistics [*Lane et al.*, 1998]. Spectral analysis was used as a secondary means of detecting problems in the velocity signals. At higher frequencies and high Reynolds numbers, velocity spectra should tend towards local isotropic turbulence indicated by a -5/3 slope as predicted by Kolmogorov's theory for the inertial subrange [*Tennekes and Lumley*, 1972]. Velocity time series which produced generally flat spectra in this range due to excessive signal noise were removed from further analysis. The U, V, and W velocity time series were back transformed to beam velocities and velocity spikes were removed using the *Goring and Nikora* [2002] phase-space thresholding method

replacing them with interpolated values based on adjacent time-step velocities. While attempts were made in the field to align the support frame and the ADVs with the longitudinal flow direction, spatial mean time-averaged lateral velocities, $< \overline{V} >$, were slightly offset from zero (where the overbar represents time-averaged quantities and the angled brackets represent spatially averaged quantities). All velocity time series measured at a site were, therefore, rotated in the horizontal plane, such that $< \overline{V} > = 0.0$ m s^{-1}. A rotation was also performed on the time series obtained from sites that were resampled at several flow stages. The velocity series were detrended and tested for stationarity using a reverse arrangement test at a significance level, α, of 0.05 [*Bendat and Piersol*, 1986]; all data series were found to be stationary.

Flow parameters for the upper and lower measurement planes estimated for each site include: mean water depth, Z; sampling plane height, z; sampling plane relative height, z/Z; mean free-stream velocities estimated outside the roughness element wake zone for upper, $\overline{U}_{Up}$, lower, $\overline{U}_{Lw}$, and interpolated to $z/Z = 0.4$, $\overline{U}_{0.4}$; Froude number, Fr; and Reynolds number, Re (based on Z and $\overline{U}_{0.4}$). Time-averaged turbulence statistics were estimated at each measurement location. These included velocity component root mean square, u', v', w'; turbulent kinetic energy $k_e = 0.5(u'^2 + v'^2 + w'^2)$; Reynolds shear stresses, $-\rho\overline{u'v'}$, $-\rho\overline{u'w'}$, and $-\rho\overline{v'w'}$, where ρ is the water density and u, v and w represent the fluctuating velocity components (e.g., $U = \overline{U} + u$). The longitudinal, u component integral time scale, ITS_u, was estimated by integrating the u component autocorrelation coefficient, R_{uu}, over time:

$$ITS_u = \int_0^{t_1} R_{uu}(\Delta t)\,dt \tag{7.1}$$

where

$$R_{uu}(\Delta t) = \frac{\frac{1}{n}\sum_{k=1}^{n} u(t_k)\cdot u(t_k + \Delta t)}{(u')^2} \tag{7.2}$$

where t_1 is the time step for the first zero crossing or for which the correlation is not significantly different than zero at $\alpha = 0.05$; and Δt is the time step. ITS_u is a rough measure of the interval over which u is correlated with itself and gives an indication of the average duration of turbulent coherent flow structures.

7.3.1. Redundancy analysis

We used bivariate plots and correlation coefficients to identify significant relationships between mean flow and LRE morphometric (explanatory) variables and time-averaged wake statistics (response variables). Special focus was paid to the LRE wake zone, as previous studies have shown that the predominant hydrodynamic effects of LREs occur in the wake [*Lacey and Roy*, 2007a]. Given the large number of both explanatory and response variables investigated, a multivariate analysis technique, canonical redundancy analysis (RDA), was used to extract the most significant relationships between variables. The RDA technique alleviates the difficulties of evaluating each explanatory variable (or multiple variables) in turn, which can be an encumbering task given the number of possible permutations between explanatory and response variables. RDA is an extension of multiple linear regression used to model multivariate data and provides an efficient means of summarising explained variance and correlations between numerous variables. This technique assumes linear relationships between explanatory and response variables, but known nonlinear relationships can be incorporated into the RDA by preprocessing the explanatory data sets (i.e., taking cross-products or powers of terms). Nonlinear transformations should only be chosen with theoretical underpinnings otherwise results become difficult to interpret. *Legendre and Legendre* [1998] argue that the best statistical model is the simplest one that adequately describes the relationships between a response and explanatory variables.

RDA is based on the eigenvalue decomposition of the table of regressed fitted values, it reduces the large number of associated (linearly correlated) fitted vectors to a smaller composite of linearly independent variables [*Legendre and Legendre*, 1998]. In RDA, each canonical ordination axis corresponds to a direction in the response variable space that is maximally correlated to a linear combination of the explanatory variables. RDA is used extensively in ecological studies and has shown its usefulness in explaining turbulent flow spatial relationships [*Lacey et al.*, 2007]. RDA graphically displays their regressed interrelationships through correlation biplots [*ter Braak*, 1994]. The contribution of the independent variables to the explanation of the response variables is given by the bimultivariate redundancy statistic, canonical R^2, and its adjusted form, canonical R_a^2 [*Peres-Neto et al.*, 2006].

A table of possible explanatory variables for RDA was compiled (Table 7.1) incorporating roughness element morphometrics, mean flow parameters, a metric representing the quadratic stress law, $\rho\overline{U}^2$; and a metric representing drag force, $0.5A_s\rho\overline{U}^2$. The full forms of the quadratic stress law and the drag force equation which include a drag coefficient, C_d, were not used due to the difficulty of defining C_d which is dependent on body shape and *Re* and is usually obtained through experimentation. The quadratic stress law and drag force metrics were specifically added to the analysis to incorporate their well known nonlinear relationships with turbulence statistics which could not be captured using only first degree variables such as $\overline{U}$. Turbulence statistics were estimated from the instantaneous velocities measured in the wake region of the largest roughness element of each site and include: $k_{e\text{-max}}$; distance to $k_{e\text{-max}}$, Δx_{ke}; $ITS_{u\text{-min}}$; $-\rho\overline{uv}_{max}$; $-\rho\overline{uw}_{max}$; and wake area, A_{wk}. Δx_{ke} was defined as the longitudinal distance downstream from the roughness element lee edge where $k_{e\text{-max}}$ was observed. Due to the discreet nature of the sampling scheme the above turbulence statistics likely do not represent the true maximum and minimum values which may be somewhat higher or lower. While $k_{e\text{-max}}$, $ITS_{u\text{-min}}$, $-\rho\overline{uv}_{max}$ and $-\rho\overline{uw}_{max}$ were estimated directly from the ADV measurements, A_{wk} was estimated from the interpolated *x*-*y* planar area downstream of the roughness element where k_e values were a factor of 1.5 times greater than the standard deviation of the spatially distributed planar k_e values, k_e'. Several thresholds were tested, and the $k_e > 1.5\,k_e'$ was found to give a good balance between minimizing false detections and maximizing the zone of high k_e values observed in the lee of the LRE. The estimated A_{wk} is likely conservative as it identifies the zone of relatively high k_e, while the true wake area where flow is influenced by the LRE may be somewhat greater. A_{wk} is estimated from interpolated values and is therefore dependent on the interpolation method used (i.e., cubic interpolation) and on the ADV measurement grid spacing. Given the relative coarseness of the ADV measurements (0.2 m in both *x* and *y*) an exact identification of the wake zone was difficult. The coarse grid spacing may as well have resulted in a slight underestimation of the true peak values of k_e and of the Reynolds stresses. From the estimated wake dimensions (where $k_e >$

$1.5\,k_s'$), lateral wake widths, $\varnothing_{wk}$, and longitudinal wake lengths, L_{wk}, were as well estimated for discussion purposes but were not included in the RDA.

Table 7.1. Large roughness element morphometrics and mean flow variables[a]

Site	h_s, m	$\varnothing_s$, m	A_s, m^2	Z/h_s	Z, m	z_{Up}, m	z_{Lw}, m	$\overline{U}_{Up}$, $m\,s^{-1}$	$\overline{U}_{Lw}$, $m\,s^{-1}$	$\overline{U}_{0.4}$, $m\,s^{-1}$	Re, $*10^5$	Fr	$\rho\overline{U}^2$, $N\,m^{-2}$	$0.5A_s\rho\overline{U}^2$, N
1	0.18	0.33	0.039	2.1	0.37	0.21	0.11	0.82	0.66	0.72	2.61	0.38	513	9.94
2R1	0.14	0.23	0.021	2.4	0.33	0.14	0.08	0.80	0.64	0.77	2.51	0.43	596	6.20
2R2	0.13	0.24	0.021	2.5	0.33	0.14	0.08	0.80	0.64	0.77	2.51	0.43	596	6.18
3	0.19	0.39	0.048	2.0	0.37	0.19	0.08	0.67	0.53	0.62	2.24	0.33	384	9.14
4A	0.12	0.20	0.016	3.8	0.46	0.26	0.12	0.54	0.48	0.51	2.32	0.24	255	2.05
4B	0.12	0.20	0.016	4.4	0.55	0.25	0.11	0.68	0.61	0.67	3.60	0.29	442	3.54
5A	0.23	0.30	0.045	1.9	0.45	0.23	0.14	0.60	0.55	0.57	2.54	0.27	328	7.42
5B	0.23	0.30	0.045	2.2	0.51	0.25	0.16	0.74	0.67	0.70	3.55	0.31	494	11.16
5C	0.23	0.30	0.045	2.5	0.57	0.26	0.16	0.87	0.80	0.85	4.77	0.36	721	16.30
6A	0.18	0.37	0.043	2.6	0.46	0.26	0.16	0.64	0.59	0.60	2.76	0.28	360	7.80
6B	0.18	0.37	0.043	3.5	0.61	0.27	0.17	0.85	0.80	0.84	5.11	0.34	706	15.29
7A	0.14	0.41	0.038	1.9	0.26	–[b]	0.08	–[b]	0.62	0.62[c]	1.59	0.39	387	7.40
7B	0.14	0.41	0.038	2.5	0.36	0.18	0.09	0.74	0.59	0.68	2.40	0.36	463	8.86
7C	0.14	0.41	0.038	3.3	0.47	0.18	0.09	0.78	0.63	0.78[d]	3.62	0.37	614	11.74
8R1	0.14	0.27	0.025	2.2	0.31	–[b]	0.12	–[b]	0.69	0.69[c]	2.12	0.40	481	6.02
8R2	0.15	0.28	0.028	2.0	0.31	–[b]	0.12	–[b]	0.69	0.69[c]	2.12	0.40	481	6.78
9A	0.13	0.18	0.015	2.7	0.34	0.17	0.09	0.46	0.41	0.44	1.49	0.24	192	1.43
9B	0.13	0.18	0.015	3.1	0.40	0.19	0.10	0.58	0.52	0.56	2.23	0.29	319	2.38
9C	0.13	0.18	0.015	4.3	0.55	0.18	0.10	0.82	0.70	0.82[d]	4.48	0.35	673	5.01
10A	0.15	0.35	0.035	2.3	0.35	0.17	0.10	0.51	0.46	0.49	1.71	0.26	241	4.24
10B	0.15	0.35	0.035	3.3	0.50	0.18	0.10	0.86	0.77	0.86[d]	4.28	0.39	737	12.95

[a]Ratio values z_{up}/Z and z_{Lw}/Z were also included in the forward selection procedure but are not presented in Table 6.1. The letter index attached to the site number is to identify multiple sampling events; the index increments from low to high flow stages (i.e., $Z(A) < Z(B) < Z(C)$). Sites 2 and 8 have two LREs each labelled R1 and R2.

[b]No data - upper plane velocity measurements were not possible due to insufficient water depth, Z.

[c] $\overline{U}_{Lw}$ value as upper measurements not available

[d] $\overline{U}_{Up}$ value as z_{Up} less than $z/Z = 0.4$

RDA was performed to obtain models for both the upper and lower measurement planes. Prior to RDA computations, a forward selection Monte Carlo permutation procedure from the CANOCO program [*ter Braak and Smilauer*, 2002] was used to determine which independent variables (Table 7.1) explained a significant level (α = 0.05) of variation in the turbulent flow parameters of each model. The forward selection aids in the construction of the RDA models by identifying highly correlated explanatory and non-significant variables, the inclusion of which would decrease the global significance of the model. Correlation coefficients, r, were estimated between the

possible explanatory variables to identify the highly correlated variables. The RDA lower model was further detailed by partitioning the variance between the identified significant variables. Variance partitioning is a way of estimating how much of the variation of the response variable(s) can be attributed exclusively to one or more explanatory variables, once the effect of another set of explanatory variable(s) has been taken into account. All variables were standardized prior to analysis and the RDA was computed using the CANOCO program [*ter Braak and Smilauer*, 2002]. The canonical axes were tested for significance using 9999 Monte Carlo unrestricted permutations. Biplots of canonical eigenvectors and explanatory variables are presented focussing on the correlations between the fitted variables.

7.4. Results

The presentation of the results is divided into four main sections. Initially, selected sites are used to show the diversity and contrast in topographies and LRE morphometrics between sites. The second section briefly discusses the range of values in mean flow, LRE morphometric variables and turbulent wake variables for all sites and also investigates their intracorrelations. Thirdly, the spatial distributions of time-averaged turbulent parameters around LREs are presented for selected sites showing typical patterns observed in the data. Several sites are used as examples to show the small between site differences in time-averaged turbulent parameters. A site with a large isolated boulder, Site 7, which has a moderate h_s of 0.14 m, is shown first. Then the results for other more complex cases (Sites 2, 8, and 10) with multiple LREs are used to show the effect varied LRE geometries. In addition the spatial distributions of the Reynolds stresses around two sites with larger sized isolated LREs, Site 3 and Site 5, are used to show the typical patterns observed at most sites and the effect of rising river stage. Finally, results of bivariate linear regressions and RDA performed on the upper and lower models are shown with the aid of correlation biplots.

7.4.1. Bed topography and LRE morphometrics

In this study, LRE sites were specifically chosen to explore the effects of the variability in bed topography and LRE configurations. To show the range of bed roughness and of LRE morphometrics, the bed topography of six sites (with three isolated LREs and three

multiple LREs) are presented in Figure 7.1. These sites are as well used later on in the results to show examples of the spatial patterns of the turbulence statistics investigated. The site specific LRE *x-y* cross-sections at the height of the lower plane sampling locations is outlined in black in Figure 7.1, while the morphometric variables of the LREs are given in Table 7.1. The standard deviation of bed height, z', at each site was used as a measure to compare the general bed roughness between sites. z' ranged from 0.028 m to 0.052 m with an averaged value $z' = 0.040$ m. The maximum z' was estimated at Site 5 which had the highest protrusion height, h_s. Sites 3, 5, and 7 are dominated by isolated boulders of somewhat rounded shape and varying protrusion heights $h_s = 0.19$ m, 0.23 m, 0.14 m, respectively. Sites 2 and 8 contain two pebble clusters each aligned in the lateral direction, with much smaller elements imbricated in the surrounding bed structure between the two pebble clusters. The clusters of Site 8 are slightly larger than those of Site 2 with protrusion heights of approximately $h_s = 0.15$ m. Site 10 is characterized by a large pebble cluster which is downstream from a sequence of two longitudinally aligned clusters located $x = -0.1$ m and 0.4 m (which are not outlined in Figure 7.1f). The sites with multiple LREs were specifically chosen to investigate the potential interactions between the wakes generated in the lee of each protruding elements.

7.4.2. Flow conditions and turbulent wake statistics

The wide range of experimental conditions investigated in this study (Table 7.1) is not only characteristic of this section of the Eaton North River but is also typical of other gravel-bed rivers. Mean water depths covered a range from $Z = 0.26$ to 0.61 m while mean free-stream *u* component velocities (estimated at $z/Z = 0.4$) varied from $\overline{U}_{0.4} = 0.44 - 0.86$ m s^{-1}. The range of discharges sampled, scaled by bankfull discharge, was approximately from 3% to 17%. Reynolds numbers ranged from $Re = 1.5 \times 10^5$ to 5.1×10^5 and relative submergence ranged from $z/h_s = 1.8$ to 4.4. Table 7.2 presents the matrix of correlation coefficients, *r*, between all possible explanatory variables (mean flow and LRE morphometric variables) for the upper and lower planes of measurement. h_s and $\varnothing_s$ are moderately correlated ($r = 0.41$ and 0.35, for upper and lower planes, respectively) and similarly $\overline{U}_{0.4}$ and Z show correlations of $r = 0.48$ and 0.43 for upper and lower

planes, respectively. Correlations between simple variables are relatively low, while strong spurious correlations are evident between composite variables and the simple variables which compose them (e.g., $\varnothing_s$ and A_s or $\overline{U}_{0.4}$ and $0.5A_s\rho\overline{U}^2$). This was taken into account when developing the RDA statistical models.

Table 7.2. Correlation coefficients, r, between the LRE morphometrics and mean flow variables for the upper and lower planes

Upper / Lower	h_s	$\varnothing_s$	A_s	Z/h_s	Z	τ_{Up}/τ_{Lw}	τ/Z	$\overline{U}_{Up/Lw}$	$\overline{U}_{0.4}$	Re	Fr	$\rho\overline{U}^2$	$0.5A_s\rho\overline{U}^2$
h_s		0.41	0.82	-0.47	0.34	0.69	0.38	0.29	0.16	0.32	-0.09	0.16	0.64
$\varnothing_s$	0.35		0.85	-0.43	-0.09	0.05	0.12	0.21	0.20	0.05	0.25	0.17	0.64
A_s	0.80	0.84		-0.52	0.16	0.44	0.28	0.29	0.21	0.22	0.09	0.19	0.77
Z/h_s	-0.59	-0.42	-0.59		0.66	0.03	-0.65	0.10	0.21	0.54	-0.25	0.24	-0.17
Z	0.31	0.01	0.19	0.57		0.72	-0.34	0.40	0.48	0.88	-0.09	0.49	0.48
τ_{Up}/τ_{Lw}	0.52	0.09	0.37	0.17	0.64		0.40	0.02	0.00	0.43	-0.43	-0.01	0.32
τ/Z	0.29	0.13	0.26	-0.51	-0.35	0.47		-0.49	-0.63	-0.57	-0.47	-0.66	-0.20
$\overline{U}_{Up/Lw}$	0.21	0.30	0.30	0.10	0.42	0.37	0.04		0.98	0.76	0.85	0.97	0.75
$\overline{U}_{0.4}$	0.16	0.25	0.23	0.21	0.43	0.14	-0.27	0.93		0.82	0.82	1.00	0.73
Re	0.28	0.14	0.25	0.46	0.89	0.51	-0.37	0.75	0.78		0.36	0.80	0.68
Fr	-0.03	0.25	0.12	-0.12	-0.28	-0.31	0.00	0.68	0.74	0.16		0.71	0.42
$\rho\overline{U}^2$	0.15	0.23	0.21	0.23	0.46	0.14	-0.30	0.92	1.00	0.84	0.81		0.73
$0.5A_s\rho\overline{U}^2$	0.63	0.68	0.78	-0.22	0.45	0.45	0.01	0.75	0.72	0.70	0.50	0.72	

As with the flow conditions, the turbulence variables estimated for each measurement plane from the wake zone of the LREs show a wide range of values (Table 7.3). Highest magnitudes of $k_{e\text{-}max}$, $-\rho\overline{uw}_{max}$, and $-\rho\overline{uv}_{max}$ were estimated from the lower plane measurements. For the upper plane, $k_{e\text{-}max}$ ranged from $k_{e\text{-}max} = 37 - 336$ cm^2 s^{-2}, while minimum integral time scales ranged from $ITS_{u\text{-}min} = 0.13 - 0.38$ s. Estimated wake areas, A_{wk}, are generally larger for the lower plane where the average for all sites is $A_{wk} = 0.14$ m^2. The lower plane average wake width, $\varnothing_{wk}$, scaled by their respective LRE $\varnothing_s$ is $\varnothing_{wk} = 1.0\varnothing_s$, while the average wake length, L_{wk}, scaled by LRE h_s, is $L_{wk} = 3.4h_s$. The highest magnitude $k_{e\text{-}max}$, $-\rho\overline{uw}_{max}$ and largest A_{wk} (617 cm^2 s^{-2}, 24.9 N m^{-2} and 0.29 m^2, respectively) were estimated at Site 6B, while the highest absolute magnitude $-\rho\overline{uv}_{max}$ (13.2 N m^{-2}) was estimated at Site 3. The lowest magnitude $ITS_{u\text{-}min}$ (0.06 s) was estimated at Sites 2R2 and 3. Table 7.4 presents the matrix of correlation coefficients, r, between turbulent wake variables for the upper and lower planes of measurement. $k_{e\text{-}max}$ is strongly correlated with all variables with the exception of Δx_{ke}

for both the upper and lower measurement planes. k_e is most strongly correlated with $-\rho\overline{uw}$ ($r > 0.93$) and a marked negative correlation is observed with $ITS_{u\text{-min}}$ ($r = -0.72$, lower plane measurements).

Table 7.3. Turbulence variables in the wake of LREs

	$k_{e\text{-max}}$, $cm^2\ s^{-2}$		Δx_{ke}, m		$ITS_{u\text{-min}}$, s		$-\rho\overline{uv}_{max}$,[a] $N\ m^{-2}$		$-\rho\overline{uw}_{max}$, $N\ m^{-2}$		A_{wk}, m^2		$\varnothing_{wk}$,[b] m		L_{wk},[b] m	
Level	Up	Lw	Up	Lw	Up	Lw	Up	Lw	Up	Lw	Up	Lw	Up	Lw	Up	Lw
1	212	470	0.5	0.3	0.24	0.09	2.46	5.5	5.55	12.76	0.12	0.14	0.38	0.36	0.54	0.49
2R1	207	273	0.35	0.15	0.16	0.12	-1.24	-4.59	5.68	7.15	0.12	0.12	0.28	0.39	0.63	0.39
2R2	119	214	0.7	0.3	0.28	0.06	0.93	-6.76	2.6	6.74	0	0	0	0	0	0
3	294	470	0.45	0.25	0.15	0.06	6.05	-13.18	8.93	12.7	0.2	0.18	0.34	0.41	0.68	0.63
4A	73	135	0.05	0.45	0.23	0.22	-0.9	-1.15	1.01	3.32	0	0.06	0	0.20	0	0.31
4B	90	152	0.05	0.45	0.24	0.22	-0.98	1.65	1.63	3.59	0	0.01	0	0.08	0	0.16
5A	266	219	0.32	0.32	0.21	0.16	-2.64	2.61	9.43	6.3	0.18	0.2	0.29	0.35	0.82	0.83
5B	261	319	0.32	0.32	0.16	0.16	2.52	-6.87	8.95	8.68	0.16	0.18	0.26	0.28	0.72	0.78
5C	332	486	0.52	0.32	0.2	0.11	-3.03	6.69	11.22	16.4	0.13	0.22	0.26	0.38	0.57	0.72
6A	196	396	0.81	0.21	0.18	0.08	2.23	5.19	6.47	12.88	0.18	0.26	0.41	0.45	0.56	0.85
6B	336	617	0.81	0.21	0.17	0.1	2.59	-6.11	12.45	24.86	0.14	0.29	0.35	0.46	0.51	0.80
7A	–[c]	498	–[c]	0.12	–[c]	0.08	–[c]	-7.28	–[c]	14.05	–[c]	0.21	–[c]	0.39	–[c]	0.71
7B	174	307	0.92	0.32	0.13	0.06	4.19	-7.58	4.09	7.58	0.07	0.28	0.32	0.39	0.34	0.94
7C	255	590	0.72	0.12	0.17	0.09	-6.05	-11.3	7	21.22	0.15	0.21	0.36	0.41	0.50	0.67
8R1	–[c]	428	–[c]	0.32	–[c]	0.1	–[c]	4.64	–[c]	14.22	–[c]	0.11	–[c]	0.22	–[c]	0.68
8R2	–[c]	460	–[c]	0.07	–[c]	0.1	–[c]	10.02	–[c]	7.74	–[c]	0.06	–[c]	0.23	–[c]	0.37
9A	37	100	0.22	0.22	0.41	0.34	-0.16	1.6	0.9	3.28	0	0.1	0	0.26	0	0.42
9B	54	89	0.42	0.02	0.38	0.35	-0.5	0.5	1.13	2.32	0	0.01	0	0.10	0	0.12
9C	190	283	0.42	0.42	0.41	0.23	0.92	6.21	5.7	8.11	0.1	0.11	0.25	0.26	0.42	0.42
10A	90	126	0.02	0.28	0.25	0.16	-0.63	-1.35	2.09	3.67	0.07	0.02	0.27	0.17	0.32	0.21
10B	150	327	0.02	0.28	0.27	0.13	-1.42	-4.01	3.96	10.38	0	0.06	0	0.26	0	0.29

[a]Absolute values were used in RDA.
[b]Not included in RDA
[c]No data - Upper plane velocity measurements were not possible due to insufficient water depth, Z.

Table 7.4. Correlation coefficients, r, between the turbulence variables in the wake region for the upper and lower measurement planes

Upper / Lower	$k_{e\text{-max}}$	Δx_{ke}	$ITS_{u\text{-min}}$	$\lvert-\rho\overline{uv}_{max}\rvert$	$-\rho\overline{uw}_{max}$	A_{wk}
$k_{e\text{-max}}$		0.48	-0.62	0.69	0.98	0.85
Δx_{ke}	-0.28		-0.37	0.52	0.45	0.45
$ITS_{u\text{-min}}$	-0.72	0.04		-0.67	-0.54	-0.59
$\lvert-\rho\overline{uv}_{max}\rvert$	0.76	-0.25	-0.70		0.59	0.67
$-\rho\overline{uw}_{max}$	0.93	-0.21	-0.60	0.59		0.84
A_{wk}	0.67	-0.10	-0.51	0.48	0.69	

7.4.3. Spatial distribution of turbulent parameters

Turbulence intensity in all three velocity dimensions is well summarized through the estimation of turbulent kinetic energy values. Figure 7.2 presents the spatial distribution of k_e observed at Site 7C for the upper and lower planes of measurement, $z/Z = 0.39$ and $z/Z = 0.19$, respectively. Flow condition C was the highest stage sampled at Site 7 where $Z = 0.47$ m and $\overline{U}_{04} = 0.78$ m s^{-1}. The spatial distribution plot illustrates the general trends observed in k_e between upper and lower planes of measurement at most sites. The highest turbulent energy occurs lower in the water column close to the boulder lee edge with values of k_e reaching 590 cm^2 s^{-2} which are approximately three to four times greater than the values for the unobstructed flow (left and right sides of the sampling site, $y = 0.1$ m and 1.3 m). The turbulent kinetic energy magnitudes estimated in the wake are similar to those estimated from the protruding boulder study of *Tritico and Hotchkiss* [2005]. The width of the wake is equal to the boulder cross-stream width $\varnothing_{wk} = \varnothing_s = 0.41$ m. In the upper measurement plane, the wake is characterized by much weaker energy levels, is narrower and is shown to occur further downstream than for the lower level.

The effect of LRE morphometry on the spatial distribution of turbulence variables is illustrated using the results obtained at Sites 2, 8 and 10 which contain relatively large elements. Sites 2 and 8 contain laterally aligned LREs separated by a lateral distance of approximately $\Delta y = \varnothing_s$. The spatial distribution of k_e for the lower measurement planes of these sites are shown in Figure 7.3. High values of k_e are observed in the wake of individual elements reaching magnitudes four times the values measured upstream of the LRE for Site 8. The wake widths of Site 8 are estimated as $\varnothing_{wk} = 0.22$ m and 0.23 m for R1 and R2 which are quite similar to their respective LRE widths ($\varnothing_s = 0.27$ m and 0.28 m). The narrowness of the LRE wakes appears to limit the lateral interaction between LREs. The hydrodynamic effect of the LREs is restricted to the region directly downstream of each element. Site 10B contains multiple longitudinally aligned LREs (only the downstream LRE is outlined in Figure 7.3) and gives an example where wake interference was found to occur. The combined wake produced by the upstream roughness elements located $x = -0.1$ m and 0.4 m is disrupted by the LRE located at $x = 0.8$ m. The wake produced by the downstream LRE located at $x = 0.8$ m is

approximately equal in magnitude but smaller in area than the wake generated upstream. Under this flow condition, the longitudinal separation distance between the downstream LRE and the closest element upstream Δx = 0.4 m is small enough to cause a wake interference flow condition.

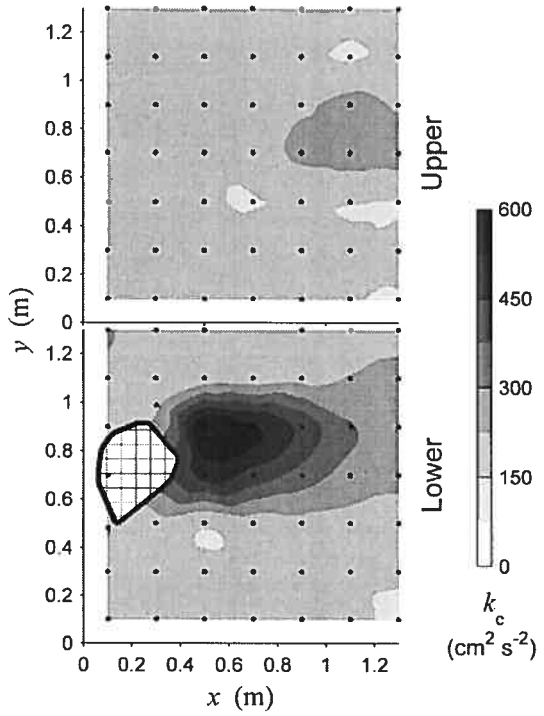

Figure 7.2. Turbulent kinetic energy, k_e, at Site7C for the upper and lower measurement x-y planes. Black dots represent locations of the velocity measurements. Flow is from left to right. Cross-hatching indicates the LRE location.

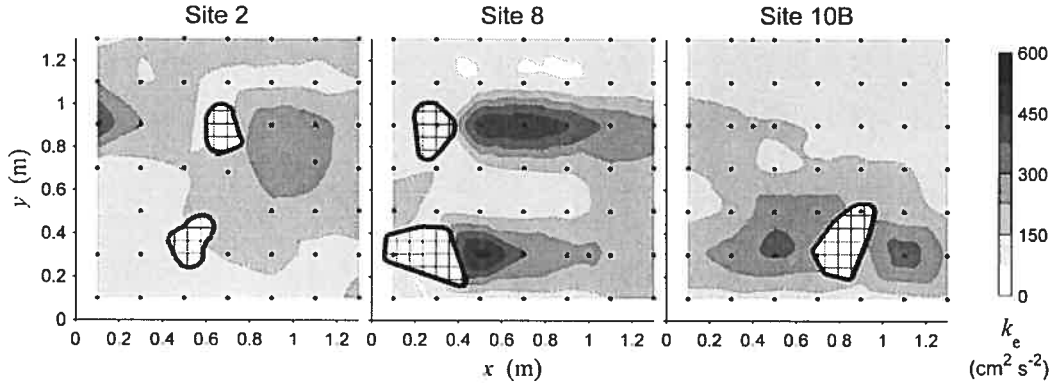

Figure 7.3. Turbulent kinetic energy, k_e, at Site 2, Site 8 and Site 10B for the lower measurement x-y planes. Black dots represent sampling locations of the velocity measurements. Flow is from left to right. Cross-hatching indicates the LRE location.

Figure 7.4 presents the spatial distributions of the integral time scale for the u velocity component, ITS_u, for the same sites presented in Figure 7.3. A strong inverse relationship, r = -0.72, is shown in Table 7.4 between $k_{e\text{-max}}$ and $ITS_{u\text{-min}}$ for the lower plane of measurement. This inverse relationship is clear when comparing the k_e and ITS_u spatial distributions plots. The marked decrease of ITS_u values in the wake of LREs supports previous hydrodynamic studies of LREs in gravel-bed rivers [*Lacey and Roy*, 2007c]. The spatial distributions of ITS_u for Site 2 and Site 8 indicate a minimal interaction between the wake zones of the laterally spaced roughness elements. The k_e and ITS_u spatial distributions show the relatively local hydrodynamic effect of LREs. The lateral widths of the turbulent wake, $\varnothing_{wk}$, are generally limited to the width ($\varnothing_s$) of their associated LREs. This relationship can be observed in the spatial distributions of the turbulence variables and is also seen in Figure 7.5 for all sites at both planes of measurement. Zero $\varnothing_{wk}$ values in Figure 7.5 were generally associated with the upper plane measurements of four sites with generally smaller LREs where the wake could not be identified through the detection scheme $k_e > 1.5\,k_e'$ (Table 7.3). The localized effect of the LREs is not only shown by their narrow wake zones, but also by the diminished magnitude of the turbulence variables in the upper plane turbulence statistics (Figure 7.2 and Table 7.3). The results for sites investigated at multiple flow stages indicate a marginal effect of flow stage on $\varnothing_{wk}$ (Table 7.3).

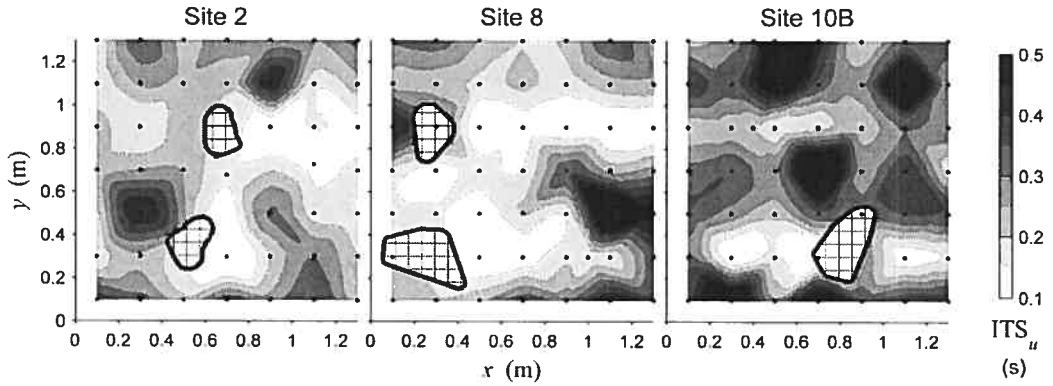

Figure 7.4. Spatial distributions of the u component integral time scale, ITS_u at Site 2, Site 8 and Site 10B for the lower measurement x-y planes. Black dots represent sampling locations of the velocity measurements. Flow is from left to right. Cross-hatching indicates the LRE location.

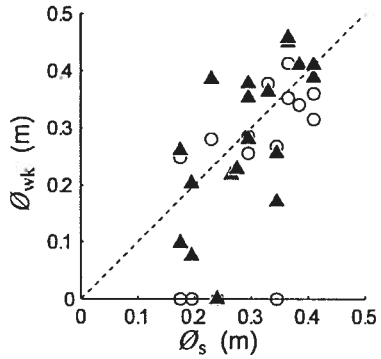

Figure 7.5. Scatter plot of LRE wake lateral width, $\varnothing_{wk}$, as a function of LRE lateral width, $\varnothing_s$. Open circles represent upper plane measurements and filled triangles represent lower plane measurements. Dashed line indicates 1:1 ratio.

Spatial distributions of time-averaged Reynolds shear stresses, $-\rho\overline{\tilde{u}\tilde{v}}$, $-\rho\overline{\tilde{u}\tilde{w}}$, and $-\rho\overline{\tilde{v}\tilde{w}}$ for Site 3 under flow conditions Z = 0.37 m and $\overline{U}_{0.4}$ = 0.62 m s^{-1} are presented in Figure 7.6. This site is a good example of the typical patterns of Reynolds stresses observed at most sites. $-\rho\overline{\tilde{u}\tilde{v}}$ and $-\rho\overline{\tilde{u}\tilde{w}}$ values are much greater for the lower measurement plane than for the upper plane. $-\rho\overline{\tilde{v}\tilde{w}}$ values are shown to remain relatively low at both planes. The location of the maximum $-\rho\overline{\tilde{u}\tilde{v}}$ and $-\rho\overline{\tilde{u}\tilde{w}}$ occurs directly downstream of the cluster in the near-wake for the lower measurement plane and further downstream for the upper measurement plane. A well defined high shear stress region is observed in the lower plane near-wake ($x < 1.5h_s$ downstream from the LRE lee edge) with values reaching $-\rho\overline{\tilde{u}\tilde{w}}$ = 12.7 N m^{-2}. The near-wake peak magnitude of $-\rho\overline{\tilde{u}\tilde{v}}$ = 13.2 N m^{-2} is equally as strong as $-\rho\overline{\tilde{u}\tilde{w}}$, and $-\rho\overline{\tilde{u}\tilde{v}}$ is divided into two well defined zones of positive and negative values that are elongated in the streamwise direction. The spatial pattern of shear stresses indicates a dominance of $-\rho\overline{\tilde{u}\tilde{w}}$ along the downstream centerline and an approximate equal contribution of $-\rho\overline{\tilde{u}\tilde{w}}$ and $-\rho\overline{\tilde{u}\tilde{v}}$ over to the side of the wake zone.

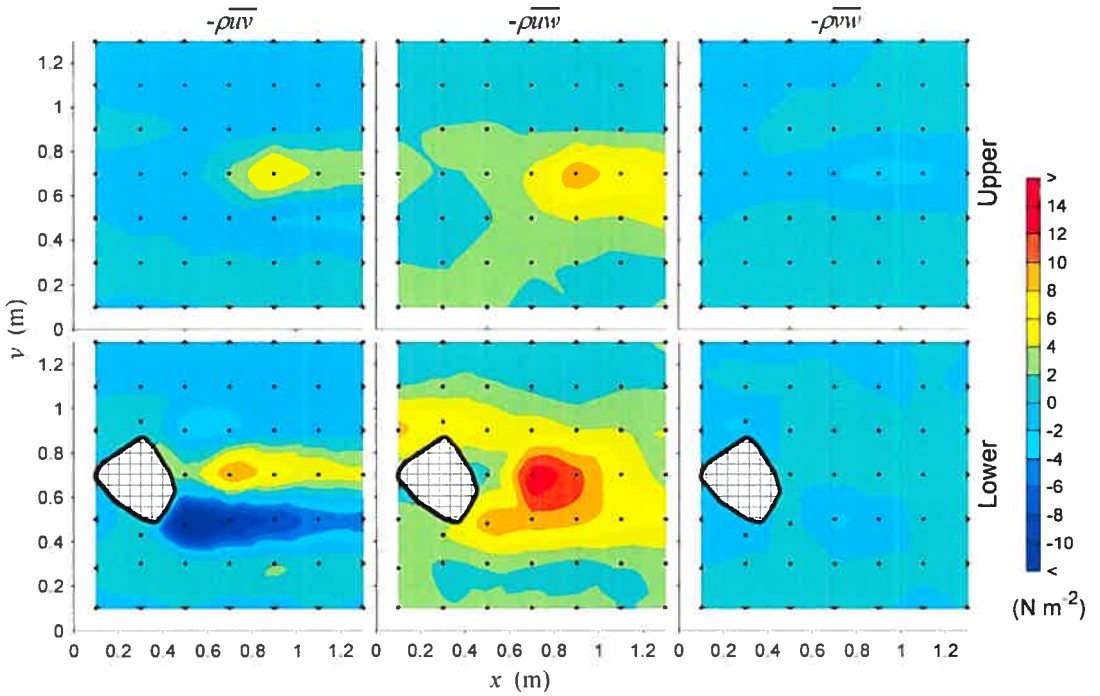

Figure 7.6. Reynolds shear stresses at Site 3 for the upper and lower measurement *x*-*y* planes. Black dots represent sampling locations of the velocity measurements. Flow is from left to right. Cross-hatching indicates the LRE location.

The effect of changing flow conditions (stage and velocity) on the spatial patterns of $-\rho\overline{uv}$ and $-\rho\overline{uw}$ for Site 5 is presented in Figure 7.7. The spatial distributions of $-\rho\overline{vw}$ are not presented due to their marginal values which were relatively unaffected by flow stage. For the low flow case, Site 5A, the $-\rho\overline{uv}$ contribution is seen to be relatively minor (Figure 7.7a). With increased flow stage and velocity (flow 5B) the positive and negative $-\rho\overline{uv}$ zones in the wake become more evident for the lower measurement plane. As Z and $\overline{U}_{0.4}$ increase further (flow 5C), the peak magnitude in the negative $-\rho\overline{uv}$ zones remain relatively stable while the magnitude of the positive $-\rho\overline{uv}$ zone increases to a value of 6.7 N m^{-2}. Alternatively, as shown in Figure 7.7b, the peak magnitude of $-\rho\overline{uw}$ in the LRE wake increases markedly as stage increases. At the highest flow stage, the peak magnitude of $-\rho\overline{uw}$ is 2.5 times greater than the peak $-\rho\overline{uv}$ value. Increases in $-\rho\overline{uw}$ with flow are as well apparent in the upper measurement plane where values attain 11.2 N m^{-2} which is the second largest value estimated for the upper plane for all sites (see Table 7.3). The dominance of $-\rho\overline{uw}$ at

higher flows was not specific to Site 5C and was observed at all sites where measurements were carried out at several flow stages. For instance, as seen in Table 7.3, the shift to higher and faster flows for Site 6A to 6B causes only a slight increase in the peak magnitude of $-\rho\overline{uv}$, while there is a significant increase in $-\rho\overline{uw}$ with a peak value of $-\rho\overline{uw} = 25$ N m^{-2} which was the highest value estimated at all sites.

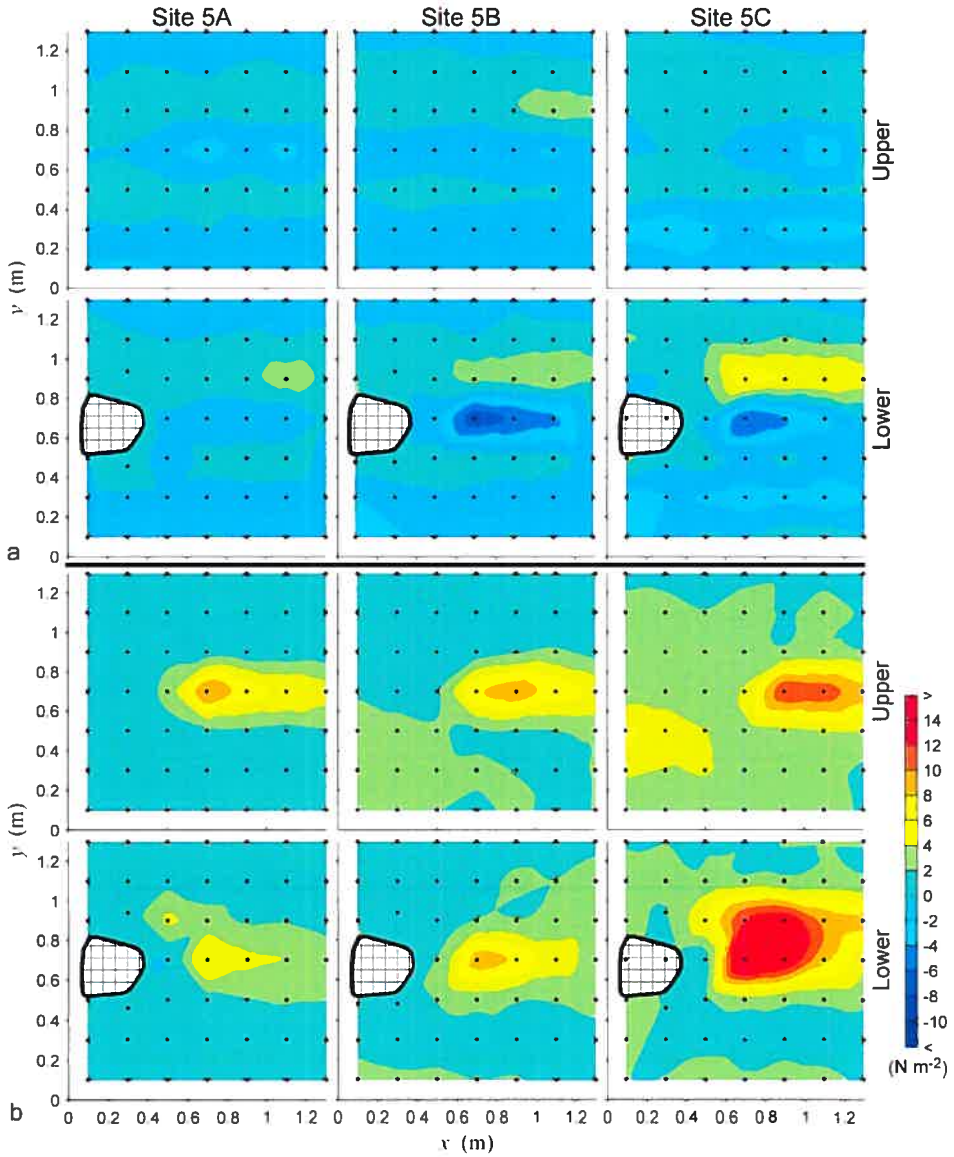

Figure 7.7. Spatial distribution of: (a) $-\rho\overline{uv}$; and (b) $-\rho\overline{uw}$ at Site 5A,B,C for the upper and lower measurement *x*-*y* planes showing variability with river stage under flow conditions: A: $Z = 0.45$ m, $\overline{U}_{0.4} = 0.57$ m s^{-1}; B: $Z = 0.51$ m, $\overline{U}_{0.4} = 0.70$ m s^{-1}; C: $Z = 0.57$ m, $\overline{U}_{0.4} = 0.85$ m s^{-1}. Black dots represent sampling locations of the velocity measurements. Flow is from left to right. Cross-hatching indicates the LRE location.

7.4.4. Redundancy analysis

Several general trends between mean flow, LRE morphometric variables and the turbulence variables in the wake were first examined through bivariate linear plots and correlations. Figure 7.8 presents three different scatterplots exemplifying some of the trends in the turbulent wake data. These examples were selected as they show a range of linear dependence between the selected explanatory and response variables. A weak non-significant dependence ($r^2 = 0.17$, p = 0.065) of Δx_{ke} on Z is observed in Figure 7.8a for the lower measurement plane while no significant ($\alpha = 0.05$) relationship is observed for the upper plane. The distance to maximum k_e occurs in general further away from the LRE for the upper plane than for the lower plane measurements (Figure 7.8a). This is likely because the turbulence generated by the shear layer at the lower level convects upwards at an inclined angle as shown by *Buffin-Bélanger and Roy* [1998]. A positive relationship is observed between LRE lateral width, $\varnothing_s$, and $k_{e\text{-max}}$ (Figure 7.8b). For the lower plane measurements, $\varnothing_s$ explains a significant proportion, $r^2 = 0.47$ ($p < 0.001$) of the variance in $k_{e\text{-max}}$. The composite drag force metric $0.5A_s\rho\overline{U}^2$ presented in Figure 7.8c explains large proportions of the variation in $-\rho\overline{uw}_{max}$ both the upper and lower levels ($r^2 = 0.66$ and 0.64, respectively, $p < 0.001$). These results demonstrate that linear relationships are present between mean flow and LRE morphometric variables; and the turbulent wake parameters.

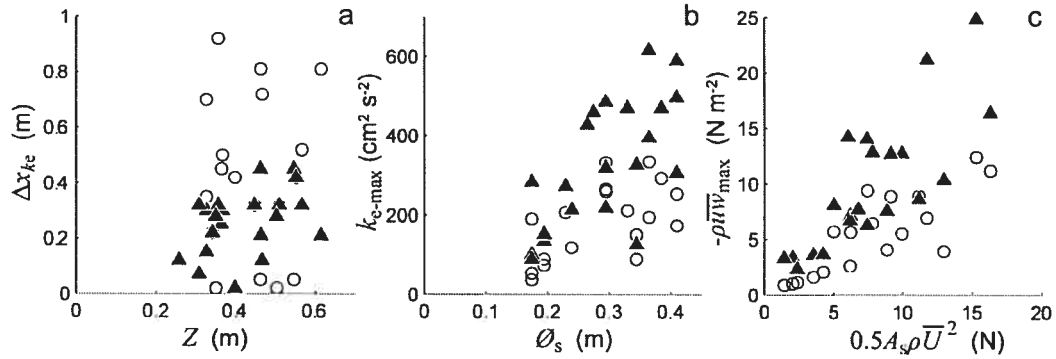

Figure 7.8. Bivariate scatter plots of: (a) Δx_{ke} vs. Z; (b) $k_{e\text{-max}}$ vs. $\varnothing_s$ (c) $-\rho\overline{uw}_{max}$ vs. $0.5A_s\rho\overline{U}^2$. Open circles represent upper plane measurements and filled triangles represent lower plane measurements.

The forward selection procedure performed on the two RDA models (upper plane and lower plane) helped identify the combination of LRE morphometric and mean flow variables that significantly (α = 0.05) explain the most variance in the LRE wake turbulence statistics. Given that both positive and negative high magnitude values of $-\rho\overline{uv}$ were observed in the wake, absolute values of $-\rho\overline{uv}_{max}$ were used for the RDA as both positive and negative $-\rho\overline{uv}$ represent longitudinal-lateral turbulent momentum exchange regardless of sign. Prior to the forward selection, the marginal effects of all explanatory variables were estimated (Table 7.5). The marginal effect represents the variance explained by a variable in the response data individually (i.e., a marginal effect of an explanatory variable is equivalent to estimating the average bivariate r^2 value between the explanatory variable and all response variables). Table 7.5 shows that the three LRE morphometrics (i.e., h_s, A_s and $\varnothing_s$) each explains a large proportion of the variance in wake turbulence. The only other variable explaining a similar amount of variation is $0.5A_s\rho\overline{U}^2$, a measure of drag force that is highly related to the LRE morphometry (Table 7.2) which is estimated in part using A_s. The forward selection procedure is used to identify variables of high explanation and eliminate redundant, highly correlated explanatory variables (which if included in the model would not explain significantly more variation). The explanatory variables included in the RDA models are based partly on the forward selection procedure and on user judgement which ensures that the variables included are physically based and respond to the research objectives. For instance, one of the main objectives of this study was to relate wake turbulence to LRE morphometry as it is well know that LRE size (lateral frontal area) influences the pressure drag and thereby the turbulence in the wake.

Table 7.6 presents explanatory variables used in the upper and lower plane models and their respective conditional effects. The conditional effect of a variable is the additional variance explained as the variable is included in the model (while considering the explained variation of all preceding variables included). For correlated variables, the explained variance is dependent on the order the variables are included. For instance for the upper plane model, it is apparent from Table 7.5 that $\varnothing_s$ and h_s each explain more than 34% of the variance, yet the conditional effect of the two variables sum to only 55% due to their inter-correlation. While α = 0.05 was used to select the significant

explanatory variables for each model, for the upper plane model, $\overline{U}_{04}$ was also included even though it is slightly below the significance threshold (p = 0.07), as the bivariate linear correlations and boundary layer theory indicated it has an important structuring variable. The marginal effects of the composite variables (i.e., A_s and $0.5A_s\rho\overline{U}^2$) were in some instances equal or greater than the simple variables, yet their inclusion in the models added little to (or reduced) the overall *can* R^2 and made the interpretation of the results more difficult. Since the objective of this study was to investigate the effect of LREs and flow conditions on wake hydrodynamics the simple variables $\varnothing_s$, h_s and/or $\overline{U}_{04}$ were used instead of the combined variables.

Table 7.5. Marginal effects (individual explained variance) of LRE morphometrics and mean flow variables[a]

Variable	Model	
	Upper	Lower
h_s	0.34	0.11
$\varnothing_s$	0.38	0.39
A_s	0.49	0.34
Z/h_s	0.11	0.1
Z	0.08	0.06
z	0.09	0.07
z/Z	0.03	0.03
$\overline{U}_{Up/Lw}$	0.18	0.21
$\overline{U}_{04}$	0.15	0.2
Re	0.14	0.1
Fr	0.09	0.2
$\rho\overline{U}^2$	0.13	0.18
$0.5A_s\rho\overline{U}^2$	0.42	0.39

Table 7.6. Conditional effects (additional explained variance, λ) of explanatory variables

Model	Variable	λ	p-value
Upper model	$\varnothing_s$	0.38	0.001
	h_s	0.17	0.002
	$\overline{U}_{04}$	0.07	0.073
Lower model	$\varnothing_s$	0.39	0.001
	$\overline{U}_{Lw}$	0.12	0.001
	Z	0.06	0.037

The RDA upper and lower plane models both explain significant ($p \leq 0.0002$) proportions of the variance in the estimated LRE wake turbulence statistics. The RDA model for the upper plane based on $\varnothing_s$, h_s, and $\overline{U}_{0.4}$ explains $R_a^2 = 0.56$ of the variance in the upper plane wake turbulence statistics, while the RDA model for the lower plane based on $\varnothing_s$, $\overline{U}_{Lw}$ and Z explains $R_a^2 = 0.52$ of the variance in the lower wake turbulence statistics. While the R_a^2 gives a good account of the fit of each model, the details concerning the explained variance for individual turbulence statistics (expressed by the fractions of the unadjusted coefficients of multiple determination per canonical axis, R_i^2) are presented in Table 7.7. The upper plane model, based mostly on the LRE morphometric variables, explains a very high fraction 82% and 80% of the variation in $k_{e\text{-max}}$ and $-\rho\overline{uw}_{max}$, respectively. Similarly, the lower plane model explains a large portion of the variation in $-\rho\overline{uw}_{max}$, $k_{e\text{-max}}$, and $ITS_{u\text{-min}}$ (68%, 73%, and 76%, respectively). The goal of RDA is not to explain 100% of the variance as part of the variance in the response variables may be due to noise or estimation error in correlation coefficients, fitted values [*ter Braak*, 1994] and measurements; therefore the high explanation of the main turbulence variables suggests that the explanatory variables used in each model can account for most of the true variance.

Table 7.7 Estimated fractions of unadjusted variance (R_i^2) of turbulence variables expressed by canonical axes I, II and full model[a]

	Upper plane model			Lower plane model		
	R_1^2	R_2^2	R^2	R_1^2	R_2^2	R^2
$k_{e\text{-max}}$	0.75	0.05	0.82	0.71	0.00	0.73
Δx_{ke}	0.19	0.06	0.30	0.05	0.18	0.23
$ITS_{u\text{-min}}$	0.48	0.07	0.55	0.71	0.05	0.76
$\lvert-\rho\overline{uv}_{max}\rvert$	0.48	0.12	0.60	0.42	0.02	0.44
$-\rho\overline{uw}_{max}$	0.70	0.10	0.80	0.62	0.06	0.68
A_{wk}	0.56	0.01	0.61	0.42	0.06	0.54
Canonical eigenvalue[b]	0.53	0.07	0.62	0.49	0.06	0.57
p-value[c]	0.0011	0.14	0.0002	≤0.0001	0.14	≤0.0001

[a] R^2 is the unadjusted coefficients of multiple determination for each model.

[b] Unadjusted canonical eigenvalues, λ_i, of each axis (λ_i are estimated as the mean R_i^2 value for all 6 response variables).

[c] Monte Carlo significance test (9999 unrestricted permutations).

The relative contribution of each explanatory variable to canonical axes I and II is shown by the correlation biplots presented in Figure 7.9. The canonical eigenvalues, λ_i, for each canonical axis (Table 7.7) must be considered when interpreting the correlation biplots because the variation explained per axis cannot be derived from the plots alone. The upper RDA model (Figure 7.9a) canonical axis I explains 53% of the variance and is described mostly by a LRE morphometric gradient ($\varnothing_s$ and h_s). For the lower RDA model (Figure 7.9b), $\varnothing_s$ forms a strong gradient along with $\overline{U}_{Lw}$ and are highly correlated with canonical axis I which explains 49% of the variance in the turbulent wake statistics, while Z is highly correlated with axis II which only explains 6% of the total variance. The projection of a response variable on an explanatory variable reflects its correlation. For the upper RDA model, projection of $-\rho\overline{uw}_{max}$ and $k_{e\text{-}max}$ on h_s indicates that high magnitude values of these variables are well correlated with h_s. The upper plane biplot also suggests a strong correlation between high $|-\rho\overline{uv}_{max}|$, low $ITS_{u\text{-}min}$ and $\varnothing_s$. A similar high correlation between high magnitude turbulence statistics and LRE morphometrics ($\varnothing_s$) is observed in the lower RDA model (Figure 7.9b). Although axis II is not significant ($p = 0.14$), it does suggests much more correlation between $\overline{U}_{Lw}$ and $-\rho\overline{uw}_{max}$ than between $\overline{U}_{Lw}$ and $|-\rho\overline{uv}_{max}|$. While correlations do not indicate causal link, these correlations indicate a stronger interdependence between $\overline{U}_{Lw}$ and $-\rho\overline{uw}_{max}$. Projection of Z on $|-\rho\overline{uv}_{max}|$ reveals relatively little correlation. Generally, both RDA models show a high negative correlation between $ITS_{u\text{-}min}$ and $|-\rho\overline{uv}_{max}|$, $-\rho\overline{uw}_{max}$, A_{wk} and $k_{e\text{-}max}$. Δx_{ke} is the least explained response variable in all models, yet is shown to be generally correlated with Z.

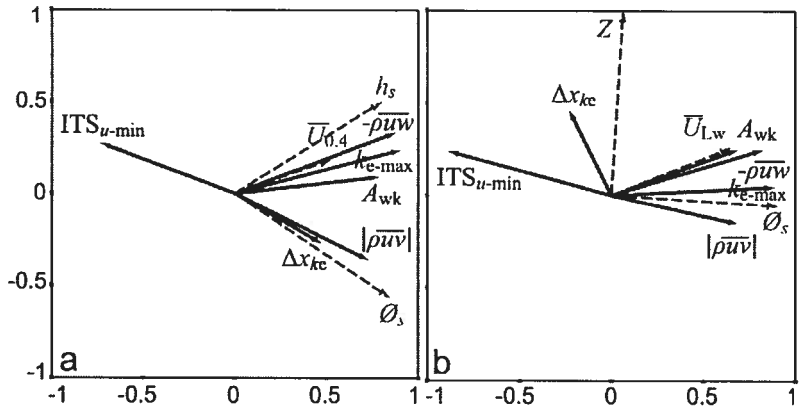

Figure 7.9: RDA correlation biplots for all sites estimates from: (a) upper measurement plane model, (b) lower measurement plane model. Canonical axis I is the abscissa while canonical axis II is the ordinate. Dashed vectors explanatory (independent) variables while solid vectors are time-averaged turbulent (response) variables.

Given the much higher turbulence associated with the lower measurement plane, the insights suggested by the lower plane RDA model biplot, and the objective to determine the isolated effect of LRE morphometrics, the variance between the mean flow variables (Z and $\overline{U}_{Lw}$) and $\emptyset_s$ was partitioned. The first submodel, is based Z and $\overline{U}_{Lw}$ controlling for the variance explained by $\emptyset_s$; whereas submodel 2 is based on $\emptyset_s$ controlling for the variance explained by Z and $\overline{U}_{Lw}$. Table 7.8 and Figure 7.10 present the results of submodels 1 and 2 RDA. Both submodels 1 and 2 explain significant ($p \leq 0.001$) fractions of the variance of *Can* $R^2 = 0.18$ and 0.28, respectively. For the first submodel, canonical axis I, for which $\overline{U}_{Lw}$ is strongly correlated, explains 27% and 24% of the variance in $k_{e\text{-max}}$ and $-\rho\overline{uw}_{max}$, respectively. Axis II, for which Z is strongly correlated, explains 17% of the variation in Δx_{ke} and 7% of the variation in A_{wk}. As with the lower plane model (Figure 7.9b), Figure 7.10a indicates little correlation between Z and $|-\rho\overline{uv}_{max}|$ and only small correlation with $k_{e\text{-max}}$. The second submodel RDA isolates the effect of the LRE on the lower measurement plane turbulent flow parameters by controlling for the mutual variation explained by $\overline{U}_{Lw}$ and Z. $\emptyset_s$ explains 29% of the variation in $k_{e\text{-max}}$ and $-\rho\overline{uw}_{max}$, 37% of the variation in ITS$_{u\text{-min}}$ and 45% of the variation in A_{wk} (Table 7.8). Figure 7.10b shows subtle difference in the correlations between $\emptyset_s$ and the turbulent response variables, but in general there are still strong

positive correlations with A_{wk}, $k_{e\text{-}max}$, $-\rho\overline{uw}_{max}$ and $|-\rho\overline{uv}_{max}|$ and a strong negative correlations with $ITS_{u\text{-}min}$.

Table 7.8. Partitioned lower measurement plane submodels – estimated fractions of unadjusted variance (R_i^2) of turbulence variables expressed by canonical axes and full model[a]

	Submodel 1[b]			Submodel 2[c]	Mutual Variation
	R_1^2	R_2^2	R^2	R^2	R^2
$k_{e\text{-}max}$	0.27	0.00	0.27	0.29	0.18
Δx_{ke}	0.00	0.17	0.17	0.03	0.03
$ITS_{u\text{-}min}$	0.12	0.06	0.18	0.37	0.21
$\lvert-\rho\overline{uv}_{max}\rvert$	0.07	0.03	0.10	0.22	0.12
$-\rho\overline{uw}_{max}$	0.24	0.03	0.28	0.29	0.12
A_{wk}	0.01	0.07	0.08	0.45	0.01
Canonical eigenvalue[d]	0.12	0.06	0.18	0.28	0.11
p-value[e]	0.0118	0.0549	0.0012	≤0.0001	

[a] R^2 is the unadjusted coefficients of multiple determination for each model.

[b] Based on Z and $\overline{U}_{Lw}$ controlled by $\varnothing_s$

[c] Based on $\varnothing_s$ controlled by Z and $\overline{U}_{Lw}$.

[d] Unadjusted canonical eigenvalues, λ_i, of each axis (λ_i are estimated as the mean R_i^2 value for all 6 response variables).

[e] Monte Carlo significance test (9999 unrestricted permutations). Mutual variation can not be tested for significance.

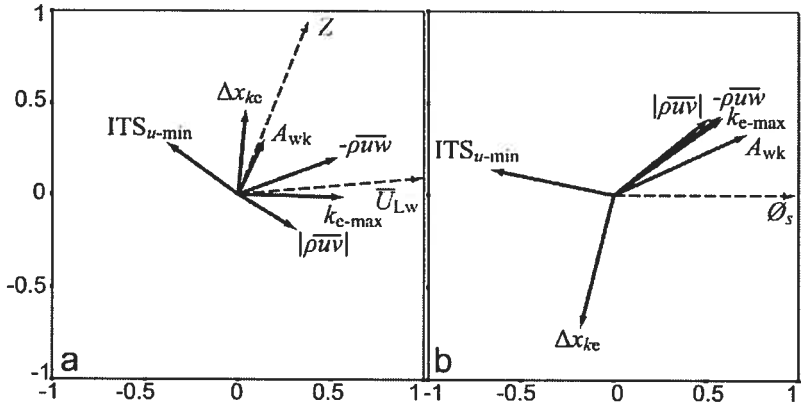

Figure 7.10: RDA correlation biplots for lower measurement plane model controlling for: (a) $\varnothing_s$ – submodel 1; (b) Z and $\overline{U}_{Lw}$ – submodel 2. Canonical axis I is the abscissa while canonical axis II is the ordinate. Dashed vectors explanatory (independent) variables while solid vectors are time-averaged turbulent (response) variables.

7.5. Discussion

The spatial distributions of the turbulent flow data around the LREs at the 10 sites examined in this study show intense turbulence is generated by the LRE wakes that is mostly localized directly downstream of the LREs in a narrow zone below the LRE tops. In general, this wake zone is characterised by high magnitude k_e, $-\rho\overline{uv}$ and $-\rho\overline{uw}$ of up to ten times the values measured upstream from the LRE and by a complex 3D flow structure with turbulent mixing occurring in both the vertical and horizontal dimensions. The alternating pattern of elongated high magnitude zones of negative and positive $-\rho\overline{uv}$ in the wake indicates strong horizontal turbulent momentum exchange circulating in opposing directions on either side of the wake. With increasing flow stage $-\rho\overline{uw}$ dominates the turbulent momentum exchange in the LRE wakes having values up to 2.5 times those of $-\rho\overline{uv}$. The dominance of *uw* turbulent momentum exchange in the wake of a LRE corroborates previous work [Lacey and Roy, 2007c]. The following discussion focuses on the results of the RDA, the general wake characteristics and implied flow structures associated with the Reynolds shear stress spatial patterns and the implications for river dynamics and aquatic biota.

The redundancy analysis strongly suggests that roughness element morphometrics are the dominant parameters determining submerged LRE wake turbulence statistics both below the tops of the LRE and higher up in the water column. Mean free-stream velocity (either estimated at $z/Z = 0.4$ or at the height, z, of the velocity measurements) is the second main parameter – adding additional explanation in the turbulent wake statistics. The upper measurement plane RDA model based primarily on h_s and $\varnothing_s$ explains 82% and 80% of the variation in $k_{e\text{-max}}$ and $-\rho\overline{uw}_{max}$, respectively and 60% and 61% of $|-\rho\overline{uv}_{max}|$ and A_{wk}, respectively. Closer to the bed, below the tops of the LRE, 30% of the variation in $k_{e\text{-max}}$ and $-\rho\overline{uw}_{max}$ can be exclusively related to $\varnothing_s$ and approximately 25% is almost exclusively explained by $\overline{U}_{Lw}$. This result is supported by flume studies investigating the hydrodynamics downstream of LREs which have indicated a positive relationship between mean velocity and turbulence statistics under constant depth [*Smith et al.*, 2005].

In order to fully explore the available field data collected, we decided to included all the sampled and resampled sites in the upper and lower RDA models. The inclusion of the resampled sites will artificially increase the weight of these sites in the models and could therefore bias the results. The effect of this increased weighting was evaluated by performing RDA using the same explanatory variables (i.e., h_s, $\varnothing_s$ and $\overline{U}_{04}$ for the upper RDA model and $\varnothing_s$, $\overline{U}_{Lw}$ and Z for the lower model) on subsets of the full data set using a single flow condition for each site. The RDA performed on these independent subsets gave similar results to those obtained using the entire data set, yet a higher explained variance was obtained for both the upper and lower plane RDA subset models. The upper RDA subset model based on h_s, $\varnothing_s$ and $\overline{U}_{04}$ explains $R_a^2 = 0.71$ ($p < 0.01$) of the variance in the upper wake turbulence statistics, while the lower plane RDA subset modal based on $\varnothing_s$, $\overline{U}_{Lw}$ and Z explains $R_a^2 = 0.55$ ($p = 0.01$) of the variance in the lower wake turbulence statistics.

Many independent variables which are commonly used to describe flow conditions or wake turbulence were tested, yet were not included in the RDA models as they added negligibly to the conditional (combined) explained variance. Individually some of these independent variables (i.e., drag force metric) explained as much variation or slightly more than individual LRE morphometrics. Figure 7.8c shows a strong relationship between the drag force metric and $-\rho\overline{uw}$ ($r^2 = 0.64$, lower plane). But this metric is a nonlinear cross-product term and the linear model which includes its component parts separately (LRE morphometrics and mean velocity) explains a larger proportion of the variance in the wake statistics. The nonlinear quadratic stress law metric which (when multiplied by C_d) is often used to estimate shear stress was found to be a poorer predictor of the turbulence statistics than $\overline{U}_{04}$ (Table 7.5). *Shamloo et al.* [2001] investigated the hydrodynamics associated with hemispheres under different Z/h_s from submerged to emerged flow conditions and suggest Z/h_s to be the most important parameter in classifying wake geometry, velocity field, bed shear stress and scour. Yet, in our experiments, Z/h_s explains less variation than most of the flow parameters and h_s alone. This discrepancy is likely due to the larger range of relative submergence (Z/h_s = 0.62 – 4.27) investigated by *Shamloo et al.* [2001] than in our study (z/h_s, =1.8 – 4.4). h_s

by itself does not explain nearly as much variation as $\emptyset_s$ which is somewhat surprising given the relative dominance of $-\rho\overline{u'w'}$ in the wake (especially at higher flows). For the upper plane RDA model, the correlation biplot (Figure 7.9b) indicates that h_s is more strongly correlated with $-\rho\overline{u'w'}$ than with $|-\rho\overline{u'v'}_{max}|$ and should have a greater influence on the vertical-longitudinal momentum exchange than $\emptyset_s$. Yet, the good fit of $\emptyset_s$ could be explained by the supposition that as the lateral width of a LRE increases more flow separation occurs along its crest, causing greater vertical-longitudinal momentum exchange and hence higher $-\rho\overline{u'w'}$.

The flow interaction induced by multiple LRE was assessed by selecting some sites with laterally and longitudinally spaced LREs. It has been suggested that laterally spaced LREs in rivers may exhibit different flow patterns than isolated elements based on laboratory studies [*Kucukali and Cokgor*, 2007]. Conversely in our study, the spatial distribution of the main turbulence statistics for sites with laterally spaced LREs (where $\Delta y > \emptyset_s$) suggests very little lateral interaction between LREs at low and high flow. The wake zones of all sites are generally narrow with the highest magnitude k_e occurring directly downstream of the LREs. The wake itself does not expand much beyond the width of the LREs (Figure 7.5). *Shamloo et al.* [2001] under similar relative submergence conditions observed minimal velocity defect beyond a lateral distance of $\Delta y = 0.8\emptyset_s$. Different results would most likely be obtained as the lateral separation distances, Δy, between LRE decreases less than $\emptyset_s$, as flow is increasingly constricted and forced overtop of both elements. On the other hand while only one case of longitudinal aligned LREs was investigated in this study, there appears to be interaction between LREs when spacing $\Delta x < 0.4$ m. This is evident in the k_e and ITS_u distributions for Site 10 where the wake of the upstream element is disrupted as it encounters the downstream LRE. The new wake generated by the most downstream LRE appears smaller in area than other LRE of similar size at other sites. This may be due to a reduction in the vertical velocity gradient overtop of the downstream LRE caused by the upstream wake.

Inferences on the physical processes responsible for the spatial distribution patterns of time-averaged Reynolds stresses around the LREs can be made by considering previous research investigating time-dependent coherent structures shedding from

instream LREs. Lacey and Roy [2007c] also observed high $-\rho\overline{u'w'}$ values in the wake and using flow visualization were able to relate the intense $-\rho\overline{u'w'}$ to the shedding of lateral vortices. Similarly, the high $-\rho\overline{u'v'}$ values towards the sides of the wake likely represent the shedding of vertical vortices as argued by *Tritico and Hotchkiss* [2005]. The pattern of elongated zones of alternating negative and positive $-\rho\overline{u'v'}$ (well defined in Figure 7.6) is indicative of counter rotating vortices resulting from the lateral separation and shear layer at both lee sides of the LREs. Further the sign of the $-\rho\overline{u'v'}$ zones (i.e., positive on the left hand side and negative on the right hand side of the wake) suggests clockwise and counterclockwise vortical circulation, respectively. Recent laboratory and numerical modeling study by *Strom et al.* [2007] also observed lateral shearing and counter rotating vortices in the wake of the micro-bedform lending support for this suggested process. Both high values of $-\rho\overline{u'w'}$ and $-\rho\overline{u'v'}$ occur concurrently indicating tubular 3D counter rotating flow structures with possible similarities to the downstream trailing legs of stationary near-bed horseshoe vortices proposed by some studies [*Paola et al.*, 1986; *Acarlar and Smith*, 1987]. The RDA model and submodels for the lower plane show a much stronger relationship between $\overline{U}_{Lw}$ and $-\rho\overline{u'w'}$ than for $\overline{U}_{Lw}$ and $-\rho\overline{u'v'}$, showing that as mean velocity increases due to increased flow stage, $-\rho\overline{u'w'}$ increasingly dominates the turbulent momentum exchange in the wake. The strong inverse relationship between ITS_u and k_e (r = -0.62 to -0.72, Table 7.4) shown in both RDA model correlation biplots (Figure 7.9) is likely due to the increased dominance of small scale vortices shedding from the shear layer into the wake zone, thereby disrupting or replacing the larger-scale coherent free-stream structures as shown by *Lacey and Roy* [2007c]. The view that large eddies are broken down by roughness elements is supported by *Nezu and Nakagawa* [1993].

The results of this study have implications for general river dynamics and aquatic biota habitat. Even though the range of flows investigated is well below bed formative discharges, the results suggest that the localized intense turbulence occurring in the wake of LREs increases in intensity with flow stage. Previous studies of the spatial distribution of LREs in gravel-bed rivers streams have suggested that LREs rarely occur downstream of each other [*Hassan and Reid*, 1990; *Lamarre and Roy*, 2001]. The

intense turbulence and shear stresses occurring in the wake are likely to promote the displacement of secondary LREs found in the wake zone further downstream and should enhance the mixing and suspension of sediments (and nutrients). The acceleration of flow around the sides of LREs is likely to discourage other LRE from depositing next to isolated LREs. The localized influence of LRE hydrodynamics infers that aside from a minimum downstream distance requirement, LRE channel deposition may be a somewhat random process related to large clast delivery and transport capacity throughout the channel. LRE in gravel-bed rivers do provide cover and localized heterogeneous flow conditions which is believed to be desirable for fish [*Van Zyll de Jong et al.*, 1997; *Smith et al.*, 2006]. But the decreased u component velocities in the wake, is associated with flow separation, shear layer generation, a highly turbulent wake and elevated Reynolds shear stresses. If the geometry of the LRE is such that flow separation occurs, LREs are necessarily associated with higher turbulence. There has been conflicting results comparing the effects and preference of turbulence by fish [*Enders et al.*, 2003; *Liao et al.*, 2003b; *Smith et al.*, 2005, 2006]. The discrepancies in these studies may be due to velocity sample locations in relation to the fish location (i.e., nose velocity or higher up in the water column). In the complex flow generated by LRE, the turbulent values can change dramatically (based on whether samples are obtained inside or outside the shear layer). While we cannot address the conflicting results on fish behaviour in a turbulent flow field, our study does provide some useful insights on the generation of turbulence by LRE which could be used when initiating fish habitat studies. For both upper and lower measurement planes, the turbulence statistics were well explained by the LRE morphometrics and mean free-stream velocity. These parameters are very easy to measure in the field and comparisons with our results would provide valuable information on turbulence generation. Turbulent intensities, wake area and more specifically uw component Reynolds shear stress increase with mean velocity and LRE size which may be a determining factor in selecting habitat structures. These elevated values seem to be restricted to a localized region with characteristic dimensions of L_{wk}/h_s = 3.5, $\varnothing_{wk}/\varnothing_s$ = 1.0 and A_{wk}/A_s = 17.4 for the lower measurement plane (averaged over all sites). These results imply that for fish restoration designs, LREs

should be spaced with separation distances of a least $\Delta x = 5h_s - 15h_s$ and $\Delta y = 1h_s - 3h_s$ in order to maximize flow heterogeneity and provide regions of lower turbulence.

7.6. Conclusions

Through the spatial distribution plots of turbulence variables presented in this study, it has been shown that in general, the intense effects of LREs on the flow field were confined to a localized zone in the lee of the LREs – not extending much vertically beyond the LRE height and having mean lateral and longitudinal dimensions of $\varnothing_s$ and $3.4h_s$, respectively. The turbulent structure generated in the wake of LREs is predominantly explained by $\varnothing_s$, h_s, and mean free-stream u component velocity. For the lower plane wake, where the turbulence was most intense, variance partitioning showed that the dominant variable structuring all the turbulence statistics analysed was $\varnothing_s$. $\overline{U}_{Lw}$ was found to be nearly as important for specific turbulence estimators (i.e., $k_{e\text{-}max}$ and $-\rho\overline{uw}_{max}$). Water depth explained an unexpectedly small amount of variance suggesting that in natural rivers turbulence levels behind LREs increase with flow stage primarily as a result of the associated increase in mean velocity. The results presented in this study such as k_e and LRE wake width are dependent on the selected height of the sampling measurement plane. Slightly different results may have been obtained had the sampling strategy allowed for a characterization of the flow structure down to the bed.

The associated preference of fish for LREs in steams is difficult to interpret considering the high turbulence generated in the wake of such elements and the suggested negative effect of turbulence on fish. The heterogeneous flow environment associated with LREs must provide sufficient lower turbulent zones that are attractive habitat. While fish are likely to be negatively affected by the high turbulent fluctuations in LRE wakes, they are able to seek out these lower velocity/turbulent zones which minimize energy expenditure. Velocities and turbulent estimates can differ appreciably on centimetre scales downstream of LREs indicating the importance of sampling as close as possible to the fish nose position. The effect of LRE lateral width on wake turbulence found in our study should interest fish scientists and managers who may want to investigate further the effect of limiting habitat structure size in order to provide optimum benefit for fish. Furthermore, the results of this study should help with the

understanding of turbulent dynamics in other natural rivers with similar sized submerged LRE and comparable flow conditions.

8. IMPLICATIONS

This thesis presents a detailed spatial characterization of *in situ* 3D hydrodynamics around submerged large roughness elements (LREs) in gravel-bed rivers. The flow field around LREs was characterised using time-averaged turbulence statistics, and the shear layer and wake processes were characterised through instantaneous visualization and conditional sampling in order to investigate unsteady coherent motions. While we did not explicitly measure LRE reach-scale spatial distributions or aquatic biota densities, the fine-scale characterization presented in this thesis does provide insight into sediment transport processes, the spatial distribution of LREs, and the influence of LREs on fish habitat. The results of previous studies investigating these relationships have been inconsistent and this thesis helps illuminate these inconsistencies by clearly identifying the characteristics, magnitude and extent of turbulent zones associated with LREs.

8.1. Sediment transport

A marked increase in turbulent energy in the wake of LREs is consistently shown in all article chapters of this thesis (Chapters 4 – 7). In Chapter 6 and 7, mean *uw* Reynolds shear stress, $-\rho\overline{uw}$, was shown to increase markedly in the wake of LREs (by a factor of 5 – 10 of free-stream values) and extend towards the bed. *Nezu and Nakagawa* [1989] observed a similar increase in $-\rho\overline{uw}$ (factor of 5 from free stream values) for a backward facing step study. Under certain LRE configurations, $-\rho\overline{uv}$ was as well observed to show marked increases in the LRE wake occurring in fairly symmetrical high magnitude positive and negative longitudinally elongated zones. With increased flow stage and free-stream u component velocity the peak $-\rho\overline{uw}$ in the wake was observed to increase relative to $-\rho\overline{uv}$ and dominate the turbulent momentum exchange.

The increased $-\rho\overline{uw}$ indicates that considerable turbulent energy is generated along the dividing streamline primarily as a result of the shedding laterally oriented vortices. For sediment transport, it is well recognized that the $-\rho\overline{uw}$ values estimated in the shear layer away from the bed do not necessarily represent wall shear stress τ_o values. Moreover, τ_o has been found to be close to zero before the reattachment point

(below the shear layer) [*Nezu and Nakagawa*, 1989; *Shamloo et al.*, 2001]. Similarly *Simpson* [1989] has suggested that maximum shear stress occurs near the maximum velocity gradient and decreases in the recirculation zone where little correlation is observed between u and w (and a tendency towards isotropy [*Nezu and Nakagawa*, 1989]). If turbulence is isotropic its statistics are invariant under reflections or rotations of the coordinate system [*Tennekes and Lumley*, 1972]. In other words, isotropic flows are statistically independent of direction (i.e., $u' = v' = w'$) so that their contribution to Reynolds shear stresses is zero [*Bradshaw*, 1971]. *McLean et al.* [1994] observed $-\rho\overline{u'w'}$ values in the shear layer to be an order of magnitude greater than τ_0. The shear stress induced by the LRE wake is often referred to as form drag (τ'') and it is generally taken into consideration when estimating τ_0 from the log-law in the presence of LREs [*Lawless and Robert*, 2001], since skin or friction drag, τ', is considered to be the determining stress for bedload transport. As the shear layer curves downward towards the reattachment point, the velocity gradient is lessened due to the increased entrainment and mixing between outer flow and the recirculation zone resulting in a decrease in $-\rho\overline{u'w'}$. While τ_0 has been found to be much lower in magnitude than shear layer values, the impinging shear layer does have an measurable effect on τ_0. Bed shear stress has been found to increase at reattachment and further downstream compared to upstream values [*McLean et al.*, 1994; *Shamloo et al.*, 2001], thus having a direct effect on sediment transport.

Near-bed velocity measurements are difficult to obtain in gravel-bed rivers due to the random protrusion of discreet particles of different sizes, shapes and orientation. Because of the high heterogeneity and general unevenness of the bed, determining the exact height of the sampling volume or the appropriate zero-datum is difficult [*Carling*, 1992]. For a gravel-bed river such as the Eaton North which has a D_{50} = 0.035 m, velocity measurements obtained at near-bed locations ($z \approx 0.03$ m) may be influenced by small-scale flow separation and shedding caused by immediately upstream grains protruding slightly higher above the bed. This shadow effect when recording near-bed measurements over gravel was described by *Lawless and Robert* [2001] and induced variations in their measured velocity gradients. For the experiment presented in Chapter 7, near-bed ADV measurements were attempted on several occasions. Figure 8.1

presents the bed topography of Site 8 (previously presented in Figure 6.1) and the spatial distribution of $-\rho\overline{u'w'}$ for two measurement planes above the bed at z = 0.12 m and z = 0.04 m.

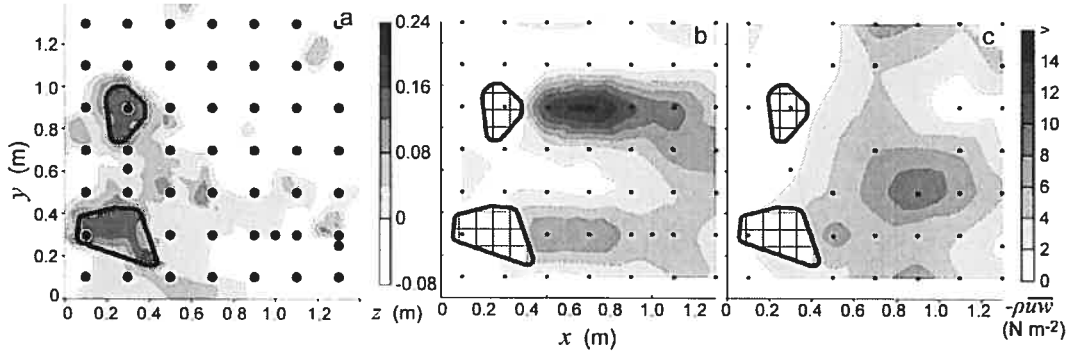

Figure 8.1. Spatial distribution of: a) bed topography; b) $-\rho\overline{u'w'}$ at z = 0.12 m; c) $-\rho\overline{u'w'}$ at z = 0.04 m at Site 8. Black dots represent sampling locations of velocity measurements. Flow is from left to right. LRE location represented by thick black line and cross-hatching.

The first noticeable feature between the two $-\rho\overline{u'w'}$ maps is that the region of high $-\rho\overline{u'w'}$ values in the wake of the left side LRE at y = 0.9 m seen in the upper plane is not observed in the near-bed plane. Close inspection of Figure 8.1c indicates that velocity measurements from the left LRE wake are missing due to an inability to resample these points at the lower level and obtain quality time-series. These sampling locations were either below the tops of the bed roughness elements lying in the wake of the LRE or the recorded time-series had poor ADV signal correlations and were therefore rejected from the analysis. As noted in Chapter 5, poor signal correlations were often attributed to excessive bottom echo noise arising from the pulse signals rebounding off the heterogeneous gravel bed. Near-bed measurements using ADVs were in general sparse and difficult to obtain throughout all the experiments presented in this thesis. Even in smooth bed flume studies, ADVs inadequately resolve velocities within a few centimetres of the bed [*Voulgaris and Trowbridge*, 1998; *Finelli et al.*, 1999; *Dombroski and Crimaldi*, 2007]. Good quality near-bed measurements were obtained in a recent study by *Buffin-Bélanger et al.* [2006], but these measurements were performed over a cast of polyurethane resin which is likely to be much less reflective to sound

pulses than solid stone. *Snyder and Castro* [1999] have as well obtained noisy signals when sampling close to the boundary with ADVs. The authors attributed this noise to sound reflections off the boundary which were resolved by covering the boundary with a thin rubber mat.

Figure 8.1c shows elevated $-\rho\overline{\tilde{u}\tilde{w}}$ located at $x,y = (0.9,0.5)$ which is not related to either of the LREs outlined in black. Comparison with the bed topography maps (Figure 8.1a) shows that this high $-\rho\overline{\tilde{u}\tilde{w}}$ value could be associated with small-scale flow structures shedding from a small protruding element directly upstream at $x,y = (0.7,0.5)$. The effect of this small-scale shedding is localized near the bed and can not be observed in the higher measurement plane ($z = 0.12$ m). In general, the spatial-distribution plot of near-bed $-\rho\overline{\tilde{u}\tilde{w}}$ (Figure 8.1c) does indicate elevated values $-\rho\overline{\tilde{u}\tilde{w}} = c.\ 5\ \text{N m}^{-2}$ which may be associated with the impinging shear layer and wake of the two LREs. These values are a factor of 3 – 4 less than maximum values observed for the upper plane $-\rho\overline{\tilde{u}\tilde{w}} = 14\ \text{N m}^{-2}$ (Figure 8.1b). This result is in disagreement with the order of magnitude decrease between shear layer and bed measurements of $-\rho\overline{\tilde{u}\tilde{w}}$ suggested by *McLean et al.* [1994]. This increased near-bed $-\rho\overline{\tilde{u}\tilde{w}}$ would favour the removal of bed sediments from the wake region (until an equilibrium is reached through bed armouring).

Perhaps due to the lack of near-bed velocity measurements, we were not able to identify the flow acceleration along the flanks of the LRE investigated which has been suggested to take place in other studies [*Brayshaw et al.*, 1983; *Best and Brayshaw*, 1985]. The occurrence of flow acceleration would promote corridors of greater sediment transport and armouring adjacent to the LRE. Even with near-bed measurements, *Lawless and Robert* [2001b] were as well unable to identify flow acceleration along the flanks of LREs in their rough-bed flume experiments, suggesting that it may be difficult to identify in gravel-bed rivers.

In Chapter 6 and 7, zones of high values of $-\rho\overline{\tilde{u}\tilde{v}}$ were observed downstream of the lee edge of LREs slightly towards the lateral sides and often coincided with zones of high $-\rho\overline{\tilde{u}\tilde{w}}$. Such spatial-patterns indicate high flow complexity and intense 3D (horizontal and vertical) momentum exchange in the wake of the LREs. This strong

turbulent activity in the wake of LREs would greatly enhance the mixing of suspended sediments, as well as nutrients and dissolved oxygen primarily in the localized vicinity of the LREs and depending on relative LRE size throughout the water column. The positive and negative high magnitude zones of $-\rho\overline{u'v'}$ in the wake support in part the downstream counter rotating vorticity models suggested by previous studies [*Acarlar and Smith*; 1985; *Best and Brayshaw*, 1985; *Paola et al.*, 1986]. These studies suggest the formation of an upstream standing vortex with downstream trailing tails which form the 3D counter rotating vortices. While the positive and negative $-\rho\overline{u'v'}$ zones were observed downstream of the lee edge of a number of the LREs investigated in Chapter 7, we were not able identify an upstream stationary vortex structure either through mean flow velocity vectors or though turbulent momentum fluxes. On the stoss side of the LREs and along the sides, Reynolds shear stresses were found to be relatively low suggesting that the downstream $-\rho\overline{u'v'}$ zones may be formed solely from the lateral separation along the lee sides of the LREs. This observation is supported by a recent laboratory and numerical modeling study by *Strom et al.* [2007] who were unable to detect the formation of the stationary horseshoe vortex although they did observe lateral shearing and counter rotating vortices in the wake of the micro-bedform under investigation. *Bradshaw* [1987] has suggested that the size and strength of stationary vortices depend on the LRE leading edge shape – for a sharp leading edge the stationary vortex may be very close to the bed and rapidly diffused. Our velocity measurements on the stoss side of the LREs were likely too course to identify these structures. The 3D flow aspects and turbulent secondary currents in the wake of the LREs alter the linear shear stress distribution predicted by 2D uniform flow as the flow ceases to be unidirectional [*Nezu and Nakagawa*, 1993; *Papanicolaou and Hilldale*, 2002]. *Papanicolaou and Hilldale* [2002] found that bed shear stress estimated through conventional estimation methods using u_* underpredicted the true τ_0 by almost 42% when turbulent secondary flows were present. When estimating bed shear stress *Nikora et al.* [2002a] included both horizontal near-bed Reynolds stress components responsible for the vertical flux of momentum towards the bed (i.e., $-\rho\overline{u'w'}$ and $-\rho\overline{v'w'}$). The results of Chapter 6 and 7 indicate that while strong zones of $-\rho\overline{u'v'}$ occurred in the wake,

$-\rho\overline{vw}$ values were generally low and including this term would add marginally to the estimated τ_o.

The discussion to this point has referred to time-averaged shear stress values (i.e., $-\rho\overline{uw}$, $-\rho\overline{uv}$ and τ_o). Reynolds shear stress values of individual events detected through quadrant analysis in the shear layer were observed to be as much as an order of magnitude greater than mean values (Figure 5.8). These events in the wake are primarily due to shedding shear layer flow structures. Periodically, as shown in Chapter 6, LS flow structures advecting from upstream interact with ejection or sweep events by enhancing either the upward or downward movement. This would suggest that LS flow structures may play a role in temporarily bringing the LRE shedding high energy structures nearer to the bed where they could exert a greater influence on shear stresses grain mobilization. High magnitude events induced by flow separation play a key role in sediment transport [*Nelson et al.*, 1995]. In Chapter 6, sweep and ejection events were found to dominate the fractional contribution to local $-\rho\overline{uw}$ in the wake region: sweeps dominate in magnitude and frequency in the near wake and ejections dominate both near and far wake. The backward facing step study by *Nelson et al.* [1995] shows sweep events to be responsible for the majority of the bedload transport, primarily due to their high frequency of occurrence. Outward interaction events which were relatively rare were as well related to bedload movement. Similar results were obtained by *Williams et al.* [1989] who observed bedload movement to be a highly intermittent process and related to strong intermittent events. High magnitude ejection events (burst like motions) in the wake of large bedforms were found to be highly effective in vertically mixing suspended sediment and thus are suggested as key processes in maintaining suspended sediment transport [*Lapointe*, 1992]. Similarly upwelling boils are associated with large suspended sediment concentrations [*Jackson*, 1976; *Kostaschuk and Church*, 1993].

From the above discussion, it can be inferred that LREs and the intense 3D hydrodynamics associated with their wake should contribute markedly to the local resuspension of fine sediments and transport of larger grains mobilized into the wake zone from upstream. Intermittently, LS flow structures advecting form upstream, would coincide with LRE shedding events possibly enhancing shear stresses and sediment transport capacities in the wake.

8.2. Spatial Organization

The fine-scale spatial characterization of turbulence around individual and multiple submerged LREs investigated in this thesis suggests a localized hydrodynamic effect. The LREs generate high turbulent energy in the wake zone directed towards the bed, yet this zone was found to be relatively narrow and not to extend much laterally beyond the sides of the LREs. The localized hydrodynamic effect of LREs has been suggested in a coarser reach-scale study [*Lamarre and Roy*, 2005] using 2D velocity measurements. In Chapter 7, the flow interaction induced by multiple LREs was assessed by specifically selecting some sites which contained closely spaced LREs (either laterally and longitudinally). *Kucukali and Cokgor* [2007] have suggested laterally spaced LREs in rivers may exhibit different flow patterns than isolated elements, yet their remarks are based on laboratory flume studies with high constriction widths. The spatial distribution of turbulence statistics investigated in Chapter 7 does not reveal much lateral interaction between LREs when the lateral separation distance was greater than approximately $1.5\emptyset_s$. Maximum turbulent energy was observed to occur directly downstream of the LREs with a relatively narrow wake which supports the results of *Shamloo et al.* [2001]. For the isolated LRE investigated in Chapter 4, the majority of the variance in the turbulent parameters sampled over the longitudinal-vertical plane was explained by spatial scales of $\Delta x = 5h_s - 10h_s$. This longitudinal extent, Δx, is similar to the extent of influence of the LREs shedding eddies and wake zone observed in Chapters 5 through 7. Results from Chapter 7 showed the mean longitudinal length of the wake zone where turbulence was most intense (defined by elevated k_e values > $1.5k_e'$) to extend $3.4h_s$ downstream from the lee edge of the LREs. The effect of close longitudinal spacing between LREs was only observed at one site in Chapter 7, where an apparent disruption of the upstream LRE wake is observed due to the physical presence of the downstream element.

The fine-scale characterization presented in this thesis provides insights on the spatial distribution of LREs throughout gravel-bed river reaches. Studies have indicated that separate LREs rarely occur immediately downstream from each other [*Hassan and Reid*, 1990; *Lamarre and Roy*, 2001]. This is likely due to the intense turbulent activity in the wake of LREs and the high Reynolds shear stresses impinging on the bed. While

particles with minimal bed protrusion would experience lower magnitude stresses, larger elements which are mobilized into the wake of an upstream LRE would experience much greater fluctuating stresses as demonstrated by Figure 8.1. The higher shear stresses would promote the transportation of these large particles further downstream out of the influence of the wake thus creating an immediate downstream zone clear of LREs. If many LREs were available and mobilized during a flood event than the local hydrodynamics of each LRE would determine a certain minimal spacing between longitudinally aligned LREs (which would be dependent on the LRE size as supported by *Wittenberg and Newson* [2005]). If the number of LREs was not supply limited this would lead to the tendency of maximum flow resistance as suggested by *Hassan and Reid* [1990]. Yet if the grain size characteristics of the bed material were such that relatively few LREs are available for mobilization the result may be a somewhat random distribution of LREs as suggested by *Lamarre and Roy* [2001]. The diamond pattern formations of LREs by *de Jong and Ergenzinger* [1995], although not generally observed, would as well be dependent on LRE supply and grain size characteristics. *de Jong and Ergenzinger* [1995] proposed a subcritical ($Fr < 1$) "shear wave" model for the diamond pattern, yet the spatial distribution of LREs is likely a reflection of the influence of the highly turbulent wake and the staggered appearance a reflection of flow acceleration around the sides of the LREs which would promote a certain lateral spacing between LREs ($\Delta y > \emptyset_s$).

It has been suggested that roughness elements situated in the wake zone of LREs experience lower drag and lift forces [*Brayshaw et al.*, 1983]. The results of *Brayshaw et al.* [1983] are consistent with the results of this thesis, if it is assumed that the majority of *Brayshaw et al.* [1983] pressure measurements were obtained from the surface of downstream roughness elements located within the wake recirculation zone. As suggested by *Simpson* [1989], a rapid decay of Reynolds normal and shear stress occurs within the recirculation zone. Outside the recirculation zone, in the shear layer, high shear stress values are observed. Furthermore, time averaged drag values as estimated by *Brayshaw et al.* [1983] may not well represent the processes responsible for sediment transport. Infrequent strong events would exert many times the forces estimated by the mean drag forces. A similar suggestion was put forth by *Billi* [1988] who speculated that

bursting events were responsible for intermittently transporting marked lee-side sediments.

8.3. On the origin and maintenance of LS coherent flow structures

The results of this thesis have shed some light on the mechanisms of the origin and formation of LS turbulent flow structures in grave-bed rivers and the role of LREs in their maintenance. LS flow structures are consistent features of gravel-bed rivers consisting of alternating high- and low-speed depth-scaled wedges [*Roy et al.*, 2004]. *Yalin* [1992] proposed LS flow structures organize themselves in a checkerboard pattern of alternating wedges both laterally and longitudinally throughout the channel. *Kirkbride* [1993] argued that LS flow structures originate from the interaction of multi-sized vortices shedding from bed roughness elements. The results of this thesis, specifically Chapters 5 and 6, suggest that LS coherent structures advecting overtop of LREs are marginally affected by the intense turbulence generated in the LRE wake. In Chapter 5, it was shown that for the intermediate flow region z/Z = 0.4, there was no apparent difference in LS flow structure behaviour or size with and without the presence of a LRE. At most there was a subtle increase in cross-correlations directly downstream of the LRE perhaps indicating some type of maintenance process. A disruption of LS flow structures was observed below the LRE top, yet the disruption was localized to the wake region and the LS flow structures regained much of their pre-disturbed coherence $6.0h_s$ downstream. The LS flow structures spatial scales ($\Delta x = 4.6Z$ and $\Delta y = 1.0Z$) are in good agreement with the previous studies in gravel-bed rivers [*Roy et al.*, 2004], and as well are of similar length to the largest scale, time-averaged turbulent patterns observed in Chapter 4 ($\Delta x = 5.3Z$). Yet this may be a result of the similar flow stages and LRE sizes between the study site of Chapter 5 and that of *Buffin-Bélanger and Roy* [1998] and different results may be obtained under other flow conditions. While LS flow structures have been found to scale with both Z and $\overline{U}$ [*Marquis and Roy*, 2006a], the results of Chapter 7 indicate a weak dependence of wake area on Z and $\overline{U}$.

In Chapter 6, visualization identified the process of roll-up of small-scale initial shear layer vortices and their amalgamation into larger mesoscale flow structures which subsequently shed from the lee of the cluster. Much rotation was observed in the initial

shear layer vortices which were associated with sweep and ejection events detected simultaneously through the ADV measurements, yet little rotation was observed in the amalgamated meso-scale structures. *Schvidchenko and Pender* [2001] have suggested LS flow structures are due to depth-scaled vortical movements. Large-scale vorticity was not apparent in the visualization results of Chapter 6, however. The model that shedding vortices from roughness elements are responsible for the generation of LS coherent flow structures is not complete. The quasi-random spacing of LREs observed qualitatively at our study site and quantitatively in previous studies [*Brayshaw*, 1984; *Lamarre and Roy*, 2001] could not lend directly to the ubiquitous well organised occurrence of LS coherent flow structures throughout river channels. LREs and the amalgamated meso-scale shedding structures may provide a key generation mechanism for the turbulent energy required for the maintenance of LS flow structures in gravel-bed rivers, yet their ubiquitous formation (even in the absence of LREs) suggests a self-organisation as argued by *Paiement-Paradis et al.* [2003].

8.4. Fish habitat

The ongoing discussion on the high values of τ_0 and $-\rho\overline{uw}$ and the role of ejection and sweep events occurring in the wake of LREs which promote sediment transport would have a direct effect on fish holding downstream. It is not clear whether fish are able to cope or take advantage of increased stresses and turbulence in the wake of LREs or whether they seek out quiescent zones related to LREs with relatively low turbulence intensity. Fine-scale hydrodynamics are often ignored in fish habitat studies; instead depth averaged velocities are used to represent the flow field. This thesis has shown that LREs generate a complex 3D flow environment that cannot be adequately described by depth averaged velocities. As outlined in Chapter 2, there is a general inconsistency of results relating fish behaviour and preference to LREs and flow complexity. LRE in gravel-bed rivers have been found to provide cover and localized heterogeneous flow conditions and have been shown to be desirable environments for fish [*Bachman* 1984; *Van Zyll de Jong et al.*, 1997; *Mitchell et al.*, 1998; *Coulombe-Pontbriand and Lapointe*, 2004; *Smith et al.*, 2006]. Highly turbulent environments have been shown to increase swimming costs [*Enders et al.*, 2003], and the turbulence generated in the wake of LREs

have been shown to lower feeding rates and increase energy expenditure (time spent holding in the water column) [*Kemp et al.*, 2005]. The review article by *Liao* [2007] suggests that fish rely on multiple sensory inputs to negotiate complex flow environments and take advantage of altered flow environments to reduce swimming costs. *Liao et al.* [2003a] have shown under specific flume conditions that rainbow trout utilise vertical vortices shed from the sides of upstream obstacles to reduce energy expenditure. As discussed in Chapter 2, these laboratory experiments were preformed under low to moderate *Re* with patterns of quasiperiodic turbulent flow structures. The shedding flow structures are likely much different at high *Re* in natural rivers as has been shown in this thesis. The results of Chapter 6 have documented a dominance of lateral vortices being intermittently shed from LREs. While these "roller" eddies and associated sweep and ejection events would facilitate vertical nutrient exchange – possibly enhancing the availability of nutrients to stream biota – they could not be readily utilized by fish for energy expenditure minimization as proposed by *Liao et al.* [2003a]. Shedding structures were as well observed to have intermittent unpredictable behaviours which as pointed out by *Liao* [2007] could not be utilized by fish. Recent studies have suggested that visual isolation is the dominant reason for high correlations between LREs and juvenile Atlantic salmon (JAS) [*Dolinsek et al.*, 2007a;b]. *Bachman* [1984] has previously refuted this theory by suggesting it is more likely that LREs increase the number of energy-saving near-bed low flow velocity sites. *Dolinsek et al.*, 2007b have shown that mean velocities at fish locations (5 cm from the bed) were quite similar to randomly distributed mean velocities over their treatments. In contrast, the authors found that the predicted field of view of their territorial JAS was much smaller amongst their cobble/boulder treatments suggesting that their increased density among boulder was due to this decrease in territory size. While visualization is likely to be a factor for detemining JAS habitat density, these studies did not investigate the fine-scale hydrodynamics. The discrepancies between studies investigating the relationships between fish preference and LREs (e.g., *Smith et al.* [2005] and [2006]) are likely due to an inadequate characterization of the hydrodynamics and differences in velocity sampling locations in relation to the fish location (i.e., nose velocity, higher up in the water column or depth averaged values). In the complex flow generated by LRE, the

turbulent values can change dramatically (based on whether samples are obtained inside or outside the shear layer). To investigate the relationships between fish habitat, LREs and the effect of velocity sampling location an exploratory study was conducted on the *in situ* holding location of juvenile Atlantic salmon (JAS) in a gravel-bed river.

The goal of the study was to conduct a fine-scale spatial characterisation of the hydrodynamics associated with the holding position of JAS. The experimental set-up and results of a single site are presented here. These results were part of a larger scale experiment, yet during the experiment, the ADV probe was physically damaged resulting in intermittent erroneous low quality velocity measurements and a rejection of many of the results. The study was conducted on a boulder- and cobble-bed reach of the Little Southwest Miramichi River, New Brunswick. The diurnal holding and feeding position of JAS was identified through snorkelling and viewing tube techniques. The behaviour of the JAS was observed for several minutes in order to ensure a positive identification of the holding position (i.e., the JAS made feeding departures but returned to the same location). Nine detailed velocity profiles, consisting of five to twelve measurement points above the bed, were recorded using an ADV supported by a tripod. The profiles were obtained at the fish holding position and at surrounding locations in order to characterise the hydrodynamics surrounding the selected habitat. Velocity measurements were recorded at 25 Hz for 100 seconds.

The detailed topography around the fish holding location was measured using a Leica TC702 total station and is presented in Figure 8.2. The JAS was observed to hold very close to the bed in the lee of a LRE shown in the centre of Figure 8.2 x,y = (-0.25,0). The topography is relatively complex with a LRE located on the right-hand side of the sampling site x,y = (-0.3,-0.3) and a very large boulder located upstream at x,y = (-1.0,0.5) which protrudes almost to the water surface (Z = 0.35 m).

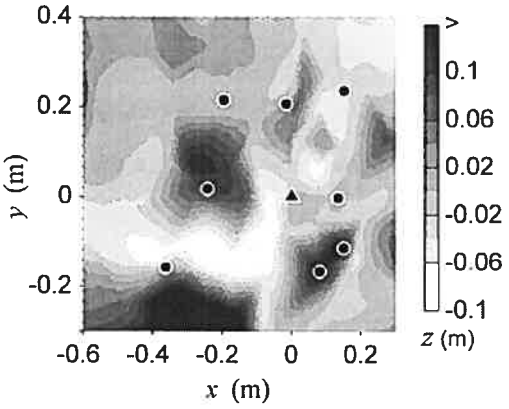

Figure 8.2. Site topography. Black triangle and dots represent sampling profile locations. Triangle represents JAS holding location. Flow is from left to right.

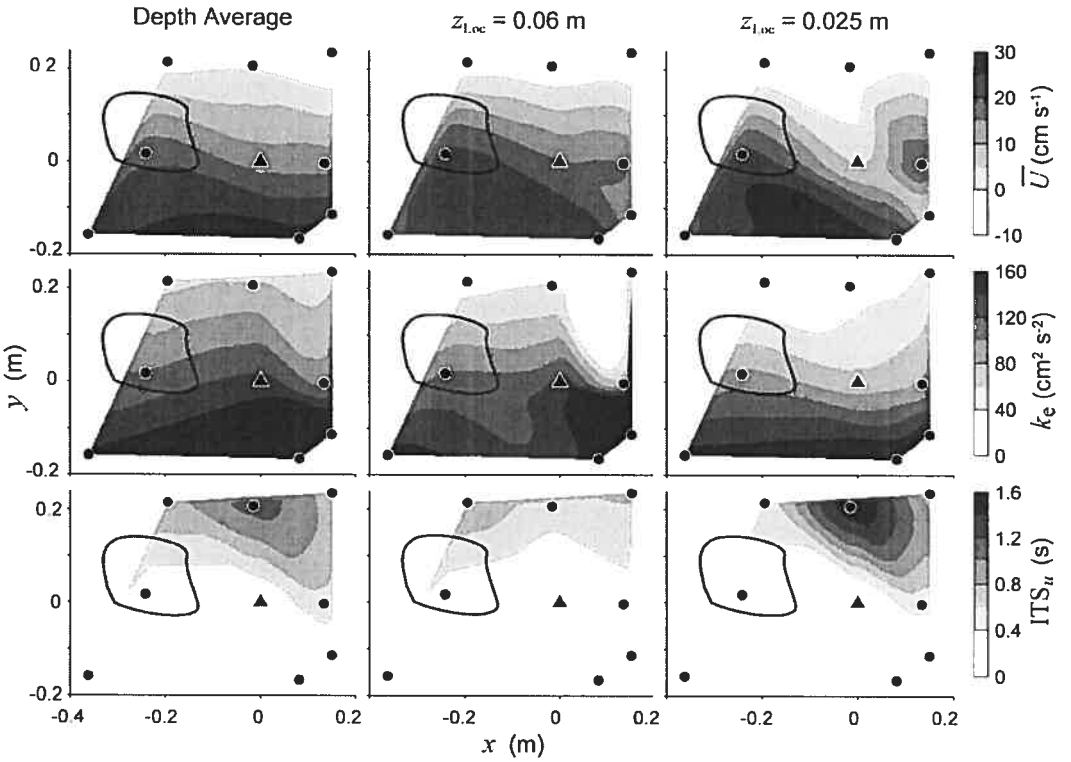

Figure 8.3. Spatial distribution of $\overline{U}$, k_e and ITS$_u$ for depth averaged values; and values estimated at z_{Loc} = 0.06 m; and at z_{Loc} = 0.025 m. Black triangle and dots represent sampling locations of the velocity measurements. Triangles represents JAS holding location. Flow is from left to right. LRE location is outlined by black line.

Mean u component velocity, $\overline{U}$, turbulent kinetic energy, k_e, and u component integral time scales, ITS_u, were estimated from the ADV velocity measurement profiles. Three spatial distributions of $\overline{U}$, k_e and ITS_u over the experimental site are presented in Figure 8.3. The spatial distributions were estimated using the average value per vertical profile, and measurements obtained at z_{Loc} = 0.06 m and z_{Loc} = 0.025 m, where z_{Loc} is the vertical height above the local bed or rock surface. The three spatial distributions exemplify the variation in mean and turbulence statistics estimated from different measurements within the same vertical profile. This is particularly true of complex flow environments (such as in the wake of LREs) where points may be measured within or outside of the shear layer. The topography of the site (Figure 8.2) should be taken into consideration when interpreting Figure 8.3 as the measurement locations are relative to a local datum and do not all lie on the same horizontal plane, as is the case for the experiments in Chapters 5 through 7. The negative $\overline{U}$ values shown on the left side (facing downstream) of all $\overline{U}$ subplots reflects the recirculation induced by the large upstream boulder (not shown) and little variation in $\overline{U}$ is shown between the three spatial distributions presented. Flow is seen to accelerate overtop of the central LRE where $\overline{U}$ = 20 cm s^{-1} at z_{Loc} = 0.025 m. Flow acceleration discerned as wedge-shaped velocity profiles over boulder surfaces has been previously observed by *Hoover and Ackerman* [2004]. At the fish holding position x,y,z_{Loc} = (0,0,0.025), velocities are markedly lower ($\overline{U}$ = 4.5 cm s^{-1}) than those observed within the same profile at z_{Loc} = 0.06 m ($\overline{U}$ = 14.7 cm s^{-1}). Similarly, *Bachman* [1984] observed brown trout to positioned themselves close to the substrate or rock surface with much higher velocities occurring millimetres overhead. k_e at the near-bed JAS holding location is 50% lower in magnitude than values at z_{Loc} = 0.06 m. The high k_e values at x,y,z_{Loc} = (0,0,0.06) is likely related to the wake and shear layer of the central LRE. The spatial gradient in k_e (increasing k_e with decreasing y) is similar for depth averaged and z_{Loc} = 0.025 m values, yet the relative magnitudes of k_e averaged over the vertical profiles is shown to markedly overestimate k_e near-bed values. With the exception of the profile at x,y = (0,-0.2), the spatial distributions of ITS_u are similar in all three spatial estimates of Figure 8.3. The near-bed estimates of ITS_u for the fish holding location are relatively small. The long

duration ITS_u estimated at x,y,z_{Loc} = (0,0,0.025) is either a reflection of large recirculation eddies due to the upstream boulder or instrument error due to a possibly damaged probe tip. Long duration ITS_u has been observed at channel margins under low flow conditions possibly due to recirculation zones (MacVicar *et al.*, manuscript accepted for publication, 2007).

Figure 8.4 presents scatter plots of $\overline{U}$, k_e and ITS_u as a function of z_{Loc} (with z_{Loc} as the ordinate) for all site measurement locations (combining all profiles). Figure 8.4 indicates that for this site, the JAS selected a holding position with a relatively low positive near-bed $\overline{U}$ compared with available measured near-bed $\overline{U}$. While the low velocity preference of salmonids supports some studies [*Smith et al.*, 2005], a recent study by *Dolinsek et al.* [2007b] has shown opposing results. Fish were found to select holding locations (assumed to be 5 cm above the bed) of increased velocity relative to randomly distributed velocities in a boulder/cobble field. These conflicting results may be due to the differences in velocity measurement location. JAS (with lengths less than 7 cm) have been shown to hold within 2 cm of the bed [*Heggenes et al.,* 2002] with their pectoral fins placed directly on the substrate [*Arnold et al.*, 1991]. The discrepancies between our results and those presented by *Dolinsek et al.* [2007b] (obtained from the same river) only highlight the importance of measuring velocities on scales relevant to the biota studied. Figure 8.4 shows that the near-bed k_e value estimated at the holding position of the JAS was relatively moderate compared to the surrounding near-bed measurements. The avoidance of high turbulent locations supports the findings of previous studies [*Smith et al.*, 2005; *Cotel et al.*, 2006] and is likely due to the higher swimming costs associated with increased turbulence [*Enders et al.*, 2003]. Additionally, Figure 8.4 shows that the JAS did not select the lowest k_e locations available which supports previous work by *Cotel et al.* [2006]. This suggests that JAS tolerate (or have a preference for) a certain level of turbulent intensity and other factors are perhaps important in dictating the preferred location. ITS_u is an indicator of the average duration of coherent flow structures and if the Taylor frozen turbulence hypothesis is assumed to be applicable, ITS_u can be used to estimate the average size of coherent flow structures. The ITS_u at the selected holding position was among the lowest

estimated from all near-bed measurements suggesting that JAS may avoid locations of larger turbulent coherent flow structures.

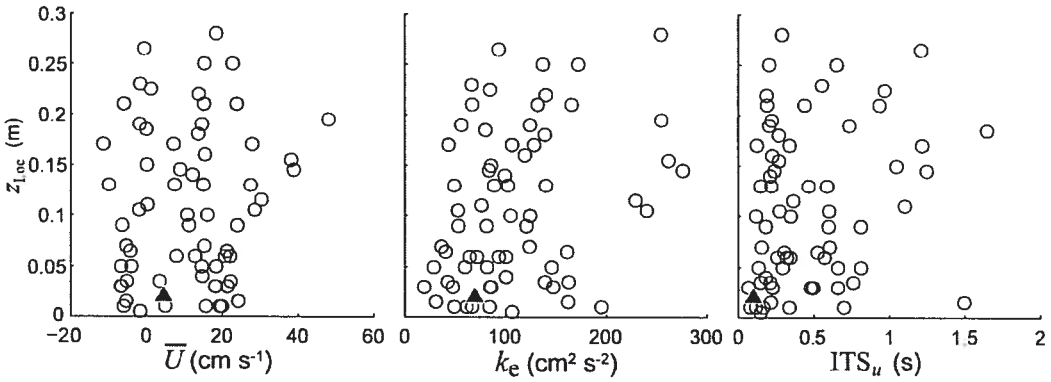

Figure 8.4. $\overline{U}$, k_e and ITS$_u$ scatter plots. Triangles represents JAS holding location.

The spatial distribution of velocity profiles was not sufficient to fully characterise the wake region of the central LRE or the extent of the recirculation zone. The positive u component velocity measured at the nose of the JAS along with the upstream orientation of the JAS indicates that the fish holding location was outside of or at the limits of the recirculation zone. k_e values at the fish holding position were moderate and increased higher up in the vertical profile and just downstream. This may indicate that the JAS was positioned just upstream or off to the side of the impinging shear layer and the reattachment point, but due to the lack of spatial coverage of velocity measurements these inferences remain speculative.

The foregoing spatial distribution of mean and turbulent flow variables illustrates the importance of sampling instantaneous velocities as close to the fish holding position as possible. Due to the complex flow patterns induced by the LREs, marked differences in $\overline{U}$, k_e and ITS$_u$ were obtained from velocities measured within the same profile and in adjacent profiles. In this thesis, mean velocity and turbulent flow statistics have been shown to vary markedly between locations outside or within the shear layer. The importance of characterising the local flow environment at scales experienced by benthic organisms and fish is well recognized [*Hart and Finelli*, 1999] and should be taken into consideration especially in complex flow environments. At fine scales, JAS tend to chose lower positive velocity holding locations with only moderate turbulence levels,

yet the profile depth averaged $\overline{U}$ and k_e at the fish holding location suggest magnitudes 2 – 3 times those estimated at z_{Loc} = 0.025 m. These differences in $\overline{U}$ and k_e obtained through depth averaging may explain some of the discrepancies observed between studies investigating the links between LRE and fish behaviour such as *Smith et al.* [2005] and [2006].

The preliminary results presented here show how mean and turbulence statistics can vary markedly due to small-scale differences in measurement location. Yet in order to fully characterise and generalise the fine-scale relationships between LREs and aquatic biota a much more detailed experiment is required which would investigate numerous JAS holding positions. A sampling scheme similar to that used in Chapter 7 could be followed with the addition of near-bed 3D measurements. As previously mentioned in Section 8.1, near-bed measurements over rough heterogeneous substrate are difficult to obtain with ADVs and these difficulties should be considered in the sampling scheme.

The addition of LREs to streams has been shown by [*Mitchell et al.*, 1998] to increase the availability and diversity of habitat and to provide protective cover for juvenile fish. The authors also observed an increase in drift abundance close to the LREs, where due to the flow acceleration the drift is "funnelled" around the LREs. The intense 3D hydrodynamics in the wake of LREs is likely to provide increased mixing of nutrients and promote the resuspension of macroinvertebrates and their availability for fish downstream of LREs. Chapter 4, showed that the spatial distribution of turbulence in the longitudinal direction overtop and downstream of a LREs was best explained at scales of $5h_s$ to $10h_s$, while Chapter 7 identified the most intense portion of the wake zone was relatively narrow and restricted on average to $3.4h_s$ downstream of the lee edge. Without knowing the exact hydrodynamic characteristics sought by fish it is difficult to suggest guidelines and optimal spacing of LREs required to create habitat, yet from this thesis it can be inferred that positioning LREs a distance of approximately $\Delta x > 15h_s$ and $\Delta y > 3\emptyset_s$ would likely create the most heterogeneous flow conditions. These minimum distances are three times larger than the dimensions of the most intense portion of the wake zone and would allow sufficient distance between LREs for the separated boundary layer to reattach and possibly recover to near free-stream conditions.

This would then provide habitat in the near- and far-wake with low velocities and high turbulence as well as low turbulent zones with higher velocities downstream and to the sides of the LRE. Heterogeneity would be increased by distributing the LREs along the entire width of the river, thereby providing varying relative submergent conditions and ensuring heterogeneity flow conditions at various flow stages. Following the minimum spacing specified above a quasirandom distribution of LREs is likely more appropriate than a staggered or parallel deployment of LRE as it better represents the natural environment.

8.5. Conclusions

The results of this thesis help to clarify the possible implications LREs have on sediment transport and the spatial distribution of LREs in gravel-bed rivers. Furthermore, explanations are given for previous differing views on relationships between LREs, turbulence and fish preference. Bed shear stress values increase where the shear layer impinges on the bed at reattachment. The wake is associated with high $-\rho\overline{uw}$ and strong intermittent sweep and ejection events which would discourage large particles from settling directly downstream in the wake zone, thus providing a mechanism explaining the minimum separation distance between LREs shown by previous spatial distribution studies. Studies with divergent results in fish preference with respect to LREs are likely related to the coarseness of the velocity and turbulent field characterization. Velocities and turbulent estimates can differ appreciably on centimetre scales downstream of LREs (as the preliminary study presented in this chapter has shown) indicating the importance sampling exactly at JAS holding locations. Fish are likely to be negatively affected by the high turbulent fluctuations in LRE wakes, but are able to seek out lower velocity and turbulent zones which minimize energy expenditure.

9. GENERAL DISCUSSIONS AND CONCLUSIONS

This thesis has investigated in detail the hydrodynamic characteristics associated with submerged large roughness elements (LREs) in gravel-bed rivers. Using an *in situ* approach with a range of sampling techniques and data analyses of flow turbulence, we have provided a comprehensive description of the physical processes and associated hydrodynamics of LREs as well as their interaction with LS coherent flow structures. This concluding chapter is divided into four parts. Initially the key findings of the four main article chapters are summarised, followed by a discussion of the general understanding of LRE hydrodynamics obtained in this thesis. The originality of the work is highlighted and areas of future research are identified.

9.1. Summary of key findings

Each article chapter on its own has been targeted to meet a specific thesis objective as outlined in Chapter 3, but together the results of the four chapters give an integrated characterization of the *in situ* LRE hydrodynamics. In chapter 4, principal coordinates of neighbour matrices (PCNM) analysis and redundancy analysis (RDA) are used to successively partition, over four spatial scales, the variance in the mean and turbulent flow data obtained from a 2D plane crossing over a LRE. A large proportion (41%) of the variation in the turbulent data is significantly ($\alpha = 0.01$) explained by spatial scales on the order of $\Delta x = 2.6Z - 5.3Z$ and $\Delta z = 0.5Z - 1.0Z$ (or alternatively $\Delta x = 5h_s - 10h_s$ and $\Delta z = 1.0h_s - 2h_s$). More specifically, these spatial scales are able to explain 75% of the variance of the main turbulent flow indicators u', w', and $-\rho\overline{u'w'}$, with the majority of variation explained at the $\Delta x = 5h_s$ and $\Delta z = 1.0h_s$ scales. The smaller spatial scales explain < 15% of the variance. These results suggest that for the x-z plane the core hydrodynamic effect of LREs is at vertical scales of h_s and longitudinal scales of $5h_s$ and that smaller scale spatial patterns do not contribute markedly to the variation in the turbulent data. This is a key result which indicates the relative spatial scales influenced by LREs which can be directly related to LRE size. The longitudinal scale of $5h_s$ is a consistent result with the distance of perturbation induced by the LRE examined in Chapter 5. The 2D velocity measurements of Chapter 4 gave a detailed characterization

of the centreline turbulent patterns (where the turbulent generation is generally most intense), but could not show any lateral hydrodynamic effect. Chapters 5 – 7 are complementary to Chapter 4 and include 3D velocity measurements over horizontal (and vertical) planes in order to properly assess the lateral effect.

In Chapter 5 we have directly tested the effect of a pebble cluster on the turbulent flow field. The key result of the chapter is the identification and observed persistence and robustness of LS turbulent coherent flow structures convecting past LREs. These LS flow structures in the intermediate flow region, $z/Z = 0.4$, identified through space-time correlation analysis remain remarkably unchanged with or without the LRE in place. The LRE has an intense localized effect on the hydrodynamics in the wake which is noticeable up to approximately $x = 6h_s$. k_e values double in the LRE wake and peak energies in the w component velocity spectra indicate the shedding of shear layer vortices at frequencies similar to those estimated using U-level analysis and predicted using a Strouhal number of 0.18. While the behaviour of LS flow structures under the influence of a LRE could be assessed, the effect of LS flow structures on the shedding wake structures required a different experimental approach.

In Chapter 6, a novel experimental technique using the *in situ* simultaneous deployment of ADVs and flow visualization is used and the results show an intermittent effect of LS flow structures on the LRE shear layer and shedding vortices. While horizontal and vertical spatial distributions of turbulence statistics are estimated, the later half of this chapter again focuses on a 2D vertical plane crossing over the LRE (where the turbulent generation was most intense). Key results are the identification of physical bimodal shedding processes where small scale instability vortices grow through entrainment and amalgamation into mesoscale flow structures which are subsequently shed downstream. These laterally oriented vortices dominate the turbulent momentum exchange in the wake and are associated with intense sweep and ejection events identified through quadrant analysis. The results confirm previous studies by *Roy et al.* [1999] and *Buffin-Bélanger et al.* [2001a] suggesting the shear layer compresses towards the bed and ejects upwards with the passage of LS sweep and ejection events, respectively but these interactions are much more intermittent than previously thought. The spatial distribution of turbulence variables over the 2D vertical centreline plane

show somewhat different patterns to those discussed in Chapter 4 (where the original data set was collected by *Buffin-Bélanger and Roy* [1998]) and reflect a difference of LRE geometries and flow conditions. In order to isolate these effects on LRE hydrodynamics, Chapter 7 investigates various LRE geometries and flow conditions.

In Chapter 7, the turbulent structure generated in the wake of numerous LREs is predominantly explained (approximately 60%) by $\emptyset_s$, h_s, and $\overline{U}$. Specifically, these independent variables explain more than 80% of the variance in $k_{e\text{-}max}$ and $-\rho\overline{uw}_{max}$ in the upper plane measurements (z/Z = 0.47) and predominantly $\emptyset_s$ and $\overline{U}_{Lw}$ explain *c.* 70% of the variance in $k_{e\text{-}max}$ and $-\rho\overline{uw}_{max}$ for measurements below the LRE tops. Water depth explains an unexpectedly small amount of variance suggesting that in natural rivers turbulence levels behind LREs increase with flow stage primarily as a result of the associated increase in mean velocity. The intense effects of LREs on the flow field are shown to be confined to a localized zone in the lee of the LREs which highlights a general trend observed in the previous article chapters. The high stress 3D turbulence in the wake is restricted to a zone below the LREs tops and does not extend much beyond the lateral widths of the LREs. The longitudinal extent of the elevated wake values is $3.4h_s$. Similarly to Chapter 6, $-\rho\overline{uw}$ was generally shown to dominate the turbulent momentum exchange in the wake.

9.2. Towards a better understanding of LRE hydrodynamics

Through an integrated approach combining multiple sampling techniques and data analyses a much better understanding of the hydrodynamic influence of LREs in gravel-bed rivers is achieved. The schematic of knowledge gaps of Figure 2.33 is re-drawn in Figure 9.1 summarising the gain in knowledge obtained by integrating the results of the four article chapters. Revisiting the two-dimensional high density *x-z* plane measurements of *Buffin-Bélanger and Roy* [1998] allowed for the identification of scale-dependence in the vertical and longitudinal directions. This data set was exceptional due to the high density sampling grid which allowed for the partitioning of the variance into four scales. The large spatial scale ($\Delta x = 5h_s$ and $\Delta z = 1.0h_s$) significantly explained the majority of the variation in the main turbulent parameters and matches with later

chapters identifying the longitudinal and vertical extent of the elevated turbulent values in the wake zone. For centerline measurements across a LRE, a reasonable approximation of the flow field was obtained by 2D measurements due to the dominance of the *uw* Reynolds stress component in the wake. Yet, a much more comprehensive view of the LRE and its impact on the surrounding hydrodynamics was obtained by measuring the 3D velocities over laterally spaced horizontal planes. The *v* velocity component was found to provide an important contribution to the turbulent energy and momentum exchange predominantly downstream of the lee side edges of the LREs but as well towards the centre of the wake. For certain LREs and for others at high flow stages $-\rho\overline{uw}$ clearly dominated throughout the wake. At lower flow stages the patterns of elevated $-\rho\overline{uw}$ and $-\rho\overline{uv}$ values were found to be more complex and in some cases both Reynolds stresses contributed equally to the momentum transfer in the wake.

Only through a detailed focus on flow processes using synchronous flow visualization and fine-scale ADV measurements (Chapter 6) could the intense *uw* Reynolds stress (and sweep and ejection events) in the lee of LREs be attributed to small- and meso-scale laterally oriented roller vortices. From this result, inferences could be made about the high positive and negative $-\rho\overline{uv}$ patterns in the LRE wake zones observed in Chapter 7. These patterns are the result of shearing from the lateral sides of the LREs in the form of counter-rotating *z*-axis lateral separation vortices. Through the focus on physical processes we were able to identify the intermittent nature of the shedding from the lee of LREs and the interaction with LS coherent flow structures convecting from upstream. The fine-scale measurement approach allowed for a good characterization of the LRE wake zone which was associated with intense 3D turbulence generally localized below the LRE tops and within the lateral widths of the LREs. The longitudinal extent of the most intense part of the wake was approximately $3.4h_s$ (Chapter 7) but the full extent of wake could be as much as $10h_s$ downstream for the lee edge (Chapters 4 – 6).

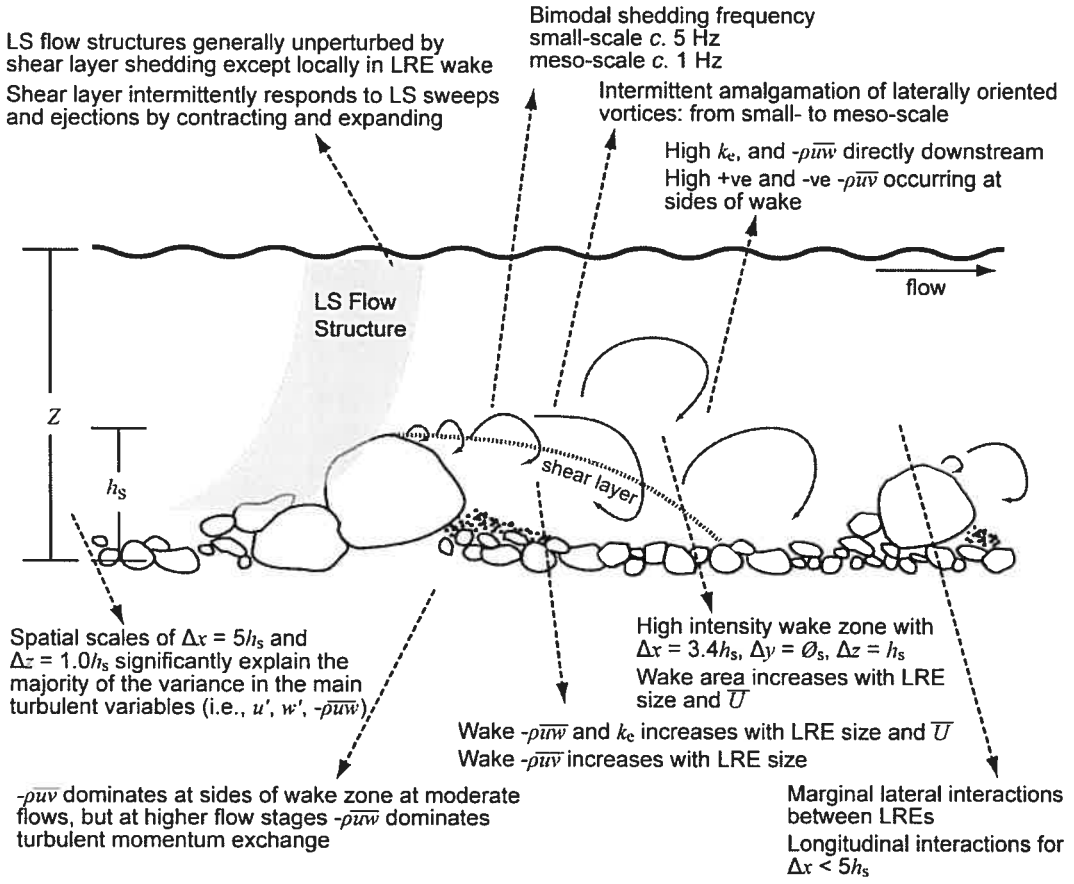

Figure 9.1. Schematic integrating and summarizing salient results on the hydrodynamic effects associated with LREs.

The intense 3D turbulence in the wake of LREs shown here suggests that LRE play an important role in the generation of turbulence in gravel-bed rivers and that they are likely responsible for much of the turbulent mixing of suspended material, dissolved oxygen and nutrients within the water column. Their spatial distribution is likely affected by their specific geometry but the main determining factor is their size which through the generated turbulent wake would discourage or limit the settlement of secondary LREs in close longitudinal proximity. The minimum longitudinal spacing between LREs should be greater than the most energetic part of the wake (i.e., $\Delta x > 3.4h_s$) but may be as much as $\Delta x > 10h_s$ given that distance required for the boundary layer to redevelop and return to unobstructed conditions. The turbulent energy generated by LREs and the amalgamation of shedding vortices may provide a maintenance mechanism for LS coherent flow structures, yet the quasi-random distribution of LREs

in the river channels can not explain the well organized spatial distribution of LS flow structures or their existence in the absence of LREs. LS flow structures are likely limited in size by the flow depth given the consistent scalings found in the literature [*Nakagawa and Nezu*, 1981; *Yalin*, 1992; *Schvidchenko and Pender*, 2001; *Roy et al.*, 2004; *Marquis and Roy*, 2006b]. Flow depth is therefore a more relevant scaling parameter for these flow structures than LRE size.

The gains for such a fine-scale hydrodynamic focus and the detailed knowledge obtained of the hydrodynamic influence of LREs may help clarify many divergent views in fluvial geomorphology and aquatic biology on the role of LREs in gravel-bed rivers as discussed in Chapter 8. For instance, there seems to be a recent trend to equate behavioural flume experiments conducted on fish under low Reynolds number conditions with fish behaviour in natural environments which have inherently high *Re* [*Liao et al.*, 2003a, *Liao* 2007]. These studies suggest that fish use periodic vertically oriented vortices for energy conservation. Our *in situ* results tend to show that shedding vortices from submerged LREs have an unpredictable, intermittent periodicity shown by the flow visualization results and the relatively small and rounded peaks in the velocity spectra (Chapter 6). Furthermore the wake under many flow conditions is dominated by roller vortices which could not be used by fish as suggested by *Liao* [2007]. The intense turbulent energy in the wake of LREs would indicate that fish biologists may have to look elsewhere to elucidate the reason fish abundance has been found to be positively correlated with LREs in rivers.

More generally, the results of this thesis show that LREs are important sources of river system turbulence: generating wake turbulence levels several factors greater than unobstructed values. At higher flow stages (with increased free-stream velocities), the wake turbulence, predominantly in the u and w components, is intensified due to the increased velocity gradient at the lee of LREs. LREs provide zones of intense vertical and lateral mixing which are likely to enhance the resuspension of sediment, nutrients and invertebrate drift. The turbulent wake zone is generally localized below the LRE tops and is more difficult to discern in the intermediate and outer flow regions particularly at higher *Re* and relative submergence as the turbulent flow structures

generated in the wake are quickly mixed and amalgamated with the surrounding unobstructed flow.

9.3. Originality of the results

This thesis presents a detailed spatial characterization of *in situ* 3D hydrodynamics around submerged LREs in gravel-bed rivers. To our knowledge there are no other published studies which have conducted such a fine-scale study of *in situ* submerged LRE hydrodynamics.

The measurement and statistical analysis techniques are original in their own right. The PCNM method of extracting scale dependent spatial patterns is a recently developed [*Borcard and Legendre*, 2002] powerful analysis technique allowing for the quantification of spatial or temporal scale dependence in data sets which has only been used in a limited number of ecological studies. Its use in Chapter 4 represents a first time application of this method in water resources sciences and illustrates the power of the method and its potential for a broad range of applications in water resources and the earth sciences. The synchronous flow visualization and 3D velocity measurement technique developed here to investigate the shedding structures and its behaviour under the influence of LS coherent flow structures is novel. Through this technique, valuable insights were gained in the characterization of *in situ* turbulent flow structures and processes.

While preliminary studies [*Kirkbride*, 1993; *Roy et al.*, 1999; *Buffin-Bélanger et al.*, 2001a] have suggested LS coherent flow structures influence shear layer shedding vortices, this thesis provides clear evidence that LS flow structures have a direct, albeit intermittent, effect on the shear layer and the shedding vortices. Conversely through quasi-3D space-time correlation analysis it was shown that the effect of shear layer vortices on LS coherent flow structures was relatively minor and localized below the LRE top. These represent new results which add to the growing knowledge base on LS coherent flow structures and their interactions with microtopographic units. In rivers due to the high *Re* and fully developed turbulent conditions, previous studies have found it difficult to quantify shedding frequencies from shear layers (e.g., *Rhoads and Sukhodolov* [2004]). The identification of *in situ* shedding frequencies from LREs using

flow visualization and velocity spectra is as well a novel result of this thesis which was obtained only through diligent experimental procedures.

9.4. Future research

Many avenues of future work are possible based on the results of this thesis. While this thesis investigates in detail the hydrodynamics above and below the top of LREs, given time and instrumentation constraints (discussed in Chapter 8) on most sampling deployments we were not able to sample close to the heterogeneous bed. Because of this lack of near-bed measurements, the hydrodynamics of the recirculation and reattachment zones associated with shear layer separation remain uncharacterized and could only be alluded to. A fuller understanding of LRE hydrodynamics would be achieved if the *in situ* recirculation, shear layer reattachment, and boundary layer re-development processes were investigated. Furthermore, near-bed measurements are required to accurately estimate shear velocity and the shear stresses, which if accurately estimated would give a better idea of the role LRE play in the transport of sediment in gravel-bed rivers. While LS coherent flow structures were found to be relatively undisturbed as they passed over the LRE in Chapter 5, their behaviour and response to the 3D dynamics of larger-scale bedforms such as pools and riffles could potentially be much different. There as well remains a missing link between the meso-scale vortices generated from LREs and the ubiquitous well organized occurrence of LS flow structures. While it has been suggested here and by previous authors [*Buffin-Bélanger et al.*, 2001a] that the meso-scale shedding flow structures may strengthen LS flow structures, their interaction should be more fully investigated possibly through the use of concurrent flow visualization and 3D velocity measurements.

In situ river studies offer many benefits such as direct applicability of results, but the main drawback to such studies is a lack of control on flow conditions and the inability to isolate independent variables and processes. Further research on the hydrodynamic effects of LREs could be pursued through laboratory flume experiments and numerical modeling. Under controlled conditions, flume work could provide supporting evidence on the effect of flow stage on LRE turbulent wakes by isolating and individually varying flow depth and free-stream velocity. Given the width constraints in

flumes, 3D numerical models would be ideal for investigating the hydrodynamics around spatially distributed LREs where various spacing configurations could be tested.

The combined ADV and flow visualization technique is constrained by several disadvantages such as the 2D representation of what is a highly 3D environment in the LRE wake; and the quick dissipation of the tracer in the high *Re* environment such that the meso-scale shedding behaviour was difficult to distinguish. These disadvantages could be improved by the use of a 2D light sheet projected in an *x-z* plane directly below the ADV array; the use of a second downward facing camera positioned above the injection point; and the use of a less diffusive (conservative) non-toxic dye tracer appropriate for use in natural rivers. The analysis of the films which is often a subjective procedure could as well be automated through image analysis algorithms to extract further information from the images such as vorticity and convection velocities.

The divergent views of the relationships between LREs, fish preference and turbulence should be addressed through a rigorous *in situ* experimentation such as suggested in Chapter 8. Fine-scale high frequency velocity measurements are required at a high spatial resolution to characterize the hydrodynamics at the fish holding location and over the surrounding substrate. Given the autonomous nature of fish, numerous fish should be investigated in order to generalize the results. Without such a thorough hydrodynamic analysis directly related to the fish and its *in situ* habitat at relevant Reynolds numbers this conflicting issue may be difficult to resolve.

BIBLIOGRAPHY

Acarlar, M.S. and C.R. Smith (1987) A study of hairpin vortices in a laminar boundary layer. Part 1/ Hairpin vortices generated by hemisphere protuberance, *Journal of Fluid Mechanics, 175*, 1-41.

Achenbach, E. (1974) Vortex shedding from spheres, *Journal of Fluid Mechanics*, *62*, 209-221.

Adrian, R.J., C.D. Meinhart, and C.D. Tomkins (2000) Vortex organization in the outer region of the turbulent boundary layer, *Journal of Fluid Mechanics*, *422*, 1-54.

Armstrong, J.D., P.S. Kemp, G.J.A. Kennedy, M. Ladle, and N.J. Milner (2003) Habitat requirements of Atlantic salmon and brown trout in rivers and streams, *Fisheries Research*, *62*, 143-170.

Arnold, G.P., P.W. Webb, and B.H. Holford (1991) The role of the pectoral fins in station-holding of Atlantic salmon parr (*Salmo salar L*), *Journal of Experimental Biology*, *156*, 625-629.

Babaeyan-Koopaei, K., D.A. Ervine, P.A. Carling, and Z. Cao (2002) Velocity and turbulence measurements for two overbank flow events in River Severn, *Journal of Hydraulic Engineering*, *128*, 891-900.

Bachman, R.A. (1984) Foraging behavior of free-ranging wild and hatchery brown trout in a stream, *Transactions of the American Fisheries Society*, *113*, 1-32.

Bakken, O.M., P.A. Krogstad, A. Ashrafian, and H.I. Andersson (2005) Reynolds number effects in the outer layer of the turbulent flow in a channel with rough walls, *Physics of Fluids* 17, 065101.

Batchelor, G.K. (1970) *The theory of homogeneous turbulence*, Cambridge University Press.

Bendat, J.S. and A.G. Piersol (1986) *Random data: analysis and measurement procedures*, John Wiley & Sons, New York.

Bennett, S.J. and J.L. Best (1995) Mean flow and turbulence structure over fixed, 2-dimensional dunes - implications for sediment transport and bedform stability, *Sedimentology*, *42*(3), 491-513.

Berkooz, G., P. Holmes, and J.L. Lumley (1993) The proper orthogonal decomposition in the analysis of turbulent flows, *Annual Review of Fluid Mechanics*, *25*, 539-575.

Best, J.L. (1993) On the interactions between turbulent flow structure, sediment transport and bedform development: some considerations from recent experimental research, in *Turbulence: perspectives on flow and sediment transport*, edited by N.J. Clifford, J.R. French, and J. Hardistry, pp. 61-92, John Wiley & Sons Ltd, Chicester.

Best, J.L. (1996) The fluid dynamics of small-scale alluvial bedforms, in *Advances in Fluvial Dynamics and Stratigraphy*, edited by P. Carling and M.R. Dawson, pp. 67-125, John Wiley & Sons, Chicester.

Best, J.L. and A.C. Brayshaw (1985) Flow separation - a physical process for the concentration of heavy minerals within alluvial channels, *Journal of the Geological Society of London*, *142*(5), 747-755.

Best, J.L. and A.G. Roy (1991) Mixing-layer distortion at the confluence of channels of different depth, *Nature*, 350, 411-412.

Biggs, B.J.F., M.J. Duncan, S.N. Francoeur, and W.D. Meyer (1997) Physical characterisation of microform bed cluster refugia in 12 headwater streams, New Zealand, *New Zealand Journal of Marine and Freshwater Research*, *31*, 413-422.

Billi, P. (1988) A note on cluster bedform behavior in a gravel-bed river, *Catena*, *15*, 473-481.

Biron, P., B. De Serres, A.G. Roy, and J.L. Best (1993) Shear layer turbulence at an unequal depth channel confluence, in *Turbulence: perspectives on flow and sediment transport*, edited by N.J. Clifford, J.R. French, J. and Hardisty, pp. 197-213, John Wiley & Sons Ltd., Chicester.

Biron, P.M., C. Robson, M.F. Lapointe, and S.J. Gaskin (2004) Comparing different methods of bed shear stress estimates in simple and complex flow fields, *Earth Surface Processes Landforms*, *29*(11), 1403-1415.

Blackwelder, R.F. and L.S. Kovasznay (1972) Time scales and correlations in a turbulent boundary layer, *Physics of Fluids*, *15*, 1545-1554.

Blackwelder, R.F. and H. Eckelman (1979) Streamwise vortices associated with the bursting phenomenon, *Journal of Fluid Mechanics*, *94*, 577-594.

Bogard, D.G. and W.G. Tiederman (1986) Burst detection with single-point velocity-measurements, *Journal of Fluid Mechanics*, *162*, 389-413.

Borcard, D. and P. Legendre (2002) All-scale spatial analysis of ecological data by means of principal coordinates of neighbour matrices, *Ecological Modelling*, *153*, 51-68.

Borcard, D., P. Legendre, C. Avois-Jacquet and H. Tuomisto (2004) Dissecting the spatial structure of ecological data at multiple scales, *Ecology*, *85*, 1826-1832.

Bouckaert, F.W. and J. Davis (1998) Microflow regimes and the distribution of macroinvertebrates around stream boulders, *Freshwater Biology*, 40, 77-86.

Bovee, K.D. (1978) *Probability of Use Criteria for the Family Salmonidae*, U.S.D.I., Fish and Wildlife Service, Office of Biological Services. Instream Flow Information Paper No. 4.

Boyer, C., A.G. Roy, and J.L. Best (2006) Dynamics of a river channel confluence with discordant beds: flow turbulence, bed load sediment transport, and bed morphology, *Journal of Geophysical Research-Earth Surface*, *111*, F04007, doi:10.1029/2005JF000458.

Bradshaw, P. (1971) *An introduction to turbulence and its measurement*, Pergamon Press, New York.

Bradshaw, P. and F.Y.F. Wong (1972) Reattachment and relaxation of a turbulent shear layer, *Journal of Fluid Mechanics*, 52, 113-135.

Bradshaw, P. (1987) Turbulent secondary flows, *Annual Review of Fluid Mechanics*, *19*, 53-74.

Brayshaw, A.C. (1984) Characteristics and origin of cluster bedforms in coarse-grained alluvial channels, in *Sedimentology of Gravels and Conglomerates*, edited by E.H. Koster and R.J. Steel, pp. 77-85, Canadian Society of Petroleum Geologists.

Brayshaw, A.C. (1985) Bed microtopography and entrainment thresholds in gravel-bed rivers, *Geologist Society of America Bulletin*, *96*, 218-223.

Brayshaw, A.C., L.F. Frostick, and I. Reid (1983) The hydrodynamics of particle clusters and sediment entrainments in coarse alluvial channels, *Sedimentology*, *30*, 137-143.

Bridge, J.S. and J. Jarvis (1977) Velocity profiles and bed shear stress over various bed configurations in a river bend, *Earth Surface Processes and Landforms*, *2*, 281-294.

Brind'Amour, A., D. Boisclair, P. Legendre and D. Borcard (2005) Multiscale spatial distribution of a littoral fish community in relation to environmental variables, *Limnology and Oceanography*, *50*, 465-479.

Browand, F.K. and P.D. Weidman (1976) Large scales in the developing mixing layer, *Journal of Fluid Mechanics*, *76*, 127-144.

Brown, G.L. and A.S.W. Thomas (1977) Large structure in a turbulent boundary-layer, *Physics of Fluids*, *20*, S243-S251.

Buffin-Bélanger, T. and A.G. Roy (1998) Effects of a pebble cluster on the turbulent structure of a depth-limited flow in a gravel-bed river, *Geomorphology*, *25*(3-4), 249-267.

Buffin-Bélanger T. and A.G. Roy (2003) On the use of the Reynolds number to scale the effects of obstacles on a depth-limited flow in a gravel-bed river, in *Reynolds number scaling in turbulent flow*, edited by A.J. Smits, pp. 301-304, Kluwer, Academic Publisher.

Buffin-Bélanger, T. and A.G. Roy (2005) 1 min in the life of a river: selecting the optimal record length for the measurement of turbulence in fluvial boundary layers, *Geomorphology*, *68*(1-2), 77-94.

Buffin-Bélanger, T., A.G. Roy, and A.D. Kirkbride (2000) On large-scale flow structures in a gravel-bed river, *Geomorphology*, *32*(3-4), 417-435.

Buffin-Bélanger T., A.G. Roy, and A.D. Kirkbride (2001b) Vers l'intégration des structures turbulentes de l'écoulement dans la dynamiques d'un cours d'eau à lit de graviers, *Géographie physique et Quaternaire*, *54*(1), 105-117.

Buffin-Bélanger, T., A.G. Roy, and M. Levasseur (2001a) Interactions entre les structures d'échappement et les structures a grande échelle dans l'écoulement turbulent des rivières a lit de graviers, *Revue des Sciences de l'Eau 14*(3), 381-407.

Buffin-Belanger, T., S. Rice, I. Reid and J. Lancaster (2006) Spatial heterogeneity of near-bed hydraulics above a patch of river gravel, *Water Resources Research*, *42*, W04413, doi:10.1029/2005WR004070.

Carling, P.A. (1992) The nature of the fluid boundary-layer and the selection of parameters for benthic ecology, *Freshwater Biology*, *28*, 273-284.

Cenedese, A., G.P. Romano, and F. Defelice (1991) Experimental testing of Taylor hypothesis by LDA in highly turbulent-flow, *Experiments in Fluids*, *11*(6), 351-358.

Chen, J. and F. Hu (2003) Coherent structures detected in atmospheric boundary-layer turbulence using wavelet transforms at Huaihe River basin, China, *Boundary-Layer Meteorology*, *107*, 429-444.

Church, M. (2007) Multiple scales in rivers, in *Gravel Bed Rivers VI*, edited by H. M. Habersack, H. Piégay, and M. Rinaldi, St. Jakob, Austria, Elsevier, in press.

Clifford, N.J. (1993) Formation of riffle pool sequences - field evidence for an autogenetic process, *Sedimentary Geology*, *85*, 39-51.

Clifford, N.J., K.S. Richards, and A. Robert (1992) The influence of microform bed roughness elements on flow and sediment transport in gravel bed rivers – comment, *Earth Surface Processes Landforms*, *17*(5), 529-534.

Clifford, N.J., P.J. Soar, O.P. Harmar, A.M. Gurnell, G.E. Petts, and J.C. Emery (2005) Assessment of hydrodynamic simulation results for eco-hydraulic and eco-hydrological applications: a spatial semivariance approach, *Hydrological Processes*, *19*(18), 3631-3648.

Coles, D. (1956) The law of the wake in the turbulent boundary layer, *Journal of Fluid Mechanics*, *1*, 191-226.

Cotel, A.J., P.W. Webb, and H. Tritico (2006) Do brown trout choose locations with reduced turbulence? *Transactions of the American Fisheries Society*, *135*, 610-619.

Coulombe-Pontbriand, M. and M. Lapointe (2004) Landscape controls on boulder-rich, winter habitat availability and their effects on Atlantic salmon (*Salmo salar*) parr abundance in two fifth-order mountain streams, *Canadian Journal of Fisheries and Aquatic Sciences*, *61*, 648-658.

Dal Cin, R. (1968) Pebble clusters: their origin and utilization in the study of paleocurrents, *Sedimentary Geology*, *2*, 233-241.

de Jong, C. and P. Ergenzinger (1995) The interrelations between mountain valley form and river-bed arrangement, in *River geomorphology*, edited by E.J. Hickin, pp. 55-91, John Wiley & Sons, Chichester.

De Serres, B., A.G. Roy, P.M. Biron, and J.L. Best (1999) Three-dimensional structure of flow at a confluence of river channels with discordant beds, *Geomorphology*, *26*, 313-335.

Dinehart, R.L. (1999) Correlative velocity fluctuations over a gravel river bed, *Water Resources Research*, *35*, 569-582.

Dolinsek, I.J., J.W.A. Grant, and P.M. Biron (2007a) The effect of habitat heterogeneity on the population density of juvenile Atlantic salmon *Salmo Salar L.*, *Journal of Fish Biology*, *70*, 206-214.

Dolinsek, I.J., P.M. Biron, and J.W.A. Grant (2007b) Assessing the effect of visual isolation on the population density of Atlantic salmon (*Salmo salar*) using GIS, *River Research and Applications*, *23*(7), 763-774.

Dombroski, D.E. and J.P. Crimaldi (2007) The accuracy of acoustic Doppler velocimetry measurements in turbulent boundary layer flows over a smooth bed, *Limnology and Oceanography-Methods*, *5*, 23-33.

Dray, S., P. Legendre, and P. R. Peres-Neto (2006) Spatial modelling: a comprehensive framework for principal coordinate analysis of neighbour matrices (PCNM), *Ecological Modelling, 196*, 483-493.

Duncan, W. J. (1970) *Mechanics of fluids*, American Elsevier Pub. Co., New York.

Emery, J.C., A.M. Gurnell, N.J. Clifford, G.E. Petts, I.P. Morrissey, and P.J. Soar (2003) Classifying the hydraulic performance of riffle-pool bedforms for habitat assessment and river rehabilitation design, *River Research and Applications*, *19*(5-6), 533-549.

Enders, E.C., D. Boisclair, and A.G. Roy, (2003) The effect of turbulence on the cost of swimming for juvenile Atlantic salmon (*Salmo salar*), *Canadian Journal of Fisheries and Aquatic Sciences*, *60* (9), 1149-1160.

Ezekiel, M. (1930) *Methods of correlation analysis*, John Wiley and Sons, New York.

Falco, R.E. (1977) Coherent motions in the outer region of turbulent boundary layers, *Physics of Fluids*, *20*, S124-S132.

Falco, R.E. (1991) A coherent structure model of the turbulent boundary layer and its ability to predict Reynolds number dependence, *Philosophical Transactions of the Royal Society of London Series A*, *336*, 103-129.

Fritsch, F.N. and R.E. Carlson (1980) Monotone piecewise cubic interpolation, *Siam Journal on Numerical Analysis*, *17*, 238-246.

Fuchs, H.V, E. Mercker, and U. Michel (1980) Mode expansion of coherent structures in the wake of a circular disk, in *Turbulent Shear Flows 2*, edited by L.J.S. Bradbury, F. Durst, B.E. Launder, F.W. Schmidt & J.H. Whitelaw, pp. 282-296, New York: Springer-Verlag.

Gerrard, J.H. (1966) The mechanics of the formation region of vortices behind bluff bodies, *Journal of Fluid Mechanics*, *25*, 401-413.

Ghisalberti, M. and H.M. Nepf (2002) Mixing layers and coherent Structures in vegetated aquatic flows, *Journal of Geophysical Research-Oceans*, *107*(12), 1277, doi:10.1029/2002WR001409.

Goring, D.G. and V.I. Nikora (2002) Despiking acoustic Doppler velocimeter data, *Journal of Hydraulic Engineering*, *128*(1), 117-126.

Grant, H.L. (1958) The large eddies of turbulent motion, *Journal of Fluid Mechanics*, *4*(2), 149-190.

Grass, A.J. (1971) Structural features of turbulent flow over smooth and rough boundaries, *Journal of Fluid Mechanics*, *50*, 233-255.

Grass, A.J., R.J. Stuart, and M. Mansour-Tehrani (1991) Vortical structures and coherent motion in turbulent-flow over smooth and rough boundaries, *Philosophical Transactions of the Royal Society of London Series A*, *336*, 35-65.

Grass, A.J. and M. Mansour-Tehrani (1996) Generalized scaling of coherent bursting structures in the near-wall region of turbulent flow over smooth and rough boundaries, in *Coherent Flow Structures in Open Channels*, edited by P.J. Ashworth, S.J. Bennett, J.L. Best, and S.J. McLelland, pp. 41-61, John Wiley & Sons Ltd., Chicester.

Hart, D.D., B.D. Clark, and A. Jasentuliyana (1996) Fine-scale field measurement of benthic flow environments inhabited by stream invertebrates, *Limnology and Oceanography*, *41*, 297-308.

Hart, D.D. and C.M. Finelli (1999) Physical-biological coupling in streams: the pervasive effects of flow on benthic organisms, *Annual Review of Ecology and Systematics*, *30*, 363-395.

Hasan, M.A.Z. (1992) The flow over a backward-facing step under controlled perturbation - laminar separation, *Journal of Fluid Mechanics*, *238*, 73-96.

Hassan, M.A. and I. Reid (1990) The influence of microform bed roughness elements on flow and sediment transport in gravel bed rivers, *Earth Surface Processes Landforms*, *15*(8), 739-750.

Herbich, J.B. and S. Shulits (1964) Large-scale roughness in open-channel flow, *Journal of the Hydraulics Division – ASCE*, *90*, 203-230.

Heggenes, J., S.J. Saltveit, D. Bird and R. Grew (2002) Static habitat partitioning and dynamic selection by sympatric young Atlantic salmon and brown trout in South-West England streams, *Journal of Fish Biology*, *60*, 72-86.

Hinze, J.O. (1959) *Turbulence*, McGraw-Hill, New York.

Hogan, D.L. and M. Church (1989) Hydraulic geometry in small, coastal streams - progress toward quantification of salmonid habitat, *Canadian Journal of Fisheries and Aquatic Sciences*, *46*, 844-852.

Holmes, P., J.L. Lumley, and G. Berkooz (1996) *Turbulence, coherent structures, dynamical systems and symmetry*, Cambidge University Press, Cambridge.

Hondzo, M. and H. Wang (2002) Effects of turbulence on growth and metabolism of periphyton in a laboratory flume, *Water Resources Research*, *38*(12), 1277, doi:10.1029/2002WR001409.

Hoover, T.M. and Ackerman, J.D. (2004) Near-bed hydrodynamic measurements above boulders in shallow torrential streams: implications for stream biota, *Journal of Environmental Engineering and Science*, *3*, 365-378.

Hussain, A.K.M.F. (1986) Coherent structures and turbulence, *Journal of Fluid Mechanics*, *173*, 303-356.

Hussain, A.K.M.F. and K.B.M.Q. Zaman (1985) An experimental study of organized motions in the turbulent plane mixing layer, *Journal of Fluid Mechanics*, *159*, 85-104.

Imamoto, H. and T. Ishigaki (1987) Visualization of longitudinal eddies in an open channel flow, in *Flow Visualisation IV* , edited by C. Véret, pp. 333-337, Hemisphere.

Jackson, R.G. (1976) Sedimentological and fluid-dynamic implications of the turbulent bursting phenomenon in geophysical flows, *Journal of Fluid Mechanics*, *77*, 531-560.

Jirka, G.H. (2001) Large scale flow structures and mixing processes in shallow flows, *Journal of Hydraulic Research*, *39*, 567-573.

Kadota, A. and I. Nezu (1999) Three-dimensional structure of space-time correlation on coherent vortices generated behind dune crest, *Journal of Hydraulic Research*, *37*(1), 59-80.

Kalleberg, H. (1958) Observations in a stream tank of territoriality and competition in juvenile salmon and trout (*Salmo salar L.* and *S. trutta L.*), Report of the Institute of Freshwater Research Drottingholm, *39*, 55–98.

Kaftori, D., G. Hetsroni, and S. Banerjee (1994) Funnel-shaped vortical structures in wall turbulence, *Physics of Fluids*, *6*, 3035-3050.

Kemp, P.S., J.D. Armstrong, and D.J. Gilvear (2005) Behavioural responses of juvenile Atlantic salmon (*Salmo salar*) to presence of boulders, *River Research and Applications*, *21*, 1053-1060.

Kim, K.C. and R.J. Adrian (1999) Very large-scale motion in the outer layer, *Physics of Fluids*, *11*, 417-422.

Kim, S.C., C.T. Friedrichs, J.P.Y. Maa, and L.D. Wright (2000) Estimating bottom stress in tidal boundary layer from acoustic Doppler velocimeter data, *Journal of Hydraulic Engineering*, *126*, 399-406.

Kirkbride, A.D. (1993) Observations of the influence of bed roughness on turbulence structure in depth limited flows over gravel beds, in *Turbulence, Perspectives on Flow and Sediment Transport*, edited by N.J. Clifford, J.R. French, and J. Hardistry, pp. 185-196, John Wiley & Sons, Chicester.

Kirkbride, A.D. and R. Ferguson (1995) Turbulent flow structure in a gravel-bed river: Markov chain analysis of the fluctuating velocity profile, *Earth Surface Processes Landforms*, *20*(8), 721-733.

Kironoto, B.A. and W.H. Graf (1994) Turbulence characteristics in rough uniform open-channel flow, *Proceedings of the Institution of Civil Engineers-Water Maritime and Energy*, *106*, 333-344.

Kline, S.J., W.C. Reynolds, F.A. Schraub, and P.W. Runstadler (1967) The structure of turbulent boundary layers, *Journal of Fluid Mechanics*, *95*, 741-773.

Komori, S., Y. Murakami, and H. Ueda (1989) The relationship between surface-renewal and bursting motions in an open-channel flow, *Journal of Fluid Mechanics*, *203*, 103-123.

Kostaschuk, R.A. and M.A. Church (1993) Macroturbulence generated by dunes – Fraser River, Canada, *Sedimentary Geology*, *85*, 25-37.

Krogstad, P.A. and R.A. Antonia (1999) Surface roughness effects in turbulent boundary layers, *Experiments in Fluids*, *27*, 450-460.

Krogstad, P.A., R.A. Antonia, and L.W.B. Browne (1992) Comparison between rough-wall and smooth-wall turbulent boundary-layers, *Journal of Fluid Mechanics*, *245*, 599-617.

Kucukali, S. and S. Cokgor (2007) Discussion of "Unobstructed and obstructed turbulent flow in gravel-bed rivers" by H.M. Tritico and R.H. Hotchkiss, *Journal of Hydraulic Engineering*, *133*, 117-118.

Lacoursiere, J.O. (1992) A laboratory study of fluid flow and microhabitat selection by larvae of simulium vittatum (diptera: simuliidae), *Canadian Journal of Zoology* 70 (3):582-596.

Lacey, R.W.J., and A.G. Roy (2006) Turbulent wake region of large roughness elements: combining flow visualization and high frequency velocity measurements, in *River Flow 2006: Proceedings of the International Conference on Fluvial Hydraulics, Lisbon, Portugal, 6-8 September 2006*, vol. 1, edited by R.M.L. Ferreira, E.C.T.L. Alves, J.G.A.B. Leal, and A. H. Cardoso, pp. 125-134, Taylor & Francis/Balkema, London.

Lacey, R.W.J., and A.G. Roy (2007a) A comparative study of the turbulent flow field with and without a pebble cluster in a gravel-bed river, *Water Resources Research*, *43*, W05502, doi:10.1029/2006WR005027.

Lacey, R.W.J., and A.G. Roy (2007b) The use of concurrent ADV and flow visualization in exploring in situ coherent flow structures, in *Proceedings of 32nd IAHR Congress, Venice, Italy, 1-6 July 2007*, 9p, CD-ROM.

Lacey, R.W.J. and A.G. Roy (2007c) Fine-scale characterization of the turbulent shear layer of an instream pebble cluster, *Journal of Hydraulic Engineering, in press.*

Lacey, R.W.J., Legendre, P. and A.G. Roy (2007) Spatial scale partitioning of in situ turbulent flow data over a pebble cluster in a gravel-bed river. *Water Resources Research*, *43*, W03416, doi:10.1029/2006WR005044.

Lamarre, H. and A.G. Roy (2001) Organisation morphologique des blocs et des amas de galets dans les cours d'eau a lit de graviers, *Géographie physique et Quaternaire*, *55*(3), 275-287.

Lamarre, H. and A.G. Roy (2005) Reach scale variability of turbulent flow characteristics in a gravel-bed river, *Geomorphology*, *68*, 95-113.

Lane, S.N., P.M. Biron, K.F. Bradbrook, J.B. Butler, J.H. Chandler, M.D. Crowell, S.J. Mclelland, K.S. Richards, and A.G. Roy (1998) Three-dimensional measurement of river channel flow processes using acoustic Doppler velocimetry, *Earth Surface Processes Landforms*, *23*(13), 1247-1267.

Lane, S.N., K.F. Bradbrook, K.S. Richards, P.M. Biron, and A.G. Roy (2000) Secondary circulation cells in river channel confluences: measurement artefacts or coherent flow structures? *Hydrological Processes*, 14, 2047-2071.

Lapointe, M. (1992) Burst-like sediment suspension events in a sand bed river, *Earth Surface Processes and Landforms*, *17*, 253-270.

Lawless, M. and A. Robert (2001a) Scales of boundary resistance in coarse-grained channels: turbulent velocity profiles and implications, *Geomorphology*, *39*, 221-238.

Lawless, M. and A. Robert (2001b) Three-dimensional flow structure around small-scale bedforms in a simulated gravel-bed environment, *Earth Surface Processes Landforms*, *26*(5), 507-522.

Leclair, S.F. and A.G. Roy (1997) Variability of bed morphology and sedimentary structures at a discordant river confluence during low flows. *Géographie Physique et Quaternaire*, *51*, 125-139.

Leeder, M. R. (1983) On the interactions between turbulent flow, sediment transport and bedform mechanics in channelized flows, *International Association of Sedimentologists Special Publication*, *6*, 5-18.

Legendre, P. and D. Borcard (2006) Quelles sont les échelles spatiales importantes dans un écosystème? in *Analyse Statistique de Données Spatiales*, edited by J.-J. Droesbeke, M. Lejeune and G. Saporta, pp 425- 442, Éditions TECHNIP, Paris.

Legendre, P. and L. Legendre (1998) *Numerical Ecology*, Elsevier, Amsterdam.

Liao, J.C., D.N. Beal, G.V. Lauder, and M.S. Triantafyllou (2003a) The Karman gait: novel body kinematics of rainbow trout swimming in a vortex street, *Journal of Experimental Biology*, *206*, 1059-1073.

Liao, J.C., D.N. Beal, G.V. Lauder, and M.S. Triantafyllou (2003b) Fish exploiting vortices decrease muscle activity, *Science*, *302*, 1566-1569.

Liao, J.C. (2007) A review of fish swimming mechanics and behaviour in altered flows, *Philosophical Transactions of the Royal Society B*, doi:10.1098/rstb.2007.2082, *Available online*.

Ligrani, P.M. and R.J. Moffat, (1986) Structure of transitionally rough and fully rough turbulent boundary-layers, *Journal of Fluid Mechanics*, *162* , 69-98.

Lin, J.C., J. Towfighi, and D. Rockwell (1995) Instantaneous structure of the near-wake of a circular-cylinder - on the effect of Reynolds number, *Journal of Fluids and Structures*, *9*, 409-418.

Liu, Z., R.J. Adrian, and T.J. Hanratty (2001) Large-scale modes of turbulent channel flow: transport and structure, *Journal of Fluid Mechanics*, *448*, 53-80.

Luchick, T.S. and W.G. Tiederman (1987) Timescale and structure of ejections and bursts in turbulent channel flows, *Journal of Fluid Mechanics*, *174*, 529-552.

Lu, S.S. and W.W. Willmarth (1973) Measurements of the structure of the Reynolds stress in a turbulent boundary layer, *Journal of Fluid Mechanics*, *60*, 481-511.

Marquis, G.A. and A.G. Roy (2006a) Effect of flow depth and velocity on the scales of macroturbulent structures in gravel-bed rivers, *Geophysical Research Letters*, *33*, L24406, doi:10.1029/2006GL028420.

Marquis, G., and A.G. Roy (2006b) Turbulent processes at the entrance of a pool using flow visualization, in *River Flow 2006: Proceedings of the International Conference on Fluvial Hydraulics, Lisbon, Portugal, 6-8 September 2006*, vol. 1, edited by R.M.L. Ferreira, E.C.T.L. Alves, J.G.A.B. Leal, and A. H. Cardoso, pp. 109-118, Taylor & Francis/Balkema, London.

McLean, S.R., J.M. Nelson, and S.R. Wolfe (1994) Turbulence structure over 2-dimensional bed forms - implications for sediment transport, *Journal of Geophysical Research-Oceans*, *99*, 12729-12747.

Mirajgaoker, A.G. and K.L.N. Charlu (1963) Natural roughness effects in rigid open channels, *Journal of the Hydraulic Division*, *89*, 29-44.

Mitchell, J., R.S. McKinley, G. Power, and D.A. Scruton (1998) Evaluation of Atlantic salmon parr responses to habitat improvement structures in an experimental channel in Newfoundland, Canada, *Regulated Rivers-Research & Management*, *14*, 25-39.

Moin, P. and R.D. Moser (1989) Characteristic-eddy decomposition of turbulence in a channel, *Journal of Fluid Mechanics*, *200*, 471-509.

Monin, A. S. and A.M. Yaglom (1971) *Statistical Fluid Mechanics*, Vol 1., edited by J. Lumley, MIT Press, Cambridge, Mass.

Morris, H.M. (1955) A new concept of flow in rough conduits, *Transactions – ASCE*, *120*, 373-410.

Mulhearn, P.J. (1978) A wind-tunnel boundary-layer study of the effects of a surgace roughness change: rough to smooth, *Boundary-Layer Meteorology*, *15*, 3-30.

Muller, A. and A. Gyr (1986) On the vortex formation in the mixing layer behind dunes, *Journal of Hydraulic Research*, *24*, 359-375.

Nakagawa, H. and I. Nezu (1977) Prediction of the contributions to the Reynolds stress from bursting events in open-channel flows, *Journal of Fluid Mechanics*, *80*(1), 99-128.

Nakagawa, H. and I. Nezu (1981) Structure of space-time correlations of bursting phenomena in an open-channel flow, *Journal of Fluid Mechanics*, *104*, 1-43.

Nakamura, Y. (1996) Vortex shedding from bluff bodies and a universal Strouhal number, *Journal of Fluids and Structures*, *10*, 159-171.

Nelson, J.M., S.R. McLean, and S.R. Wolfe (1993) Mean flow and turbulence fields over two-dimensional bed forms. *Water Resources Research*, 29, 3935-3953.

Newson, M.D. and C.L. Newson (2000) Geomorphology, ecology and river channel habitat: mesoscale approaches to basin-scale challenges, *Progress in Physical Geography*, *24*(2), 195-217.

Nezu, I. and H. Nakagawa (1989) Turbulent structure of backward-facing step flow and coherent vortex shedding from reattachment in open-channel flows, in *Turbulent Shear Flows 6*, edited by J.-C. Andre, J. Cousteix, F. Durst, B.E. Launder, F.W. Schmidt, and Whitela, pp. 313-337, Springer-Verlag, Berlin.

Nezu, I. and H. Nakagawa (1993) *Turbulence in Open-channel Flows*, A.A. Balkema, Rotterdam.

Nikora, V. (1999) Origin of the "-1" spectral law in wall-bounded turbulence, *Physical Review Letters*, *83*(4), 734-736.

Nikora, V. (2007) Hydrodynamic effects in gravel-bed rivers: from micro- to macro- turbulence, in *Gravel Bed Rivers VI*, edited by H. M. Habersack, H. Piégay, and M. Rinaldi, St. Jakob, Austria, Elsevier, in press.

Nikora, V.I. and D.G. Goring (1998) ADV measurements of turbulence: can we improve their interpretation? *Journal of Hydraulic Engineering*, *124*(6), 630-634.

Nikora, V.I. and D.G. Goring (2000) Flow turbulence over fixed and weakly mobile gravel beds, *Journal of Hydraulic Engineering*, *126*(9), 679-690.

Nikora, V.I., D.G. Goring, and B.J.F. Biggs (2002b) Some observations of the effects of micro-organisms growing on the bed of an open channel on the turbulence properties, *Journal of Fluid Mechanics*, 450, 317-341.

Nikora, V., D. Goring, and A. Ross (2002a) The structure and dynamics of the thin near-bed layer in a complex marine environment: a case study in Beatrix Bay, New Zealand, *Estuarine Coastal and Shelf Science*, *54*, 915-926.

Nikora, V.I. and G.M. Smart (1997) Turbulence characteristics of New Zealand gravel-bed rivers, *Journal of Hydraulic Engineering*, *123*, 764-773.

Nowell, A.R.M. and M. Church (1979) Turbulent flow in a depth-limited boundary layer, *Journal of Geophysical Research*, *84*, 4816-4824.

Ovidio, M., E.C. Enders, E.J. Hallot, M.L. Roy, J.C. Philippart, F. Petit, and A.G. Roy (2007) Mobility and home-range use of Atlantic salmon parr over short time scales, *Aquatic Living Resources*, *20*, 95-101.

Paiement-Paradis, G., T. Buffin-Bélanger, and A.G. Roy (2003) Scalings for large turbulent flow structures in gravel-bed rivers, *Geophysical Research Letters*, 30(14), 1773, doi:10.1029/2003GL017553.

Paola, C., G. Gust, and J.B. Southard (1986) Skin friction behind isolated hemispheres and the formation of obstacle marks, *Sedimentology*, *33*, 279-293.

Papanicolaou, A.N. and R. Hilldale (2002) Turbulence characteristics in gradual channel transition, *Journal of Engineering Mechanics*, *128*, 948-960.

Peres-Neto, P.R., P. Legendre, S. Dray and D. Borcard (2006) Variation partitioning of species data matrices: estimation and comparison of fractions, *Ecology*, *87*, 2614-2625.

Perry, A.E., S.M. Henbest, and M.S. Chong (1986) A theoretical and experimental-study of wall turbulence, *Journal of Fluid Mechanics*, *165*, 163-199.

Perry, A.E., K.L. Lim, and S.M. Henbest (1987) An experimental-study of the turbulence structure in smooth-wall and rough-wall boundary-layers. *Journal of Fluid Mechanics*, *177*, 437-466.

Quinn, J.M., C.W. Hickey, and W. Linklater (1996) Hydraulic influences on periphyton and benthic macroinvertebrates: simulating the effects of upstream bed roughness, *Freshwater Biology*, *35*, 301-309.

Ranga Raju, K.G.R., G.L. Asawa, and H.K. Mishra (2000) Flow-establishment length in rectangular channels and ducts, *Journal of Hydraulic Engineering*, *126*, 533-539.

Raupach, M.R. (1981) Conditional statistics of Reynolds stress in rough-wall and smooth-wall turbulent boundary-layers, *Journal of Fluid Mechanics*, *108*, 363-382.

Raupach, M.R., J.J. Finnigan, and Y. Brunet (1996) Coherent eddies and turbulence in vegetation canopies: the mixing-layer analogy, *Boundary-Layer Meteorology*, *78*, 351-382.

Raupach, M.R., A.S. Thom, and I. Edwards (1980) A wind-tunnel study of turbulent-flow close to regularly arrayed rough surfaces, *Boundary-Layer Meteorology*, *18*, 373-397.

Reid, I., L.E. Frostick, and A.C. Brayshaw (1992) Microform roughness elements and the selective entrainment and entrapment of particles in gravel-bed rivers, in *Dynamics of Gravel-bed Rivers*, edited by P. Billi, R.D. Hey, C.R. Thorne, and P. Tacconi, pp. 253-276, John Wiley & Sons, Chichester.

Rhoads, B.L. and A.N. Sukhodolov (2004) Spatial and temporal structure of shear layer turbulence at a stream confluence, *Water Resources Research*, *40*, W06304, doi:10.1029/2003WR002811.

Robert, A. (1990) Boundary roughness in coarse-grained channels, *Progress in Physical Geography*, *14*, 42-70.

Robert, A., A.G. Roy, and B. Deserres (1992) Changes in velocity profiles at roughness transitions in coarse-grained channels, *Sedimentology*, *39*(5), 725-735.

Robert, A., A.G. Roy, and B. Deserres (1996) Turbulence at a roughness transition in a depth limited flow over a gravel bed, *Geomorphology*, *16*, 175-187.

Robinson, S.K. (1991) Coherent motions in the turbulent boundary-layer, *Annual Review of Fluid Mechanics*, *23*, 601-639.

Robson, B.J., E.T. Chester, and J.A. Davis (1999) Manipulating the intensity of near-bed turbulence in rivers: effects on benthic invertebrates, *Freshwater Biology*, *42*, 645-653.

Rockwell, D. (1998) Vortex-body interactions, *Annual Review of Fluid Mechanics*, *30*, 199-229.

Roshko, A. (1961) Experiments on the flow past a circular cylinder at very high Reynolds number, *Journal of Fluid Mechanics*, *10*, 345-356.

Roy, A.G., P.M. Biron, T. Buffin-Bélanger, and M. Levasseur (1999) Combined visual and quantitative techniques in the study of natural turbulent flows, *Water Resources Research*, *35*, 871-877.

Roy, A.G., P.M. Biron, and M.F. Lapointe (1997) Implications of low-pass filtering on power spectra and autocorrelation functions of turbulent velocity signals, *Mathematical Geology*, *29*(5), 653-668.

Roy, A.G. and T. Buffin-Bélanger (2001) Advances in the study of turbulent flow structures in gravel-bed rivers, in *Gravel-Bed Rivers V*, edited by P. Mosley, pp. 375-404, New Zealand Hydrological Society

Roy, A.G., T. Buffin-Bélanger, and S. Deland (1996) Scales of turbulent coherent flow structures in a gravel bed river, in *Coherent Flow Structures in Open Channels*, edited by P.J. Ashworth, S.J. Bennett, J.L. Best, and S.J. McLelland, pp. 147-164, John Wiley & Sons Ltd., Wallingford, U.K.

Roy, A.G., T. Buffin-Bélanger, H. Lamarre, and A.D. Kirkbride (2004) Size, shape and dynamics of large-scale turbulent flow structures in a gravel-bed river, *J. Fluid Mech.*, *500*, 1-27.

Rubin, D.M. and R.R. McDonald (1995) Nonperiodic eddy pulsations, *Water Resources Research*, *31*, 1595-1605.

Sambrook Smith, G.H. and A.P. Nicholas (2005) Effect on flow structure of sand deposition on a gravel bed: results from a two-dimensional flume experiment, *Water Resources Research*, *41*, W10405, doi:10.1029/2004WR003817.

Shamloo, H., N. Rajaratnam, and C. Katopodis (2001) Hydraulics of simple habitat structures, *Journal of Hydraulic Resources*, *39*(4), 351-366.

Shvidchenko, A.B. and G. Pender (2001) Macroturbulent structure of open-channel flow over gravel beds, *Water Resources Research*, *37*(3), 709-719.

Simpson, R.L. (1989) Turbulent boundary-layer separation, *Annual Review of Fluid Mechanics*, *21*, 205-234.

Simpson, R.L., Y.T. Chew, and B.G. Shivaprasad (1981) The structure of a separating turbulent boundary-layer. Part 1. Mean flow and Reynolds stresses, *Journal of Fluid Mechanics*, *113*, 23-51.

Singh, S.P. and S. Mittal (2005) Flow past a cylinder: shear layer instability and drag crisis, *International Journal for Numerical Methods in Fluids*, 47, 75-98.

Smart, G.M. (1999) Turbulent velocity profiles and boundary shear in gravel bed rivers, *Journal of Hydraulic Engineering*, 125, 106-116.

Smith, C.R. (1996) Coherent flow structures in smooth-wall turbulent boundary layers: facts, mechanisms and speculation, in *Coherent Flow Structures in Open Channels*, edited by P.J. Ashworth, S.J. Bennett, J.L. Best, and S.J. McLelland, pp. 1-39, John Wiley & Sons, Chichester.

Smith, C.R., J.D.A. Walker, A.H. Haidari, and U. Sobrun (1991) On the dynamics of near-wall turbulence, *Philosophical Transactions of the Royal Society of London Series A*, 336, 131-175.

Smith, D.L., E.L. Brannon, and M. Odeh (2005) Response of juvenile rainbow trout to turbulence produced by prismatoidal shapes, *Transactions of the American Fisheries Society*, *134*, 741-753.

Smith, D.L., E.L. Brannon, B. Shafii, and M. Odeh (2006) Use of the average and fluctuating velocity components for estimation of volitional rainbow trout density, *Transactions of the American Fisheries Society*, *135*, 431-441.

Smith, J.A. and A.J. Dartnall (1980) Boundary layer control by water pennies (*Coleoptera : Psephenidae*), *Aquatic Insects*, *2*, 65-72.

Snyder, W.H. and I.P. Castro (1999) Acoustic Doppler velocimeter evaluation in stratified towing tank, *Journal of Hydraulic Engineering*, 125 , 595-603.

Song, T. and Y.M. Chiew (2001) Turbulence measurement in nonuniform open-channel flow using acoustic Doppler velocimeter (ADV), *Journal of Engineering Mechanics*, *127*, 219-232.

Soulsby, R.L. (1977) Similarity scaling of turbulence spectra in marine and atmospheric boundary layers, *Journal of Physical Oceanography*, *7*, 934-937.

Soulsby, R.L. (1980) Selecting record length and digitization rate for near-bed turbulence measurements. *Journal of Physical Oceanography*, *10*, 208-219.

Soulsby, R.L. (1983) The bottom boundary layer of shelf seas, in *Physical Oceanography of Coastal and Shelf Seas*, edited by B. Johns, pp. 189-267, Elsevier, Amsterdam.

Stapleton, K.R. and D.A. Huntley (1995) Seabed stress determinations using the inertial dissipation method and the turbulent kinetic energy method, *Earth Surface Processes and Landforms*, 20, 807-815.

Statzner, B., J.A. Gore, and V.H. Resh (1988) Hydraulic stream ecology: observed patterns and potential applications, *Journal of the North American Benthological Society*, *7*(4), 307-360.

Statzner, B. and T.F. Holm (1982) Morphological adaptations of benthic invertebrates to stream flow – an old question studied by means of a new technique (laser Doppler anemometry), *Oecologia*, *53*(3), 290-292.

Strom, K.B., A.N. Papanicolaou, and G. Constantinescu (2007) Flow heterogeneity over 3D cluster microform: laboratory and numerical investigation, *Journal of Hydraulic Engineering*, *133*(3), 273-287.

Sukhodolov, A.N. and B.L. Rhoads (2001) Field investigation of three-dimensional flow structure at stream confluences. 2. Turbulence, *Water Resources Research*, *37*(9), 2411-2424.

Taneda, S. (1978) Visual observations of the flow past a sphere at Reynolds numbers between 10^4 and 10^6, *Journal of Fluid Mechanics*, *85*(part 1), 187-192.

Tennekes, H. and J.L. Lumley (1972) *A first course in turbulence*, MIT Press, London.

ter Braak, C.J.F. (1994) Canonical community ordination. Part I: basic theory and linear methods, *Écoscience*, *41*, 127-140.

ter Braak, C. J. F. and P. Smilauer (2002) *Canoco reference manual and CanoDraw for Windows user's guide: software for canonical community ordination*, version 4.5, Microcomputer Power, Ithaca, New York.

Thomson, J.R., M.P. Taylor, K.A. Fryirs, and G.J. Brierley (2001) A geomorphological framework for river characterization and habitat assessment, *Aquatic Conservation-Marine and Freshwater Ecosystems*, *11*(5), 373-389.

Thompson, C.E.L., C.L. Amos, T.E.R. Jones, and J. Chaplin (2003) The manifestation of fluid-transmitted bed shear stress in a smooth annular flume - a comparison of methods, *Journal of Coastal Research 19*, 1094-1103.

Townsend, A. A. (1976) *The structure of turbulent shear flow*, Cambridge University Press, Cambridge.

Tritico, H.M. and R.H. Hotchkiss (2005) Unobstructed and obstructed turbulent flow in gravel bed rivers, *Journal of Hydraulic Engineering*, *131*(8), 635-645.

Tritton, D.J. (1988) *Physical Fluid Dynamics*, 2ed., Oxford University Press, New York.

Uijttewaal, W.S.J. and J. Tukker (1998) Development of quasi two-dimensional structures in a shallow free-surface mixing layer, *Experiments in Fluids*, *24*(3), 192-200.

Van Zyll de Jong, M.C., I.G. Cowx, and D.A. Scruton (1997) An evaluation of instream habitat restoration techniques on salmonid populations in a Newfoundland stream, *Regulated Rivers-Research & Management*, *13*(6), 603-614.

Vehanen, T., A. Huusko, T. Yrjana, M. Lahti, and A. Maki-Petays (2003) Habitat preference by grayling (*Thymallus thymallus*) in an artificially modified, hydropeaking riverbed: a contribution to understand the effectiveness of habitat enhancement measures, *Journal of Applied Ichthyology*, *19*, 15-20.

Venditti, J.G. and B.O. Bauer (2005) Turbulent flow over a dune: Green River, Colorado, *Earth Surface Processes Landforms*, *30*(3), 289-304.

Voulgaris, G. and J.H. Trowbridge (1998) Evaluation of the acoustic Doppler velocimeter (ADV) for turbulence measurements, *Journal of Atmospheric and Oceanic Technology*, *15*(1), 272-289.

Webel, G. and M. Schatzmann (1984) Transverse mixing in open channel flow, *Journal of Hydraulic Engineering*, *110*, 423-435.

Welch, P.D. (1967) The use of fast Fourier transform for the estimation of power spectra, *IEEE Transactions on Audio and Electroacoustics*, *15*(2), 70-73.

Wilcock, P.R. (1996) Estimating local bed shear stress from velocity observations, *Water Resources Research*, *32*, 3361-3366.

Williams, J.J., P.D. Thorne, and A.D. Heathershaw (1989) Measurements of turbulence in the benthic boundary-layer over a gravel bed, *Sedimentology*, *36*(6), 959-971.

Williamson, C.H.K. (1996) Vortex dynamics in the cylinder wake, *Annual Review of Fluid Mechanics*, 28, 477-539.

Winant, C.D. and F.K. Browand (1974) Vortex pairing: the mechanism of turbulent mixing-layer growth at moderate Reynolds number, *Journal of Fluid Mechanics*, *63*(2), 237-255.

Wittenberg, L. and M.D. Newson (2005) Particle clusters in gravel-bed rivers: an experimental morphological approach to bed material transport and stability concepts, *Earth Surface Processes and Landforms*, *30*, 1351-1368.

Wooding, R.A., F.E. Bradley, and J.K. Marshall (1973) Drag due to regular arrays of roughness elements of varying geometry, *Boundary-Layer Meteorology*, *5*, 285-308.

Yalin, M.S. (1992) *River Mechanics*, Pergamon Press, New York.

APPENDIX B – AUTORISATION DE RÉDIGER LA THÈSE SOUS FORME D'ARTICLES